




**ADVERTIMENT.** L'accés als continguts d'aquesta tesi queda condicionat a l'acceptació de les condicions d'ús establertes per la següent llicència Creative Commons:  <https://creativecommons.org/licenses/?lang=ca>

**ADVERTENCIA.** El acceso a los contenidos de esta tesis queda condicionado a la aceptación de las condiciones de uso establecidas por la siguiente licencia Creative Commons:  <https://creativecommons.org/licenses/?lang=es>

**WARNING.** The access to the contents of this doctoral thesis it is limited to the acceptance of the use conditions set by the following Creative Commons license:  <https://creativecommons.org/licenses/?lang=en>

# Harnessing topology in photonic waveguide systems

David Viedma Palomo

Submitted in fulfillment of  
the requirements for the degree of  
Doctor of Physics

Thesis supervisor:  
Prof. Verònica Ahufinger Breto

Departament de Física  
Universitat Autònoma de Barcelona

Bellaterra, September 2024





*A mis padres,  
por todo lo que me han dado.*



---

## Acknowledgments

---

Con estas líneas pongo el broche final a mi etapa como doctorando. Durante estos cuatro años he vivido multitud de experiencias que me han enriquecido como profesional y como persona. He sufrido y tenido malos momentos, pero también he podido sentir la profunda satisfacción de ver cómo mi esfuerzo se convertía en trabajos cada vez mejores, más variados y, para mí, más interesantes. Y también, de poder disfrutar de la Física que tanto me gusta de una forma nueva, más profunda y la vez más divertida. Obviamente, no podría haber llegado hasta aquí yo solo. Por ello, me gustaría dedicar unas palabras de cariño a todas las personas que han contribuido a que pueda decir, con orgullo, que estoy listo para ser doctor.

Els agraïments més grans són sense dubte per la Verònica. Tan bona persona com professional, és gràcies al seu esforç incansable que aquesta tesi existeix. Malgrat que la seva llibreta de coses per fer s'omple més ràpidament del que es buida, sempre ha trobat temps per ajudar-me i guiar-me; però també m'ha donat la independència per explorar idees i treballar al meu ritme, cosa que m'ha facilitat molt les coses. Els seus consells i correccions m'han fet millorar molt i, tot i que potser li agrada una mica massa utilitzar el boli violeta, per sort amb el temps cada vegada l'ha hagut de fer servir menys. Moltíssimes gràcies per aquests quatre anys, espero no haver-te donat més mals de cap dels necessaris. I malgrat que encara m'hauràs d'aguantar uns pocs mesos més, espero que com a mínim el record que t'emportis de mi sigui la meitat de bo del que m'emporto jo de tu.

També m'agradaria donar les gràcies al Jordi que, tot i que va abandonar el vaixell relativament aviat per vestir la blaugrana, em va ajudar molt a les primeres etapes del doctorat, quan encara anava molt perdut.

I also want to give heartfelt thanks to Anselmo and Ricardo for how warmly they welcomed me in Aveiro during my stay, where they made sure that I felt at home. The

latter part of the thesis is also directly thanks to them. Through our many discussions and collaborations, they rekindled my passion for Physics when I was at a low point, and for that I will always be grateful. I especially want to thank Anselmo, with whom I have spent the most hours discussing our works and physics in general, it has been really fun to learn from you.

I am grateful to Prof. Alexander Szameit for allowing me to spend two weeks at his group. It was very interesting to catch a glimpse of the experimental side of things. I also want to thank Profs. Rodrigo Vicencio and Marco Ornigotti for their careful reports of this manuscript, and Profs. Anna Sanpera, Christina Jörg and Nathan Goldman for agreeing to be part of the thesis committee.

També vull agrair als meus companys de despatx: el Josep, l'Eulàlia i més recentment el Yunjia. Tot i la meva tendència a teletreballar, i que majoritàriament treballem en temes diferents, he tingut el plaer de parlar amb ells tant de temes de Física, com de la vida en general. No em vull oblidar de l'Alessio, l'Ayaka, l'Adam, el Claudio, la Julia, el Marc i la resta de la família QAOS, amb qui he pogut compartir dinars, sopars i molts cafès. Tambien quiero mencionar a nuestros vecinos clásicos, en especial a Irene y Mónica, que siempre me chinchán por no ir a la UAB, pero luego hay que pedirles cita para tomar un café. También a Albert y Carla, con quien compartí asignatura además de con Irene. La parte de docencia de la tesis ha sido inesperadamente entretenida, y agradezco a los alumnos que se interesaron en hacerme preguntas que iban más allá de la asignatura.

Fuera de lo académico, quiero agradecer a todas las personas que me han acompañado en esta etapa tan convulsa. Empezando por mis padres, que siempre me han dado apoyo incondicional, cariño y amor, y a los cuales dedico esta tesis. También quiero agradecer a mis amigos de toda la vida, Kilian, Rubén y Víctor, por todos los momentos que hemos compartido. A mis compañeras físicas, Mireia y Sofía, con quienes me alegro mucho de haber conseguido mantener el contacto tras la carrera. Y a Aitor, quien más que un amigo es ya para mí un hermano.

Y por último, quiero darle las gracias a Indira, mi compañera vital y mi mejor amiga. Me faltan palabras para agradecer lo que me has cuidado y arropado, sin ti dudo que hubiera podido siquiera empezar este camino. Estoy emocionado por lo que nos queda por vivir juntos, y espero que podamos seguir celebrando los éxitos del otro durante mucho tiempo.

*David Viedma Palomo*  
*Bellaterra, Septiembre de 2024.*

---

## List of publications by David Viedma

---

The research contained in this thesis is supported by the following publications:

### Chapter 3: Stark-Chirped Rapid-Adiabatic-Passage in Optical Waveguides

1. D. Viedma, V. Ahufinger and J. Mompart, *Supersymmetry-enhanced Stark-Chirped Rapid Adiabatic-Passage in multimode optical waveguides*, [Optics Express](#) **29**(24), 39200 (2021).
2. D. Viedma, J. Mompart and V. Ahufinger, *Mode pumping in photonic lattices using a single tailored auxiliary waveguide*, [Phys. Rev. A](#) **107**(2), 023506 (2023).

### Chapter 4: Topological pumping with Supersymmetry

3. D. Viedma, G. Queraltó, J. Mompart, V. Ahufinger, *High-efficiency topological pumping with discrete supersymmetry transformations*, [Optics Express](#) **30**(13), 23531 (2022).

### Chapter 5: Effective topological systems in a photonic diamond chain

4. D. Viedma, A. Marques, R. Dias, V. Ahufinger, *Flux-mediated effective Su-Schrieffer-Heeger model in an impurity decorated diamond chain*, [arXiv:2407.15789](#) (2024). Submitted to Communications Physics.
5. A. Marques, D. Viedma, V. Ahufinger, R. Dias, *Impurity flat band states in the diamond chain*, [arXiv:2407.14405](#) (2024). Submitted to APL Photonics.

**Chapter 6: Root topological insulators of arbitrary order in Non-Hermitian photonic ring resonators**

6. D. Viedma, A. M. Marques, R. G. Dias and V. Ahufinger, *Topological  $n$ -root Su-Schrieffer-Heeger model in a non-Hermitian photonic ring system*, [Nanophotonics](#), **13**(1), 51 (2024).

Other publications by David Viedma not included in this thesis:

7. D. Viedma and M. Modugno, *Effective self-similar expansion of a Bose-Einstein condensate: Free space versus confined geometries*, [Phys. Rev. Research](#) **2**(3), 033478 (2020).

---

## Contents

---

<b>Acknowledgments</b>	<b>i</b>
<b>List of Publications</b>	<b>iii</b>
<b>1 Introduction</b>	<b>1</b>
<b>2 Theoretical foundations</b>	<b>9</b>
2.1 Light propagation in optical waveguides . . . . .	10
2.1.1 Electromagnetism and light propagation . . . . .	10
2.1.2 Optical waveguides . . . . .	11
2.1.3 Coupled-mode model . . . . .	20
2.1.4 Coupling between OAM modes . . . . .	26
2.1.5 Fabrication of optical waveguides . . . . .	29
2.1.6 Optical waveguides as quantum simulators . . . . .	30
2.2 Supersymmetry in optics . . . . .	32
2.2.1 SUSY formalism . . . . .	33
2.2.2 SUSY in optical waveguides . . . . .	36
2.2.3 Discrete Supersymmetry . . . . .	38
2.2.4 2D Supersymmetry . . . . .	42
2.3 Topology in optics . . . . .	43
2.3.1 Basics of topology . . . . .	43
2.3.2 Su-Schrieffer-Heeger model . . . . .	49
2.3.3 Square-root topology . . . . .	53



<b>3</b>	<b>Mode demultiplexing and topological mode engineering with Stark-chirped rapid-adiabatic-passage in coupled waveguides</b>	<b>59</b>
3.1	Introduction . . . . .	60
3.2	SCRAP in optical waveguides . . . . .	62
3.2.1	Combining SCRAP with Supersymmetry . . . . .	66
3.2.2	SCRAP in lattices of optical waveguides . . . . .	67
3.3	Applications for multimode optical waveguides . . . . .	69
3.3.1	Mode demultiplexing . . . . .	70
3.3.2	SUSY-enhanced demultiplexing . . . . .	72
3.3.3	Excitation of the $TE_1^{(1)}$ mode . . . . .	73
3.3.4	Exciting higher-order modes . . . . .	74
3.4	Applications for discrete waveguide lattices . . . . .	74
3.4.1	Single auxiliary waveguide . . . . .	76
3.4.2	Auxiliary lattice . . . . .	81
3.5	Conclusions . . . . .	85
<b>4</b>	<b>Exciting topological modes with single-waveguide injection via discrete Supersymmetry transformations</b>	<b>87</b>
4.1	Introduction . . . . .	88
4.2	Theoretical background . . . . .	89
4.3	Physical system . . . . .	91
4.4	Results . . . . .	93
4.4.1	Edge state . . . . .	93
4.4.2	Interface state . . . . .	97
4.4.3	Quasi-degenerate and bulk states . . . . .	101
4.5	Conclusions . . . . .	102
<b>5</b>	<b>Effective topological impurity systems in a diamond chain of optical waveguides guiding orbital angular momentum modes</b>	<b>105</b>
5.1	Introduction . . . . .	106
5.2	Diamond chain . . . . .	107
5.3	Effective impurity systems . . . . .	109
5.3.1	Opposite impurities . . . . .	112
5.3.2	Equal impurities . . . . .	113
5.3.3	Single impurity . . . . .	115
5.3.4	Coupling between impurity states . . . . .	117
5.4	Effective SSH impurity chains . . . . .	119
5.4.1	Disorder . . . . .	122
5.5	Implementation in optical waveguides . . . . .	127
5.6	Conclusions . . . . .	131

<b>6</b>	<b>Root topological insulators of arbitrary order in Non-Hermitian photonic ring resonators</b>	<b>135</b>
6.1	Introduction . . . . .	136
6.2	Cubic-root SSH . . . . .	137
6.2.1	Symmetries of the system . . . . .	144
6.2.2	Topological characterization . . . . .	147
6.2.3	Disorder and dilution of the topological protection . . . . .	149
6.3	Generalization to $n$ -root systems . . . . .	152
6.4	Implementation in ring resonator lattices . . . . .	155
6.4.1	Mathematical description of the ring system . . . . .	157
6.4.2	Implementation of $n = 3, 4$ and $5$ roots . . . . .	160
6.4.3	Deviation from unidirectionality . . . . .	165
6.4.4	Lossy ring resonators . . . . .	166
6.5	Conclusions . . . . .	167
<b>7</b>	<b>Conclusions and outlook</b>	<b>171</b>



# CHAPTER 1

---

## Introduction

---

Optics is the study of light across all its stages, from its generation in light sources to its propagation through different media, its interaction with matter and ultimately its detection. The origins of optics can be traced back many centuries. Still, arguably the most important theoretical step was the development of the electromagnetic theory of light by Maxwell [1], as the equations that bear his name have been employed at the forefront of physics to this very day. Perhaps the most important technological advancement of the field was achieved with the invention of the laser by Maiman in 1960 [2], which propelled the field by making available very bright sources of coherent light that led to innumerable applications in science and technology [3]. The existence of the laser kindled an interest on optical communications [4], which started to take shape with the discovery of low-loss optical waveguides and fibers [5, 6]. These advances, together with the importance that integrated electronic circuits were taking at the time, gave rise to the concept of integrated optics [7]. This encompasses planar optical circuits with both active and passive elements that are integrated in a single common substrate, and are connected with optical waveguides [8]. Furthermore, the development of semiconductor optical devices for the generation and detection of light [9–11] allowed for an efficient miniaturization of integrated optics. The main advantage over integrated electronics was that light with very high frequencies could be guided by the structures, thus allowing for transmission of larger amounts of information, and in a faster way [12]. On top of that, multiplexing techniques [13, 14] were introduced to further enhance the transmission capacity of optical devices by encoding information in several physical dimensions, such as in different space channels [15, 16] or by using different guided modes of the structure [17, 18], different optical wavelengths [19, 20] or polarizations [21, 22]. The

advent of integrated optics, much like what happened with integrated electronics, has brought with it a technological revolution [23] encompassed in the term *photonics*. Over time the field has expanded, as advanced photonic devices have been fabricated with applications in optical communications [24, 25], sensing [26, 27], lasing [28, 29], filtering [30, 31], among many others. Additionally, photonic devices have been paramount for fundamental and applied studies of many disciplines, such as of quantum [32–34] and nonlinear physics [35, 36].

From the umbrella of integrated optics, we focus on systems of coupled optical waveguides. What started with one-dimensional (1D) arrangements of waveguides fabricated with beam lithography techniques [37] quickly developed, with two-dimensional (2D) waveguide structures being experimentally realized first by using optical induction in photorefractive crystals [38, 39], and after that by direct laser-writing with ultrashort pulsed lasers [40, 41]. Currently, optical waveguides are an exceptionally flexible platform that has gathered widespread attention [42], and that can be fabricated in a long list of materials such as silicon, silica glasses, lithium niobate, semiconductors, polymers, and more [43–45]. Part of this interest, aside from the applications mentioned above, is due to their immense potential as simulators of quantum systems [46–48]. The dynamics and quantum effects encountered in various fields such as atomic, molecular or condensed-matter physics can be emulated in systems of optical waveguides due to the formal analogy that exists between the Schrödinger equation in quantum physics, and the paraxial Helmholtz equations in optics [49]. Furthermore, optical waveguides generally entail a simpler fabrication and experimental control than quantum or atomic systems. Additionally, they provide a way to probe the evolution of the wavefunction by directly observing the propagation of light in the system through imaging techniques such as fluorescence microscopy [50–52]. Thanks to this quantum-optical analogy, several control techniques stemming from different fields can be employed in systems of optical waveguides. For this thesis, we highlight two of them: Stark-Chirped Rapid-Adiabatic-Passage (SCRAP) and Supersymmetry (SUSY). SCRAP [53], among the large family of adiabatic passage schemes [54], is a technique that was introduced for the purpose of transferring population to a metastable atomic state [55–57]. SCRAP features a combination of two pulses: a Stark pulse that modifies the energy of the two levels and causes energy crossings, and a pump pulse that drives the population adiabatically. This technique was later generalized to three-level systems [58–61], and exploited for other purposes such as wave-mixing and frequency conversion [62, 63]. SCRAP can be implemented in optical waveguides to achieve faithful transfer of light between optical modes, where the energy variation is now a modulation of the refractive index of the waveguide core, and the pumping laser is simulated through the control of the coupling. On the other hand, SUSY was initially developed in the context of particle physics [64–67] as an attempt to go beyond the Standard Model [68]. Despite the fact that

supersymmetric particles have not been found experimentally, the ideas and mathematical framework of SUSY has been applied to other fields such as condensed-matter [69], optics [70–72], quantum mechanics [73], statistical mechanics [74] and cosmology [75]. In optics, SUSY has been primarily employed to control the modal content of optical waveguides and fibers [76–78], as well as the scattering properties of a system [79–81], among others. To exploit the control of the modal content in waveguides, one may couple the supersymmetric partners between them [72], or rather deform one into the other [82].

In parallel to the inception of integrated optics, the mathematical concepts of topology also started seeing applications in physics. In essence, topology may be thought of as the theory of the geometrical properties of objects that remain unchanged under continuous deformations. Although the first notions of topology date from much earlier [83], its applications to physics truly gained force with the emergence of quantum physics, starting with the study of magnetic monopoles by Dirac in 1931 [84] and the discovery of the Aharonov-Bohm effect in 1959 [85], with the latter obtaining immediate experimental confirmation in 1960 [86]. But perhaps the biggest leap was taken with the discovery of the quantum Hall effect (QHE) in 1980 [87], which led to a rapid expansion of the role of topology in condensed-matter physics. When exposed to a magnetic field, the resistivity of a 2D electronic material displays constant plateaus instead of the continuous increase that appears in the classical Hall effect [88]. This is due to the quantization of the Hall conductivity [89], which was later shown to be topological in nature [90]. Shortly after, it was shown that these topological effects could occur even in the absence of external magnetic fields [91]. It was the birth of what we now know as topological insulators (TIs) [92], which are materials that are insulating in their bulk but that possess conducting edge or surface states that are protected by a certain symmetry of the system. Many different TIs have been studied throughout the years [93], each fitting into a different category depending on their dimensionality and their protecting symmetry [94]. Perhaps the most paradigmatic example of a TI is the Su-Schrieffer-Heeger (SSH) model, which was initially proposed to study the properties of polyacetylene polymers [95] and has since then been the go-to model to exploit topological effects.

TIs are characterized by topological invariants, which are globally defined quantities that do not change under perturbations of the system, as long as those perturbations do not close any energy band gap and thus do not cause a topological phase transition. An example of a topological invariant can be seen in Berry’s phase [96], a nondynamical phase that appears in quantum systems when taking a closed path in parameter space. The Berry phase is one example of a geometrical phase [97], a concept that had already appeared years prior to Berry’s work in the study of polarization optics by Pancharatnam [98]. The application of the Berry phase to the band structure of solid-state systems,

also known as the Zak phase [99], has been of particular importance for the study of topology in condensed-matter systems [100]. One of the most attractive properties of the Zak phase is that its value in a system with periodic boundary conditions can be related to the appearance of topological edge states in a particular gap when the boundaries are opened. These boundary modes are topologically protected, and as such possess a general immunity to defects and imperfections on the system. This connection between global invariants and edge states is known as the bulk-boundary correspondence [101]. On a related note, of particular importance are flat-band (FB) systems [102–109], which have one or more dispersionless energy bands. FBs can appear due to certain symmetries of the system or the fine-tuning of its parameters [110]. In FBs, transport can be halted due to the appearance of compact localized states (CLSs) [111]. Excitations cannot thus freely expand throughout the lattice due to destructive interference over different hopping paths. This effect is known as Aharonov-Bohm caging [85, 112–117]. CLSs are eigenstates possessing strictly zero amplitude beyond a finite number of unit cells, but that in general can be degenerate and not orthogonal to each other [118]. In a similar context, within the field of TIs a new branch known as root topology has recently emerged. Square-root TIs ( $\sqrt{\text{TI}}$ s) [119] were first proposed to characterize lattice models that are related to a parent TI via a squaring operation of the Hamiltonian. Most notably, the  $\sqrt{\text{TI}}$  inherits the topological features from the parent TI while presenting twice as many energy bandgaps [115, 120, 121]. As a consequence, the edge states of the  $\sqrt{\text{TI}}$  are protected against any disorder that preserves the symmetry of the parent model.  $\sqrt{\text{TI}}$  were soon experimentally realized in different platforms [122–126], and subsequently the idea was generalized to  $2^n$ -root TIs ( ${}^{2^n}\sqrt{\text{TI}}$ s) [127–132], meaning models that connect to their parent TI through a sequence of  $n$  squaring operations. To explore all the effects that are highlighted here, TIs have been experimentally implemented in multiple platforms, such as ultracold atoms [133–135], electric circuits [136–138], acoustic [139–141] and photonic systems [142–145], in which we now place the focus.

The hitherto separate fields of photonics and topology were joined in 2008 by the works of Haldane and Raghu [146, 147], who proposed a photonic analogue of the QHE in photonic crystals [148], and proved that energy bands in periodic photonic systems could also possess non-trivial topology. Shortly after, a viable platform for observing the photonic QHE was proposed [149] and experimentally realized [150]. Unlike electrons, photons lack charge, which makes exploration of magnetic-induced effects challenging. To be able to probe the same kind of physics, artificial gauge fields (AGF) [151–154] can be used to simulate the effect of a magnetic field in the system, while periodically-driven systems [155–157] allow to explore Floquet topological insulators. Particularly, AGF permit the generation of negative and in general complex-valued couplings in photonic systems, which make possible the exploration of interesting phenomena such as the photonic Aharonov-Bohm caging effect [113, 114, 122, 158–160]. The combination of

all these concepts has blossomed into an entirely new field which is now known as topological photonics [142, 143]. Currently, an almost overwhelming amount of applications have appeared of photonic TIs in one [161–166], two [103, 167–172] or higher dimensions [173, 174]. To go beyond the geometrical limits of conventional applications, the usage of synthetic dimensions has been proposed [175–179]. This consists on exploiting a particular degree of freedom of the system, such as the different resonant frequencies in rings [176] or the guided modes of a structure [180, 181], within which one encodes an additional non-spatial dimension. One can even use time-division-multiplexing with multiple pulses, and use the different time slots as a synthetic dimension [182, 183]. Furthermore, this strategy allows to implement long-range couplings that may be impossible to replicate with geometrical means [184]. In addition, there has also been recent interest in extending the field of TIs to the non-Hermitian realm [185–187], where exotic phenomena such as the skin effect [188] can be explored. Although they seemed out of reach just a few years ago, nowadays different theoretical proposals and experimental implementations of non-Hermitian couplings have appeared in several platforms such as ultracold atoms [189–192], electrical circuits [138, 193–196] or mechanical lattices [197, 198]. In the world of photonics, ring resonators [199–204], fibers and waveguides [205–208] and photonic crystals [209–211] are promising platforms to explore non-Hermitian effects.

In this vein, the main aims of this thesis are (i) to explore and exploit the topological properties of various systems, (ii) to combine these topological properties with other techniques, stemming from different fields, to create novel or enhanced applications in photonic setups, and ultimately (iii) to provide realistic proposals for experimental implementation in systems of optical waveguides for every study. In a sense, optical waveguides are the basis of this thesis, and topology is the topic that threads the different techniques in every chapter together. The thesis is organized in the following way:

In Chapter 2, we set the general theoretical framework upon which we build the research performed in the thesis. The tools and techniques that are employed across different chapters are introduced, divided in three blocks. We start with a detailed description of light propagation in optical waveguides in various geometries, including planar waveguides, cylindrical waveguides that guide light carrying orbital angular momentum (OAM) and ring resonators. We also delve into how to describe the coupling between waveguides, and comment on different fabrication techniques and the potential of waveguides as simulators. Then, we discuss the application to optics of the formalism of SUSY [72], which is used in Chapter 3 in its continuous form and in Chapter 4 in its discrete version. To end the chapter, we present the basic concepts of topology. We also review the celebrated Su-Schrieffer-Heeger model, which serves as a good introduction for important concepts such as edge states and their topological protection, and finally we show the main ideas behind the concept of square-root topology, which we generalize and employ in Chapter 6.



We start our results in Chapter 3, where we discuss multiple applications based on a photonic implementation of the SCRAP technique [212, 213], and how some of them are enabled or enhanced by the usage of SUSY transformations. After introducing the ideas behind the scheme, and of its combination with SUSY, we dedicate the first half of the chapter to multimode optical waveguides [212]. There, we employ SCRAP to achieve (de)multiplexing of superpositions of different modes. Then, we show how combining the technique with SUSY allows the device to reach higher fidelities, and also enables the possibility to produce an efficient excitation of the higher-order modes of the waveguide with a fundamental-mode injection. In the second half, we explore lattices of coupled single-mode waveguides. There, we focus on the excitation of the topological modes of the SSH model [213]. A faithful excitation can be achieved with a fundamental-mode injection on a modulated auxiliary waveguide, thus greatly simplifying the complexity of the input. We also prove how the method can be used to excite extended bulk modes of the lattice, as well as to perform mode transfer and mode conversion between different lattices.

In Chapter 4 we make use of the isospectrality of SUSY transformations, this time of its discrete formalism, to perform an excitation of gapped topological modes of the SSH model [214]. Using discrete SUSY (DSUSY), we generate a superpartner lattice to the topological chain, with both containing the same modal content. The superpartner has a single isolated waveguide containing the eigenmode targeted by the transformation, and a chain containing the rest of the spectrum. Any eigenmode can be isolated in such a way, which implies that any eigenmode can be excited by the scheme. The excitation technique is based on adiabatically connecting the topological lattice with its superpartner along the propagation direction of light, with the superpartner being the input facet. Then, a single-waveguide injection into the isolated waveguide is adiabatically deformed into the desired mode of the lattice at the output facet, reproducing the amplitudes and the phase structure. Although we focus on topological modes, we show how bulk modes can also be faithfully excited for low number of waveguides. In contrast to the previous chapter, for zero-energy modes we do not require any modulation of the propagation constants of the waveguides, and thus the excitation can be completed just by controlling the coupling along the propagation direction.

In Chapter 5, we explore how an effective topological model can be imprinted on a FB system, such as the diamond chain with constant flux per plaquette, by decorating it with controlled onsite impurities [215, 216]. By introducing small impurities in a plaquette of the chain, the CLSs with finite amplitude in the perturbed sites are shifted in energy. This system can be studied by projecting the impurity operator onto the FB, and working on a dual basis where the analysis can be restricted to only two states. For finite fluxes, adjacent CLSs become coupled and generate a set of exponentially decaying impurity states, whose amplitudes and phases depend on the distribution of

impurities and whose localization length depends on the flux [215]. By decorating the diamond lattice with impurities, and controlling both the distance between them as well as the value of the flux, a wide range of effective systems can be realized. To benchmark the method, we imprint the SSH model onto a diamond chain lattice with constant flux per plaquette [216]. We describe the theoretical method behind the formation of the effective system, based on the usage of dual bases of non-orthogonal states, and then focus on the characteristics of the effective system itself, including the appearance of edge states localized around the end of the chain of impurities. Furthermore, we study the robustness of the effective system against different types of disorder, and show how it displays enhanced protection even against disorder that breaks its chiral symmetry. This enhanced robustness is shown to be due to an averaging effect of the disorder over the extension of the impurity states [217], and numerically quantified in terms of the effective number of sites that the state occupies. Finally, we propose a route for experimental implementation by using optical waveguides guiding orbital angular momentum (OAM)  $l = 0$  and  $l = 1$  modes [159, 218, 219]. The different circulations of the  $l = 1$  modes are split in a synthetic dimension that simulates the top and bottom sites of the lattice [181], and the flux can be finely controlled geometrically.

After that, in Chapter 6 we design a strategy to obtain root TIs of arbitrary order  $n$  based on unidirectional hopping loops, and propose a realistic implementation on a lattice of non-Hermitian ring resonators [220]. Square-root topology [119] and its extensions to roots of order  $2^n$  [128] have recently appeared in the field of TIs. Essentially, they consist on taking advantage of the relations between the root and parent Hamiltonians via a power operation. Several interesting effects appear in the root systems, such as an increased amount of energy bandgaps and an inheritance of the topological protection of the parent. Here, we go one step further and develop the framework for designing general  $n$ -root TIs, with  $n$  any positive integer, and demonstrate the method by using the SSH model as the parent TI. To obtain the  $n$ -root system, one requires a way to generate a  $n$ -partite lattice, which we accomplish by employing loops of unidirectional couplings that make the system non-Hermitian. This coupling structure bestows the system with a generalized chiral symmetry [221], due to which  $n$  separate and identical branches appear in the complex energy band spectrum. Across all branches,  $n$  edge states are shown to appear in a ring gap on the complex plane, which is a novel kind of gap that cannot be reduced to point or line gaps. For the implementation, we propose to employ a lattice of ring resonators coupled through antiresonant link rings. To achieve the required unidirectionality, the link rings are made to have a split gain and loss distribution, thereby enhancing the coupling in one direction and suppressing it in the opposite one. We start the chapter by analyzing the cubic root of the SSH model, including a thorough description of its symmetries, its topological characterization and how its robustness against disorder compares with the parent model. Then, we

comment on how to generalize the root method to any arbitrary order  $n$  by extending the length of the coupling loops through the inclusion of additional sites in the unit cell. After that, we describe in detail the implementation in ring resonators, and present our simulations for the roots of order 3, 4 and 5. Lastly, we reflect on how deviations from perfect unidirectionality, and perfect balance between gains and losses, affect the spectrum of the root system.

We end the thesis in Chapter 7 by summarizing our main results, laying out our conclusions and discussing possible extensions stemming from the works in each chapter.

## CHAPTER 2

---

### Theoretical foundations

---

In this chapter, we set the theoretical framework upon which the research performed in this thesis is built. We present the main tools and techniques that will be used across different chapters, as well as the main ideas that join the different presented topics. We start in Sec. 2.1 with a detailed description of the physical platform serving as the cornerstone of the thesis, optical waveguides, which serve as a basis for all our proposed photonic devices and implementations. We obtain the equations that describe guided modes in multiple geometries, including planar waveguides, cylindrical waveguides that guide light carrying orbital angular momentum (OAM) and closed waveguides that form ring resonators. We also describe how these modes overlap and enable coupling in systems of nearby waveguides through the coupled-mode model. Finally, we characterize the experimental techniques to fabricate optical waveguides and the mathematical analogies that allow to use them as simulators of other systems. After that, in Sec. 2.2 we outline the application of the Supersymmetry (SUSY) formalism to optical waveguides, both in its continuous and discrete forms. The continuous formalism is used in Chapter 3 to obtain efficient demultiplexing and pumping of excited modes in multimode waveguides, while the discrete formalism is exploited in Chapter 4 to perform precise excitation of topological modes in waveguide lattices. We finish with Sec. 2.3, where we present the main ideas behind topology in optics and photonics, which we exploit in nearly all presented applications, and that serves as a line that connects the different topics in the thesis. After a general description, we discuss the ubiquitous Su-Schrieffer-Heeger model, which allows to introduce important concepts such as edge states and their topological protection. We end the section with a description of the idea of root topology.

## 2.1 Light propagation in optical waveguides

We now introduce the physical platform upon which this thesis is built, namely optical waveguides. We start with a description of the electromagnetic theory of light leading up to the concept of guided optical modes, with specific highlights for each of the considered geometries in the rest of the chapters. We also tackle the description of the coupling between these guided modes, how to quantify it and its effects on light propagation. Finally, we comment on the most prominent fabrication techniques for optical waveguides, as well as their importance as simulators of other physical systems.

### 2.1.1 Electromagnetism and light propagation

The electromagnetic theory of light [12, 222, 223] describes the dynamics of electromagnetic radiation as it flows through space or through a medium. This radiation consists of two vector fields, the electric field  $\mathcal{E}(\mathbf{r}, t)$  and the magnetic field  $\mathcal{H}(\mathbf{r}, t)$ , which are in general coupled between them and depend on both position and time. The behavior of these fields is contained in four elegant differential equations known as Maxwell's equations [12]. Even if these equations are more general, for the purposes of this thesis we restrict ourselves to linear, isotropic and dielectric media. If the medium is also homogeneous, then Maxwell's equations take the form:

$$\nabla \cdot \mathcal{E}(\mathbf{r}, t) = 0, \quad (2.1)$$

$$\nabla \cdot \mathcal{H}(\mathbf{r}, t) = 0, \quad (2.2)$$

$$\nabla \times \mathcal{E}(\mathbf{r}, t) = -\mu \frac{\partial \mathcal{H}(\mathbf{r}, t)}{\partial t}, \quad (2.3)$$

$$\nabla \times \mathcal{H}(\mathbf{r}, t) = \epsilon \frac{\partial \mathcal{E}(\mathbf{r}, t)}{\partial t}, \quad (2.4)$$

where  $\epsilon$  and  $\mu$  are the medium's permittivity and permeability, respectively. They are related to the speed of light in the medium,  $v^2 = 1/\epsilon\mu$ , which in turn is related to the speed of light in the vacuum through the refractive index,  $n = c/v$ . Maxwell's equations can be combined making use of the vector identity  $\nabla \times (\nabla \times \mathbf{A}) = \nabla(\nabla \cdot \mathbf{A}) - \nabla^2 \mathbf{A}$ , which yields:

$$\nabla^2 \mathcal{E} - \mu\epsilon \frac{\partial^2 \mathcal{E}}{\partial t^2} = 0, \quad (2.5)$$

$$\nabla^2 \mathcal{H} - \mu\epsilon \frac{\partial^2 \mathcal{H}}{\partial t^2} = 0. \quad (2.6)$$

These equations admit solutions in the form of harmonic functions. For the case of monochromatic waves, characterized by a single angular frequency  $\omega$ , one can express

them with the following complex notation:

$$\mathcal{E}(\mathbf{r}, t) = \text{Re} [\mathbf{E}(\mathbf{r}) \exp(i\omega t)], \quad (2.7)$$

$$\mathcal{H}(\mathbf{r}, t) = \text{Re} [\mathbf{H}(\mathbf{r}) \exp(i\omega t)], \quad (2.8)$$

which allows to rewrite (2.5)–(2.6) as wave equations for the envelopes as:

$$[\nabla^2 + n^2 k_0^2] \mathbf{E}(\mathbf{r}) = 0, \quad (2.9)$$

$$[\nabla^2 + n^2 k_0^2] \mathbf{H}(\mathbf{r}) = 0, \quad (2.10)$$

and these are known as the Helmholtz equations. In these, we have substituted  $n^2 k_0^2 = \mu\epsilon\omega^2$  where  $k_0 = 2\pi/\lambda_0$  is the vacuum wavenumber and  $\lambda_0$  the vacuum wavelength. The solutions for these equations are plane waves propagating in the direction of the wavevector  $\mathbf{k}$ :

$$\mathbf{E}(\mathbf{r}) = \mathbf{E}_0 \exp(-i\mathbf{k} \cdot \mathbf{r}), \quad (2.11)$$

$$\mathbf{H}(\mathbf{r}) = \mathbf{H}_0 \exp(-i\mathbf{k} \cdot \mathbf{r}), \quad (2.12)$$

with  $\mathbf{E}_0$  and  $\mathbf{H}_0$  being constant complex envelopes. These are known as Transverse Electromagnetic (TEM) waves, since they oscillate in a plane that is orthogonal to the direction of propagation. In linear media, they are also orthogonal to each other. This can be proved by introducing (2.11) and (2.12) into the last two Maxwell's equations, (2.3) and (2.4).

### 2.1.2 Optical waveguides

Optical waveguides, in their simplest form, consist of a region of a material (core), which is surrounded by a region of lower refractive index (cladding). Optical waveguides guide light due to total internal reflection at the interfaces between the core and the cladding. Total internal reflection can occur when a wave propagating in a dielectric medium with refractive index  $n_1$  reaches the interface with a second medium with refractive index  $n_2 < n_1$ . If the angle of incidence is larger than the critical angle [12]:

$$\theta_c = \sin^{-1}(n_2/n_1), \quad (2.13)$$

then light is reflected at the interface. This, however, does not imply that no light crosses the interface. The electromagnetic wave extends to the cladding beyond the interface but decays exponentially, forming an evanescent wave, and therefore power is not transmitted in the transverse direction. In general, the refractive index depends on the frequency of the light that propagates through the medium [222], with the measure of the strength of that dependency being called dispersion. Hence, (2.13) is in fact

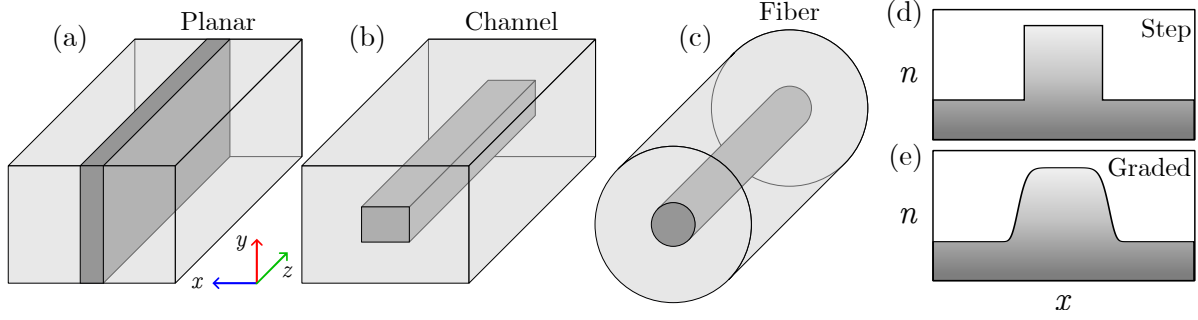


Figure 2.1: Profiles of different types of waveguides: (a) Planar waveguide, (b) Channel waveguide, (c) Optical fiber. (d)–(e) Index profile  $n(x)$  for step-index and graded-index planar waveguides. The boundary between core and cladding is sharp (d) for step-index waveguides and smooth (e) for graded-index waveguides.

frequency-dependent, making some materials more efficient at guiding light at certain frequencies than others.

Optical waveguides can take different geometries, and can be categorized depending on the dimensionality of their light confinement. *Planar waveguides* have refractive indices that only depend on one coordinate,  $n = n(x)$ , so light is confined only along that axis. In contrast, *channel waveguides* confine light in two dimensions,  $n = n(x, y)$ . Optical fibers, which have a cylindrical profile, are a type of channel waveguide. Examples of these waveguides are sketched in Figs. 2.1(a)–(c). We note that waveguides can also have refractive indices that change along the propagation direction  $z$ , but these variations are commonly weak compared to the index contrast between core and cladding. Furthermore, one can also classify waveguides depending on the abruptness of the border between their core and cladding. *Step-index* waveguides display a steep variation in refractive index, akin to what one finds in an interface between different materials, see Fig. 2.1(d). Conversely, in *graded-index* waveguides the boundary is characterized by a smooth function in position, which is what is commonly found in laser-writing setups (see Sec. 2.1.5) where one locally modifies the refractive index of a material. An schematic example of this profile for a planar waveguide is shown in Fig. 2.1(e).

Light propagation in optical waveguides is again described by Maxwell's equations, where we now consider inhomogeneous media. The medium is characterized by a position-dependent refractive index distribution,  $n(\mathbf{r})$ , that relates the material permittivity to that of the vacuum  $\epsilon(\mathbf{r}) = \epsilon_0 n^2(\mathbf{r})$ . Assuming that the medium is non-magnetic, meaning that the permeability takes its value in the vacuum  $\mu = \mu_0$ , Eqs. (2.3) and (2.4)

now lead to [12]:

$$\nabla^2 \mathcal{E} + \nabla \left( \frac{1}{n^2(\mathbf{r})} \nabla n^2(\mathbf{r}) \cdot \mathcal{E} \right) - \mu_0 \epsilon_0 n^2(\mathbf{r}) \frac{\partial^2 \mathcal{E}}{\partial t^2} = 0, \quad (2.14)$$

$$\nabla^2 \mathcal{H} + \frac{1}{n^2(\mathbf{r})} \nabla n^2(\mathbf{r}) \times (\nabla \times \mathcal{H}) - \mu_0 \epsilon_0 n^2(\mathbf{r}) \frac{\partial^2 \mathcal{H}}{\partial t^2} = 0. \quad (2.15)$$

Considering the monochromatic waves in (2.7) and (2.8), these equations take the form:

$$[\nabla^2 + n^2(\mathbf{r})k_0^2] \mathbf{E}(\mathbf{r}) = -\nabla \left( \frac{1}{n^2(\mathbf{r})} \nabla n^2(\mathbf{r}) \cdot \mathbf{E}(\mathbf{r}) \right), \quad (2.16)$$

$$[\nabla^2 + n^2(\mathbf{r})k_0^2] \mathbf{H}(\mathbf{r}) = -\frac{1}{n^2(\mathbf{r})} \nabla n^2(\mathbf{r}) \times (\nabla \times \mathbf{H}(\mathbf{r})), \quad (2.17)$$

implying that the components of each field are coupled to one another and, unlike in (2.9) and (2.10), one cannot find an independent equation for each of them. Nevertheless, when  $n(\mathbf{r})$  varies sufficiently slowly in space when compared to the wavelength, the right-hand sides in Eqs. (2.16) and (2.17) can be neglected [222]. When the refractive index depends only on the transverse coordinates,  $n(x, y)$ , or when variations along  $z$  are much weaker than along the transverse plane, one can separate the evolution into transverse and longitudinal components:

$$\mathbf{E}(\mathbf{r}) = [\mathbf{E}_T(x, y) + \hat{\mathbf{z}}E_z(x, y)] \exp(-i\beta z), \quad (2.18)$$

$$\mathbf{H}(\mathbf{r}) = [\mathbf{H}_T(x, y) + \hat{\mathbf{z}}H_z(x, y)] \exp(-i\beta z), \quad (2.19)$$

which are both independent of  $z$ , as the propagation is entirely contained within the global exponential in each equation that features the propagation constant  $\beta = k_z$ . Introducing these expressions into (2.16) and (2.17) leads to the following expressions for the transverse components [223]:

$$\mathbf{E}_T(x, y) = i \frac{\beta \nabla_T E_z(x, y) - \omega \mu_0 \hat{\mathbf{z}} \times \nabla_T H_z(x, y)}{\beta^2 - n^2(x, y)k_0^2}, \quad (2.20)$$

$$\mathbf{H}_T(x, y) = i \frac{\beta \nabla_T H_z(x, y) - \omega \epsilon_0 n^2(x, y) \hat{\mathbf{z}} \times \nabla_T E_z(x, y)}{\beta^2 - n^2(x, y)k_0^2}, \quad (2.21)$$

where  $\nabla_T = (\partial_x, \partial_y)$  contains the transverse derivatives. Since in general transverse and longitudinal components are not independent, one can determine the transverse components by solving for  $E_z$  and  $H_z$ . These are also coupled, so in general this requires the usage of finite-difference numerical methods [224]. In the particular case of planar waveguides where the refractive index only depends on one direction,  $n(x)$ , the longitudinal components of the fields decouple, with all fields being independent of  $y$ :

$$\mathbf{E}(x, z) = [\hat{\mathbf{x}}E_x(x) + \hat{\mathbf{y}}E_y(x) + \hat{\mathbf{z}}E_z(x)] \exp(-i\beta z), \quad (2.22)$$

$$\mathbf{H}(x, z) = [\hat{\mathbf{x}}H_x(x) + \hat{\mathbf{y}}H_y(x) + \hat{\mathbf{z}}H_z(x)] \exp(-i\beta z), \quad (2.23)$$



and there are two independent possible polarizations: Transverse Electric (TE) fields, for which  $E_z = 0$ , and Transverse Magnetic (TM) fields, for which  $H_z = 0$ . Introducing (2.22) and (2.23) into Maxwell's equations (2.3) and (2.4) allows to rewrite them into a set of equations for the different field components. For the TE modes, the only nontrivial equations are [223]:

$$\beta E_y(x) = -\omega\mu_0 H_x(x), \quad (2.24)$$

$$\frac{dE_y(x)}{dx} = -i\omega\mu_0 H_z(x), \quad (2.25)$$

$$-i\beta H_x(x) - \frac{dH_z(x)}{dx} = i\omega\epsilon_0 n^2(x) E_y(x), \quad (2.26)$$

with the only nonzero components in this polarization being  $E_y$ ,  $H_x$  and  $H_z$ . For the TM modes we instead have:

$$\beta H_y(x) = \omega\epsilon_0 n^2(x) E_x(x), \quad (2.27)$$

$$\frac{dH_y(x)}{dx} = i\omega\epsilon_0 n^2(x) E_z(x), \quad (2.28)$$

$$i\beta E_x(x) + \frac{dE_z(x)}{dx} = i\omega\mu_0 H_y(x), \quad (2.29)$$

meaning that the only nonzero components are  $H_y$ ,  $E_x$  and  $E_z$ . Comparing the nonzero elements in both polarizations, it is easy to see that they are orthogonal. We can combine these sets of equations into a single differential equation for each transverse component. For TE modes, combining (2.24)–(2.26) yields:

$$\frac{d^2 E_y(x)}{dx^2} + [n^2(x)k_0^2 - \beta^2] E_y(x) = 0, \quad (2.30)$$

and combining (2.27)–(2.29) produces the corresponding equation for the TM modes:

$$\frac{d^2 H_y(x)}{dx^2} - \frac{1}{n^2(x)} \frac{dn^2}{dx} \frac{dH_y(x)}{dx} + [n^2(x)k_0^2 - \beta^2] H_y(x) = 0. \quad (2.31)$$

The second term in (2.31) cancels out in regions of constant refractive index, making the TE and TM equations look identical.

## Guided modes

Equations (2.30) and (2.31) can be solved after specifying the refractive index profile  $n(x)$ . In waveguides, the solutions of these equations are called guided modes, which are fields that maintain a constant spatial distribution during propagation. For each index profile, there is a finite number  $m$  of guided modes with different propagation constants  $\beta_m$ , which are orthogonal between them.

For a step-index waveguide of core width  $\omega$ , with core refractive index  $n_{\text{co}}$  and cladding index  $n_{\text{cl}}$ , guided modes will have propagation constants ranging between:

$$n_{\text{cl}}k_0 < \beta_m < n_{\text{co}}k_0, \quad (2.32)$$

and will be mainly contained within the core, with an evanescent tail extending into the cladding. We showcase in Fig. 2.2(a) the propagation constants and field profiles of a step-index waveguide with two guided modes, which are indeed unchanged during propagation as can be seen in Figs. 2.2(b) and (c). Modes with propagation constants below  $n_{\text{cl}}k_0$  are instead called radiation modes [12], which are extended throughout the material instead of being confined, and thus can leak and escape the system. Unlike guided modes, there is an infinite amount of radiation modes which form a continuum of effective refractive indices  $n_{\text{eff}} = \beta/k_0$  below  $n_{\text{cl}}$ .

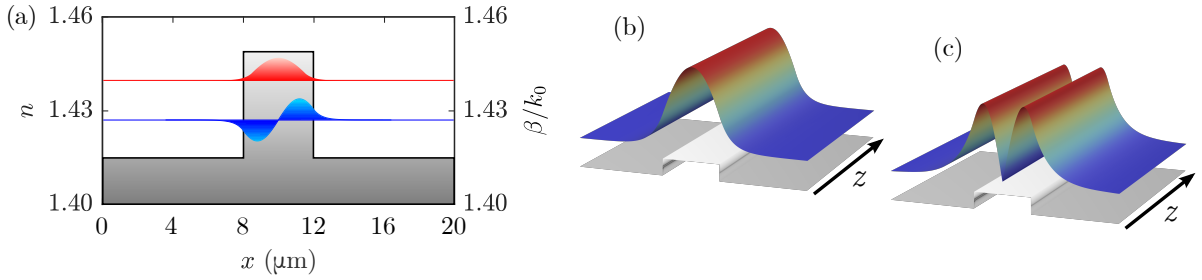


Figure 2.2: (a) Step-index waveguide hosting two guided modes. The fundamental mode has a larger propagation constant,  $\beta$ , than the excited mode. (b)–(c) Electric field norm,  $|E|$ , for the propagation of the fundamental (b) and first excited (c) modes. Both modes maintain their transverse profile along  $z$ .

Although the derivation for TM modes is similar, we focus on TE modes. Solutions of Eq. (2.30) will display different behaviors in the core and the cladding, seeing how the term in brackets changes sign between both regions. In the core region, for  $|x| \leq \omega/2$ , solutions will be oscillatory [222]:

$$E_{y,m}(x) = \begin{cases} E_{0,m} \cos(k_m x), & m = 0, 2, \dots \\ E_{0,m} \sin(k_m x), & m = 1, 3, \dots \end{cases} \quad (2.33)$$

where  $k_m = \sqrt{n_{\text{co}}^2 k_0^2 - \beta_m^2}$ . Higher-order modes have larger  $k_m$ , so they have more nodes along  $x$ . In the cladding region, solutions instead decay exponentially for any index  $m$ :

$$E_{y,m}(x) = \begin{cases} E_{c,m} \exp(-\gamma_m x), & x > \omega/2 \\ E_{c,m} \exp(\gamma_m x), & x < -\omega/2 \end{cases} \quad (2.34)$$

where  $\gamma_m = \sqrt{\beta_m^2 - n_{\text{cl}}^2 k_0^2}$ . Higher-order modes have lower  $\gamma_m$ , and as such extend deeper into the cladding region. Moreover, the electric field must be constant at the boundary between core and cladding, so one can find a relation between the amplitudes  $E_{0,m}$  and  $E_{c,m}$  for each mode. The fields in (2.34) are called evanescent. As mentioned in the beginning of the section, evanescent fields are not oscillatory and display exponential decay along  $x$ , meaning that the electric power does not transmit in that direction and is confined close to the boundary as long as the waveguide is isolated. Evanescent fields of different nearby waveguides can nonetheless overlap and produce coupling and power transfer between them, which will be a pivotal property going forward in the thesis.

The precise values of the propagation constants of the guided modes can be computed numerically from a self-consistency equation. This equation can be derived either from geometrical considerations, associating a plane wave to propagating rays and studying their bouncing angles in the waveguide [222], or from solving the differential equation (2.30) and applying the adequate boundary conditions at the interface between core and cladding [223], for both the electric field and its derivative. Both approaches yield the same relation:

$$\tan \left[ \frac{1}{2} \left( \omega \sqrt{n_{\text{co}}^2 k_0^2 - \beta_m^2} - m\pi \right) \right] = \sqrt{\frac{\beta_m^2 - n_{\text{cl}}^2 k_0^2}{n_{\text{co}}^2 k_0^2 - \beta_m^2}}, \quad (2.35)$$

for  $m = 0, 1, 2, \dots$ . For dielectric waveguides, there is always at least one solution for this equation, meaning that there is always at least one guided mode. One can also compute the number of guided modes for any given profile [222]:

$$M \doteq \frac{2\omega}{\lambda_0} \sqrt{n_{\text{co}}^2 - n_{\text{cl}}^2}, \quad (2.36)$$

where  $\doteq$  means closest integer from above. That is,  $M$  is equal to the nearest integer greater than the right hand side of (2.36). As a consequence, the waveguide will support only one guided mode if:

$$\frac{2\omega}{\lambda_0} \sqrt{n_{\text{co}}^2 - n_{\text{cl}}^2} < 1, \quad (2.37)$$

but this condition depends on the wavelength of the propagating light. Single-mode waveguides at certain wavelengths may become multi-modal for shorter ones. The single-mode behavior of waveguides, due to which one can ignore any mode crosstalk or modal dispersion, is of great importance in many applications, as well as a major simplifying factor in the mathematical treatment [225, 226].

## Guided modes in cylindrical waveguides and fibers

Channel waveguides display a more complex spectrum of guided modes. As the refractive index profile depends on more than one coordinate, the longitudinal components of electric and magnetic fields are not decoupled and guided modes are no longer

purely TE or TM, instead being denoted as hybrid modes [223], which in general display all field components. Nevertheless, when waveguides are weakly-guiding, modes are strongly polarized toward one direction and described in terms of linearly polarized (LP) modes. This occurs when  $n_{\text{co}} - n_{\text{cl}} \ll n_{\text{co}}$ , as long as the size of the core is large compared with the wavelength  $\lambda$  of the guided light [223]. In general, hybrid modes are computationally challenging to simulate, as an exact treatment is not possible. An exception to this rule is found for cylindrically symmetric refractive index profiles,  $n(r)$ , present in optical fibers. In those cases, the fields can be divided into radial, azimuthal and longitudinal components, each of which has the following shape in cylindrical coordinates:

$$E_\sigma(r, \varphi, z) = e_\sigma(r) e^{-il\varphi} e^{-i\beta z}, \quad (2.38)$$

for  $\sigma = r, \varphi, z$  and any integer  $l$ . Hence, one only needs to solve for the radial profile of the field components. For step-index radial profiles, the Helmholtz equation now reads [222]:

$$\left[ \frac{\partial^2}{\partial r^2} + \frac{1}{r} \frac{\partial}{\partial r} + \frac{1}{r^2} \frac{\partial^2}{\partial \varphi^2} + \frac{\partial^2}{\partial z^2} + n_i^2 k_0^2 \right] E_\sigma(r, \varphi, z) = 0, \quad (2.39)$$

with  $n_i = n_{\text{co}}, n_{\text{cl}}$ . Introducing the electric field in (2.38) into this equation yields:

$$\left[ \frac{d^2}{dr^2} + \frac{1}{r} \frac{d}{dr} - \frac{l^2}{r^2} - \beta^2 + n_i^2 k_0^2 \right] e_j(r) = 0. \quad (2.40)$$

This is a Bessel-type equation that admits analytical solutions in terms of Bessel functions. If we define  $k_{ml}^2 = n_{\text{co}}^2 k_0^2 - \beta_{ml}^2$  and  $\gamma_{ml}^2 = \beta_{ml}^2 - n_{\text{cl}}^2 k_0^2$ , solving for the longitudinal component leads to [222]:

$$e_{z,ml}(r) \propto \begin{cases} J_l(k_{ml}r), & r < R \\ K_l(\gamma_{ml}r), & r > R \end{cases} \quad (2.41)$$

with  $J_l$  being the Bessel function of the first kind and  $K_l$  the modified Bessel function of the second kind, both of order  $l$ . The solutions depend now on two indices,  $m$  indicating the radial order and  $l$  the azimuthal order. The other components of the field can be obtained through relations analogous to the one in (2.20). These modes can be considered to carry orbital angular momentum (OAM) of charge  $l$ , as first introduced in Ref. [227], whereby each photon carries a quantized OAM given by  $l\hbar$ . This degree of freedom of OAM modes has been exploited in many instances to increase data transmission capacities in optical devices through multiplexing [17, 228–233]. In coupled systems, one can generally restrict the light dynamics in particular OAM manifolds, as we will show further below. For index profiles with cylindrical symmetry, modes with opposite circulations  $\mathcal{K} = \pm$  are degenerate in propagation constant and orthogonal to each other. The set of OAM modes in this case forms a complete basis, and can be

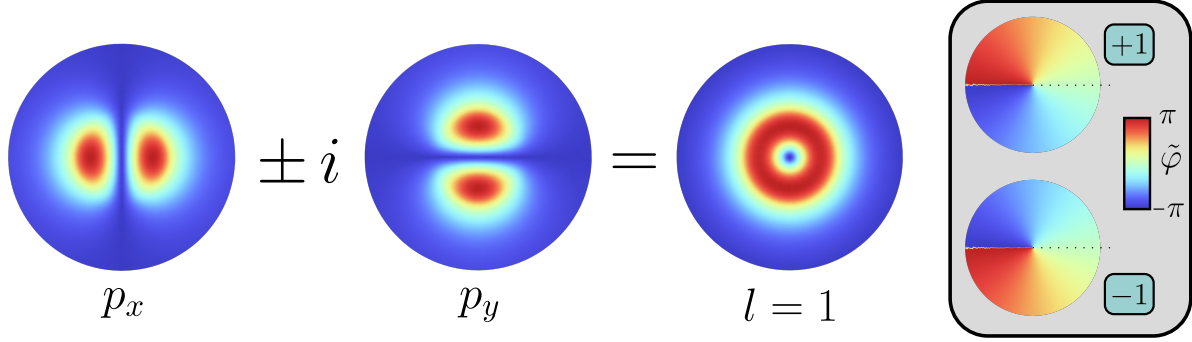


Figure 2.3: Mathematical description of OAM modes in terms of linearly polarized  $p_x$  and  $p_y$  modes, with the distribution of electric fields  $|E|$  depicted in each case. The box to the right indicates the spatial distribution of the phase  $\tilde{\varphi} = \mathcal{K}l\varphi$  for the  $\mathcal{K} = +$  (top) and  $\mathcal{K} = -$  (bottom) circulations of the  $l = 1$  mode.

expressed as a function of LP modes [234], as we show in Fig. 2.3. We call LP modes with lobes along the  $x$  or  $y$  axis  $p_x$  and  $p_y$  modes, respectively. When the profile is not perfectly circular, however, the degeneracy is lifted and the OAM vortices are no longer exact eigenmodes of the system. Instead, for an elliptical profile the eigenmodes are now  $p_x$  and  $p_y$  modes along the symmetry axes of the ellipse [235], and they are different in energy. Propagating OAM vortices in waveguides that are not sufficiently circular results in intensity beating between the constituent  $p$ -modes of the vortex.

### Whispering gallery modes in ring resonators

A ring resonator [236] consists of a waveguide that guides light in a closed loop, thus forming a resonant cavity. Only modes that fulfil the resonance condition, i.e. those whose phase changes by multiples of  $2\pi$  per loop, are supported by the resonator. As such, ring resonators have been extensively used as filters [237–239], due to their ability to select specific frequencies according to their size and refractive index. Other uses include sensing [240–242], lasing [243–246], generation of frequency combs [247], and an extensive list of other applications. Additionally, ring resonators have proven to be a very versatile platform to implement and study topological insulators [144, 151, 152, 168, 169, 200, 220, 248].

Optical modes guided by resonators are known as whispering gallery modes (WGM), whose name originates from the study of acoustic waves travelling in cathedral galleries [249]. The main difference with regular optical modes is that WGM do not require two dielectric interfaces to be guided. Instead, they are guided by the interplay of total internal reflection at the outer interface of the ring and the optical inertia that pushes them radially. The inner interface, which is not always necessary, serves to control the modal content of the resonator [236]. In contrast to straight waveguides, ring resonators

are inherently lossy due to the bending of the guiding interface. Therefore, guided modes are not entirely confined and can couple to radiation modes and consequently cause loss of power. To counteract this, ring resonators usually display a very strong index contrast between core and cladding, minimizing mode extension and bending losses. The price to pay for this high index contrast is a limit on waveguide width if single-mode behavior is desired, with higher-order ring modes being prone to higher losses and undesirable in most applications. The high mode confinement also forces very low relative distance between resonators in order to achieve efficient coupling.

To describe WGM, we write the Helmholtz equation for the  $z$  component of an azimuthally travelling TM mode [236]:

$$\left[ \frac{\partial^2}{\partial r^2} + \frac{1}{r} \frac{\partial}{\partial r} + \frac{1}{r^2} \frac{\partial^2}{\partial \varphi^2} + n^2 k_0^2 \right] E_z(r, \varphi) = 0. \quad (2.42)$$

Similarly to what we did in (2.38), we can apply separation of variables to split the field into radial and azimuthal components [250]:

$$E_z(r, \varphi) = e_z(r) e^{\pm i \beta_\varphi \varphi}, \quad (2.43)$$

where  $\beta_\varphi$  is the propagation constant of the mode, which now propagates azimuthally. As mentioned above, the resonance condition states that the phase of the mode has to change in multiples of  $2\pi$  after each round-trip. Therefore, this constraints the propagation constant to have only integer values  $l$  [250], which corresponds to the number of cycles that the field experiences in a round trip. Hence, we introduce (2.43) in (2.42), for an integer  $l$ , after which the equation reads:

$$\left[ \frac{d^2}{dr^2} + \frac{1}{r} \frac{d}{dr} + n^2 k_0^2 - \frac{l^2}{r^2} \right] e_z(r) = 0. \quad (2.44)$$

As for the mode profile, equation (2.44) is a Bessel-type equation whose solutions for a dielectric disk of radius  $R$  are [250, 251]:

$$e_{z,ml}(r) \propto \begin{cases} J_l(k_1 r), & r < R \\ \bar{H}_l^{(2)}(k_2 r), & r > R \end{cases} \quad (2.45)$$

where  $k_1 = n_{\text{co}} \omega_{ml} / c$  and  $k_2 = n_{\text{cl}} \omega_{ml} / c$ , with  $\omega_{ml}$  the resonance frequency.  $\bar{H}_l^{(2)}$  is a Hankel function that corresponds to a propagating cylindrical wave. Then, one has to apply the adequate boundary conditions at  $r = R$  to solve for the modes and obtain their relevant parameters. Compared with a disk, a ring resonator limits the higher-order radial modes for the same order  $l$  that would display radial nodes inside of the core [236]. In Fig. 2.4(a), we showcase the electric field for the lowest-order radial mode and  $l = 20$ . Due to the curvature of the ring, one can observe how the field profile is more extended

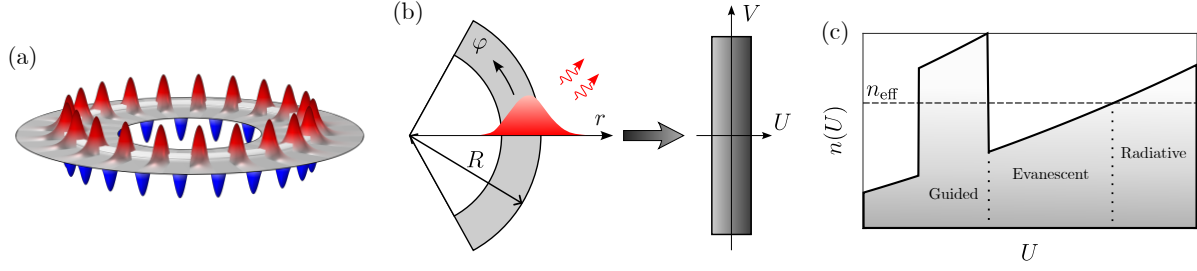


Figure 2.4: (a) Electric field distribution for a mode of azimuthal order  $l = 20$  and first radial order. (b) A conformal transformation allows to turn the curved geometry in the ring resonator into an equivalent straight waveguide with nonuniform refractive index. (c) Refractive index in the transformed coordinate system  $n(U)$ , which grows exponentially with  $U$ . In the core region, the effective index of the mode  $n_{\text{eff}}$  is lower than  $n$  and it is thus guided. Close to the ring, but in the cladding, the mode is evanescent. However, for larger  $U$ ,  $n_{\text{eff}}$  is again larger than  $n$  and the mode becomes radiative.

away from the center. As mentioned before, this curvature is also the cause that makes WGM inherently lossy. Since the mode field maintains its shape during its propagation, and the resonance condition should apply, the azimuthal phase velocity must increase away from the center of the ring. At some point, the phase velocity reaches the limit of  $c/n$  and the mode becomes radiative [252]. A more intuitive reasoning can be found in the formalism of conformal transformations [253–255]. As we sketch in Fig. 2.4(b), conformal transformations consist on finding, for a curved waveguide, the corresponding refractive index profile that reproduces the same light dynamics for a straight waveguide. A curved step-index waveguide in polar coordinates  $(r, \varphi)$  is transformed into a straight waveguide with nonuniform  $n$  in the new coordinates  $(U, V)$ . The transformation entails [253]:

$$n(r) \longrightarrow n(U) = n(r)e^{\frac{U}{R}}. \quad (2.46)$$

We sketch this new refractive index profile in Fig. 2.4(c), where it is clear that it increases away from the ring. For large distances where the effective index of the mode is lower than the cladding index at that point,  $n_{\text{eff}} < n(U)$ , the mode becomes radiative.

### 2.1.3 Coupled-mode model

As showcased in (2.34), the fields propagating in optical waveguides extend beyond the boundary between core and cladding in the form of evanescent fields. When waveguides are in close proximity to each other, the tails of the evanescent fields of each waveguide can overlap, resulting in a coupling that leads to power transfer between them. Although the whole picture can be obtained from the resolution of Maxwell's



equations, it is highly convenient to work in the regime of weak couplings, also known as the tight-binding regime, where we can apply the coupled-mode model [226, 256]. Within that regime, we can consider that the mode profiles in each waveguide are highly confined within each core and thus remain unaltered in the presence of a neighboring waveguide. In that case, only the amplitudes of the modes are subject to change due to the coupling along the propagation direction. Although we introduce the model for the case of two waveguides, it can be straightforwardly extended to arrays of any number of waveguides.

A directional coupler is a set of two evanescently-coupled waveguides. For simplicity, we consider parallel single-mode step-index waveguides, having  $n_1$  and  $n_2$  as their core refractive indices, and both sharing the same cladding refractive index,  $n_{\text{cl}}$ . In general,  $n_1$  need not be equal to  $n_2$ . Each waveguide then supports a single mode, corresponding to the following electric fields in isolation:

$$E_1(x, z) = a_1 e_1(x) \exp(-i\beta_1 z), \quad (2.47)$$

$$E_2(x, z) = a_2 e_2(x) \exp(-i\beta_2 z), \quad (2.48)$$

with each waveguide having their own mode amplitude,  $a_j$ , mode transverse profile,  $e_j(x)$ , and propagation constant,  $\beta_j$ , with  $j = 1, 2$ . If one brings these waveguides closer together, the total field can be computed as the sum of the fields on each waveguide:

$$E(x, z) = a_1(z) e_1(x) \exp(-i\beta_1 z) + a_2(z) e_2(x) \exp(-i\beta_2 z), \quad (2.49)$$

where the only variables that acquire a dependence on  $z$  are the mode amplitudes  $a_1(z)$  and  $a_2(z)$ . As such, instead of solving the whole set of Maxwell's equations, one can solve a simpler set of equations for the amplitudes of the modes. Here, the presence of the second waveguide acts as a perturbation on the field propagating through the first one. The excess of refractive index  $n_2^2 - n_{\text{cl}}^2$  and the field  $E_2$  create an excess of polarization that acts as a source of radiation from the point of view of the first waveguide [222]. In this situation, the Helmholtz equations for the coupled fields take the form:

$$[\nabla^2 + k_0^2 n_1^2(x)] E_1(x, z) + k_0^2 [n_2^2(x) - n_{\text{cl}}^2] E_2(x, z) = 0, \quad (2.50)$$

$$[\nabla^2 + k_0^2 n_2^2(x)] E_2(x, z) + k_0^2 [n_1^2(x) - n_{\text{cl}}^2] E_1(x, z) = 0. \quad (2.51)$$

We now introduce (2.47) and (2.48) into these equations. Following our assumption that we are in the weakly-coupled regime,  $e_1$  and  $e_2$  fulfill the sourceless Helmholtz equation (2.9) as if they were isolated, so we are left with:

$$\left[ \frac{d^2 a_1}{dz^2} - 2i\beta_1 \frac{da_1}{dz} \right] e_1 \exp(-i\beta_1 z) = k_0 [n_{\text{cl}}^2 - n_2^2(x)] a_2 e_2 \exp(-i\beta_2 z), \quad (2.52)$$

$$\left[ \frac{d^2 a_2}{dz^2} - 2i\beta_2 \frac{da_2}{dz} \right] e_2 \exp(-i\beta_2 z) = k_0 [n_{\text{cl}}^2 - n_1^2(x)] a_1 e_1 \exp(-i\beta_1 z). \quad (2.53)$$



We can further approximate the equations by considering that the mode amplitudes  $a_j(z)$  vary slowly in  $z$ , which is again consistent with the weak coupling assumption, so that we can neglect the first term of both equations. To get rid of the transverse dependence, we multiply (2.52) by  $e_1(x)$  and (2.53) by  $e_2(x)$  and integrate over the transverse coordinate  $x$ . Considering that  $e_1^2$  and  $e_2^2$  are normalized to one, we obtain:

$$\frac{da_1}{dz} = -it_{21}a_2(z) \exp[i(\beta_1 - \beta_2)z], \quad (2.54)$$

$$\frac{da_2}{dz} = -it_{12}a_1(z) \exp[i(\beta_2 - \beta_1)z], \quad (2.55)$$

where the coupling coefficients are:

$$t_{21} = \frac{1}{2\beta_1} k_0^2 (n_2^2 - n_{\text{cl}}^2) \int_{\omega_1} e_1(x) e_2(x) dx, \quad (2.56)$$

$$t_{12} = \frac{1}{2\beta_2} k_0^2 (n_1^2 - n_{\text{cl}}^2) \int_{\omega_2} e_2(x) e_1(x) dx. \quad (2.57)$$

The integral in (2.56) spans over the core of the first waveguide, whereas the one in (2.57) spans over that of the second. These couplings are only equal when we have identical waveguides, that is, when the propagation constants of left and right modes are equal,  $\beta_1 = \beta_2$ . Eqs. (2.54) and (2.55) can be put in a compact matrix form by defining  $\tilde{a}_j(z) = a_j(z) \exp(-i\beta_j z)$ :

$$i \frac{d}{dz} \begin{pmatrix} \tilde{a}_1 \\ \tilde{a}_2 \end{pmatrix} = \begin{pmatrix} \beta_1 & t_{21} \\ t_{12} & \beta_2 \end{pmatrix} \begin{pmatrix} \tilde{a}_1 \\ \tilde{a}_2 \end{pmatrix}. \quad (2.58)$$

Solving the system and reversing the relation between  $\tilde{a}_j$  and  $a_j$  yields [222]:

$$a_1(z) = \left[ a_1(0) \left( \cos \gamma z - i \frac{\Delta\beta}{2\gamma} \sin \gamma z \right) - a_2(0) \frac{it_{21}}{\gamma} \sin \gamma z \right] \exp \left( \frac{i\Delta\beta z}{2} \right), \quad (2.59)$$

$$a_2(z) = \left[ -a_1(0) \frac{it_{12}}{\gamma} \sin \gamma z + a_2(0) \left( \cos \gamma z + i \frac{\Delta\beta}{2\gamma} \sin \gamma z \right) \right] \exp \left( \frac{-i\Delta\beta z}{2} \right), \quad (2.60)$$

where  $\gamma^2 = \left( \frac{\Delta\beta}{2} \right)^2 + t^2$  with  $t^2 = t_{12}t_{21}$ , and the difference in propagation constants of both modes,  $\Delta\beta = \beta_1 - \beta_2$ , is called the detuning. The efficiency of the power transfer will directly depend on this parameter. We can see this by computing the power in each waveguide,  $P_j(z) \propto |a_j(z)|^2$ . If we consider an initial input of light only on the first waveguide,  $a_1(0) = 1$  and  $a_2(0) = 0$ , the power on each waveguide along  $z$  is:

$$P_1(z) = P_1(0) \left[ \cos^2 \gamma z + \left( \frac{\Delta\beta}{2\gamma} \sin \gamma z \right)^2 \right], \quad (2.61)$$

$$P_2(z) = P_1(0) \left( \frac{|t_{21}|}{\gamma} \sin \gamma z \right)^2. \quad (2.62)$$

When both waveguides are identical,  $\Delta\beta = 0$  and  $t_{12} = t_{21} = t$ , so these reduce to:

$$P_1(z) = P_1(0) \cos^2 tz, \quad (2.63)$$

$$P_2(z) = P_1(0) \sin^2 tz, \quad (2.64)$$

and there can be full power transfer between the two. However, when the detuning is not zero, there can never be total power transfer. That is to say, a non-zero detuning hinders power transfer between evanescently-coupled waveguides. This can be readily observed by comparing Fig. 2.5(a) and (b), where light propagation between matched and detuned waveguides, respectively, is shown.

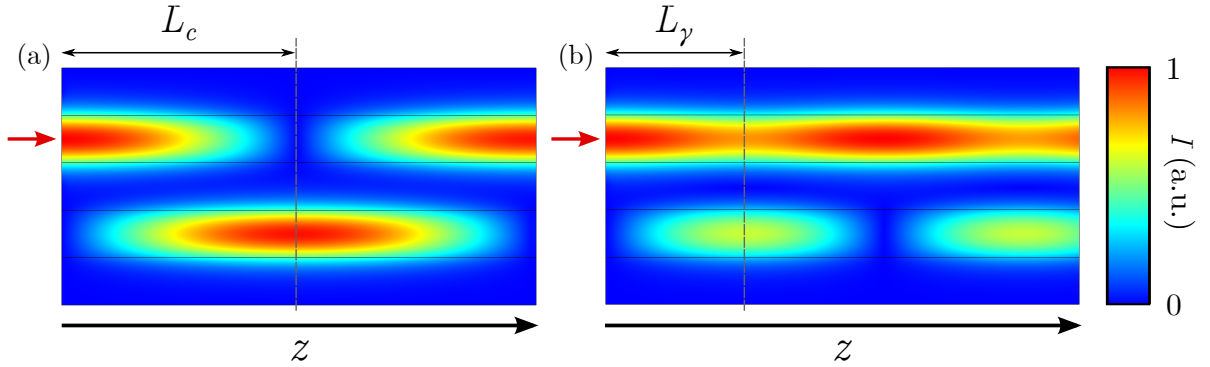


Figure 2.5: Light propagation in an optical directional coupler. (a) When the waveguides are identical, full transfer occurs in a distance of  $L_c$ . (b) When the waveguides are not identical, the coupling is suppressed. Maximum transfer occurs at  $L_\gamma$ , but the intensity contrast never reaches unity.

It is also common to describe directional couplers in terms of a transfer matrix that relates input and output fields. By taking  $A_1(z) = a_1(z)e^{-i\Delta\beta z/2}$  and  $A_2(z) = a_2(z)e^{i\Delta\beta z/2}$ , and assuming  $t_{12} = t_{21} = t$ , we can recast Eqs. (2.59) and (2.60) as:

$$\begin{pmatrix} A_1(z) \\ A_2(z) \end{pmatrix} = \begin{pmatrix} \mathcal{T} & i\kappa \\ i\kappa & \mathcal{T}^* \end{pmatrix} \begin{pmatrix} A_1(0) \\ A_2(0) \end{pmatrix}, \quad (2.65)$$

with  $\mathcal{T} = \cos \gamma z - i\frac{\Delta\beta}{2\gamma} \sin \gamma z$  and  $\kappa = -\frac{t}{\gamma} \sin \gamma z$  being the transmission and coupling coefficients of the optical coupler, respectively. For matched waveguides where  $\Delta\beta = 0$ ,  $\mathcal{T} = \mathcal{T}^* \in \mathbb{R}$ . This formalism is useful when chaining several optical components consecutively, as one can determine the total optical output by multiplying the individual transfer matrices of each component [222].

We have established in (2.61) and (2.62) that, in an optical directional coupler, the power exchange between both waveguides directly depends on the coupling strength, and that the rate at which it occurs is determined by the parameter  $\gamma$ . For general

waveguides, maximum power transfer will occur at a length:

$$L_\gamma = \frac{\pi}{2\gamma} = \frac{\pi\sqrt{\Delta P}}{2t}, \quad (2.66)$$

where  $\Delta P = [\max(P_1) - \min(P_1)] / \max(P_1)$  accounts for the intensity contrast between coupled waveguides. For identical waveguides, full transfer occurs at:

$$L_c = \frac{\pi}{2t}, \quad (2.67)$$

since for those the contrast  $\Delta P = 1$ . These distances are known as coupling or beating lengths. Generally, it is more convenient to compute the coupling strengths by experimentally measuring these lengths, which already contain that information, than to do it by using the general expressions in Eqs. (2.56) and (2.57). Note that, for equal couplings, the beating length is shorter for larger detunings. From the expression in (2.66) we can obtain both the coupling strength and detuning as:

$$t = \frac{\pi\sqrt{\Delta P}}{2L_\gamma}, \quad \Delta\beta = \frac{\pi\sqrt{1 - \Delta P}}{L_\gamma}. \quad (2.68)$$

Furthermore, it is known that the coupling strength depends exponentially on the separation  $d$  between waveguides [257]. As such, we can express:

$$t(d) = t_0 \exp(-\bar{k}d), \quad (2.69)$$

One can then measure  $L_\gamma$  for different separations and fit the results to an exponential function, thus producing a mapping between couplings strengths and relative distances.

The coupled-mode model can be directly extended to one-dimensional (1D) waveguide arrays of any size. Considering that we are in the weak coupling regime, and that the coupling strength decays exponentially with the distance, it is sensible to work in the nearest-neighbor (NN) coupling approximation, since the overlap between the modes in waveguides  $j$  and  $j \pm 2$  will be negligible. Furthermore, couplings beyond NN are also inhibited by the presence of the nearest waveguides [258]. Therefore, the equation for the amplitude of the single mode in each waveguide  $j$  is [259]:

$$i \frac{d\tilde{a}_j}{dz} = \beta_j \tilde{a}_j + t_{j-1,j} \tilde{a}_{j-1} + t_{j+1,j} \tilde{a}_{j+1}, \quad (2.70)$$

which can be written in matrix form:

$$i \frac{d\tilde{\mathbf{a}}}{dz} = \mathcal{H} \tilde{\mathbf{a}}, \quad (2.71)$$

where  $\tilde{\mathbf{a}} = (\tilde{a}_1, \dots, \tilde{a}_N)^T$  contains the amplitudes in each waveguide and  $\mathcal{H}$  is a tridiagonal matrix featuring all propagation constants and coupling strengths:

$$\mathcal{H} = \begin{pmatrix} \beta_1 & t_{21} & 0 & \dots & 0 \\ t_{12} & \beta_2 & t_{32} & \ddots & \vdots \\ 0 & t_{23} & \beta_3 & \ddots & \vdots \\ \vdots & \ddots & \ddots & \ddots & t_{N,N-1} \\ 0 & \dots & \dots & t_{N-1,N} & \beta_N \end{pmatrix}. \quad (2.72)$$

For the special case of  $N$  identical waveguides,  $t_{j,j\pm 1} = t_{j\pm 1,j}$  for all  $j$ , and all propagation constants are equal. By making an appropriate energy shift, we can set all  $\beta_j = 0$  without loss of generality, and  $\mathcal{H}$  becomes:

$$\mathcal{H} = \begin{pmatrix} 0 & t_1 & 0 & \dots & 0 \\ t_1 & 0 & t_2 & \ddots & \vdots \\ 0 & t_2 & 0 & \ddots & \vdots \\ \vdots & \ddots & \ddots & \ddots & t_{N-1} \\ 0 & \dots & \dots & t_{N-1} & 0 \end{pmatrix}. \quad (2.73)$$

Light propagation can then be described in terms of the eigenmodes of the waveguide lattice, sometimes called the supermodes of the structure, by diagonalizing (2.73). So far, we have considered single-mode waveguides for the coupled-mode formalism, but it can be easily extended to systems of similar or identical multimode waveguides. In principle, all modes can interact with one another and lead to a fairly complicated light propagation scheme. However, recall from (2.63) and (2.64) that power transfer between waveguides is suppressed for nonzero detunings. Moreover, the coupling between modes with different parities is also suppressed due to the nature of the coupling coefficients in (2.56) and (2.57). Both these reasons imply that one can usually consider the propagation of modes of different order independently of each other. Hence, for each mode  $m$ , the amplitudes are determined by a separate equation of the form of Eq. (2.71) containing only the coupling information for that mode in each waveguide. Of course, if nearby waveguides are sufficiently different, modes of different order on each waveguide can have similar propagation constants and thus can achieve significant coupling strengths. A paramount example of this will be shown in Section 2.2, when we explore the coupling between a waveguide and its superpartner, which has a different number of guided modes. We will also exploit the coupling between the excited mode of a waveguide and the fundamental mode of its superpartner for several purposes in Chapter 3.

Finally, we note that although highly useful, the coupled-mode model can only be accurately applied when the relative distance between waveguides is large. For shorter

distances, where couplings are larger, the overlap between modes is important enough that they cannot really be regarded as unaltered, rendering the initial approximation invalid [226, 260]. In those cases, the two coupled modes cannot be considered to be orthogonal to each other, although recasting the modes into a new orthogonal basis allows to extend the coupled-mode formalism for these scenarios [226, 261–264]. In general, however, these modes will strongly hybridize and one needs to apply full finite-difference methods to accurately reproduce experimental results.

### 2.1.4 Coupling between OAM modes

The simple picture depicted above is sufficient to describe tight-binding systems with real couplings, which already display a vast plethora of interesting physical properties [42, 49]. However, a new dimension of opportunities appears when considering complex couplings. In photonics, one way to obtain them is through the coupling of OAM modes of the kind described in Sec. 2.1.2. Recall that these modes take the following form:

$$E_l(r, \varphi, z) = e_l(r) e^{\pm i l (\varphi - \varphi_0)} e^{-i \beta_l z}, \quad (2.74)$$

where we only consider the lowest-order radial mode, and where  $\varphi_0$  is an arbitrary phase origin. When considering the coupling between different waveguides, the detuning between modes of different order  $l$  allows to separate the dynamics into manifolds of the same OAM order, each governed by a separate set of coupled-mode equations. This can be justified by the fact that light transfer between sufficiently detuned waveguides is highly suppressed, as discussed in Sec. 2.1.3. For our purposes, we restrict the analysis to  $l = 0$  and  $l = 1$  modes. The coupling between OAM modes among two waveguides depends on the overlap integral between them, their OAM charge,  $l_1$  and  $l_2$ , their circulations,  $\mathcal{K}_1, \mathcal{K}_2 = \pm$ , and the relative angle  $\varphi$  with respect to an arbitrary origin  $\varphi_0$  [265]. In other words:

$$\tau_{l_1, l_2} = |\tau_{l_1, l_2}| e^{i(\mathcal{K}_1 l_1 - \mathcal{K}_2 l_2)(\varphi - \varphi_0)}. \quad (2.75)$$

As described in Ref. [265], symmetry considerations reduce the number of independent components in the analysis of the coupling between OAM modes. When coupling modes with the same  $l$ , all different combinations can be described via at most three independent couplings:

- $\tau_1$ : between different OAM circulations in the same waveguide.
- $\tau_2$ : between the same OAM circulations in different waveguides.
- $\tau_3$ : between different OAM circulations in different waveguides.

The  $\tau_2$  coupling links the same OAM circulation and as such is always real. In contrast, both  $\tau_1$  and  $\tau_3$  are subject to picking up a phase and becoming complex. The first

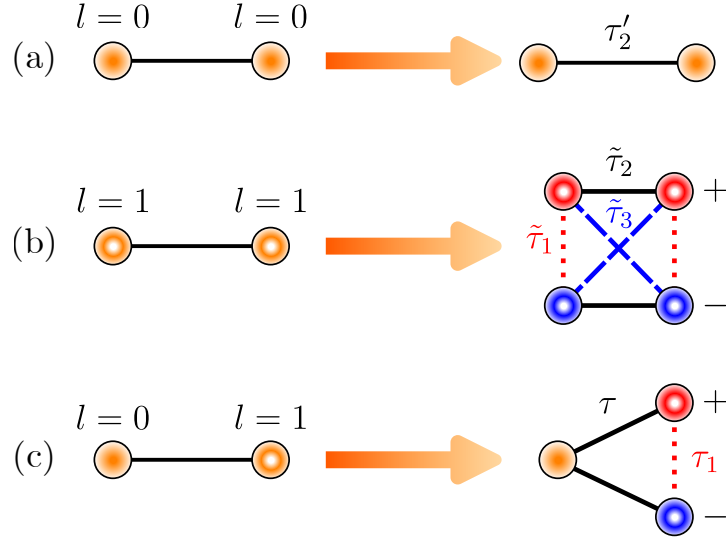


Figure 2.6: Coupling scheme between waveguides with different OAM modal content for (a)  $l = 0 \leftrightarrow l = 0$ , (b)  $l = 1 \leftrightarrow l = 1$  and (c)  $l = 0 \leftrightarrow l = 1$ . The left side corresponds to the physical waveguides, whereas in the right side different OAM circulations are represented separately.

coupling,  $\tau_1$ , appears due to the breaking of the cylindrical symmetry of the waveguide mode due to the presence of the second waveguide, which leads to nonzero coupling between otherwise orthogonal modes in the same waveguide.

To determine the value of the couplings in numerical simulations, one can compute the propagation constants of the eigenmodes in a set of two waveguides, which behave as the eigenvalues of the system. Then, by diagonalizing the corresponding Hamiltonian in each case, one can find a relation between these eigenvalues and the couplings. We consider each case separately, starting by the case of  $l = 0 \leftrightarrow l = 0$  in Fig. 2.6(a). For modes with a propagation constant  $\beta_0$ , the Hamiltonian describing the system reads:

$$\mathcal{H}_{l=0} = \begin{pmatrix} \beta_0 & \tau'_2 \\ \tau'_2 & \beta_0 \end{pmatrix}. \quad (2.76)$$

Diagonalizing directly leads to eigenvalues  $\mu_- = \beta_0 - \tau'_2$  and  $\mu_+ = \beta_0 + \tau'_2$ , and thus

$$\tau'_2 = \frac{1}{2} (\mu_+ - \mu_-). \quad (2.77)$$

This case is no different from the regular set of single-mode waveguides that was discussed in Sec. 2.1.3, with the single coupling remaining real.

For  $l = 1 \leftrightarrow l = 1$ , the sketch in Fig. 2.6(b) depicts a richer situation as all three described couplings appear. In a set of two waveguides, however, one can always choose the phase origin  $\varphi_0$  in the direction joining the two waveguides, rendering all couplings

real. For modes with propagation constant  $\beta_1$ , the Hamiltonian is:

$$\mathcal{H}_{l=1} = \begin{pmatrix} \beta_1 & \tilde{\tau}_1 & \tilde{\tau}_2 & \tilde{\tau}_3 \\ \tilde{\tau}_1 & \beta_1 & \tilde{\tau}_3 & \tilde{\tau}_2 \\ \tilde{\tau}_2 & \tilde{\tau}_3 & \beta_1 & \tilde{\tau}_1 \\ \tilde{\tau}_3 & \tilde{\tau}_2 & \tilde{\tau}_1 & \beta_1 \end{pmatrix} \quad (2.78)$$

and its eigenvalues are:

$$\begin{aligned} \mu_1 &= \beta_1 + \tilde{\tau}_1 - \tilde{\tau}_2 - \tilde{\tau}_3 \\ \mu_2 &= \beta_1 - \tilde{\tau}_1 + \tilde{\tau}_2 - \tilde{\tau}_3 \\ \mu_3 &= \beta_1 - \tilde{\tau}_1 - \tilde{\tau}_2 + \tilde{\tau}_3 \\ \mu_4 &= \beta_1 + \tilde{\tau}_1 + \tilde{\tau}_2 + \tilde{\tau}_3. \end{aligned} \quad (2.79)$$

Rearranging these leads us to the three described couplings:

$$\begin{aligned} \tilde{\tau}_1 &= \mu_1 - \mu_2 - \mu_3 + \mu_4 \\ \tilde{\tau}_2 &= -\mu_1 + \mu_2 - \mu_3 + \mu_4 \\ \tilde{\tau}_3 &= -\mu_1 - \mu_2 + \mu_3 + \mu_4. \end{aligned} \quad (2.80)$$

Phases will play a role for larger sets of waveguides, where one can play with the geometry to achieve different relative angles, as we will show later on in Chapter 5. Recall that for  $l = 1$  and different OAM circulations the exponential term is  $|\mathcal{K}_1 l - \mathcal{K}_2 l| = 2$ , and hence  $\tilde{\tau}_m = |\tilde{\tau}_m| e^{2i(\varphi - \varphi_0)}$  with  $m = 1, 3$ .

One last scenario that will be of interest for us is the crossed case of  $l = 0 \leftrightarrow l = 1$  in Fig. 2.6(c). Despite these modes having different propagation constants for identical waveguides, one can tune the refractive index of both waveguides to achieve matching between them, thus enabling a coupling that would otherwise be strongly suppressed. For this case, we define  $\tau$  as the coupling between the OAM modes in different waveguides, and  $\tau_1$  as the coupling between different circulations in the  $l = 1$  mode, as before. The Hamiltonian for that case, with propagation constants  $\beta_2$ , is:

$$\mathcal{H}_{l=0,1} = \begin{pmatrix} \beta_2 & \tau & \tau \\ \tau & \beta_2 & \tau_1 \\ \tau & \tau_1 & \beta_2 \end{pmatrix}, \quad (2.81)$$

and the eigenvalues:

$$\begin{aligned} \mu_1 &= \beta_2 - \tau_1 \\ \mu_2 &= \beta_2 + \frac{1}{2} \left( \tau_1 - \sqrt{\tau_1^2 + 8\tau^2} \right) \\ \mu_3 &= \beta_2 + \frac{1}{2} \left( \tau_1 + \sqrt{\tau_1^2 + 8\tau^2} \right). \end{aligned} \quad (2.82)$$

The couplings can again be extracted by inverting the relations above:

$$\begin{aligned}\tau_1 &= \frac{1}{3}(-2\mu_1 + \mu_2 + \mu_3) \\ \tau &= \sqrt{\frac{(\mu_3 - \mu_2)^2 - (-2\mu_1 + \mu_2 + \mu_3)^2/9}{8}}.\end{aligned}\tag{2.83}$$

### 2.1.5 Fabrication of optical waveguides

There are multiple methods that allow to fabricate optical waveguides in a variety of materials, such as in silicon, various glasses, crystals, polymers, semiconductors and a whole list of others [43, 45]. One of the main fabrication methods is the technique of direct laser writing using femtosecond laser pulses [42, 257, 266, 267]. These ultrashort pulses are tightly focused into a region of the material, which through nonlinear absorption forms a plasma around the focus point that permanently alters the refractive index of that region. This is usually caused by an increase in density due to the gathering of nearby molecules. The nearby regions, instead, suffer from a reduction of the refractive index that also contributes to the guiding. These density changes generate a stress field around the focus point [268, 269], which limits how closely one can write different waveguides. The magnitude of the change in refractive index can be controlled by the laser power and exposure time. Hence, by moving the sample at a certain speed, one can shape the trajectory and the index contrast of the waveguide. Slower speeds imply a larger amount of pulses at each point, and thus an increased index contrast. For higher laser power, if one goes beyond the damage threshold of the material, one may cause permanent damage in the focus region and cause a crater of sorts, leaving there a dip in refractive index instead of an increased value. Consequently, however, the stress fields in those cases produce a refractive index increase around the crater. So by producing two (or more) of these damage tracks near each other, light can be guided in the region between them and thus an effective waveguide is fabricated. This writing method that produces a negative index contrast  $\Delta n < 0$  has been labelled in some works as Type II laser writing [270–273], in contrast to Type I writing where  $\Delta n > 0$ . Type II writing can be used to draw a specific contour for the waveguide by drawing multiple tracks on the sample [271]. Laser writing has also been applied to polymers via two-photon polymerization, both by direct writing as well as by producing hollowing in the material, which is then infiltrated with a second polymer [159, 274–276]. Laser-writing techniques generally produce elongated waveguides that cannot guide OAM modes. However, by passing the laser through the sample multiple times, the combination of all different tracks can add up to rounder effective profiles both in type I [235, 277–279] and type II [280–282] procedures. Alternatively, polymers have also been shown to be a promising platform to produce round waveguide profiles [159, 276].



A second major technique is based on patterning materials with lithographic techniques. Essentially, electron-beam lithography [37] is used to draw shapes on a material over which a sensitive film is placed. When the beam is focused on the film, it changes its properties and allows the selective removal of either the exposed sections of the sample, or the rest that was not affected, by performing etching. Then, a cladding of choice can be used by deposition of another material. This multi-step process is more complex than direct laser writing, but allows for very precise fabrication of complicated structures, which is why it is often used for lattices of ring resonators [151, 169, 185, 283, 284] or even resonators with highly complex shapes [285–287]. The index difference is guaranteed by the usage of different materials, and the shape of the device and the frequency of light are used to control the mode properties. Alternatively to electron-beam lithography, ultraviolet photolithography can also serve the same purpose [204].

Although not following the classical definition of “fabrication”, non-permanent waveguides can be induced in photorefractive materials [288–290] wherein a collection of light beams is made to interfere, creating a common periodic pattern of intensity. This, in turn, produces a pattern of changes in refractive index in the material over which other light can be guided. The selling point of this technique is that these patterns can be reconfigured by changing the configuration of light beams, without needing new material samples. A similar process can lead to light guiding through the usage of acoustic waves that create local pressure differences in a material [291, 292]. The idea of using nonlinearities to form temporal waveguides has even been used to guide light through air [293].

### 2.1.6 Optical waveguides as quantum simulators

As a final note in the section, let us emphasize the general interest of optical waveguides in this thesis by commenting on its applications as simulators of quantum systems. What allows waveguides to fulfill this purpose is the analogy that exists between quantum and optical systems. This analogy stems from the similarity between the Schrödinger and Helmholtz equations, where the role of time in the former is played by the propagation distance in the latter. This allows to probe the dynamical behavior of multiple systems – in disciplines such as atomic, condensed matter or quantum physics – by studying light propagation in analogous photonic systems that usually entail a simpler experimental implementation. Many examples of this effect can be found in [49] and references therein. Not only is the fabrication generally simpler, but optical waveguides also allow for a direct visualization of the evolution of the wavefunction by directly observing the spatial light propagation in the system. This can be done for instance through fluorescence microscopy [42], in which the impurities known as color centers that are generated inside the waveguides are excited by the light that propagates

through the structure and emit light through fluorescence, marking the path followed by the propagated light.

Let us describe the quantum-optical analogy in several scenarios. First, starting from the Helmholtz equation (2.9) and considering a weakly-guiding waveguide that varies slowly along the propagation axis, the paraxial approximation can be applied. Under these conditions, the now paraxial Helmholtz equation for the electric field envelope  $E(x, y, z)$  takes the form [42]:

$$i\lambda \frac{\partial}{\partial z} E(x, y, z) = \left[ -\frac{\lambda^2}{2n_{\text{cl}}} \nabla_T^2 - \Delta n(x, y, z) \right] E(x, y, z), \quad (2.84)$$

where  $\lambda = \lambda/2\pi$  and  $\Delta n(x, y, z) = n_{\text{cl}} - n(x, y, z)$  with  $n_{\text{cl}}$  the cladding refractive index. This equation is formally equivalent to the time-dependent Schrödinger equation:

$$i\hbar \frac{\partial}{\partial t} \Psi(x, y, t) = \left[ -\frac{\hbar^2}{2m} \nabla^2 + V(x, y, t) \right] \Psi(x, y, t), \quad (2.85)$$

which justifies that the time evolution of a wavefunction  $\Psi$  in a potential  $V$  following the Schrödinger equation can be described by the propagation of an electrical field envelope  $E$  in a waveguide with index contrast  $\Delta n$ , thus completing the analogy. Furthermore, the Helmholtz equation for TE modes that we computed previously in (2.30) can be thought of as an eigenvalue equation:

$$\left[ -\frac{d^2}{dx^2} - k_0^2 n^2(x) \right] E_y(x) = -\beta^2 E_y(x), \quad (2.86)$$

which has the same form as the time-independent Schrödinger equation:

$$\left[ -\frac{d^2}{dx^2} + V(x) \right] \Psi(x) = \mu \Psi(x), \quad (2.87)$$

where the role of the potential  $V(x)$  is again played by the refractive index term  $k_0^2 n^2(x)$  and the propagation constant  $\beta^2$  plays the role of the energy  $\mu$ . Finally, one can also readily observe the same analogy for waveguide lattices where one can use the coupled-mode formalism. It is easy to see that Eq. (2.71) is also formally equivalent to the time evolution for a tight-binding Hamiltonian:

$$i\hbar \frac{d}{dt} \Psi = H \Psi, \quad (2.88)$$

and diagonalization of both leads to equivalent descriptions. All these analogies enrich the scope that can be covered by systems of optical waveguides. These versatile systems are then not only interesting for their potential uses in photonic devices, but also as simulators.

## 2.2 Supersymmetry in optics

Supersymmetry (SUSY) was initially introduced in the context of quantum field theory and particle physics [64–67] to unify the mathematical treatment of fermions of bosons under the same theory, which is invariant under the interchange of one by the other, and as a way to go beyond the Standard Model of particle physics [68]. Although there has not been any experimental confirmation of the existence of SUSY particles since its introduction, the mathematical framework and the ideas behind it have been extended to other fields with a substantially larger success. Notable examples are condensed-matter [69], optics [70, 72], quantum mechanics [73], statistical mechanics [74] and cosmology [75]. This framework has also been extended into what is known as 2nd- and higher-order SUSY [294–297], applied to simple many-body systems [298] and also employed in the time domain [299].

In the context of optics, the framework of Supersymmetry (SUSY) was first applied in Ref. [70], and later to discrete waveguide lattices in Ref. [71]. After that, a huge list of applications have appeared by exploiting SUSY for modal control in planar optical waveguides [72, 76, 77, 82, 300–302], fibers [303, 304] and gratings [297, 305], and has also been utilized for Mode-Division Multiplexing [212, 306, 307]. Furthermore, SUSY allows to control the scattering properties of a system [79–81, 299, 308] and generate reflectionless structures [309–311], and has also been exploited for lasing [245, 246, 312–315], to reduce losses in bent waveguides [316, 317] and to alter the topology of the lattices [78]. If the superpartner profile is experimentally achievable, one can couple the supersymmetric partners between them [72, 77, 306, 313], or rather deform one into the other [82, 212, 214] as we do in Chapters 3 and 4, to exploit the properties of SUSY transformations. Although direct fabrication of SUSY refractive index profiles has been elusive so far, recently an experimental implementation has appeared in a silicon metamaterial [318]. The authors achieve this by discretizing the index profile along the transverse direction and relating it to a physical parameter of each element, i.e. the air gap between them, that is related to the confinement of the mode.

Here, we present the formalism of SUSY first for general superpartner Hamiltonians, and after that in the context of optical waveguides. We start with the continuous formalism, where the spatial profile of the refractive index is treated as the confining potential, and which leads to the computation of a superpartner index profile. Then, we apply the formalism to discrete waveguide lattices under the coupled-mode model, which are described by a matrix Hamiltonian. In this case, the superpartner is another waveguide lattice with modified couplings and propagation constants, but the profile of each individual waveguide does not change. Finally, we briefly comment on the application of SUSY to refractive indices beyond 1D.

### 2.2.1 SUSY formalism

The SUSY algebra satisfies the following commutation and anticommutation relations [73]:

$$\{Q, Q^\dagger\} = H, \quad (2.89)$$

$$\{Q, Q\} = \{Q^\dagger, Q^\dagger\} = 0, \quad (2.90)$$

$$[H, Q] = [H, Q^\dagger] = 0, \quad (2.91)$$

where  $H$  is the super-Hamiltonian of the system, and  $Q$  the supercharge operator. These can be defined in matrix form in terms of factorization operators,  $A$  and  $A^\dagger$ , as:

$$H = \begin{pmatrix} A^\dagger A & 0 \\ 0 & A A^\dagger \end{pmatrix}, \quad (2.92)$$

$$Q = \begin{pmatrix} 0 & 0 \\ A & 0 \end{pmatrix}, \quad Q^\dagger = \begin{pmatrix} 0 & A^\dagger \\ 0 & 0 \end{pmatrix}. \quad (2.93)$$

Alternatively, one may also define what some authors designate as a supercharge Hamiltonian [244, 319–321] by taking:

$$\mathcal{H}_{SC} = Q + Q^\dagger = \begin{pmatrix} 0 & A^\dagger \\ A & 0 \end{pmatrix}, \quad (2.94)$$

which can be thought of as the root Hamiltonian of (2.92), a fact that will prove to be relevant later on (see Sec. 2.3.3). What one actually designates as a SUSY transformation is the connection between the diagonal elements of  $H$  in Eq. (2.92), the so-called superpartner Hamiltonians  $\mathcal{H}^{(1)}$  and  $\mathcal{H}^{(2)}$ , which we assume to be Hermitian:

$$\mathcal{H}^{(1)} + \alpha = A^\dagger A, \quad (2.95)$$

$$\mathcal{H}^{(2)} + \alpha = A A^\dagger, \quad (2.96)$$

where  $\alpha$  is a constant energy shift that determines the characteristics of the transformation and that can be set to a desired value. Usually, one takes  $\alpha$  to be the eigenvalue of the fundamental mode of the system, which can be taken to be  $\alpha = 0$ . For now, we follow this convention.

Each superpartner Hamiltonian  $\mathcal{H}^{(1)}$  and  $\mathcal{H}^{(2)}$  will have a set of eigenvalues and eigenvectors, but they can be shown to be related. Assume that  $\psi_m^{(1)}$  is an eigenstate of  $\mathcal{H}^{(1)}$  with eigenvalue  $\mu_m^{(1)}$ :  $\mathcal{H}^{(1)}\psi_m^{(1)} = \mu_m^{(1)}\psi_m^{(1)}$ . Acting on the left with  $A$  gets us  $A\mathcal{H}^{(1)}\psi_m^{(1)} = AA^\dagger A\psi_m^{(1)} = \mathcal{H}^{(2)}A\psi_m^{(1)}$ . Hence:

$$\mathcal{H}^{(2)}(A\psi_m^{(1)}) = \mu_m^{(1)}(A\psi_m^{(1)}), \quad (2.97)$$

which implies that  $A\psi_m^{(1)}$  is an eigenstate of  $\mathcal{H}^{(2)}$  with energy  $\mu_m^{(1)}$ . In other words,  $\mathcal{H}^{(1)}$  and  $\mathcal{H}^{(2)}$  share the same spectrum, and hence SUSY transformations possess isospectrality. Eq. (2.97) can be fulfilled in two scenarios. We can have  $\mu_m^{(1)} = \mu_m^{(2)}$  for all  $m$ , in which case we say that we have *broken* SUSY. Instead, we have *unbroken* SUSY if  $\psi_0^{(1)}$  is annihilated by  $A$ ,  $A\psi_0^{(1)} = 0$ , whereby we eliminate the ground state eigenvalue from the spectrum of  $\mathcal{H}^{(2)}$  and have [73]:

$$\begin{cases} \mu_0^{(1)} = 0, \\ \mu_m^{(2)} = \mu_{m+1}^{(1)}. \end{cases} \quad (2.98)$$

In this case, the eigenstates of both Hamiltonians are related by:

$$\begin{cases} \psi_{m+1}^{(1)} = \frac{1}{\sqrt{\mu_m^{(2)}}} A^\dagger \psi_m^{(2)}, \\ \psi_m^{(2)} = \frac{1}{\sqrt{\mu_{m+1}^{(1)}}} A \psi_{m+1}^{(1)}. \end{cases} \quad (2.99)$$

The different effects of unbroken and broken SUSY on the spectrum of the Hamiltonians are summarized graphically in Fig. 2.7.

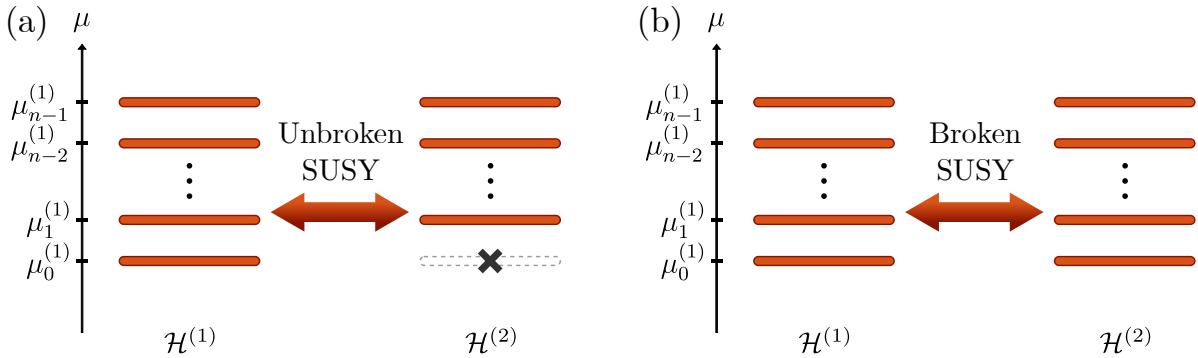


Figure 2.7: Sketch of the effect of (a) unbroken and (b) broken SUSY transformations on the spectrum of the partner Hamiltonians. In (a), the fundamental mode is removed from the spectrum of  $\mathcal{H}^{(2)}$ , while in (b) there is complete isospectrality.

Eqs. (2.98) and (2.99) state that we can obtain the whole spectrum of energies and eigenstates of the superpartner Hamiltonian  $\mathcal{H}^{(2)}$  from those of the original Hamiltonian  $\mathcal{H}^{(1)}$ , assuming that we know the factorization operators  $A$  and  $A^\dagger$ . Their concrete shape, of course, will depend on the Hamiltonian at hand. To elucidate the procedure through an example, let us find the superpartner of the following 1D single-particle Hamiltonian:

$$\mathcal{H}^{(1)} = -\frac{d^2}{dx^2} + V^{(1)}(x). \quad (2.100)$$

To do that, we express the factorization operators in terms of the so-called superpotential,  $W(x)$ :

$$A = \frac{d}{dx} + W(x) \quad (2.101)$$

$$A^\dagger = -\frac{d}{dx} + W(x). \quad (2.102)$$

By equating (2.100) to  $A^\dagger A$ , we can obtain the expression of  $V^{(1)}(x)$  in terms of  $W(x)$ :

$$V^{(1)}(x) = W^2(x) - \frac{dW(x)}{dx} \quad (2.103)$$

$$V^{(2)}(x) = W^2(x) + \frac{dW(x)}{dx}. \quad (2.104)$$

From (2.101)–(2.102) we now find the superpartner Hamiltonian,  $\mathcal{H}^{(2)} = AA^\dagger$ :

$$\mathcal{H}^{(2)} = -\frac{d^2}{dx^2} + V^{(2)}(x). \quad (2.105)$$

Thus, all we need to obtain the superpartner is the shape of  $W(x)$ . We assume that we know the ground state wavefunction of the original Hamiltonian,  $\psi_0^{(1)}$ , and that it has zero energy. Then, we impose its eigenvalue equation,  $\mathcal{H}^{(1)}\psi_0^{(1)} = 0$ , from which we obtain [73]:

$$V^{(1)}(x) = \frac{1}{\psi_0^{(1)}} \frac{d^2 \psi_0^{(1)}}{dx^2}, \quad (2.106)$$

and we can introduce it in (2.103) to finally obtain:

$$W(x) = -\frac{1}{\psi_0^{(1)}} \frac{d\psi_0^{(1)}}{dx} = -\frac{d}{dx} \left[ \ln \psi_0^{(1)} \right], \quad (2.107)$$

where we assume that the ground state wavefunction has no nodes. Beyond the formalism presented here, one can also apply SUSY transformations to non-Hermitian Hamiltonians by taking  $\mathcal{H}^{(1)} = BA + \alpha$ ,  $\mathcal{H}^{(2)} = AB + \alpha$  with  $B \neq A^\dagger$  [76, 310, 322–325]. This has proven to be an useful extension for complex Hamiltonians with real energy spectra, such as those with PT-symmetry [323]. Finally, one can also extend these ideas to transformations of higher order [294–297]. For second-order SUSY, instead of the factorization operators in (2.101)–(2.102), one can employ an intertwining operator  $\mathbb{B}$  with derivatives up to second order. The situation here is richer since the superpotential now depends on two generating functions  $W(u_1, u_2) = u_1 \partial_x u_2 - (\partial_x u_1) u_2$ , which implies that even if any of the two functions have nodes, as long as  $W(u_1, u_2)$  is nodeless the superpartner will be well-behaved.

### 2.2.2 SUSY in optical waveguides

Considering that there is a direct analogy between waveguide optics and quantum mechanics, as detailed in Section 2.1.6, the SUSY formalism can also be applied to the description of electric fields propagating in optical waveguides. Recall that the Helmholtz equation describing the propagation of TE modes, Eq. (2.30), can be put in the form of an eigenvalue equation:

$$\left[ -\frac{d^2}{dx^2} - k_0^2 n^2(x) \right] E_y(x) = -\beta^2 E_y(x), \quad (2.108)$$

which allows us to exploit the factorization process that is described in Sec. 2.2.1. The term between brackets can be thought of as a Hamiltonian,  $\mathcal{H} = -\frac{d^2}{dx^2} - k_0^2 n^2(x)$ , which upon comparison with Eq. (2.100) reveals that the term of the refractive index  $n(x)$  takes the role of the potential  $V^{(1)}(x) = -k_0^2 n^2(x)$  with  $k_0 = 2\pi/\lambda_0$  is the vacuum wavenumber. This implies that given any refractive index profile  $n^{(1)}(x)$ , we can obtain a superpartner profile  $n^{(2)}(x)$  through the SUSY transformation formalism. In the context of optical waveguides, the superpartner refractive index profile has the same modal content as the initial waveguide aside from the fundamental mode, which is not supported by the SUSY waveguide if SUSY is unbroken. This allows for a greater control of light transmission in multimodal waveguide structures, as only modes that are supported by a waveguide will be able to be transferred to it.

The superpartner Hamiltonian can be obtained from the factorization in (2.95) and (2.96), where we take  $\alpha = \left(\beta_0^{(1)}\right)^2$ , with  $\beta_0^{(1)}$  the propagation constant of the fundamental mode of the waveguide. From this, knowing the definition of the factorization operators from (2.101)–(2.102) and the form of the Hamiltonian from Eq. (2.108), we can extract an expression for the superpartner index profiles in terms of the superpotential,  $W(x)$ :

$$n^{(1)}(x) = \frac{1}{k_0} \sqrt{\left(\beta_0^{(1)}\right)^2 - W^2(x) + \frac{dW(x)}{dx}}, \quad (2.109)$$

$$n^{(2)}(x) = \frac{1}{k_0} \sqrt{\left(\beta_0^{(1)}\right)^2 - W^2(x) - \frac{dW(x)}{dx}}, \quad (2.110)$$

with the superpotential now depending on the electric field distribution of the fundamental mode of the waveguide:

$$W(x) = -\frac{d}{dx} \left[ \ln e_0^{(1)} \right]. \quad (2.111)$$

More conveniently, we can combine Eqs. (2.109) and (2.110) to express the superpartner profile  $n^{(2)}(x)$  in terms of  $n^{(1)}(x)$ :

$$n^{(2)}(x) = \sqrt{[n^{(1)}]^2 - \frac{2}{k_0^2} \frac{dW}{dx}}. \quad (2.112)$$

Again, to compute the expression of the superpotential in (2.111), we are assuming a nodeless mode, from which we infer an important property of this formalism: we can only target the fundamental mode of the structure with unbroken SUSY transformations. Higher-order modes possess nodes in their spatial field profile, and as such cannot be used to define a non-singular superpotential. The transformation can still be performed, but through (2.112) it leads to a index profile displaying singularities. This difficulty is however not present in non-Hermitian systems [323], where the zeros of both real and imaginary parts of the modes have to be taken into account, or when applying the discrete SUSY formalism that will be introduced in the next section.

Analytical expressions for  $n^{(2)}(x)$  can only be derived for those cases in which exact solutions for the fundamental mode  $e_0^{(1)}(x)$  can be found. Otherwise, both the mode shape and the index profile need to be found numerically. For the case of a step-index waveguide with core and cladding refractive indices  $n_{\text{co}}$  and  $n_{\text{cl}}$ , respectively, exact solutions exist and the SUSY partner can be shown to be:

$$n_{\text{SUSY}} = \sqrt{n_{\text{co}}^2 - 2 \left( \frac{k_x}{k_0} \right)^2 \sec^2(k_x x)}, \quad (2.113)$$

with  $k_x = \sqrt{n_{\text{co}}^2 k_0^2 - \beta_0^2}$ . Both the index profile and the mode levels for the SUSY pair are drawn in Fig. 2.8(a). Although analytical, this profile displays a shape that is extremely difficult to implement in practice, mainly due to the sharp dips at the core edges which actually go well below the cladding value. This difficulty can be lowered by considering a smoother index profile. A prime example is the super-Gaussian defined by:

$$[n(x)]^2 = n_{\text{cl}}^2 + (n_{\text{co}}^2 - n_{\text{cl}}^2) \exp \left[ - \left( \frac{2x}{w} \right)^{2p} \right], \quad (2.114)$$

and controlled through the index  $p$ . We show this profile in Fig. 2.8(b), and showcase how its superpartner is much softer than in the step-index case. These profiles are closer to what waveguides look like in laser-writing setups, but in this case the superpartner profile needs to be computed numerically as there is no analytical expression for the guided modes.

Higher-order SUSY transformations can be built by chaining consecutive individual SUSY transforms, which can be used to build a hierarchy of superpartner profiles, each one with one less supported mode than the previous one. In general, much like in Eq. (2.112), you can relate neighboring superpartners via the following expression:

$$n^{(i+1)}(x) = \sqrt{[n^{(i)}]^2 - \frac{2}{k_0^2} \frac{dW^{(i)}}{dx}}, \quad (2.115)$$



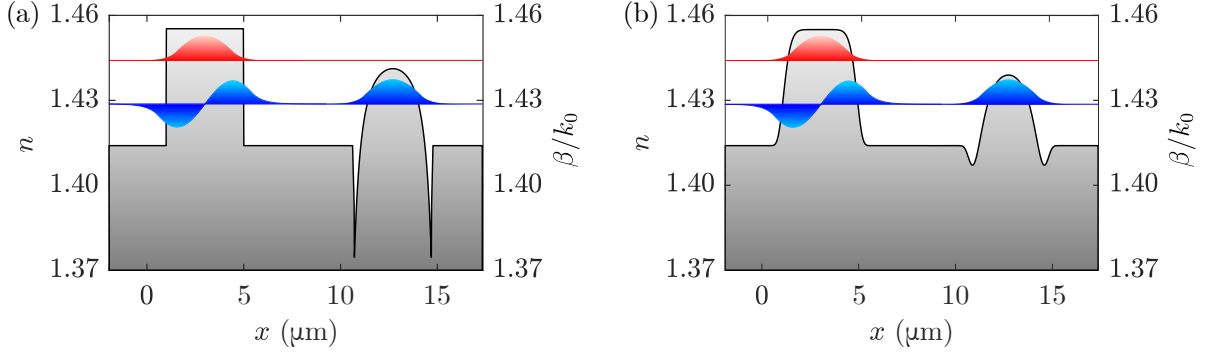


Figure 2.8: (a) Refractive index of a two-mode step-index waveguide (left) and its superpartner (right), which is single-mode. The mode propagation constants and spatial profiles are sketched on top of each core. (b) Same structure for the super-Gaussian profile defined in (2.114), where the dips in the superpartner refractive index are softened.

with the superpotential  $W^{(i)}$  being defined in terms of the fundamental mode of the  $i$ -th order superpartner:

$$W^{(i)}(x) = -\frac{d}{dx} \left[ \ln e_0^{(i)} \right]. \quad (2.116)$$

Bear in mind that each SUSY transformation targets and removes the fundamental mode of the structure of interest. One can also, however, build hierarchies of superpartners by using broken SUSY transformations [307], where each structure shares guided modes with the rest but displays different mode profiles. Recall that, even though we chose  $\alpha$  to be the eigenvalue of the ground state in (2.95) and (2.96), in general this need not be the case. If one instead chooses a different value for  $\alpha$ , the symmetry is broken and  $A\psi_0^{(1)} \neq 0$  [304]. With broken SUSY, one can generate an infinite number of isospectral profiles.

### 2.2.3 Discrete Supersymmetry

Complementary to the continuous SUSY formalism, one can also build discrete SUSY (DSUSY) transformations [72] between discrete Hamiltonians via matrix transformations. Applying these transformations to a discrete system, in general, leads to another system that has a modified geometry but shares the same spectrum of energies as the former. In the case of a tridiagonal Hamiltonian, the superpartner maintains the tridiagonal structure. In other words, the superpartner structure of a 1D lattice with nearest-neighbor couplings will maintain the nearest-neighbor configuration.

In a similar way to the continuous formalism, if SUSY is unbroken, one of the eigenvalues  $\mu_m$  of the original Hamiltonian  $\mathcal{H}^{(1)}$  is removed and thus is missing from  $\mathcal{H}^{(2)}$  after applying the DSUSY transformation. Physically, this implies that the corresponding state of the superpartner lattice is localized in an isolated site, which is decoupled

from the others. The rest of the eigenstates remain in the other part of the chain, having a different spatial distribution but without changes in energy. Successive applications of DSUSY transformations reduce in one the effective size of the lattice at each step, as one site is decoupled per transformation. One usually refers to the lattice containing the rest of the states as the superpartner of the original structure. If the symmetry is broken, however, the transformation does not remove any state from the spectrum. For optical waveguides, one can use this formalism to remove supermodes from the lattice by confining them in the decoupled waveguides, thus controlling the modal content of the structure [77, 78, 214].

DSUSY transformations can be implemented via the Cholesky factorization or the QR factorization [326] methods. Below, we will focus on QR factorization of the matrix Hamiltonians. Note that DSUSY holds a major advantage over the continuous version, as now we are not limited to removing only the fundamental mode. When building the factorization, we may choose to target any eigenvalue  $\beta_m$  to remove from the superpartner.

### QR factorization

The QR factorization relates the superpartner Hamiltonians in the following way:

$$\mathcal{H}_m^{(1)} - \beta_m^{(1)} I = QR, \quad (2.117)$$

$$\mathcal{H}_m^{(2)} - \beta_m^{(1)} I = RQ, \quad (2.118)$$

where  $I$  is the identity matrix,  $Q$  is an orthogonal matrix and  $R$  an upper triangular matrix. This method can be used to remove any desired supermode from the system by adequately choosing  $\beta_m$  to be equal to its propagation constant. One should note that, in general, this factorization is not unique [326], and this can lead to more than one superpartner structure sharing the same eigenvalues [78]. In general, if the targeted eigenmode has zero energy, the DSUSY transformation results in a superpartner where the propagation constants of the individual waveguides are not altered. That is, the superpartner Hamiltonian will not have diagonal elements associated to the transformation. This no longer occurs when removing a mode with nonzero energy. We exemplify this effect using the lattice with spectrum and coupling distribution as shown in Figs. 2.9(a) and (b), respectively. From there, computing the superpartner leads to the coupling and detuning distributions exhibited in Figs. 2.9(c) and (d) when targeting a zero and a nonzero mode, respectively. Note that in these figures, waveguide 9 is decoupled from the rest.

QR factorization can be implemented in multiple ways: via Gram-Schmidt decomposition, the Givens rotation method or by using the Householder transformation [326]. Here, we focus on the Householder method [327], which is based on applying unitary transformations to a matrix, turning it into a triangular one.

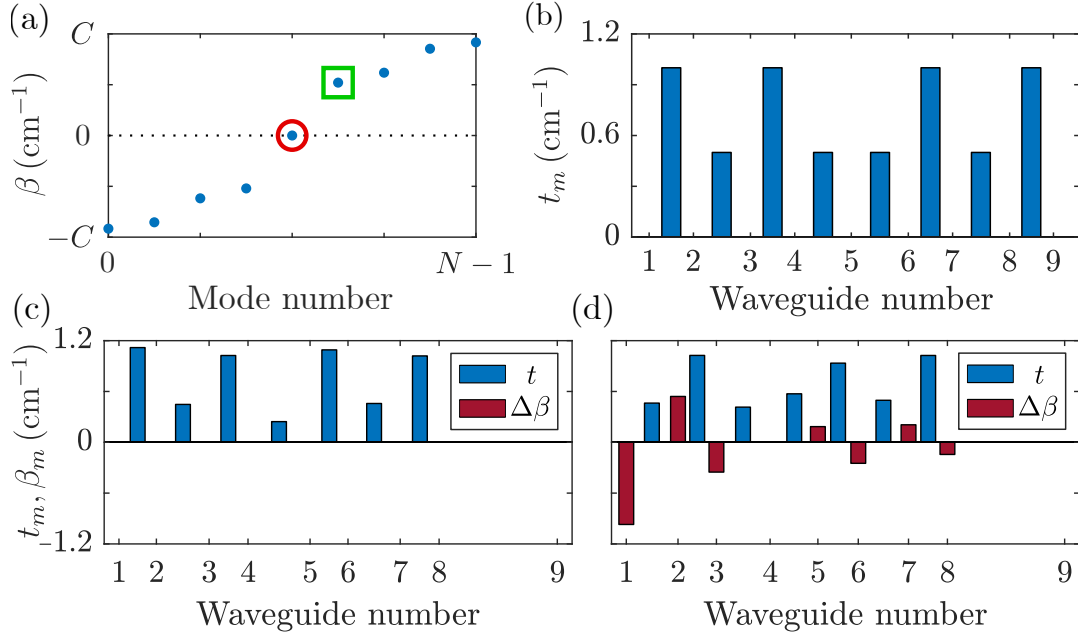


Figure 2.9: (a) Spectrum of the lattice of which we compute the discrete superpartner and (b) values of the couplings between its waveguides. (c)–(d) Coupling and detuning distribution for the superpartners of the considered lattice when targeting (c) a zero-energy mode [red circle in (a)], which generates a lattice with zero detunings, and (d) a mode with nonzero energy [green square in (a)], where detunings are nonzero.

### Householder Transformation

The Householder transformation [326] can be applied for any  $m \times n$  matrix as long as  $m \geq n$ , but we restrict ourselves to a general square matrix  $A$ . The objective of the transformation is to obtain the triangular matrix  $R$  that allows to obtain the QR factorization of the matrix  $A$ , that is:

$$A = Q \cdot R. \quad (2.119)$$

At each step  $j$  in the transformation, we impose a reflection with respect to a plane on a column vector of  $A$ ,  $\mathbf{x}_j$ , in order to project it over the unitary vector in the final direction,  $\tilde{\mathbf{e}}_j$ . As a result, we obtain a vector with the same length as  $\mathbf{x}_j$ , but collinear to  $\tilde{\mathbf{e}}_j$ . As an example, let us consider the first iteration of the transformation. We define an auxiliary vector  $\mathbf{v}$  such that:

$$\mathbf{v} = \mathbf{x}_1 - |\mathbf{x}_1| \tilde{\mathbf{e}}_1, \quad (2.120)$$

where  $\tilde{\mathbf{e}}_1 = (1, 0, \dots, 0)^T$ ,  $^T$  representing the transpose. We take the unitary vector of  $\mathbf{v}$ ,  $\mathbf{u} = \mathbf{v}/|\mathbf{v}|$ , and define:

$$Q_1 = I - 2\mathbf{u}\mathbf{u}^T, \quad (2.121)$$

which projects  $\mathbf{x}_1$  onto the unitary vector:

$$Q_1 \mathbf{x}_1 = \begin{pmatrix} |\mathbf{x}_1| \\ 0 \\ \vdots \\ 0 \end{pmatrix}. \quad (2.122)$$

After the first iteration, we have zeros below the diagonal in the first column:

$$Q_1 A = \begin{pmatrix} |\mathbf{x}_1| & A'_{1,2} & \dots & A'_{1,n-1} \\ 0 & \vdots & \ddots & \vdots \\ \vdots & \vdots & \ddots & \vdots \\ 0 & A'_{n-1,2} & \dots & A'_{n-1,n-1} \end{pmatrix}. \quad (2.123)$$

For the next step, we need to find a second matrix  $Q_2$  that reflects the next column vector but leaves the previous column unaltered, repeating the process iteratively. In general, for the  $j$ -th iteration:

$$Q_j = \begin{pmatrix} I_{j-1} & 0 \\ 0 & Q'_j \end{pmatrix}, \quad (2.124)$$

where  $I_{j-1}$  is the  $(j-1)$ -dimensional unit matrix, and  $Q'_j$  is defined in the same way as in (2.121), but with  $j-1$  less rows and columns. For square matrices, each  $Q_j$  acts on a subspace  $(n-j+1) \times (n-j+1)$  of  $A$ , so that  $Q_j \cdots Q_1 \cdot A$  has zeros below the diagonal up to column  $j$ . After  $n-1$  iterations, we obtain the matrices with the desired properties:

$$R = Q_{n-1} \cdots Q_1 \cdot A, \quad (2.125)$$

$$Q = Q_1^T \cdots Q_{n-1}^T, \quad (2.126)$$

$$A = Q \cdot R. \quad (2.127)$$

This method requires altering most of the matrix at each step, not just the relevant column vector, but is numerically stable [326].

Again, we may choose to apply a transformation where SUSY is broken to obtain isospectral lattices, which is fairly straightforward to do with QR factorization. Consider the general transformation:

$$\mathcal{H}^{(1)} - \beta I = QR, \quad (2.128)$$

$$\mathcal{H}^{(2)} - \beta I = RQ. \quad (2.129)$$

If  $\beta$  does not coincide with any eigenvalue of the system, the modified geometry defined by  $\mathcal{H}^{(2)}$  maintains all eigenvalues of the system and does not display an isolated

waveguide. This implies that broken SUSY transformations can be performed iteratively without reducing the effective size of the system, building a hierarchy of partner systems with different supermode profiles but with the same propagation constants. If we bring  $\beta$  closer to an eigenvalue, the coupling with the last waveguide starts decreasing. Once  $\beta \rightarrow \beta_m$ , the system transitions towards unbroken SUSY with the last waveguide decoupled and hosting the mode corresponding to  $\beta_m$ .

### 2.2.4 2D Supersymmetry

SUSY transformations are in essence one-dimensional, and cannot be directly applied to Hamiltonians with higher dimensions. Nevertheless, there are exceptions to this rule in some limited scenarios where the potential fulfills certain conditions. An example can be found in axially-symmetric potentials, as those present in optical fibers. Under the paraxial approximation, the variation of a field envelope  $E$  in the system is determined by [72]:

$$\left[ -\frac{\partial^2}{\partial \tilde{r}^2} - \frac{1}{\tilde{r}} \frac{\partial}{\partial \tilde{r}} - \frac{1}{\tilde{r}^2} \frac{\partial^2}{\partial \varphi^2} - V(\tilde{r}) \right] E = i \frac{\partial E}{\partial \tilde{z}}, \quad (2.130)$$

for normalized radial and longitudinal coordinates,  $\tilde{r}$  and  $\tilde{z}$ , respectively. One can then separate the envelope as  $E(\tilde{r}, \varphi, \tilde{z}) = e(\tilde{r})e^{il\varphi}e^{i\beta\tilde{z}}$  to define a Hamiltonian with only an explicit dependence on  $\tilde{r}$  on which one can apply a SUSY transformation. In terms of the fundamental mode  $e_{0l_1}^{(1)}$  of azimuthal index  $l_1$ , one can then define the superpartner potential [72, 304]:

$$V^{(2)}(\tilde{r}) = V^{(1)}(\tilde{r}) + 2 \frac{\partial^2}{\partial \tilde{r}^2} \ln \left( \tilde{r}^{(l_1^2 - l_2^2 + 1)/2} e_{0l_1}^{(1)} \right), \quad (2.131)$$

which is only supersymmetric for the radial modes  $u_{ml_2}^{(2)}$  of azimuthal order  $|l_2| = |l_1| + 1$ .

SUSY can also be applied to separable 2D potentials, i.e.  $V(x, y) = V_x(x) + V_y(y)$  [308, 328]. In those cases, one can apply the 1D SUSY formalism to each coordinate independently, and obtain the full superpartner potential through the sum of the individual superpartners. This idea can also be applied to discrete systems where the coupling rates are separable in each direction [308].

One can also apply the SUSY formalism to 1D waveguides with curved geometry, such as those used in ring resonator setups, even though the mode profiles are affected by the curvature. To see this more clearly, one can make use of conformal transformations [253]. These transformations allow to obtain the straight waveguide displaying equivalent light dynamics to another curved waveguide. One can then use the SUSY formalism in the straight waveguide and transform back to the original geometry. Alternatively, one may perform a SUSY transformation on the curvature itself [316], to obtain bent waveguides with equivalent scattering properties.

The discrete formalism can also be applied in general for 2D systems. However, recall that QR factorization only produces tridiagonal superpartners if the original Hamiltonian is also tridiagonal. 2D systems cannot in general be described by a tridiagonal matrix. Applying the QR factorization method to these systems thus may lead to non-local couplings that are challenging to implement in an experimental setup. DSUSY can also be applied in indirect ways in 2D or quasi-2D systems. One can find a 1D chain that is isospectral to a 2D lattice by tridiagonalizing its Hamiltonian via Householder transformations [224, 325, 329], and apply DSUSY to the 1D chain. Coupling this superpartner to the original lattice can lead to single-mode lasing [301, 314]. One can also exploit additional dimensionalities such as the boson number to build a quasi-2D system from a 1D superpartner [298], or build the so-called quasi-2D supercharge Hamiltonians from the SUSY transformation between two 1D superpartners [244, 320, 321].

## 2.3 Topology in optics

Throughout the rest of the thesis, topology will prove to be one of the main driving forces behind many of the interesting properties of the systems under study. Nevertheless, at first sight, it is not completely clear how this mathematical field can play such a major role in the description of physical systems. In this section, we attempt to introduce the field of topology from the physical point of view. We start with the more general concepts such as the Gauss-Bonnet theorem [88] and the concept of topological invariant, with descriptions of the Berry and Zak phases. After that, we place the focus on perhaps the most famous 1D topological insulator [101], namely the Su-Schrieffer-Heeger model [95], which will appear in most chapters of the thesis. Its description here will allow us to introduce key concepts such as topological protection and edge states. Finally, we delve into the more recent idea of square-root topology, a necessary step to understand the importance of the generalization treated in Chapter 6.

### 2.3.1 Basics of topology

Topology is the branch of mathematics that deals with the properties of geometrical objects that are invariant under continuous deformations such as bending, stretching or twisting. In plain language, if you are able to deform one object into another without breaking it or poking holes on it, the two objects are topologically equivalent. The first example that one can find of these concepts is the equivalence between a coffee mug and a doughnut (1 hole), which are in turn topologically different from a sphere or a sheet of paper (no holes). The question now is how to reconcile these ideas of mugs, doughnuts and holes to actual physical concepts.

Let us start with a prime example of the relation between a geometric object and

a topological object. It is given by the Gauss-Bonnet theorem, which states that for a given surface  $S$  the following relation holds [88]:

$$\frac{1}{4\pi} \int_S \kappa dS = 1 - g, \quad (2.132)$$

where  $\kappa$  is the curvature and  $g$  is the genus, the integer number of holes in the surface. In this case, the genus is a *topological invariant*, since there is no way to continuously deform a surface into another if they have a different number of holes. The genus is then a property of the underlying space, even if we can compute it from a local variable such as the curvature. The topological invariants are discrete and globally defined for the whole system, usually involving integration procedures. Furthermore, the fact that topological invariants are unable to change gradually bestows the properties of the system with a degree of stability, since to change them you would need to go through a topological transition.

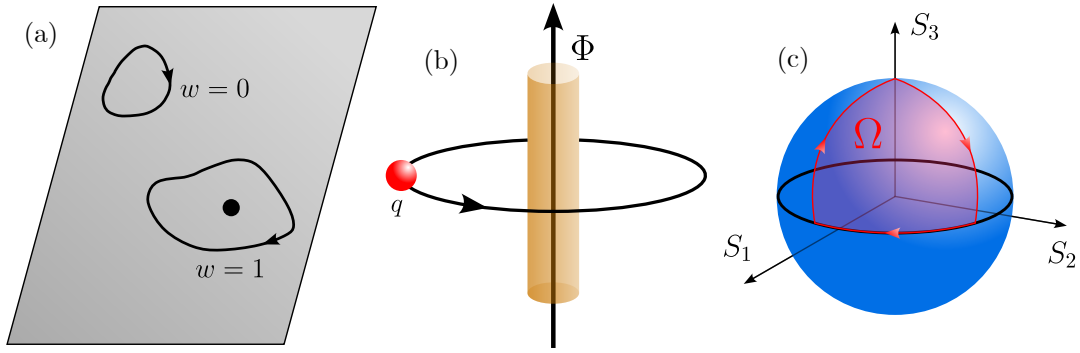


Figure 2.10: (a) Representation of winding numbers  $w = 0$  and  $w = 1$ . In a space that contains a hole (black dot), any path that encircles it ( $w = 1$ ) is topologically different to those that do not ( $w = 0$ ). (b) Sketch of the Aharonov-Bohm effect, where a particle with charge  $q$  encircles a solenoid that encloses a magnetic flux  $\Phi$ . Even though the magnetic field along the path is zero, the vector potential is not, and thus the particle still picks up a phase. (c) A light beam following a given closed path on the Poincaré sphere of polarizations, marked in red, picks up a phase equal to half of the encircled solid angle  $\Omega$ , sometimes called the Pancharatnam phase.

The above idea of holes naturally gives rise to the concept of *winding numbers*. For a given closed path  $\mathcal{C}$  or loop in a surface, the winding number  $w$  is the amount of times that the path circles a hole in the object or space. Any continuous deformation of the path will maintain a constant winding number, which means that it is also a topological invariant. Since there is no continuous deformation that can change this invariant, paths with different winding number are topologically distinct. An example of this is shown in Fig. 2.10(a). These geometrical holes can be thought of in physical

terms as singularities where some variable associated to a physical field, such as its phase, is undefined [88]. This marks a point or region of space where the fields are not well-behaved, and its existence can have physical significance. An example of this fact could be seen as early as 1959 in the form of the Aharonov-Bohm effect [85], which was experimentally verified in 1960 [86]. A particle with charge  $q$  moving along a closed path that encircles a current-carrying solenoid  $w$  times, see Fig. 2.10(b), will pick up a phase shift even if it moves through a region where the magnetic field is null. This can be explained by noting that in that region, even though the magnetic field is zero, the vector potential  $\mathbf{A}$  is not. The phase picked up by the particle amounts to:

$$\Delta\varphi = w \frac{q\Phi}{\hbar}, \quad (2.133)$$

where  $\Phi$  is the magnetic flux through the area encircled by the path. This phase is a direct consequence of the singularity of the vector potential  $\mathbf{A}$  that is contained within the solenoid [88], which can be seen as a hole in the space of field configurations. The amount of times that the particle encircles that hole,  $w$ , is the winding number, and the phase in (2.133) is proportional to it. The Aharonov-Bohm phase is purely topological, as any small path deformations do not change the value of the winding number, and any closed paths that circle the solenoid the same amount of times are topologically equivalent.

Topological concepts also appear naturally in the form of nondynamical phases in quantum systems. In quantum mechanics, the phase of a particular state does not hold any physical information on its own, since a global phase can be chosen arbitrarily. Conversely, the relative phase between two states

$$\varphi_{1,2} = \arg \langle \psi_2 | \psi_1 \rangle \quad (2.134)$$

does hold physical meaning. Nevertheless, under a local gauge transformation:

$$|\psi_j\rangle \rightarrow e^{i\alpha_j} |\psi_j\rangle \quad (2.135)$$

that phase is not invariant. If we however consider a closed sequence of transitions between states  $|\psi_1\rangle \rightarrow |\psi_2\rangle \rightarrow \dots \rightarrow |\psi_N\rangle \rightarrow |\psi_1\rangle$ , the phase gained during the loop will be gauge invariant and in general nonzero. This is known as the *Berry phase* [96, 101]. To relate this to the previous geometrical concepts, let us consider a Hamiltonian in parameter space  $\mathcal{H}(\mathbf{R}(t))$ , where  $\mathbf{R}(t)$  is the vector containing the parameters of the system. The time evolution in the system is determined by the Schrödinger equation:

$$i\hbar \frac{d}{dt} |\Psi(\mathbf{R}(t))\rangle = \mathcal{H}(\mathbf{R}(t)) |\Psi(\mathbf{R}(t))\rangle. \quad (2.136)$$

At any given time, the system has instantaneous eigenstates  $\mathcal{H}(\mathbf{R}) |\psi_j(\mathbf{R})\rangle = \mu_j(\mathbf{R}) |\psi_j(\mathbf{R})\rangle$ , and we consider the system to be in one of those eigenstates with energy



$\mu_m$  at the initial time. Now, if we allow the system parameters to change through time, the system will follow a path in parameter space. If those changes are slow enough, and we do not close the gap around  $\mu_m$ , the adiabatic theorem [330] guarantees that the state will only pick up a phase factor during evolution:

$$|\Psi(t)\rangle = e^{i\theta_m(t)} |\psi_m(\mathbf{R}(t))\rangle. \quad (2.137)$$

Introducing this state in Eq. (2.136) yields:

$$-\hbar e^{i\theta_m} \frac{d\theta_m}{dt} |\psi_m(\mathbf{R})\rangle + i\hbar e^{i\theta_m} \frac{d}{dt} |\psi_m(\mathbf{R})\rangle = \mu_m(\mathbf{R}) e^{i\theta_m} |\psi_m(\mathbf{R})\rangle, \quad (2.138)$$

where we remove the explicit  $t$  dependence for readability. Projecting over  $\langle\psi_m(\mathbf{R}(t))|$  and rearranging leads to

$$\frac{d\theta_m}{dt} = -\mu_m(\mathbf{R})/\hbar + i \langle\psi_m(\mathbf{R})| \frac{d}{dt} |\psi_m(\mathbf{R})\rangle. \quad (2.139)$$

Finally, integrating the previous expression yields

$$\theta_m(t) = -\frac{1}{\hbar} \int_0^t \mu_m(\mathbf{R}) dt' + i \int_0^t \langle\psi_m(\mathbf{R})| \frac{d}{dt'} |\psi_m(\mathbf{R})\rangle dt', \quad (2.140)$$

where the first term corresponds to the dynamical part of the phase due to the time evolution of the state, while the second is a purely geometrical part due to the path that the state has taken through the parameter space, also known as the Berry phase  $\gamma_m$  [96]. We can talk in purely geometrical terms if we remove the time dependence by doing  $\frac{d}{dt'} |\psi_m(\mathbf{R})\rangle dt' = \nabla_{\mathbf{R}} |\psi_m(\mathbf{R})\rangle d\mathbf{R}$ , allowing us to express the Berry phase as:

$$\gamma_m = i \int_{\mathbf{R}(0)}^{\mathbf{R}(t)} \langle\psi_m(\mathbf{R})| \nabla_{\mathbf{R}} |\psi_m(\mathbf{R})\rangle \cdot d\mathbf{R}, \quad (2.141)$$

where  $\mathbf{A}_m(\mathbf{R}) \equiv i \langle\psi_m(\mathbf{R})| \nabla_{\mathbf{R}} |\psi_m(\mathbf{R})\rangle$  is known as the Berry connection, and now the dependence is only on the vector of parameters  $\mathbf{R}$ . Finally, we can make the Berry phase gauge invariant by considering a closed path through parameter space:

$$\gamma_m = \oint_C \mathbf{A}_m(\mathbf{R}) \cdot d\mathbf{R}. \quad (2.142)$$

To circle back to the beginning of the section, we can rewrite (2.142) by using the Stokes theorem [101]

$$\gamma_m = \int_S [\nabla_{\mathbf{R}} \times \mathbf{A}_m(\mathbf{R})] dS, \quad (2.143)$$

and compare directly with the Gauss-Bonnet theorem in (2.132). Here, instead of the geometrical curvature  $\kappa$ , we have the Berry curvature  $\Omega_m \equiv \nabla_{\mathbf{R}} \times \mathbf{A}_m(\mathbf{R})$ . And the

role of the topological invariant, which in the Gauss-Bonnet theorem is played by the genus  $g$ , is held here by the Berry phase. Geometrical phases are in fact more general than originally expected, since they do not require a quantum framework to make an appearance. Indeed, as hinted previously, the example of the Aharonov-Bohm effect in (2.133) is often interpreted as a Berry phase. Geometrical phases can also appear in classical wave phenomena, as evidenced by the preceding work of Pancharatnam [98], which deals with the quantification of the phase differences of unequally polarized optical beams. There, it was proven that a cyclic evolution in the sphere of possible polarizations, namely the Poincaré sphere, yields a nonzero phase. As we sketch in Fig. 2.10(c), if the beam changes polarizations following a continuous path along the surface of the sphere, the phase difference with the original beam amounts to half of the encircled solid angle and can be thought of as analogous to a Berry phase [331, 332]. Other examples of geometrical phases can be found in Ref. [97].

### Zak phase

Now we jump to the context of solid-state physics, where we consider periodic systems whose potential displays translation symmetry  $V(x) = V(x + a)$  with  $a$  being the lattice spacing. In those cases, the energy spectrum displays a structure of bands, with each band characterized by an index  $n$  representing the energy level. The bands are dependent on a parameter  $k$  called the quasimomentum. In periodic systems, Bloch's theorem states that there exists a basis of eigenstates that can be written as [100]

$$\Psi_{n,k}(x) = e^{ikx} u_{n,k}(x), \quad (2.144)$$

where the functions  $u_{n,k}(x) = u_{n,k}(x + a)$  display the same periodicity as the potential. One might think of the Bloch functions as cell-periodic functions that are modulated by a plane wave envelope  $e^{ikx}$ . Due to this periodicity, quasimomenta  $k$  and  $k + 2\pi/a$  correspond to the same state. So, when computing the energy bands of the system, it is sufficient to restrict ourselves to the first Brillouin zone in  $k \in [-\frac{\pi}{a}, \frac{\pi}{a})$  or equivalently  $k \in [0, \frac{2\pi}{a})$ .

Considering the above ideas, the parameter space over which one might want to draw a closed path to compute the Berry phase appears in a natural way in the band structure: it is *the Brillouin zone*. The Brillouin zone is the space of unique quasimomenta in the system, which is periodic, since taking  $k \rightarrow k + 2\pi/a$  does not alter the set of solutions. In fact, one might consider all quasimomenta to be living in the circumference of a circle that allows for a closed path. Then, considering a Bloch function  $\Psi_{n,k}$ , sweeping the quasimomentum across the entire Brillouin zone causes the Bloch function to pick up a Berry phase that represents the entire band in a global way. In 1D systems, this phase

is usually called the Zak phase [99]

$$\mathcal{Z}_n = i \int_{-\frac{\pi}{a}}^{\frac{\pi}{a}} \langle u_{n,k} | \frac{d}{dk} | u_{n,k} \rangle dk. \quad (2.145)$$

As demonstrated in Ref. [99], in systems that possess inversion symmetry the Zak phase is quantized and can only take values  $\mathcal{Z}_n = 0, \pi (\text{mod } 2\pi)$ . These values can only be changed if the variation of the parameters is enough to close the energy gap around the gap. Thus, the Zak phase is a topological invariant and its two possible values represent topologically distinct phases ( $\mathcal{Z}_n = 0$  trivial and  $\mathcal{Z}_n = \pi$  nontrivial). Note that in systems with inversion symmetry, but where the inversion axis is not centered in the middle of the unit cell, one can also have nonquantized Zak phases [215, 333]. In systems with multiple bands, at any gap between bands, the total Zak phase corresponds to the sum of the Zak phases of all bands below the gap [164]

$$\mathcal{Z}_{m,T} = \sum_{n \leq m} \mathcal{Z}_n. \quad (2.146)$$

The Zak phase is also related to other topological invariants, such as the bulk polarization [101]. In electronic systems, the polarization gives us a measure of how displaced is the mean position of the electrons in each unit cell from its center. This can be computed in terms of Wannier states, which are the Fourier transform of the Bloch states:

$$\mathcal{W}_n(j) = \frac{1}{\sqrt{N}} \sum_k e^{i\varphi(k)} e^{-ikj} \Psi_{n,k}. \quad (2.147)$$

Wannier states are localized, in contrast to Bloch states, and the free phase factor  $\varphi(k)$  can be chosen to obtain sets of Wannier bases with different localization lengths. Moreover, the Wannier center  $\langle \mathcal{W}_n(j) | \hat{x} | \mathcal{W}_n(j) \rangle$ , with  $\hat{x} = i \frac{d}{dk}$  being the position operator, is directly related to the polarization. By comparing this expression with the one inside the integral in (2.145), one can show that, in terms of the Zak phase, the polarization is [100]

$$P = \frac{e}{2\pi} \sum_{n \in \text{occ}} \mathcal{Z}_n, \quad (2.148)$$

where  $e$  is the charge of the electron. In other words, the sum of the Zak phases of all occupied bands. The polarization is hence a quantized topological invariant that one can use interchangeably with the Zak phase.

One of the most attractive properties of the Zak phase, is that its value in a system with periodic boundary conditions allows to predict whether topologically protected edge states appear in a particular gap when the boundaries are opened. This connection between bulk properties and edge states is known as the bulk-boundary correspondence, a widely used concept in the study of topological insulators [92]. Topological insulators

(TIs) are characterized by the contrast of an insulating bulk due to an energy gap and the presence of conducting edge or surface states, which are protected by a certain symmetry of the system. When connecting two insulators with distinct topological phases, we are forcing the topological invariant to change its value along the separating boundary. This, in turn, causes the appearance of a conducting state localized at said boundary that bridges the energy gap between insulators, the so-called edge state. We may think of a single TI with open boundaries as connected to the vacuum, a topologically trivial insulator, and hence the same idea applies. We now focus on perhaps the most paradigmatic 1D TI, the Su-Schrieffer-Heeger model, which appears in every chapter of this thesis, thus hinting at the inherent potential that topology brings to the table.

### 2.3.2 Su-Schrieffer-Heeger model

The Su-Schrieffer-Heeger (SSH) model [95] is the simplest discrete model that holds interesting topological properties. It is characterized by a 1D lattice with alternating weak and strong couplings, labeled here as  $t_1$  and  $t_2$ , and can be described as two intertwined sublattices labelled as  $A$  and  $B$ , see Fig. 2.11(a). For simplicity, we consider the lattice spacing  $a = 1$ . The model is then described by the following Hamiltonian:

$$\mathcal{H} = \sum_{q=1}^{N_c} (t_1 |q, B\rangle \langle q, A| + t_2 |q+1, A\rangle \langle q, B| + \text{h.c.}) = \begin{pmatrix} 0 & t_1 & 0 & & \\ t_1 & 0 & t_2 & & \\ 0 & t_2 & 0 & & \\ & & & \ddots & \end{pmatrix}, \quad (2.149)$$

for  $N_c$  number of cells. Here, we are considering identical sites, so all diagonal elements can be set to 0, and real couplings. In Eq. (2.149),  $|q, A(B)\rangle$  denote the state at unit cell  $q$  and sublattice  $A(B)$ . The SSH chain possesses two boundaries, one at each edge, and a bulk that corresponds to its central part. For a long chain close to the thermodynamic limit, where the number of sites  $N \rightarrow \infty$ , the bulk properties are insensitive to the presence of the boundaries. As such, for its description we can set periodic boundary conditions in the model. This makes the system translationally invariant, allowing us to introduce a plane wave basis [101]:

$$|k\rangle = \frac{1}{\sqrt{N}} \sum_{m=1}^N e^{imk} |m\rangle, \quad (2.150)$$

where  $k$  are the quasimomenta in the first Brillouin zone. We can use this basis to obtain the bulk Hamiltonian in momentum space  $\mathcal{H}_b(k) = \langle k | \mathcal{H} | k \rangle = (t_1 + t_2 e^{-ik}) |A\rangle \langle B| + (t_1 + t_2 e^{ik}) |B\rangle \langle A|$  or, in matrix form:

$$\mathcal{H}_b(k) = \begin{pmatrix} 0 & t_1 + t_2 e^{-ik} \\ t_1 + t_2 e^{ik} & 0 \end{pmatrix} \quad (2.151)$$

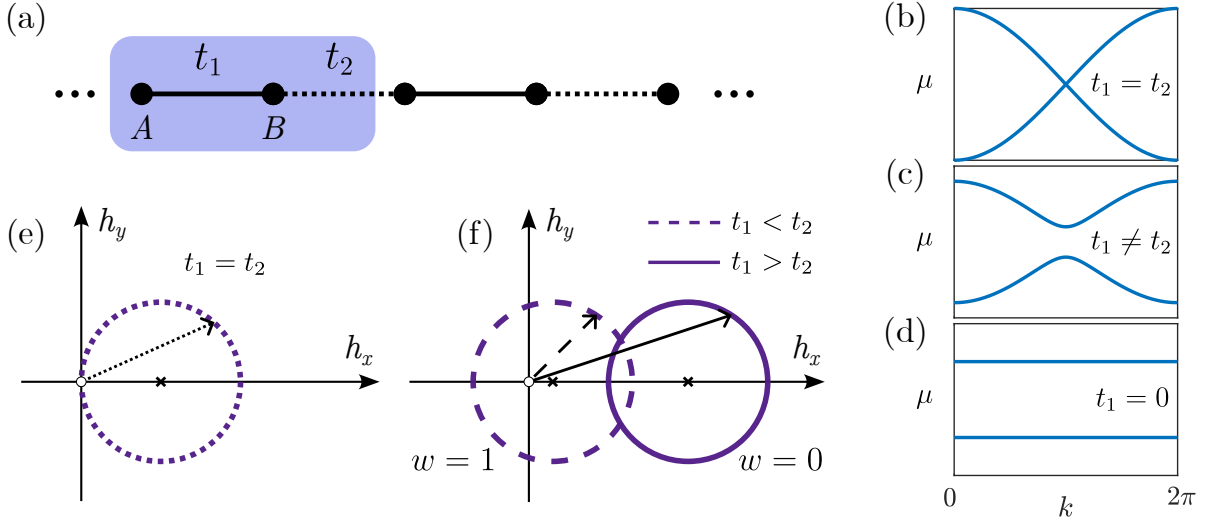


Figure 2.11: (a) Sketch of the SSH model, with the unit cell being shaded in blue. The cell contains two sites labelled  $A$  and  $B$ , that can be interpreted to correspond to two intertwined lattices, with intracell coupling  $t_1$  and intercell coupling  $t_2$ . (b)–(d) Bulk spectra of a periodic SSH chain with (b)  $t_1 = t_2$ , (c)  $t_1 \neq t_2$  and (d)  $t_1 = 0$  (or  $t_2 = 0$ ). One can observe that when the couplings are staggered, an energy gap  $2\Delta = 2|t_1 - t_2|$  is opened between top and bottom bands. (e)–(f) Trajectories (circles) of the vector  $\mathbf{h}(k)$  (arrows) on the  $h_x$ – $h_y$  plane as  $k$  is swept across the Brillouin zone for (e)  $t_1 = t_2$  and (f)  $t_1 \neq t_2$ . It is clear that in (f) the number of times  $w$  that the path winds around the origin is different depending on which coupling is larger, which indicates different topological phases. The situation in (e) corresponds to the transition point.

This can be diagonalized to obtain the energy bands of the system and the eigenvectors:

$$\mu(k) = \pm \sqrt{t_1^2 + t_2^2 + 2t_1 t_2 \cos k}, \quad (2.152)$$

$$|\pm\psi(k)\rangle = \begin{pmatrix} \pm e^{-i\phi(k)} \\ 1 \end{pmatrix}, \quad (2.153)$$

with  $\phi(k) = \tan^{-1} \left( \frac{t_2 \sin k}{t_1 + t_2 \cos k} \right)$ . As can be observed from Figs. 2.11(b) and (c), there is an energy gap  $2\Delta$  between bands, with  $\Delta = |t_1 - t_2|$ , which closes in the uniform case  $t_1 = t_2$ . For the fully dimerized limit where one of the couplings is null, as seen in Fig. 2.11(d), the model displays flat bands. Despite having the same band structure, the cases with  $t_1 > t_2$  and  $t_1 < t_2$  are topologically distinct. One of the ways to prove this is to express (2.151) in terms of the Pauli matrices,  $\sigma_i$ :

$$\mathcal{H}_b(k) = \sum_{i=x,y,z} h_i(k) \sigma_i, \quad (2.154)$$

with

$$h_x = t_1 + t_2 \cos k, \quad h_y = t_2 \sin k, \quad h_z = 0, \quad (2.155)$$

which allows us to represent the system in the Bloch sphere [101]. The vector  $\mathbf{h}(k)$  encodes both eigenvalues (magnitude) and eigenvectors (direction). Indeed, one can check that the phase factor in (2.153) fulfills  $\tan \phi(k) = h_y/h_x$ . If we go over the first Brillouin zone  $k = \{0 \rightarrow 2\pi\}$ ,  $\mathbf{h}(k)$  forms closed loops in the  $h_x$ - $h_y$  plane, as we plot in Figs. 2.11(e) and (f). In Fig. 2.11(f), where the couplings are unequal, one readily observes that the amount of times the circle winds around the origin, i.e. the winding number  $w$ , is different depending on which coupling is stronger. To go from one region to the other, we need to cross the gapless point at  $h(k) = 0$ , represented in Fig. 2.11(e), via a topological phase transition. Hence,  $w$  is a topological invariant, with values  $w = 1$  for  $t_1 < t_2$  and  $w = 0$  for  $t_1 > t_2$ . Alternatively, one might compute the Zak phase (2.145) from the eigenstates in (2.153), which takes the quantized values  $\mathcal{Z} = 0$  in the trivial phase and  $\mathcal{Z} = \pi$  in the topological phase. Equivalently, one could choose to compute the polarization (2.148), which is also quantized. The quantization of these invariants is a consequence of the inversion symmetry of the model [99].

As explained in the previous section, due to the bulk-boundary correspondence, this distinction should have observable implications for open chains. For that scenario, the bulk description is no longer sufficient and one needs to diagonalize the full Hamiltonian. One then finds that for non-zero  $w$  there exist near-zero energy states that are exponentially localized around the edges of the chain. In other words, edge states appear when the chain finishes on the weak coupling. Depending on whether the chain has an even or odd number of sites  $N$ , it may have one or two edge states. A situation for an odd  $N$  is depicted in Fig. 2.12(a), and the squared amplitudes on each site of the corresponding edge state are shown in Fig. 2.12(b). Note that the edge state only has weight on one of the sublattices, which is attributed to the chiral symmetry of the SSH model as explained below. The strength of the confinement is determined by the ratio between couplings,  $t_2/t_1$ . Furthermore, the energy spectrum of the chain is plotted in Fig. 2.12(c), where one observes that the edge state lays in the center of the gap. For chains with even  $N$  where both sides terminate with a weak coupling, there exist two edge states. These are actually symmetric and antisymmetric combination of left and right edges, namely hybridized states. In these chains, left and right edges only fully decouple in the thermodynamic limit  $N \rightarrow \infty$ .

The topological nature of edge states implies a certain degree of robustness against disorder, as long as it preserves the protecting symmetry of the system, which in this case is the chiral symmetry of the SSH model. Chiral symmetry is defined as:

$$\Gamma \mathcal{H} \Gamma^\dagger = -\mathcal{H}, \quad (2.156)$$

where  $\Gamma$  is a unitary and Hermitian operator,  $\Gamma^\dagger \Gamma = \Gamma^2 = I$ , and  $I$  is the identity

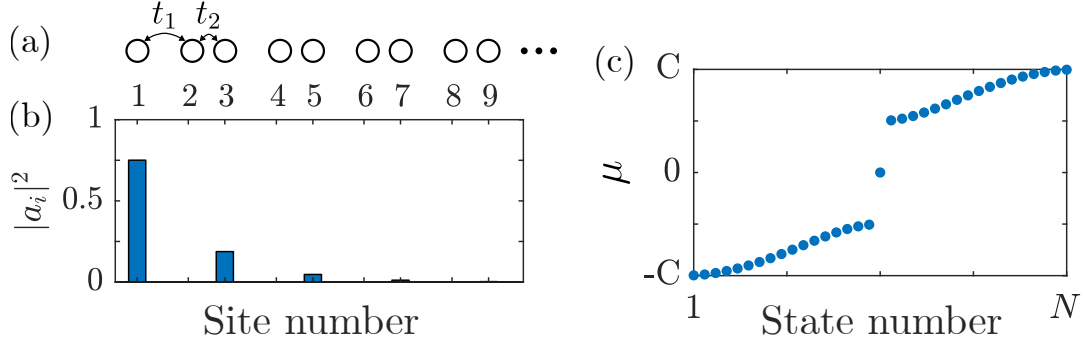


Figure 2.12: (a) Sketch of the configuration of the SSH chain with an edge state on the left side. (b) Squared amplitudes of the left edge state for the leftmost section of the chain. (c) Energy levels of a SSH chain with  $N = 35$ , with  $C = t_1 + t_2$ . The zero-energy state corresponds to the edge state in (b).

matrix. Chiral symmetry implies that the spectrum of the Hamiltonian is symmetric with respect to the zero of energies, meaning that for every eigenstate  $|\psi_m\rangle$  with energy  $\mu_m$ , there exists a partner with eigenvalue  $-\mu_m$ . One can prove this by applying the chiral symmetry to the eigenvalue problem,  $\mathcal{H}|\psi_m\rangle = \mu_m|\psi_m\rangle$ :

$$\mathcal{H}\Gamma|\psi_m\rangle = -\Gamma\mathcal{H}|\psi_m\rangle = -\mu_m\Gamma|\psi_m\rangle. \quad (2.157)$$

Another way to express chiral symmetry is in terms of a sublattice symmetry. One can define orthogonal projectors onto each of the sublattices,  $A$  and  $B$ :

$$P_A = \frac{1}{2}(I + \Gamma), \quad P_B = \frac{1}{2}(I - \Gamma). \quad (2.158)$$

Imposing chiral symmetry in the system is then the same as demanding that the Hamiltonian induces no transitions between elements of the same sublattice,  $P_A\mathcal{H}P_A = P_B\mathcal{H}P_B = 0$ . In terms of these projectors, one can prove that the edge states – which have zero energy – only have nonzero projections in one of the sublattices:

$$\mathcal{H}P_{A,B}|\psi_m\rangle = \frac{1}{2}\mathcal{H}(|\psi_m\rangle \pm \Gamma|\psi_m\rangle) = 0, \quad (2.159)$$

as was shown in Fig. 2.12(b), while the rest of the states have equal amplitude on both sublattices.

Finally, we describe the concept of topological interface states. These do not appear naturally in an SSH chain, but can be induced by including a dimer defect in a specific position of the chain [165, 166, 334–336]. This kind of defect can be implemented by repeating one of the couplings at a certain position of the staggered configuration, see Fig. 2.13(a) and 2.13(b). In essence, including these defects is equivalent to connecting two SSH chains with different topological phases. Then, a new topological state appears

in the domain wall that separates the two TIs. The interface states are closely confined around the defects independently of the number of sites of the chain and the values of the couplings, as long as the rest of the chain is topologically trivial. On the other hand, if we include a defect in a topologically nontrivial finite chain, the interface state will in general hybridize with the edge states. This idea of hybridizing edge and interface states has been shown to have applications for particle transfer in topological chains [337, 338].

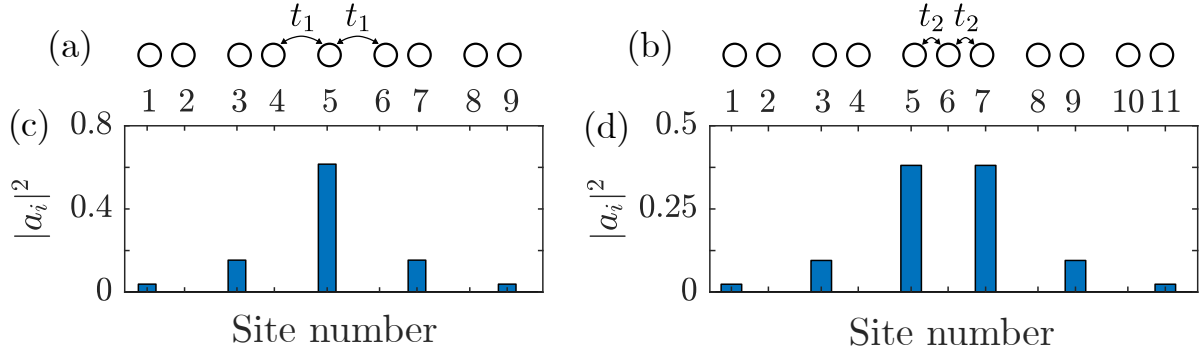


Figure 2.13: (a)–(b) Sketch of the configuration of the SSH chain with a dimer defect formed by repeating the (a) weak coupling and (b) the strong coupling in the central position. (c)–(d) Squared modal amplitude of the interface state hosted by the (c) weak and (d) strong dimer defects.

If the defect is caused by repeating the weak coupling, as in 2.13(a), the maximum of amplitude of the interface state will be located at the center of the defect, see Fig. 2.13(c). Conversely, for chains where the defect is generated by the strong coupling, as in 2.13(b), the maximum of intensity of the interface state will be split in two, see Fig 2.13(d). In both types of defects, nevertheless, the interface states have nonzero projections in only one of the sublattices. Additionally, non-topological localized states arise around the defect for the case in 2.13(b) with energies  $\mu = \pm\sqrt{2}t_2$  [166, 335], which are located above and below the two energy bands of the system and are thus no longer midgap states.

### 2.3.3 Square-root topology

We now introduce the concept of square-root TIs ( $\sqrt{\text{TI}}$ s) [119]. These are TIs in their own right, with the particularity that they are related to a parent TI through the squaring of its Hamiltonian, as we will detail below. Perhaps more interestingly, the  $\sqrt{\text{TI}}$  has an increased amount of energy gaps when compared to the parent, increasing the amount of available edge states. The  $\sqrt{\text{TI}}$  also inherits the topological properties and the consequent protection of their edge states from the parent TI. In a sense, the edge



states of the  $\sqrt{\text{TI}}$  are protected against any disorder that preserves the symmetry of the parent model. In general, this is a smaller subset of disorders than for the parent, which is an effect known as dilution of the topological protection [128]. One can then exploit the known topology of a parent TI in order to describe that of an unknown root model. This is particularly relevant since some  $\sqrt{\text{TI}}$ s do not have clear quantized topological invariants [333]. Due to these striking features, it is in our interest to introduce a method to generate the square-root model from a given Hamiltonian. However, even if it is relatively simple to square a Hamiltonian, the reverse operation of square-rooting can prove to be trickier.

The primary objective is to obtain, from a given Hamiltonian  $\mathcal{H}_{\text{TI}}$ , a square-root model  $\mathcal{H}_{\text{root}}$  which, when squared, leads back to the original Hamiltonian. One must bear in mind that the square-root procedure does not simply entail taking the mathematical root of the Hamiltonian matrix, as that can lead to unrealistic infinite-range hopping models [121]. We will detail the procedure, which is instead based on subdividing the graph representation of  $\mathcal{H}_{\text{TI}}$ , shortly. However, before starting one must note that since this method relies on increasing the matrix degrees of freedom, one does not only obtain the original Hamiltonian as a result of the squaring [121]. In general, one obtains  $(\mathcal{H}_{\text{root}})^2 = \mathcal{H}_{\text{par}} \oplus \mathcal{H}_{\text{res}}$ , where the parent Hamiltonian  $\mathcal{H}_{\text{par}}$  only differs from the original  $\mathcal{H}_{\text{TI}}$  by an additive constant, and where  $\mathcal{H}_{\text{res}}$  is a residual Hamiltonian. As the direct sum indicates,  $\mathcal{H}_{\text{par}}$  and  $\mathcal{H}_{\text{res}}$  are entirely decoupled and thus independent of each other, and hence one can recover the exact Hamiltonian of the parent. We consider a general Hermitian bipartite system:

$$\mathcal{H}_{\text{root}} = \begin{pmatrix} 0 & Q^\dagger \\ Q & 0 \end{pmatrix}, \quad (2.160)$$

where  $Q, Q^\dagger$  are off-diagonal block matrices that represent the hopping terms between sublattices. When squaring this Hamiltonian, one gets:

$$[\mathcal{H}_{\text{root}}]^2 = \begin{pmatrix} Q^\dagger Q & 0 \\ 0 & Q Q^\dagger \end{pmatrix} = \begin{pmatrix} \mathcal{H}_{\text{par}} & 0 \\ 0 & \mathcal{H}_{\text{res}} \end{pmatrix}, \quad (2.161)$$

which has a block-diagonal form. This result is expected considering the bipartite nature of Eq. (2.160), which only possesses couplings between different sublattices. Any two consecutive hoppings leads to the same sublattice, so only couplings within each sublattice remain after squaring, which makes the choice of subdividing the parent graph to find a root abundantly clear. By construction, the two diagonal blocks in (2.161) will be isospectral up to a zero-energy band. One can prove this by considering the eigenvalue equation for  $\mathcal{H}_{\text{par}}$ :

$$\mathcal{H}_{\text{par}} \Psi_{\text{par}} = Q^\dagger Q \Psi_{\text{par}} = \mu \Psi_{\text{par}}, \quad (2.162)$$

with eigenvalues  $\mu$  and eigenvectors  $\Psi_{\text{par}}$ . Multiplying both sides of the equation with

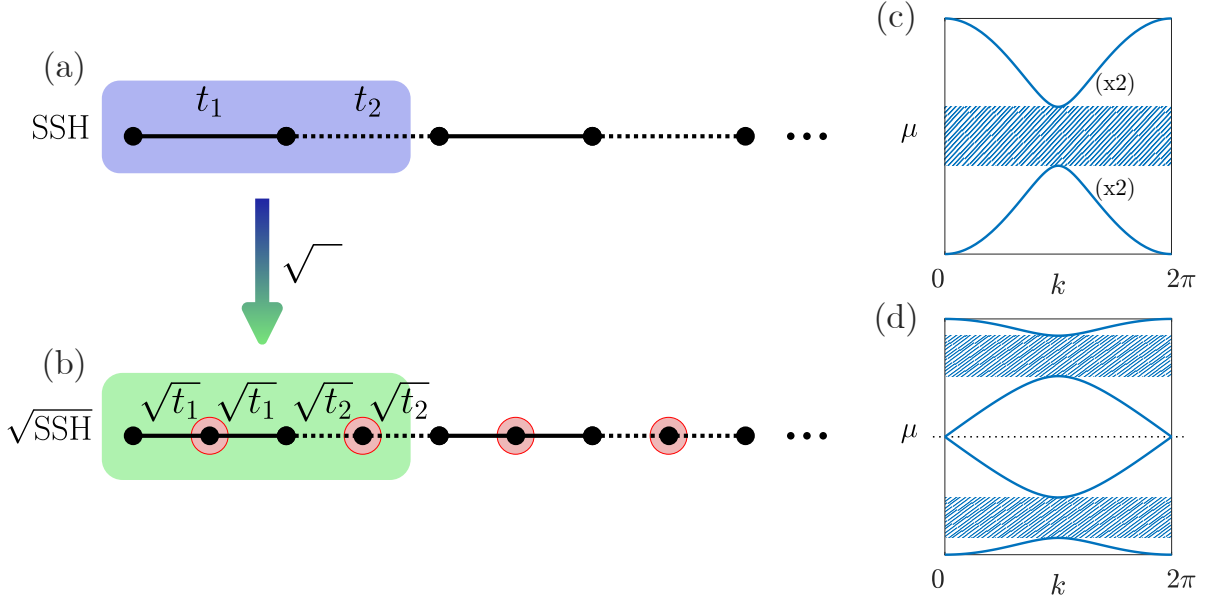


Figure 2.14: (a) Graph representation of the SSH model, with alternating couplings. The blue shaded region indicates the unit cell of two sites. (b) Graph representation of the square root of the SSH model. To obtain it, one includes additional sites on each link (marked in red) and renormalizes the couplings to  $\sqrt{t_j}$ . The shaded unit cell in green now contains four sites. Bulk spectrum for (c) the SSH model, displaying a single gap marked by the shaded region, and (d) the square-root model, displaying two band gaps and a clearly chiral-symmetric spectrum.

$Q$  from the left:

$$QQ^\dagger Q\Psi_{\text{par}} = Q\mu\Psi_{\text{par}}, \quad (2.163)$$

$$\mathcal{H}_{\text{res}}(Q\Psi_{\text{par}}) = \mu(Q\Psi_{\text{par}}), \quad (2.164)$$

implying that  $\Psi_{\text{res}} \equiv Q\Psi_{\text{par}}$  and  $\Psi_{\text{par}}$  share eigenvalues. As argued above, this square-root procedure implies obtaining a bipartite model from our original Hamiltonian  $\mathcal{H}_{\text{TI}}$ , a feat that can be achieved by exploiting graph theory [120, 121]. We will exemplify the method through the already familiar SSH model, whose graph representation we draw in Fig. 2.14(a). To produce the bipartite root model, one has to subdivide this graph by including additional sites, and renormalize the resulting hopping parameters  $t_j \rightarrow \sqrt{t_j}$ . We show the resulting lattice in Fig. 2.14(b), where the added sites are marked with red circles. It can be easily observed that the unit cell now has four sites instead of two, and so the square-root system will possess twice as many bands as the original. The bulk Hamiltonian of this new system takes the form in (2.160), with:

$$Q_{\sqrt{\text{SSH}}} = \begin{pmatrix} \sqrt{t_1} & \sqrt{t_2}e^{-ik} \\ \sqrt{t_1} & \sqrt{t_2} \end{pmatrix}. \quad (2.165)$$

Note that  $\mathcal{H}_{\text{root}}$  is hence  $4 \times 4$ . One may now check whether Eq. (2.161) is fulfilled, with  $Q$  as defined in (2.165), by squaring  $\mathcal{H}_{\text{root}}$ . Doing so, one obtains:

$$\mathcal{H}_{\text{par}} = \begin{pmatrix} t_1 + t_2 & t_1 + t_2 e^{-ik} \\ t_1 + t_2 e^{ik} & t_1 + t_2 \end{pmatrix} \equiv \mathcal{H}_{\text{SSH}} - (t_1 + t_2)I, \quad (2.166)$$

$$\mathcal{H}_{\text{res}} = \begin{pmatrix} 2t_1 & \sqrt{t_1 t_2}(1 + e^{-ik}) \\ \sqrt{t_1 t_2}(1 + e^{ik}) & 2t_2 \end{pmatrix}, \quad (2.167)$$

with  $\mathcal{H}_{\text{par}}$  being equal to the SSH Hamiltonian up to an energy shift, and  $\mathcal{H}_{\text{res}}$  being the Rice-Mele model [101].

We now compare the bulk spectra for the SSH model in Fig. 2.14(c) with the one for the square-root system in Fig. 2.14(d). We see that the root system possesses twice as many bandgaps as the original one. For an open chain with nontrivial topology, these gaps could then host twice as many protected edge states. One can thus argue that the topological features of the root system are inherited from those of the parent [130] since, as we will show later in Chapter 6, there will be a relation between topological invariants in the parent and root systems. Also, note that the spectrum in Fig. 2.14(d) clearly reveals a chiral symmetry due to its positive and negative parts around the dotted line being mirrored. This is a consequence of the bipartite nature of the model, and would occur regardless of whether the parent system was also chiral symmetric (as in this case) or not [128]. The square-root procedure is also not limited to Hermitian systems, although the roots of non-Hermitian systems are in general also non-Hermitian. It is easy to show that, in these systems, isospectrality is still found between parent and residual Hamiltonians. On the contrary, this does not exclude the possibility of having non-Hermitian roots of Hermitian parents [129, 220]. A somewhat simple generalization of this square-root procedure to higher-order roots can be readily achieved by applying successive root operations [127–130]. It is required to choose certain values for the coupling parameters or otherwise add extra dangling sites at certain positions to maintain uniform onsite energies, but in any case its application is straightforward. Nonetheless, this approach is obviously limited to roots of order  $2^n$ . The generalization to any arbitrary order  $n$  will be described in Chapter 6.

As a final note, it is interesting to highlight that if one compares the framework presented here to the one developed in Section 2.2 for SUSY Hamiltonians, in particular Eqs. (2.160) and (2.161) to Eqs. (2.94) and (2.92), one readily observes a direct parallelism. Each independent diagonal block in the squared Hamiltonian can be thought of as a superpartner of the other, with the whole Hamiltonian composed by both being a super-Hamiltonian [339]. Both of the squared systems are isospectral, up to a flat band that can be attributed to a different number of sites in the unit cell, which can also be related to the concepts of broken or unbroken SUSY. In broken SUSY, both partners are fully isospectral, whereas in unbroken SUSY the zero-energy state is removed from

the spectrum of the SUSY partner. This connection with SUSY could be explored to find potential bridges between both fields, possibly leading to new applications. The idea of a square-root procedure through SUSY had also been presented, although with a different language, in various types of systems, such as mechanical [340, 341], spin [342] and photonic [244, 320, 321] systems.



---

### Mode demultiplexing and topological mode engineering with Stark-chirped rapid-adiabatic-passage in coupled waveguides

---

In this chapter, we present a method that allows to efficiently transfer light between optical waveguides based on a photonic implementation of the Stark-Chirped Rapid Adiabatic Passage (SCRAP) technique [53]. The method is based on modulating the core refractive index of one or more waveguides, which causes crossings between the propagation constants of chosen modes. Simultaneous control over the coupling completes the scheme. In sets of two multimode waveguides, we exploit it for demultiplexing purposes. In addition, we combine the method with Supersymmetry (SUSY) transformations [72] to enhance the efficiency of this process, and for efficient excitation of excited modes [212]. On the other hand, when applied to discrete waveguide lattices, we show that SCRAP allows to excite both topological localized modes as well as extended modes as long as they present an energy gap, and that it requires only a single-mode injection. The idea of obtaining complex modes with single-waveguide inputs is also explored using SUSY in Chapter 4. Finally, we also demonstrate the possibility of transferring supermodes between two waveguide lattices using the same method, which can also be applied for mode conversion [213]. We illustrate these results with the Su-Schrieffer-Heeger model [95] throughout the chapter.

The chapter is organized as follows. In Section 3.1, we motivate the interest in applying an adiabatic transfer scheme such as SCRAP to the context of optical waveguides. In Section 3.2, we introduce the mathematical formalism of SCRAP in the context of multimode optical waveguides and waveguide lattices, and comment on the particularities of its implementation. Moreover, we mention how SCRAP can be combined with

SUSY to improve the performance of some devices. After that, in Sections 3.3 and 3.4, we present the different proposed applications for the method for multimode waveguides and waveguide lattices, respectively. The performance of the devices is analyzed in each case. We finish the chapter by laying our conclusions in Section 3.5.

## 3.1 Introduction

In recent years, optical waveguides have gathered immense interest both due to their light transmission capabilities [24], as well as for being a solid physical platform to probe the properties of nontrivial topological lattices [143]. In the first group, multimode optical waveguides and fibers [225] provide a solution to the increasing demand of transmission capacity for optical devices. Compared with single-mode waveguides, they offer an effective additional dimensionality to the system by allowing to use each guided mode as an independent information channel. This is known as Mode-Division Multiplexing (MDM) [15, 343–345], one of the different Multiplexing techniques that have been developed to increase the transmission possibilities of these optical devices [13]. The advantages that MDM provides, however, are limited by the challenging need to precisely excite the desired guided modes by matching the input field to the modes' spatial profiles. Although several techniques for this purpose exist, they either rely on carefully shaping the input pulse through e.g. spatial light modulators (SLMs) or phase plates [346], or on a specific design for the propagating medium with e.g. optical fibers featuring gratings or multiple cores [346, 347].

On the other hand, photonic lattices of single-mode waveguides have been proven to be very versatile platforms for the exploration of the properties of models with nontrivial topology [142, 143]. Topological states, being protected by the symmetries of the system, hold great promise for a wide variety of applications such as lossless information transmission [167, 348, 349], nonreciprocal processes such as unidirectional propagation [155, 350, 351], lasing applications [169, 352], enhancement of frequency-conversion processes [353, 354], and many others. For modes that are strongly confined, direct excitation on the waveguide with highest amplitude may prove to be sufficient [78]. However, with this method other unwanted modes may also be simultaneously excited, causing intensity beatings during the propagation.

Therefore, it is of high interest to develop a general method to prepare specific waveguide modes with accuracy, both for the excited modes in multimode waveguides as well as supermodes in waveguide lattices, specially so for topological modes, regardless of mode confinement. In both cases, the main difficulty for their preparation lies in the injected beam, which needs to precisely overlap with the chosen mode if one wishes to avoid exciting other unwanted modes. Although some methods based on the usage of SLMs are capable of producing accurate results [102, 106, 355–357], their precision is

limited. Thus, it is of pivotal importance to be able to accurately excite the desired modes while employing an input beam with the lowest possible complexity.

With this purpose, we develop the implementation of the Stark-Chirped Rapid-Adiabatic-Passage (SCRAP) technique to optical waveguides [212, 213]. The method was first introduced in Ref. [53] for the transfer of population to a metastable atomic state using a two-pulse scheme, one modifying the energies of the system and the other adiabatically driving the population. Since then, the method has been extensively studied in several cases [55–57], generalized to three-level systems [58–61], and then applied in other contexts such as wave mixing and frequency conversion [56, 57, 62, 201, 358–360], for the study of the dynamics in trapped condensates [361, 362] and the generation of entangled photons [363]. This scheme can be implemented in optical waveguides setups to achieve faithful transfer of light between guided modes, in agreement with the analogy presented in Sec. 2.1.6. In this case, the role of the energy eigenvalues is played by the propagation constants of the modes, whose variation is achieved through a modulation of the refractive index of the waveguide core. The transfer is then controlled by the coupling strength between the waveguide modes, which can be tuned by adjusting the relative distance between waveguides. These ideas can be applied both to coupled multimode waveguides as well as to lattices of single-mode waveguides. In each case, the dynamics are restricted to the sets of modes or supermodes that experience crossings, with minimal leakage to unwanted modes.

In multimode waveguides, SCRAP can be combined with Supersymmetry (SUSY) transformations [212]. In the context of optics, SUSY has been successfully employed for instance to control the modal content of different structures [72, 76, 77, 82, 300–303, 306, 307], their scattering properties [79–81, 299, 308] and their topology [78]. For multimode optical waveguides, one can obtain a superpartner refractive index profile whose guided modes share propagation constants with the original waveguide, but where the fundamental mode is removed from the spectrum. In conjunction with SCRAP, this modal control allows to achieve transfer to only specific modes in a multimode waveguide. The joint action of SCRAP and SUSY can thus be exploited to faithfully excite higher-order modes of multimode waveguides and to spatially separate superpositions of different modes, both challenges of high importance in the context of MDM. Previous works combining multimode waveguides and SUSY for the excitation of modes and mode sorting needed at least three waveguides to have similar results to those presented here [306], or were based on the adiabatic modification of the whole refractive index profile along the propagation direction [82, 307].

For the application to discrete lattices [213], even though the method is completely general, we choose the Su-Schrieffer-Heeger (SSH) model [95] introduced in Sec. 2.3.2 as a platform for the study. The SSH model is the simplest instance of nontrivial topology in one dimensional (1D) lattices [101], and it can host topological edge modes localized



around the ends of the chain. These states have been studied and exploited in several physical platforms [214, 244, 336, 364–374]. We showcase how we can use the proposed method to excite or transfer them between lattices with high precision. Finally, we show how the bulk supermodes of the lattice, which are completely delocalized, can be also excited with precision using the same method, which also enables mode conversion between different modes in separate waveguide lattices. Even if the light transfer is not complete, the rest of the supermodes in the main lattice are not significantly excited in the process, implying a high purity of the target supermode at the output facet of the device. Modulating the detuning between waveguides has a direct analogy to the control of the onsite energies that has been employed to achieve quantum state transfer in other contexts, such as in spin chains [375–378].

### 3.2 SCRAP in optical waveguides

The original SCRAP implementation [53] uses a combination of two different pulses to achieve population transfer between atomic states: A strong Stark pulse modifies the energy levels of the system via the Stark effect, and since the effect is stronger on the more excited state, one can cause crossings between the diabatic energy levels [55]. Then, during one of the crossings, the pump pulse adiabatically drives the population from one state to the other. In other words, the pulse is maximal during one of the energy crossings, and negligible during the other. For only two levels, choosing the first or second crossing has no effect on transfer efficiency, but for the generalization to three levels the pulse ordering has a large impact on the population transfer [58]. This scheme can be implemented in systems of both single- and multi-mode optical waveguides, following the quantum-optical analogy explained in Sec. 2.1.6. For now, we consider a set of two planar evanescently coupled waveguides, each one supporting two TE modes. Modes of different order are highly detuned and thus have their coupling heavily suppressed, so one can describe the propagation of modes of the same order  $m$  independently of the rest. The equation describing light propagation in such a system of two multimode waveguides is:

$$i \frac{d}{dz} \mathbf{a}_m(z) = H_m(z) \mathbf{a}_m(z), \quad (3.1)$$

where  $\mathbf{a}_m(z) = (a_{Lm}(z), a_{Rm}(z))$  are the probability amplitudes of mode  $m$  in the left and right waveguide, respectively. The Hamiltonian is defined as:

$$H_m(z) = \begin{pmatrix} 0 & \tau_m(z) \\ \tau_m(z) & \Delta_m(z) \end{pmatrix}, \quad (3.2)$$

where  $\tau_m$  is the coupling between the modes  $m$  of each waveguide in isolation, and the detuning is the difference between the propagation constants in both waveguides,

$\Delta_m(z) = \beta_{Rm}(z) - \beta_{Lm}(z) = \Delta_{m,0} - \Delta\beta_m(z)$ , with  $\Delta_{m,0}$  being the initial detuning and  $\Delta\beta_m$  its variation along  $z$ . Here, the coupling strength and the detuning play the role of the Rabi frequency and the Stark pulse in the original SCRAP implementation, respectively, and they are modulated along the propagation direction  $z$ . The Hamiltonian in (3.2) can be easily diagonalized [55], yielding:

$$\psi_m^-(z) = \cos \theta(z) \psi_{Lm} - \sin \theta(z) \psi_{Rm}, \quad (3.3)$$

$$\psi_m^+(z) = \sin \theta(z) \psi_{Lm} + \cos \theta(z) \psi_{Rm}, \quad (3.4)$$

$$\beta_m^\pm = \frac{\Delta_m(z)}{2} \pm \frac{1}{2} \sqrt{4\tau_m^2(z) + \Delta_m^2(z)}, \quad (3.5)$$

where  $\psi_{Lm}$  and  $\psi_{Rm}$  are the modes in each waveguide, and  $\tan 2\theta_m = 2\tau_m(z)/\Delta_m(z)$  defines the mixing angle. We consider a Gaussian dependence on  $z$  for both  $\tau_m(z)$  and  $\Delta\beta_m(z)$ , as displayed in Fig. 3.1(a). The modulation of  $\Delta\beta_m$  causes two level crossings for each mode at the points indicated by the vertical dotted lines, see Fig. 3.1(b), and we choose  $\tau_m(z)$  to be strong during the first crossing. Then, if light is injected in the left waveguide, the mixing angle evolves from  $-\pi/2$  to 0, with the system adiabatically following  $\psi_i^+$  from  $-\psi_{Lm}$  to  $\psi_{Rm}$ . In other words, we achieve complete light intensity transfer to the right waveguide. As we indicate in Fig. 3.1(b), the adiabatic transfer will occur for both supported modes in the waveguides. However, the excited modes have naturally wider evanescent tails than the fundamental modes. As such, they overlap more strongly with one another, and it is easier to enable efficient transfer between them. One can choose the geometry that optimizes the SCRAP setup for these excited modes, and leave the fundamental modes in a suboptimal coupling regime. As we will see in Section 3.3.1, this can be utilized to (de)multiplex superpositions of both modes since while most light in the excited mode will transfer between waveguides, only a small fraction of light in the fundamental mode will do the same.

Successful implementation of SCRAP requires the simultaneous control of the detuning and the coupling strength along the propagation direction. For laser-written waveguides [257], the most precise approach to control their propagation constants is to adjust the relative velocity between the sample and the laser, which directly affects the core refractive index  $n_{co}$ . The geometry in our case corresponds to the one displayed in Fig. 3.1(c), where the modulation in  $n_{co}$  is indicated by the colorbar. For a cladding refractive index of  $n_{cl} = 1.414$ , a width of  $\omega = 4 \mu\text{m}$  and a wavelength at the telecom range  $\lambda = 1.55 \mu\text{m}$ , we show the variations of the propagation constants when changing the core index in Fig. 3.2(a). We see that the waveguides stop being bi-modal below  $n_{co} \simeq 1.428$  and above  $n_{co} \simeq 1.468$  as indicated by the vertical solid lines in Fig. 3.2(a). From the same figure, however, we also observe that for values around  $n_{co} \simeq 1.455$  the propagation constants for both the  $\text{TE}_0$  and  $\text{TE}_1$  modes are nearly linear in  $n_{co}$ , meaning that we can perform a linear fit for both in that region, while also maintaining only two

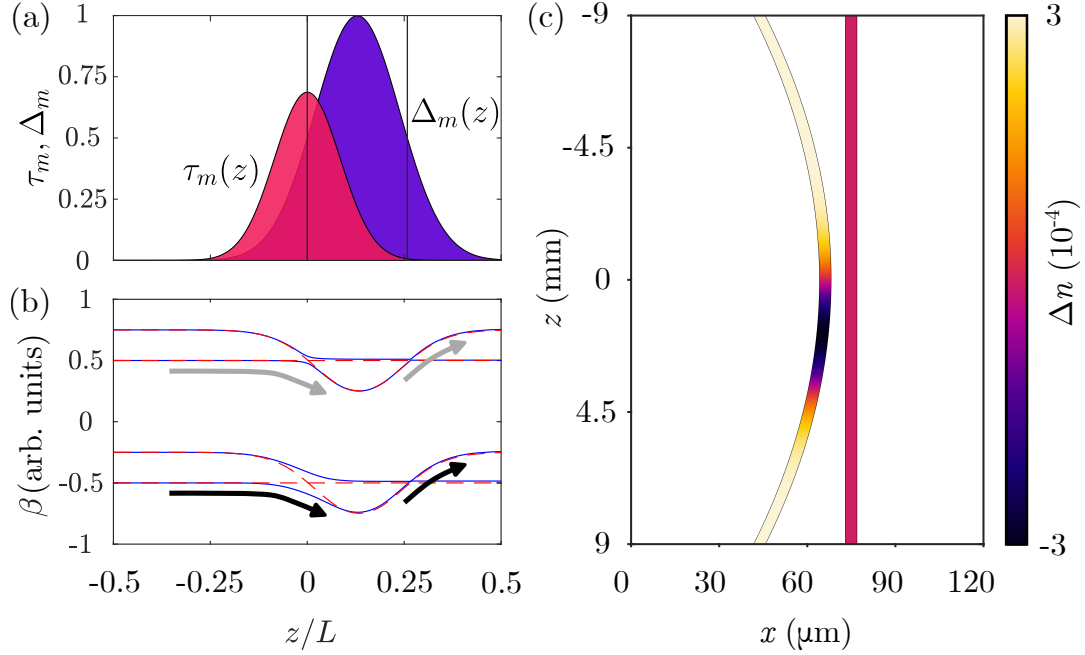


Figure 3.1: (a) Strength of the spatial modulation of the detuning  $\Delta_m$  (dark purple) and of the coupling  $\tau_m$  (light red) between modes  $m$  in each waveguide. The vertical lines indicate the positions at which the mode levels cross. (b) Variation of the eigenvalues (blue solid lines) and the individual modes (red dashed lines) of the two-waveguide system along  $z$ . The  $\text{TE}_1$  modes, lower in propagation constant, have a stronger coupling between them as can be seen by the larger separation between blue lines. In both cases, the arrows represent the adiabatic population transfer from the lower to the higher state, which is stronger for the modes of lower  $\beta$ . (c) Geometry of the SCRAP implementation and refractive index of the waveguide cores. The modulation of the core of the left waveguide is represented as  $\Delta n = n_L - n_R$ .

supported modes in the waveguide. We obtain, for each mode  $m$ :

$$\beta_m(n) = b_m n + q_m, \quad (3.6)$$

with  $b_0 = 3.876 \mu\text{m}^{-1}$ ,  $q_0 = 0.230 \mu\text{m}^{-1}$ ,  $b_1 = 3.142 \mu\text{m}^{-1}$  and  $q_1 = 1.222 \mu\text{m}^{-1}$ . Looking back to Fig. 3.1(c), in our case the right waveguide features a constant core refractive index  $n_R = 1.455$ , while the refractive index of the left core is modulated according to:

$$n_L(z) = n_L^0 - 2(n_{L,0} - n_R) \exp\left(-\frac{(z - \zeta)^2}{Z_s^2}\right), \quad (3.7)$$

where  $n_{L,0} = 1.4553$ . This Gaussian variation of the core index causes in turn a Gaussian change in the propagation constants through (3.6), and it is within current experimental reach [42].  $\zeta$  and  $Z_s$  are parameters that determine the delay with respect to the coupling

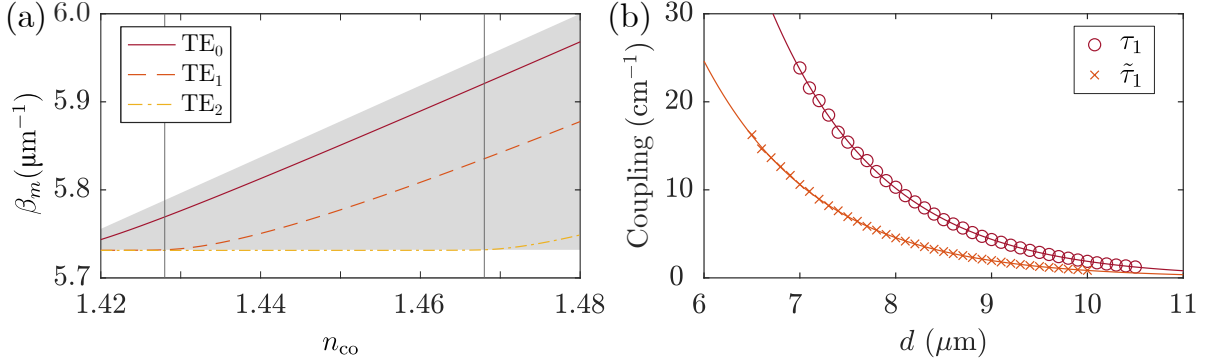


Figure 3.2: (a) Variation of the propagation constants of the TE-modes of a step-index planar waveguide with respect to the refractive index of the core, for a width of  $\omega = 4 \mu\text{m}$ , cladding index  $n_{cl} = 1.414$  and wavelength  $\lambda = 1.55 \mu\text{m}$ . The guided modes must have propagation constant values in the grey shaded region,  $k_0 n_{cl} < \beta_m < k_0 n_{co}$ . The waveguide is bi-modal in the region between vertical solid lines. (b) Coupling strength with respect to the waveguide distance between the  $\text{TE}_1^{(1)}$  modes of the two step-index waveguides (red circles),  $\tau_1$ , and between the  $\text{TE}_1^{(1)}$  mode of the step-index waveguide and the  $\text{TE}_0^{(2)}$  mode of the SUSY waveguide (orange crosses),  $\tilde{\tau}_1$ . The exponential fit for each set of values is included in solid lines.

and the width of the Gaussian, respectively. We fix  $Z_s = L/8$ ,  $L$  being the total length along  $z$ , and choose  $\zeta = Z_s \sqrt{\log 2}$  so that the first level crossing occurs at  $z = 0$  where the waveguides are closest and the coupling is maximal. Although the same effect can be achieved by performing the modulation on the right waveguide, which would actually correspond more naturally with the Hamiltonian in (3.2), we choose to vary the left core for a direct comparison with the SUSY implementation described later.

Both the coupling strength and the transfer efficiency are reduced as  $n_L$  deviates from  $n_R$  [222]. However, the relative variation of the coupling strength between the central value  $n_L = 1.455$  and the limits of the modulation has been computed to be below  $10^{-7}$  for the parameters considered in this work, and as such we can consider that the coupling does not deviate from the case of equal waveguides. In that case, as we explained in Sec. 2.1.3, the coupling strength between modes can simply be controlled by adjusting the distance between the waveguides, since the coupling decreases exponentially with their separation:

$$\tau_m(d) = \tau_m^0 \exp(-\kappa_m d). \quad (3.8)$$

Knowing this, we perform a numerical study to determine the parameters  $\tau_m^0$  and  $\kappa_m$  for the  $\text{TE}_1$  modes of identical waveguides with  $n_{co} = 1.455$ . We plot the coupling strength at different distances in Fig. 3.2(b), from which we extract the following parameters:  $\tau_1^0 = 8707.8 \text{ cm}^{-1}$  and  $\kappa_1 = 0.844 \mu\text{m}^{-1}$ . For the geometry in Fig. 3.1(c), the coupling

along  $z$  approximately follows a Gaussian expression [306]:

$$\tau_m(z) \approx \tau_m(0) \exp\left(-\kappa_m \frac{z^2}{2r}\right), \quad (3.9)$$

whose width can be controlled through the radius of curvature  $r$ . In there,  $\tau_m(0)$  corresponds to the coupling at the point where the waveguides are closest, as computed from (3.8) for  $d = x_m$ . For this work, we mainly focus on the SCRAP performance for the transfer and excitation of  $\text{TE}_1$  modes. Coupling between  $\text{TE}_0$  modes will be weaker due to their lower extension, a fact that we exploit later on. We finally note that for the scheme to work, the evolution of the modes needs to be adiabatic. This implies that the variation in the mixing angle defined below (3.5),  $|\dot{\theta}_m(t)|$ , needs to be small compared to the gap between eigenlevels,  $|\beta_m^+ - \beta_m^-|$ . In other words [55]:

$$|\dot{\theta}_m(t)| \ll \sqrt{4\tau_m^2(z) + \Delta_m^2(z)}. \quad (3.10)$$

### 3.2.1 Combining SCRAP with Supersymmetry

So far we have assumed a set of two waveguides, each supporting two modes. As we will see in the following sections, if we use this setup for demultiplexing purposes, the efficiency we can obtain is limited. The weak but nonzero evanescent coupling between fundamental modes implies that a small but non-negligible fraction of light in those modes will always be transferred, and that inevitably worsens the performance of the device as a demultiplexer. A way to circumvent this problem is to completely remove the possibility of transfer for fundamental modes by means of a SUSY transformation. As explained in Sec. 2.2.2, we can use SUSY transformations to construct a superpartner refractive index profile supporting only one mode, which we call  $\text{TE}_0^{(2)}$ , with a propagation constant matching the one for the excited mode of the original two-mode waveguide, now denoted as the  $\text{TE}_1^{(1)}$  mode. Then, we combine this with the SCRAP scheme as depicted in Fig. 3.1(c) by substituting the waveguide on the right with its superpartner. In this case, the index profile and the mode levels are the ones displayed in Fig. 3.3(a). Modulating the detuning in one waveguide now leads to crossings between the  $\text{TE}_1^{(1)}$  and  $\text{TE}_0^{(2)}$  modes only, and light can now only be transferred between these two modes. The propagation constants of the modes are drawn in Fig. 3.3(b). Compared with Fig. 3.1(b), it is clear that the fundamental mode from the step-index waveguide with refractive index  $n^{(1)}$ ,  $\text{TE}_0^{(1)}$ , is missing in its superpartner  $n^{(2)}$ .

We recall the mathematical formalism introduced in Sec. 2.2, in which we showed that for a step-index waveguide with core index  $n_{\text{co}}$ , the superpartner is defined by:

$$n^{(2)}(x) = \sqrt{n_{\text{co}}^2 - 2 \left(\frac{k_x}{k_0}\right)^2 \sec^2(k_x x)}, \quad (3.11)$$

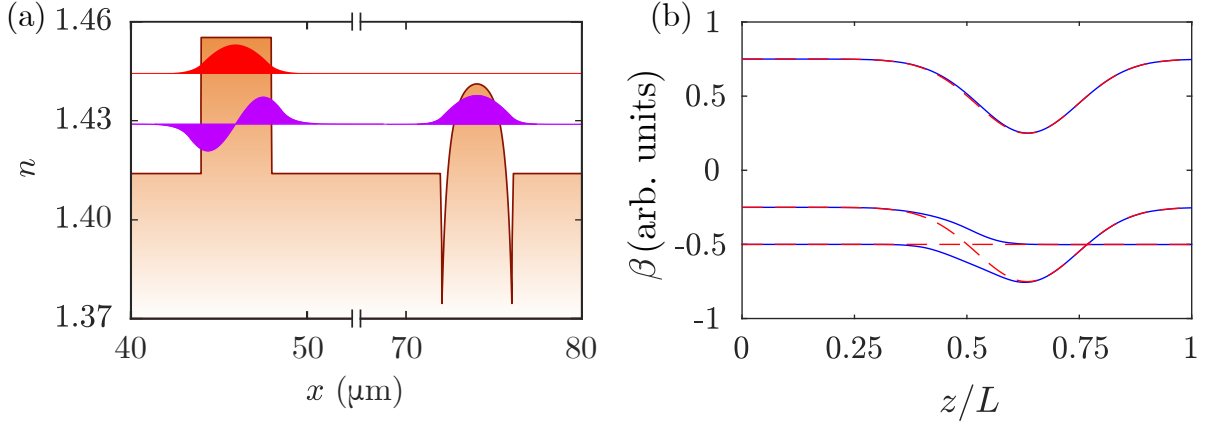


Figure 3.3: (a) Refractive index profile of a step-index waveguide (left) and its superpartner profile (right). The mode levels and mode profiles are sketched on top of each waveguide. (b) Variation of the eigenvalues (blue solid lines) and the individual modes (red dashed lines) of the modulated two-mode waveguide coupled to its superpartner.

where  $k_0$  is the vacuum wavenumber and  $k_x = \sqrt{n_{\text{co}}^2 k_0^2 - \beta_0^2}$ , with  $\beta_0$  being the propagation constant of the fundamental mode of the step-index waveguide. This refractive index profile is the one shown in Fig. 3.3(a) alongside the original step-index profile.

The propagation constants of the fundamental mode of the SUSY waveguide,  $\text{TE}_0^{(2)}$ , and the  $\text{TE}_1^{(1)}$  mode of the step-index waveguide will be equal, but the former will be much less extended into the cladding region than the latter. As such, compared to the coupling strength between the  $\text{TE}_1^{(1)}$  modes of two step-index waveguides, the coupling between SUSY and step-index waveguides will be weaker. This can be observed in Fig. 3.2(b), where the values of the coupling strength are computed for this case. From the exponential fit we can extract the parameters  $\tilde{\tau}_1^0 = 3855.8 \text{ cm}^{-1}$  and  $\tilde{\kappa}_1 = 0.842 \mu\text{m}^{-1}$ . We denote the parameters with a tilde to indicate that they correspond to the coupling between the excited mode of the step-index waveguide and the fundamental mode of its superpartner profile.

### 3.2.2 SCRAP in lattices of optical waveguides

The SCRAP scheme is not limited to the transfer of light between individual waveguides, it can also be applied to the crossings of supermodes in waveguide lattices, or between the mode of a waveguide and the supermode of a lattice. In that sense, we first consider the case of a lattice of  $N$  identical single-mode waveguides that is evanescently coupled to an auxiliary waveguide, whose propagation constant and coupling to the lattice we tailor along the propagation direction, as sketched in Fig. 3.4(a). As described in Sec. 2.1.3, assuming the tight-binding approximation to be valid, the system can be

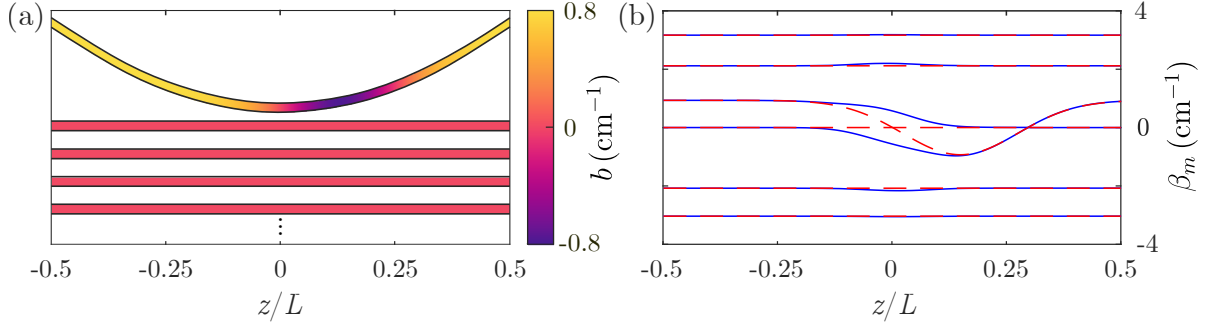


Figure 3.4: (a) Illustration of the geometry of the proposed device for discrete waveguide lattices. An auxiliary single-mode waveguide has a controlled detuning (indicated by the color scheme) and coupling to the main lattice along the propagation direction. The main lattice is not modulated. (b) Mode spectrum along the propagation direction for a lattice of 5 uniformly spaced waveguides with a coupling of  $t = 2 \text{ cm}^{-1}$ . The red dashed lines represent the propagation constants for the main lattice and the auxiliary waveguide separately, while the solid blue lines represent the ones for the modes of the joint structure.

described via a coupled-mode model in terms of a tridiagonal Hamiltonian:

$$\mathcal{H} = \begin{pmatrix} 0 & t_1 & 0 & & & \\ t_1 & 0 & t_2 & & & \\ 0 & t_2 & 0 & & & \\ & & & \ddots & & \\ & & & & 0 & t_{N-1} & 0 \\ & & & & t_{N-1} & 0 & t(z) \\ & & & & 0 & t(z) & b(z) \end{pmatrix}, \quad (3.12)$$

where  $t_j$  are the couplings between waveguides in the main lattice, and where  $b(z)$  and  $t(z)$  correspond to the detuning of the auxiliary waveguide and its coupling to the main lattice, respectively. The propagation constant of the auxiliary waveguide is modulated in order to produce crossings with the propagation constant  $\beta_p$  of a chosen supermode of the main lattice at two points in  $z$ . Namely, we impose:

$$b(z) = \beta_p + \Delta_0 - 2\Delta_0 \exp\left(-\frac{(z - \zeta)^2}{Z_s^2}\right), \quad (3.13)$$

where  $\Delta_0 = b(0) - \beta_p$  is the initial detuning of the auxiliary waveguide with respect to the target mode  $p$ , and the other parameters are defined in the same way as the modulation in (3.7) so that the first mode crossing is located at the center of the device. To complete the excitation method, the coupling strength of the auxiliary waveguide  $t(z)$  is chosen to be maximal at this first crossing and near zero during the second.



Following the same principle as for the multimode case, we symmetrically bend the auxiliary waveguide away from the main lattice to approximately obtain a Gaussian dependence for the coupling [306]:

$$t(z) \approx t(0) \exp\left(-\frac{(z - L/2)^2}{Z_t^2}\right), \quad (3.14)$$

where  $t(0) = t_0 \exp(-\kappa x_m)$  is the coupling strength at the point of minimum distance between the main lattice and the auxiliary waveguide,  $x_m$ , and  $Z_t^2 = 2r/\kappa$ , with  $r$  the radius of curvature of the waveguide. The above modulations affect the spectrum of a waveguide lattice in the manner displayed in Fig. 3.4(b), where we use a set of equidistant lattices as an example. For an adiabatic device with input in the auxiliary waveguide, the dynamics will be entirely contained in the set of crossing modes. Therefore, effectively, the system can be described by a two-level Hamiltonian:

$$H(z) = \begin{pmatrix} 0 & \bar{t}(z) \\ \bar{t}(z) & b(z) \end{pmatrix}, \quad (3.15)$$

where the coupling  $\bar{t}(z)$  depends on the overlap between the supermode and the auxiliary mode.  $\bar{t}(z)$  will in general have a different value from the coupling  $t(z)$ , but it will keep the same Gaussian dependence. The same idea can be extended to a main lattice coupled to a second auxiliary one. In this case, all waveguides in the auxiliary lattice have their propagation constants modulated equally, and crossings among all their corresponding modes are enabled, which allows for mode transfer between the supermodes of both structures with a two-level Hamiltonian describing each individual case. This application is nevertheless limited to weak propagation constant modulations. If modulations are strong enough to enable multiple crossings for each mode, the dynamics is no longer confined to only two states. To demonstrate the potential of the discrete formalism, we choose the waveguide lattice to follow the SSH model [95] discussed in Sec 2.3.2, which is a one dimensional (1D) chain with alternating weak and strong couplings,  $t_w$  and  $t_s$ , respectively.

### 3.3 Applications for multimode optical waveguides

We apply SCRAP to efficiently transfer light intensity between multimode waveguides. First, we consider the demultiplexing possibilities of the method. We start by considering the SCRAP technique without applying SUSY in subsection 3.3.1, and then demonstrate the improvement that SUSY brings in subsection 3.3.2. For this application, we define the following figure of merit:

$$\mathcal{F} = \frac{I_{L0}^{\text{out}}}{I_{L0}^{\text{in}}} \cdot \frac{I_{R1}^{\text{out}}}{I_{L1}^{\text{in}}}, \quad (3.16)$$



which is just the fraction of intensity of the  $\text{TE}_0^{(1)}$  mode that remains on the input waveguide multiplied by the fraction of intensity of the  $\text{TE}_1^{(1)}$  mode that gets transferred either to the other  $\text{TE}_1^{(1)}$  mode in subsection 3.3.1 or to the  $\text{TE}_0^{(2)}$  mode in subsection 3.3.2.

After that, in subsection 3.3.3 we exploit this efficient transfer to excite the  $\text{TE}_1^{(1)}$  mode of the step-index waveguide by injecting the fundamental mode in the SUSY partner. To quantify the accuracy of the method, we define a fidelity:

$$F = |\langle \psi_p | \psi_{\text{out}} \rangle|^2, \quad (3.17)$$

which is an integral that compares the spatial profile of the output mode  $\psi_{\text{out}}$  with the one of a particular target mode  $\psi_p$ .

### 3.3.1 Mode demultiplexing

The SCRAP scheme allows to efficiently transfer light intensity between modes in separate step-index waveguides, which can be exploited for mode demultiplexing even without applying SUSY. We first consider the geometry in Fig. 3.1(c) and perform numerical simulations for the propagation of the  $\text{TE}_0^{(1)}$  mode, the  $\text{TE}_1^{(1)}$  mode and an equally-weighted superposition of both. We display the results in Figs. 3.5(a), 3.5(b) and 3.5(c), respectively. From those figures, we can readily see that light in the  $\text{TE}_1^{(1)}$  mode is efficiently transferred, while the  $\text{TE}_0^{(1)}$  mode remains mostly confined in the left waveguide. The variation of the refractive index causes different mode levels to vary differently, see Fig. 3.2(a). Also, since the spatial profile of the  $\text{TE}_0^{(1)}$  mode is less extended into the cladding region compared to more excited states, the coupling between fundamental modes is weaker than that for the  $\text{TE}_1^{(1)}$  modes. Both these reasons cause the transmission for the  $\text{TE}_0^{(1)}$  mode to be less efficient when compared to the  $\text{TE}_1^{(1)}$  mode. Nonetheless, a small fraction of its power is still transferred, and that hinders the efficiency of the device as a demultiplexer. This can be seen most easily in Fig. 3.5(c), where the beating in intensity implies that the right waveguide holds a superposition of both TE modes, with a relative fraction that depends on the strength of the coupling for the  $\text{TE}_0^{(1)}$  mode.

To check the efficiency of the method, we compute the figure of merit defined in (3.16), and plot the results in Fig. 3.6(a) as a function of the geometrical parameters of the system, that is, the radius of curvature  $r$  and the minimum distance between waveguides  $x_m$ . We see that there is a wide region of parameter values where  $\mathcal{F} > 0.9$ , but it caps at around  $\mathcal{F} = 0.97$ . A way to enhance this efficiency is by combining the SCRAP scheme with SUSY.

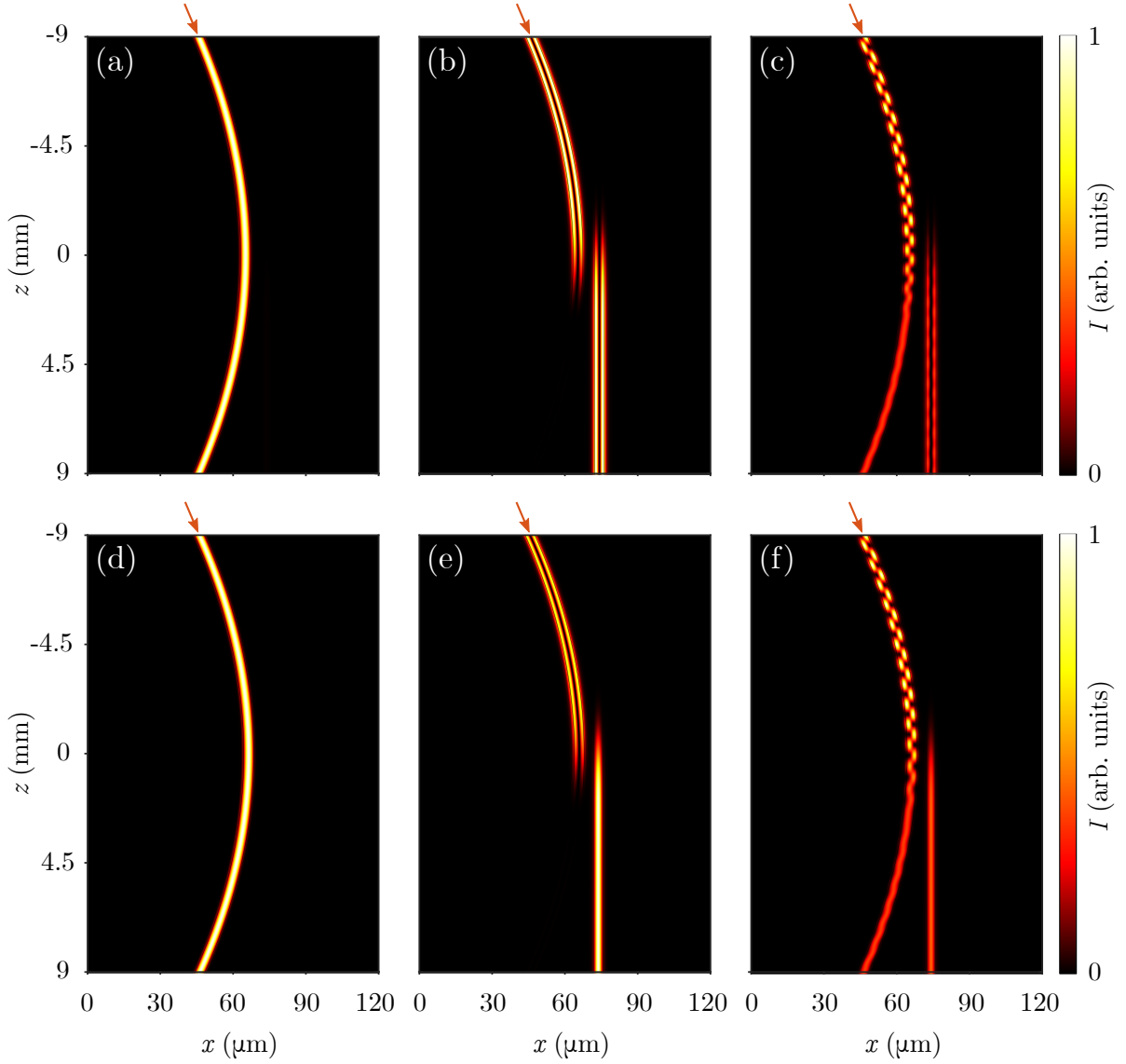


Figure 3.5: Comparison between the light intensity propagation in the SCRAP implementation between two step-index waveguides (top row) and for the case where SUSY is applied to the waveguide on the right (bottom row) when injecting (a), (d) the  $\text{TE}_0^{(1)}$  mode (b), (e) the  $\text{TE}_1^{(1)}$  mode and (c), (f) an equally-weighted superposition of both in the modulated waveguide.

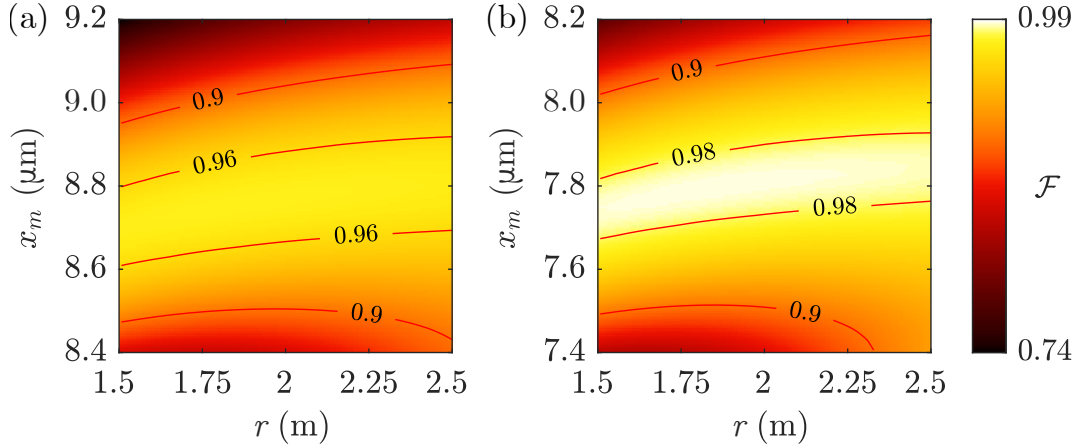


Figure 3.6: Figure of merit defined in (3.16) for the spatial separation of the  $\text{TE}_0^{(1)}$  and  $\text{TE}_1^{(1)}$  modes in (a) the step-index SCRAP implementation and (b) the SUSY implementation as a function of the minimum distance between waveguides,  $x_m$ , and the radius of curvature,  $r$ .

### 3.3.2 SUSY-enhanced demultiplexing

Replacing the right waveguide with its SUSY partner entirely removes the coupling for the  $\text{TE}_0^{(1)}$  mode, since its equivalent on the SUSY waveguide is no longer supported, whilst maintaining the possibility of implementing the SCRAP efficiently for the  $\text{TE}_1^{(1)}$  mode. We repeat the numerical simulations, and show the results of inputting the  $\text{TE}_0^{(1)}$ ,  $\text{TE}_1^{(1)}$  and a superposition of both modes in Figs. 3.5(d), 3.5(e) and 3.5(f), respectively. In this case, light in the  $\text{TE}_0^{(1)}$  mode remains entirely confined in the left waveguide, while power is efficiently transferred between the  $\text{TE}_1^{(1)}$  mode and the  $\text{TE}_0^{(2)}$  mode of the SUSY partner waveguide. This has favorable implications in the efficiency, as shown in Fig. 3.6(b). The figure of merit given in Eq. (3.16), when compared to the case of SCRAP without SUSY, is overall larger for all parameter values, and it reaches a maximum of  $\mathcal{F} = 0.99$  for  $x_m = 7.8 \mu\text{m}$  and a radius of curvature around  $r = 2 \text{ m}$ .

However, the intensity profile of the  $\text{TE}_1^{(1)}$  mode is transformed into that of the fundamental mode of the right waveguide upon transfer, and is no longer antisymmetric. Introducing a superposition of modes into the device indeed leads to efficient mode separation but alters the intensity profile of the excited mode, causing the output to resemble the one from a beam splitter instead of the one from Fig. 3.5(c). In principle, adding a third bent waveguide on the right side should allow one to perform demultiplexing without modifying the output mode profile [306] by implementing the three-state extension of the SCRAP method discussed in [58]. In that case, the spatial profile of the  $\text{TE}_1^{(1)}$  waveguide would be recovered and the suppression of the transfer for the  $\text{TE}_0^{(1)}$  mode would be maintained.

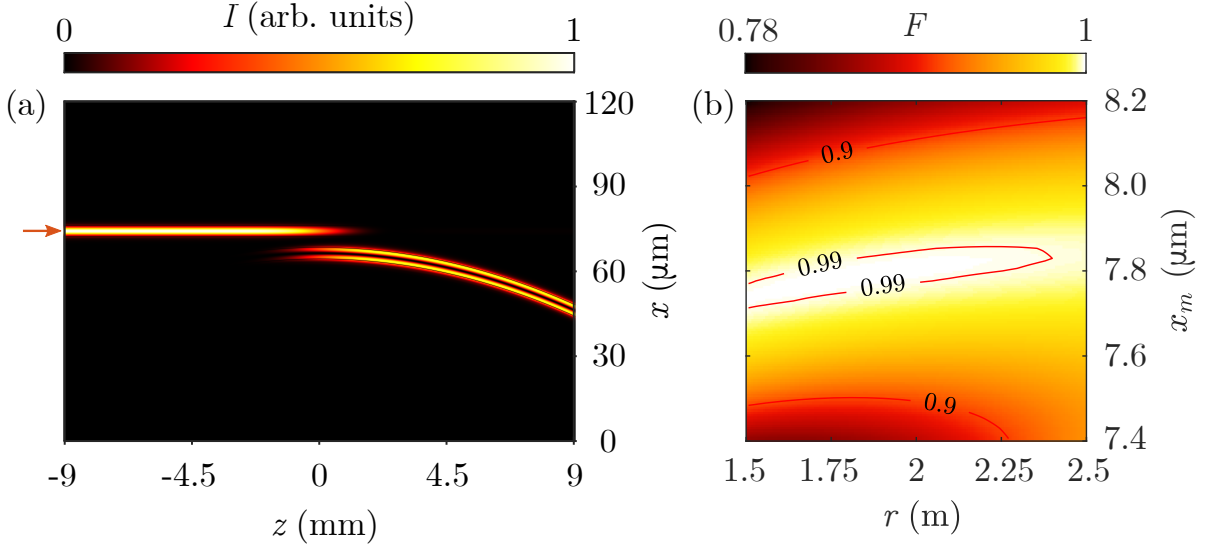


Figure 3.7: (a) Light intensity propagation for the excitation of the  $\text{TE}_1^{(1)}$  mode of the step-index waveguide in the SUSY implementation of SCRAP when propagating the injected fundamental mode of the SUSY waveguide. (b) Fidelity of the process as a function of the minimum distance between waveguides,  $x_m$ , and the radius of curvature of the left waveguide,  $r$ .

### 3.3.3 Excitation of the $\text{TE}_1^{(1)}$ mode

The change in mode profile in the SUSY waveguide, which is now single-mode as depicted in Fig. 3.3(a), can be exploited for the excitation of other modes. Starting from this fundamental  $\text{TE}_0^{(2)}$  mode, injected in the SUSY waveguide we numerically simulate light propagation through the device. The propagation of light intensity is shown in Fig. 3.7(a), where an efficient transfer to the  $\text{TE}_1^{(1)}$  mode of the step-index waveguide is readily observed.

We compute the fidelity of the excitation according to (3.17), and show in Fig. 3.7(b) that we can obtain the target mode with fidelities above  $F = 0.9$  for a wide range of parameter values, with a significant region where fidelities exceed  $F = 0.99$ . Even if the geometrical parameters are slightly off and power transfer is not complete, light on the step-index waveguide will almost entirely be comprised of the  $\text{TE}_1^{(1)}$  mode. This can be explained by noting that the SUSY fundamental mode can only be efficiently coupled to the  $\text{TE}_1^{(1)}$  mode of the step-index waveguide due to the phase-matching condition, and thus this procedure produces a negligible excitation of the  $\text{TE}_0^{(1)}$  mode. One can prove this fact by numerically computing the overlap integral between the output field and the known profile of the  $\text{TE}_0^{(1)}$  mode of the step-index waveguide. This, in essence, is a computation of the fidelity in Eq. (3.17) but with a different target mode that now corresponds to the  $\text{TE}_0^{(1)}$  mode. Performing this calculation yields values below

$1.3 \times 10^{-3}$  for all combinations of parameter values considered in this work, vastly lower than the fidelities of the  $\text{TE}_1^{(1)}$  mode for the same parameter values.

### 3.3.4 Exciting higher-order modes

This scheme can also be applied to higher-order modes in higher-order multimode waveguides by layering additional consecutive SUSY transformations to the refractive index profile. We show a diagram of the effect of applying successive SUSY transformations to a  $m$ -mode step-index waveguide in Fig. 3.8(a), in which one mode is removed at each further step. One can then couple the  $m$ -mode waveguide to its superpartner after  $m - 1$  consecutive SUSY transformations, as indicated in the image by the dark-red arrow. This  $(m - 1)$ -th order superpartner only has a single mode remaining, matched to the highest-order mode of the original waveguide that we label as the  $\text{TE}_{m-1}^{(1)}$  mode. Modulating the core of the  $m$ -mode waveguide and its distance to the superpartner allows to implement the SCRAP scheme between both these modes. With this, one can excite the  $\text{TE}_{m-1}^{(1)}$  mode of the original waveguide using a fundamental-mode input on its SUSY partner.

To prove the idea, we showcase the excitation of the  $\text{TE}_2^{(1)}$  mode of a three-mode waveguide by means of a fundamental-mode excitation on its second-order superpartner, namely the  $\text{TE}_0^{(3)}$  mode. The behavior of light propagation in such a device is presented in Fig. 3.8(b). Finally, we note that this idea could also be applied to transfer excited modes between superpartner waveguides, without needing to reach the point of single-mode behavior. For instance, in the same scenario as what was just exposed, one could enable transfer between  $\text{TE}_2^{(1)}$  and  $\text{TE}_1^{(2)}$  modes by using only a single SUSY step. Nevertheless, this relinquishes the benefit of using a simple input beam.

## 3.4 Applications for discrete waveguide lattices

We now jump to the applications of SCRAP in discrete waveguide lattices. We start by analyzing the SSH lattice coupled to a single modulated waveguide in Sec. 3.4.1, where we exploit the method to excite supermodes of the main lattice by using a fundamental-mode input on the auxiliary waveguide. This is applied both to a localized topological mode as well as an extended bulk mode of the SSH model. After that, we consider the case of an entire auxiliary lattice in Sec. 3.4.2, which is applied first to transfer edge states between lattices in two different scenarios, as well as for mode conversion between different lattices.

To check the efficiency of all these devices, we introduce two new figures of merit. First, we define the *purity*:

$$P = \left| \langle \tilde{\psi}_p | \tilde{\psi}_{\text{out}} \rangle \right|^2, \quad (3.18)$$

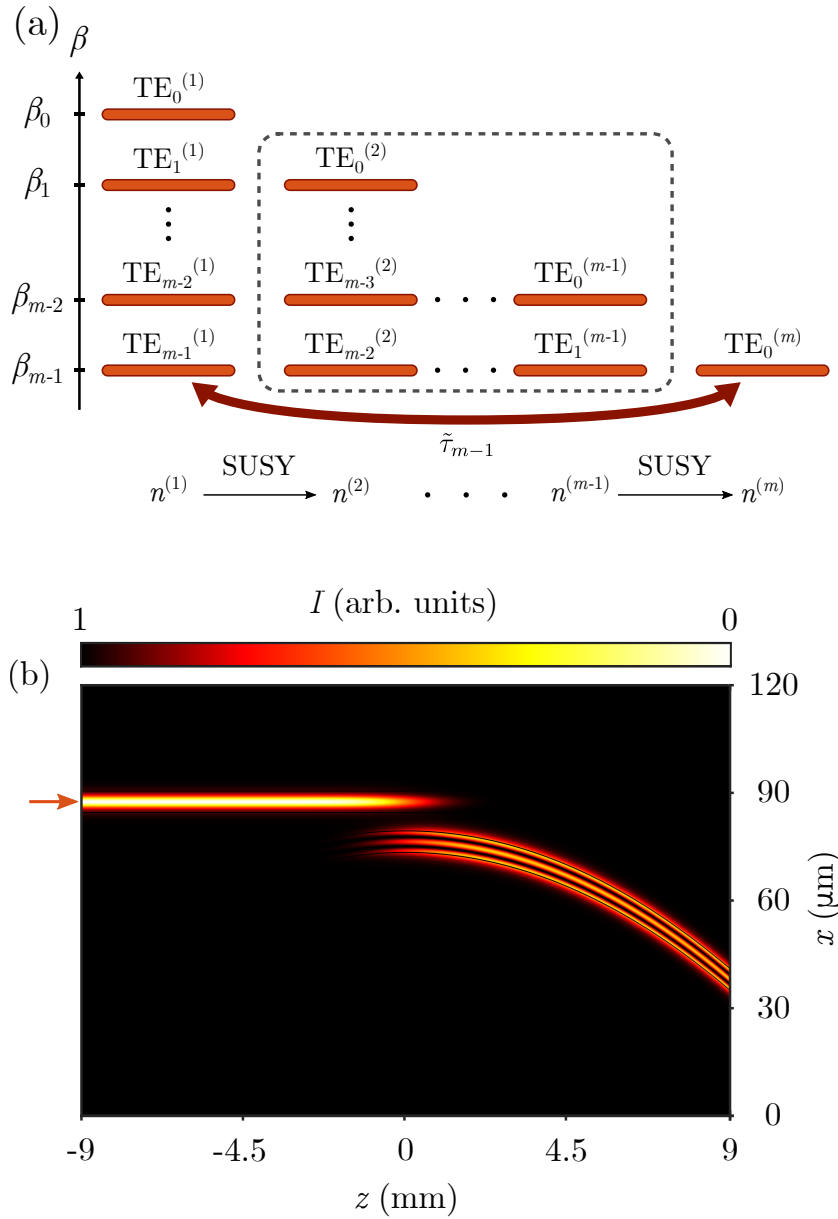


Figure 3.8: (a) Diagram of propagation constants in a  $m$ -mode step-index waveguide (left column) and its superpartners after successive SUSY transformations. After  $m - 1$  transformations, only a single guided mode remains. Coupling this  $n^{(m)}$  superpartner with the original structure only yields significant coupling between this fundamental mode and the  $(m - 1)$ -th mode of the original structure, with strength  $\tilde{\tau}_{m-1}$ . (b) Light propagation in the excitation of a  $\text{TE}_2$  mode of a three-mode step-index waveguide, by joining SCRAP with a two-step SUSY transformation.

which compares the normalized amplitudes of the output state  $\tilde{\psi}_{\text{out}}$  to the target mode  $\tilde{\psi}_p$  only in the waveguides of the main lattice. Note that the purity is the discrete equivalent of the fidelity defined in (3.17), to which we give a different name to avoid any possible confusion. This figure of merit shows the ability to obtain a particular mode without significant excitation of any others, but not how much intensity actually reaches the main lattice. For that, we define the intensity fraction:

$$\tilde{I} = \frac{I}{I_0}, \quad (3.19)$$

which compares the light intensity that is transferred from the auxiliary waveguide to the main lattice,  $I$  to the input intensity  $I_0$ . This separates the characterization of the devices in two parts: (i) How pure is the output state – or conversely which fraction of light is leaked to unwanted modes – and (ii) Which fraction of the input intensity reaches the main lattice.

### 3.4.1 Single auxiliary waveguide

#### Exciting edge modes

The above formalism is now used to excite topological modes of an SSH chain by means of an auxiliary waveguide where light is injected. By tuning  $b(z)$  in Eq. (3.13) to the propagation constant of the topological mode, the SCRAP scheme guarantees the efficient transfer of light between these modes. We first consider the case of an SSH lattice with  $N = 7$  waveguides, with couplings  $t_w = 0.8 \text{ cm}^{-1}$  and  $t_s = 2.1 \text{ cm}^{-1}$ . In Fig. 3.9(a) we showcase the light propagation in a SCRAP device, where we achieve an excitation of this mode. In Fig. 3.9(b), we plot the variation of the propagation constants along  $z$  that clearly displays the crossing between the edge and auxiliary modes, which are the only two modes that are affected by the modulation. For light injected in the auxiliary waveguide, the dynamics in the device is also restricted to these two modes. In Fig. 3.9(b), the red dashed lines represent the propagation constants of the supermodes of the SSH lattice and of the auxiliary waveguide independently, while the blue solid lines correspond to those of the eigenmodes of the joint structure. In Figs. 3.9(c) and (d), we again present the light propagation and eigenvalue variation, but this time for the excitation of the symmetric combination of the two edge modes of a lattice with  $N = 6$  and couplings  $t_w = 2.2 \text{ cm}^{-1}$  and  $t_s = 2.5 \text{ cm}^{-1}$ . From the output profile in Fig. 3.9(c), it is clear that we are able to exclusively select either the symmetric or antisymmetric combinations of edge states, depending on the tuning of  $b(z)$ . To be able to achieve this, these two eigenstates need sufficiently different propagation constants to avoid crossing both of them during the modulation, and thus ensure that light transfers only to one of them. As a consequence, for the even- $N$  chain we are restricted to small dimerizations,  $|t_s - t_w|$ .

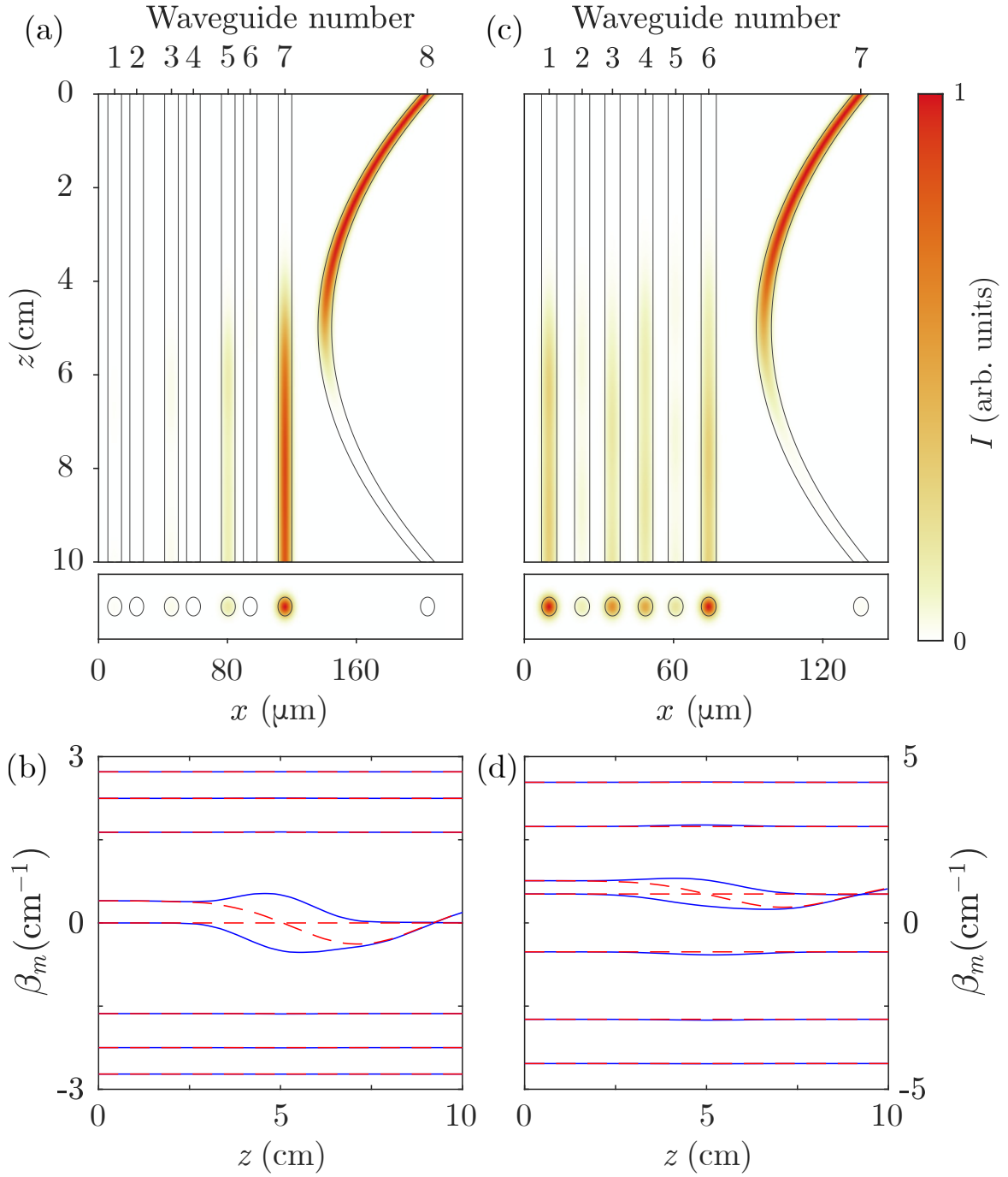


Figure 3.9: (a) Light intensity propagation and (b) spectrum of propagation constants along the propagation direction when exciting the single edge mode of the  $N = 7$  SSH lattice with a single excitation of the auxiliary waveguide as input. We use  $t(0) = 0.55 \text{ cm}^{-1}$  and  $Z_t = 1.8 \text{ cm}$ . (c), (d) Same figures as in (a) and (b), respectively, for the symmetric combination of edge modes of the  $N = 6$  SSH lattice with  $t(0) = 0.75 \text{ cm}^{-1}$  and  $Z_t = 2.3 \text{ cm}$ . For all cases,  $Z_s = 2.55 \text{ cm}$  and  $\Delta_0 = 0.4 \text{ cm}^{-1}$ .



We now analyze the efficiency of the excitation in both cases. We plot in Figs. 3.10(a) and 3.10(b) the purity of the output modes displayed in Figs. 3.9(a) and 3.9(c), respectively, with respect to the parameters of the SCRAP scheme that can be controlled geometrically. Those are the maximum strength of the outer coupling  $t(0)$  between the main lattice and the auxiliary waveguide, controlled through the minimum distance  $x_m$  between them, and the width of the Gaussian coupling function  $Z_t$ , controlled through the radius of curvature  $r$ . For those figures, we keep the propagation constant modulation fixed. We see that there is a wide region of parameter values where the purity comfortably exceeds  $P = 0.99$ , specially for low values for the outer coupling  $t(0)$ . Due to the nature of the method, which is based on the propagation constant crossing between input and target modes, it is expected that only the target mode has a significant amplitude at the output facet if the adiabatic conditions are fulfilled. The total amplitude, however, will depend on the fraction of intensity that is transferred into the main lattice. We plot this quantity in Figs. 3.10(c) and 3.10(d), where we see that there exist regions in parameter space around which the transfer of light is very efficient. Moreover, we see that the two devices are efficient for different sets of parameter values, in particular the case in Fig. 3.10(c) requires lower outer couplings than the one in Fig. 3.10(d) to be efficient. These differences can be attributed to the different profiles for the topological mode in each case. What ultimately determines the characteristics of the propagation is the coupling between the relevant supermodes, which depends on the overlap between the spatial profile. All in all, choosing a region of parameter values where both  $P$  and  $\tilde{I}$  is large yields almost full transfer of light into the target mode. Also, even if the parameters are slightly off, only the target mode will be significantly excited and minimal intensity will be transferred to other modes, as can be gathered from the wide parameter regions of high purity.

### Exciting bulk modes

Even if topological modes are usually the main focus on topologically nontrivial models such as the SSH, the proposed excitation method goes beyond them and can be used to excite any gapped mode of the main lattice. Bulk modes generally display smaller energy gaps and are thus harder to produce, implying that the fractions of transferred intensity will struggle to reach high values. However, even if the transfer is not complete and the final light intensity in the main lattice is rather low, this can be easily compensated by increasing the input beam intensity if the mode purity is high at the output, as long as the regime where the power is high enough to cause nonlinear effects is not reached.

We again consider the case of an SSH lattice coupled to a single auxiliary waveguide, and show how one can indeed accurately reach its bulk modes. Due to the chiral symmetry of the lattice, the spectrum is symmetric around the central mode, as proved

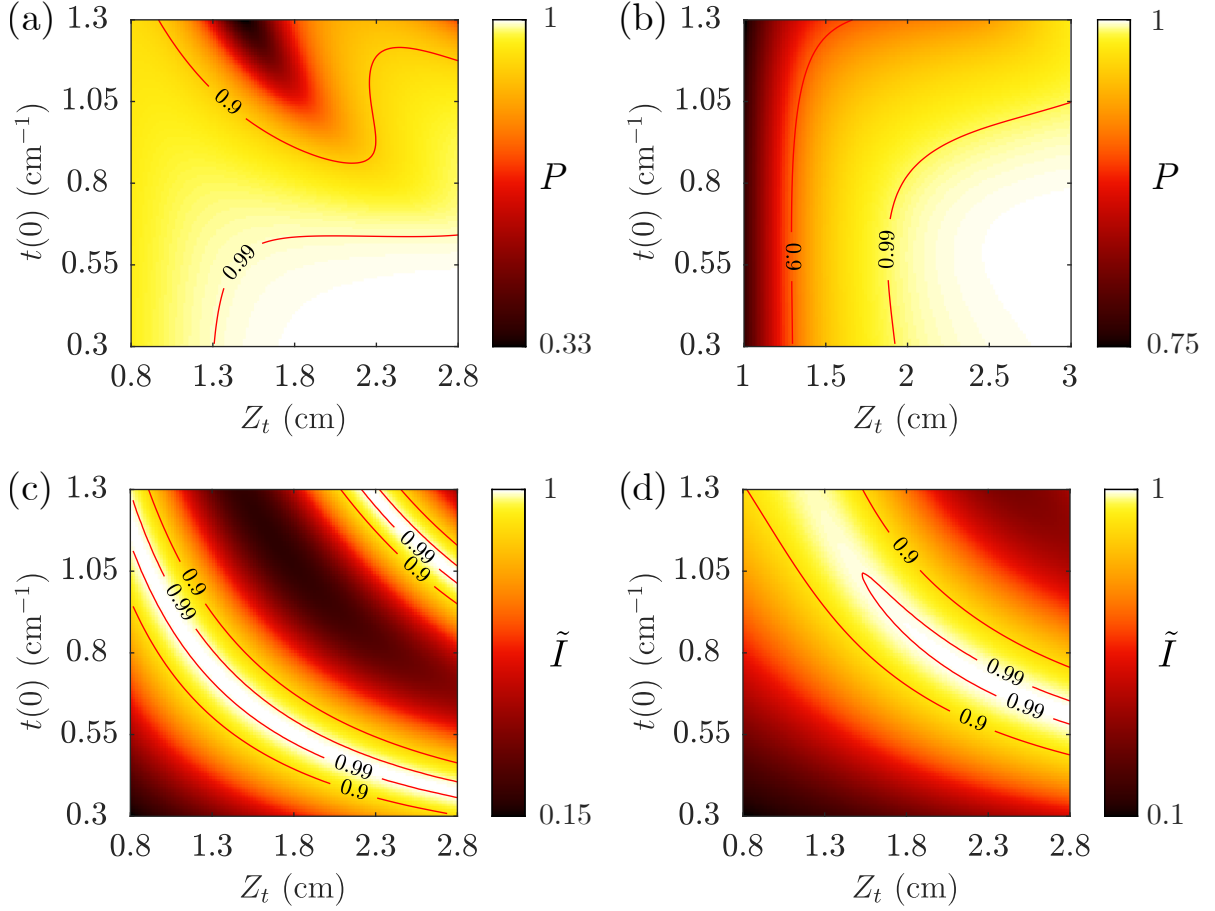


Figure 3.10: Purity of the output mode (top row) and intensity fraction of the excitation (bottom row) with respect to the width of the Gaussian coupling and its maximum strength for (a), (c) the edge mode of the  $N = 7$  lattice and (b), (d) the symmetric combination of edge modes of the  $N = 6$  lattice.

in Fig. 3.11(a) for a lattice of  $N = 7$  waveguides. Hence, we only focus on one half of the spectrum, as results for the other half of the modes will be similar. We tune  $b(z)$  in (3.13) to the propagation constant of each bulk mode in the lower half of the spectrum, and compute the purities for each of them. As shown in Figs. 3.11(b) through (d), there are significant regions of parameter values where the output modes have purities nearing unity. This is further demonstrated by comparing the normalized output profile with the profile of the target mode in Figs. 3.11(e) through 3.11(g), where one observes that they closely resemble one another. These results are remarkable, considering that to achieve all of them we only require a single input beam and index modulations on a single waveguide. However, the intensity fraction that can be transferred into the modes is lower than for gapped topological modes, reaching a maximum of 98% for Fig. 3.11(e), 94% for Fig. 3.11(f) and 61% for Fig. 3.11(g). The decrease in intensity for the bulk

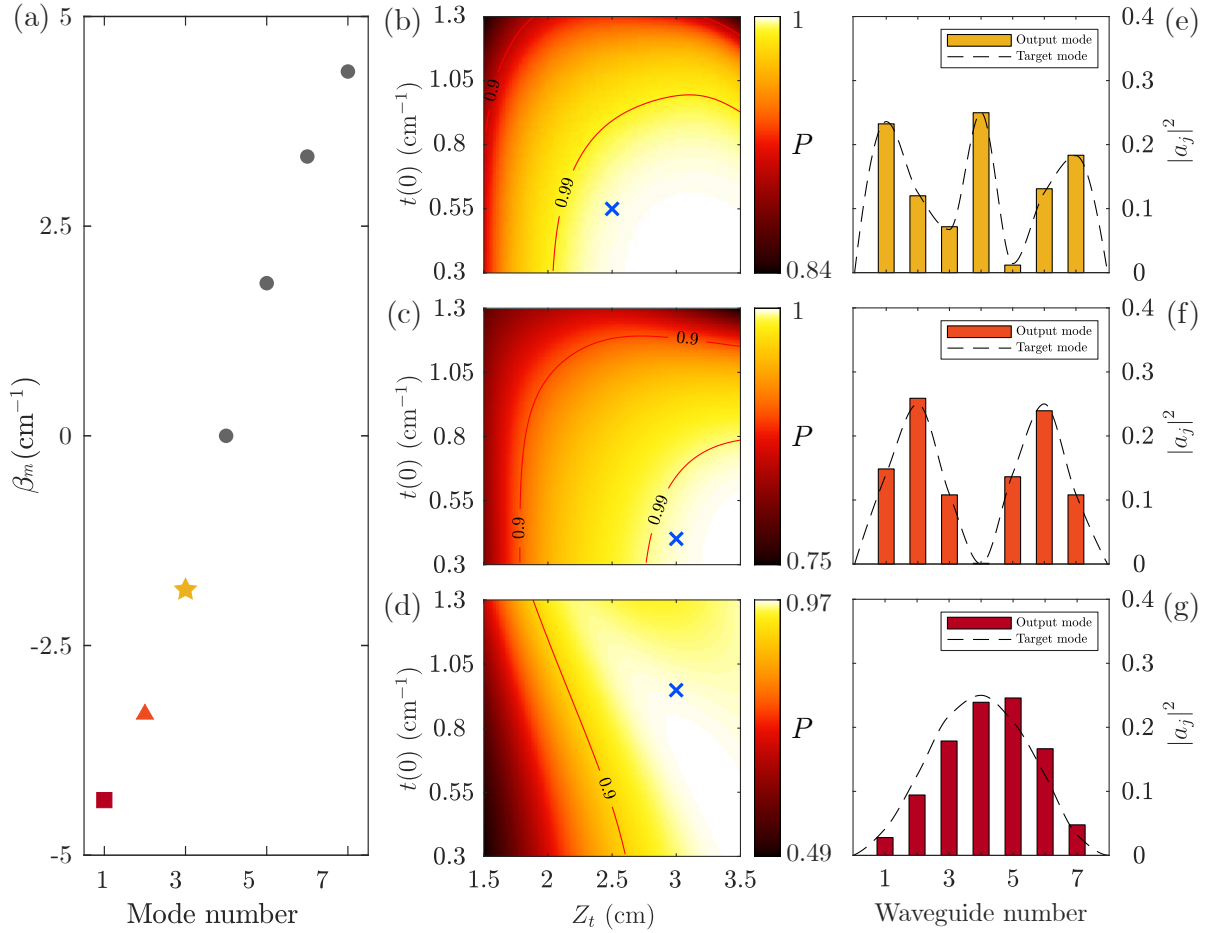


Figure 3.11: (a) Mode spectrum for the SSH lattice with  $N = 7$ . (b)–(d) Purity of the output mode for the excitation of different bulk modes of the SSH lattice with  $N = 7$  with respect to the width of the Gaussian coupling and its maximum strength. The corresponding propagation constants are marked with a yellow star, an orange triangle and a brown square, respectively, in (a). (e)–(g) Output mode in the main lattice (colored bars) and target mode (dashed line) corresponding to the figures directly to the left. The geometrical parameters are indicated by a blue cross in the figures in the central column. For all cases,  $t_w = 2.2 \text{ cm}^{-1}$  and  $t_s = 2.5 \text{ cm}^{-1}$ .

modes of the lattice is mainly due to the gap between them becoming smaller the further away they are from the center of the spectrum. Additionally, since their mode profiles are extended throughout the lattice, the effective coupling  $k(z)$  between them and the auxiliary waveguide is significantly smaller than for the edge modes, which also hinders efficient light transfer.

### 3.4.2 Auxiliary lattice

#### Mode transfer between lattices

The same kind of analysis can be performed for the case of two coupled SSH lattices, where all waveguides of the auxiliary lattice are modulated equally. In this case, there is a larger amount of supermodes present and we produce multiple crossings, see Figs. 3.12(b) and 3.12(d), since all modes of the auxiliary lattice are equivalently modulated. However, the dynamics is still restricted to the two modes between which we want to establish the transfer as long as the gap with other modes is not closed. This is indicated in both Figures by the region enclosed in dotted lines. We first show in Fig. 3.12(a) the light transfer between an SSH lattice with odd  $N$  coupled and an identical auxiliary lattice, but reflected with respect to the  $x$  axis so that their respective edge states have a significant overlap. With this setup, the edge mode of the auxiliary lattice gets fully transferred into the edge mode of the main lattice. In 3.12(c), we instead consider two lattices of even  $N$ . In that case, the symmetric combination of edge modes gets fully transferred between the two lattices. The modes in the auxiliary lattice could be prepared by using the method described in the previous section.

To relate these results to the ones for a single auxiliary waveguide, we plot the purity of the output mode in Figs. 3.13(a) and 3.13(b) and the fraction of transferred intensity in Figs. 3.13(c) and 3.13(d). A direct comparison shows that these results closely follow the corresponding ones in Fig. 3.10. This is specially true for the first case of odd  $N$ , where the edge mode is still mostly contained within the closest waveguide of the auxiliary lattice. As such, the overlap between the modes is similar to the one in the previous section. As for the symmetric combination of edge modes, the amplitude profile in the auxiliary lattice is entirely different from that of the single-waveguide case, resulting in a lower overlap with the mode of the main lattice. Hence, the outer coupling needs to be much stronger for the light intensity to be transferred completely. This can be readily observed by comparing Figs. 3.10(d) and 3.13(d). Nevertheless, we are still able to obtain purities and intensity fractions above  $P = 0.99$  and  $\tilde{I} = 0.99$ , respectively, despite the mode being delocalized throughout the whole lattice.

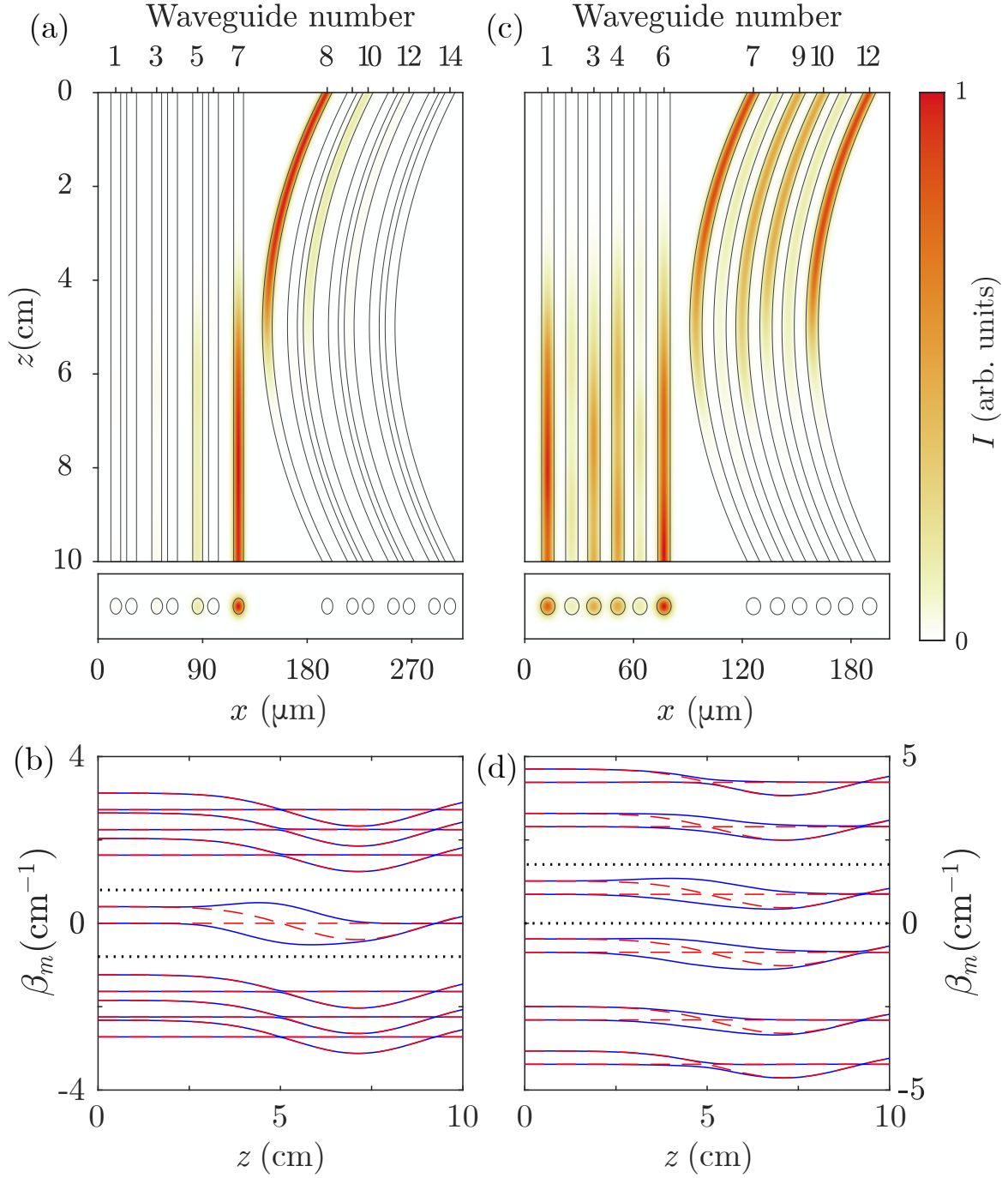


Figure 3.12: (a) Light intensity propagation and (b) spectrum of propagation constants along the propagation direction when exciting the single edge mode of the  $N = 7$  SSH lattice with the same mode of the auxiliary lattice as input. We use  $t(0) = 0.55 \text{ cm}^{-1}$  and  $Z_t = 2 \text{ cm}$ . (c)–(d) Same figures as in (a) and (b), respectively, for the symmetric combination of edge modes of the  $N = 6$  SSH lattice with  $t(0) = 1.3 \text{ cm}^{-1}$  and  $Z_t = 2.55 \text{ cm}$ . The rest of the parameter values are the same as in Fig. 3.9.

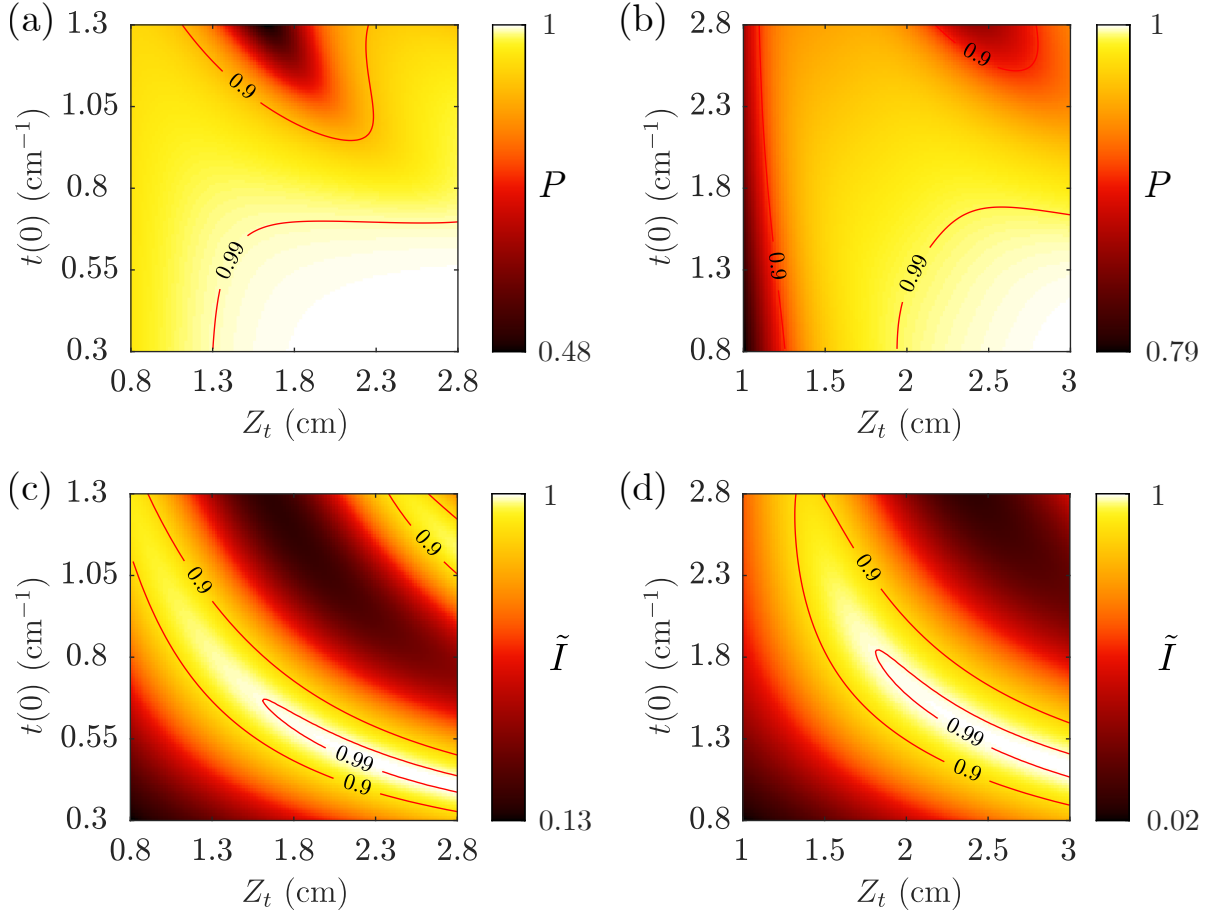


Figure 3.13: Purity of the output mode (top row) and intensity fraction of the transfer from the auxiliary lattice (bottom row) with respect to the width of the Gaussian coupling and its maximum strength for (a), (c) the edge mode of the  $N = 7$  lattice and (b), (d) the symmetric combination of edge modes of the  $N = 6$  lattice.

### Mode conversion

Another possible application of the proposed technique is enabling mode conversion between two lattices. Up until this point, when producing the modulation in the propagation constants we only considered crossings between the propagation constants of the same modes in the main and auxiliary lattices. Nevertheless, further shifting the spectrum of the auxiliary lattice can allow crossings for different modes, allowing for mode conversion. To prove this, we consider the transfer of light from an edge mode into the bulk mode displayed in Fig. 3.11(e), a process that we sketch in Fig. 3.14(a). All waveguides in the auxiliary lattice are further detuned by a quantity  $\Delta\beta = \beta_p - \beta_i$ , corresponding to the difference in propagation constant between the initial mode  $i$  and the target mode  $p$ , to cause crossings between their propagation constants during the modulation. Light propagation in this system is displayed in Fig. 3.14(b), where we see

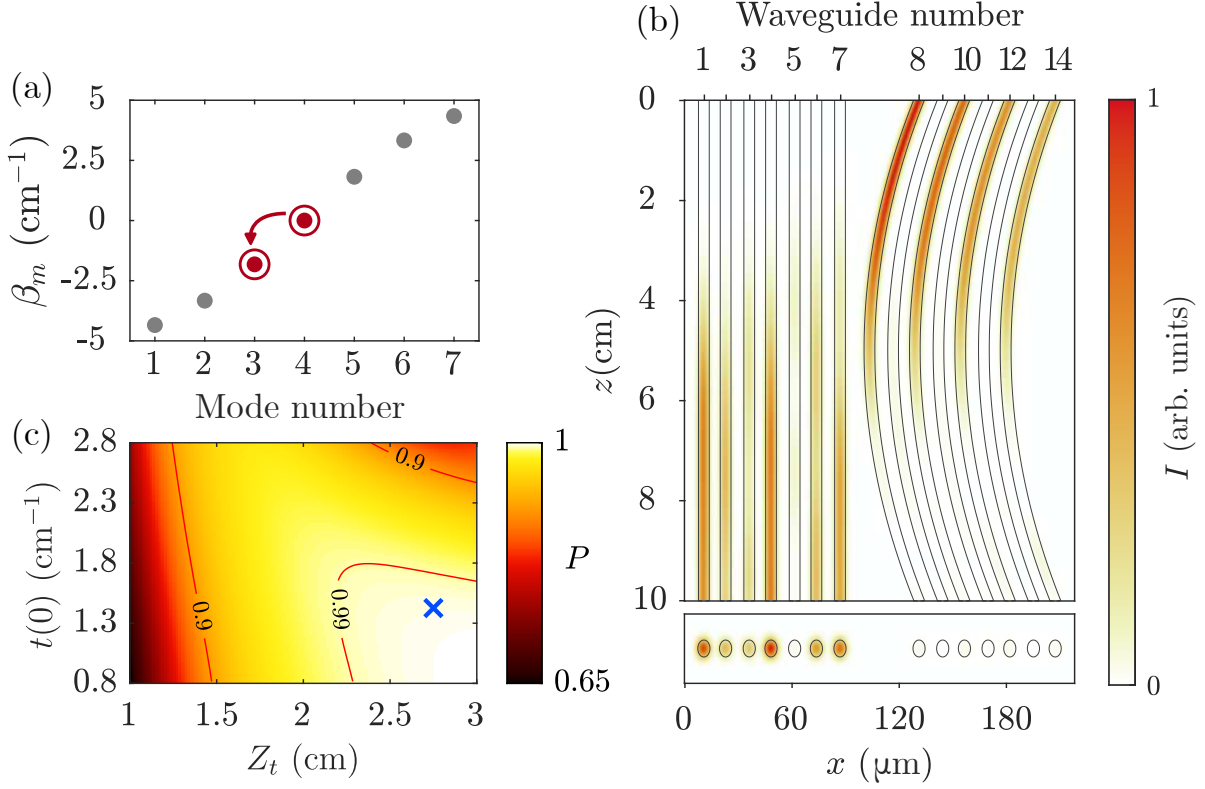


Figure 3.14: (a) Spectrum of propagation constants of the SSH model with  $N = 7$ , where the input and target modes of the mode conversion are highlighted in red. (b) Light intensity propagation in the system where the edge mode of the auxiliary lattice gets transferred into a bulk mode of the main lattice. (c) Purity of the output mode in this process. The blue cross indicates the set of parameter values chosen for (a) and (b), namely  $t(0) = 1.5 \text{ cm}^{-1}$  and  $Z_t = 2.7 \text{ cm}$ .

that a large fraction of light intensity, approximately 96% in this case, gets transferred into the target mode. Checking the purity of the final mode in Fig. 3.14(c), we can establish that for large regions of parameter values light gets transferred into the target mode only, proving a clean mode conversion between the lattices. Note that in this case, the input edge mode is strongly delocalized due to the choice of coupling parameters for the SSH lattice. Similar conversions could be established between all other modes of the lattice. Moreover, following the observed trend in the excitation of bulk modes in the previous section, we expect the intensity fractions to be reduced for modes with lower gaps, but the purity to still reach values near unity.



### 3.5 Conclusions

In this chapter, we have described how the implementation of SCRAP in systems of coupled optical waveguides can be exploited for multiple applications, both for individual multimode waveguides as well as for waveguide lattices. We now summarize the main obtained results for each of the proposed devices.

First, for the implementation in coupled multimode waveguides, we have shown how SCRAP can be used for mode division (de)multiplexing. The  $\text{TE}_0^{(1)}$  mode has a weaker coupling to the other waveguide than the excited mode, and light intensity on this mode remains mostly confined on the input waveguide, while light on the  $\text{TE}_1^{(1)}$  mode is efficiently transferred. One can take advantage of this effect to separate a superposition of these modes or, conversely, to obtain an equally-weighted superposition from individual excitations on each mode. We have introduced a figure of merit  $\mathcal{F}$  to determine the efficiency of the process, and have proved that the method easily exceeds  $\mathcal{F} = 0.9$ , but struggles to reach very high values. A way to enhance this efficiency is by combining the SCRAP scheme with SUSY transformations, which is done by substituting one of the coupled waveguides by its SUSY partner. Unlike the previous case, the  $\text{TE}_0^{(1)}$  mode in the step-index waveguide is no longer supported by the SUSY partner, which implies that light transfer to and from this mode cannot occur. In contrast, light in the  $\text{TE}_1^{(1)}$  mode can still be efficiently transferred into the SUSY fundamental mode by virtue of the SCRAP scheme. This allows for mode spatial separation with the figure of merit reaching  $\mathcal{F} = 0.99$ , and with overall higher values than without SUSY, at the cost of altering the spatial profile of the transferred mode. Additionally, this method enables the possibility of turning fundamental-mode excitations on both waveguides into a superposition of fundamental and excited modes of the step-index waveguide.

This very same device can also be used to produce the excited  $\text{TE}_1^{(1)}$  mode of a step-index waveguide, with very high precision, by using a fundamental-mode input on its SUSY partner. We have shown that the fidelity of this process can reach very high values, above  $F = 0.99$ , in a wide region of parameter values. Layering additional SUSY transformations allows to generalize this concept to excite the highest-order mode of any multimode waveguide, a fact that we prove by exciting the  $\text{TE}_2^{(1)}$  mode of a three-mode waveguide. The main technological difficulty of these applications is the implementation of the SUSY refractive index profile. This profile entails sharp transitions between negative and positive  $\Delta_n$ , which has only recently been implemented experimentally [318] in metamaterials. The implementation is based on discretizing the index profile along the transverse direction and relating it to the sizes of air gaps in a silicon metamaterial. For a larger air gap the field is less confined, which corresponds to a smaller effective index. The metamaterial is then fabricated via electron beam lithography and subsequent ion



etching. The inherent difficulty of fabrication can be lowered by using softer profiles for the initial waveguides, such as super-Gaussian profiles [379]. The corresponding superpartners have similar modal content, while displaying less steep transverse refractive index variations.

A second main branch of applications corresponds to those in discrete waveguide lattices. Namely, we have proposed an efficient and general technique to excite gapped modes of a general lattice of coupled optical waveguides, or to transfer modes between different waveguide lattices. This is achieved by tuning either an auxiliary waveguide or an entire auxiliary lattice to a particular eigenvalue of the main lattice, and modulating their propagation constants around it. We have first analyzed the performance of the technique by exciting the topological edge modes of an SSH lattice, and transferring topological modes between two SSH lattices, one being a detuned copy of the other. Aside from topological modes, we have shown that the technique can be used to transfer light into any mode that presents a gap, such as bulk modes for the cases of few waveguides. Finally, we have explored the transfer between different modes in detuned copies of the same lattice, which effectively corresponds to mode conversion. In this case, the efficiency mimics the performance that was established for the excitation of bulk modes. For lattices of waveguides, the maximum modulation in propagation constants is limited by the presence of other supermodes of the lattice, since crossings with the propagation constants of non-desired modes can cause leaking onto them and thus spoil the transfer. Despite this limitation, we have seen that we can perform efficient transfer in waveguides with parameter values within current experimental reach. Additionally, we have seen how the purity of the output modes in the main lattice compared with the target modes remains very large even when shifting away from the regions of highest intensity transfer, making the technique robust. Small variations in the geometrical parameters of the system, which may be caused by disorder or imperfections, mainly reduce the total light intensity at the output facet and do not cause transfer into unwanted modes. Throughout this part, however, we have considered that all waveguides in the system only sustain a single mode. For an experimental implementation, one should ensure that the auxiliary waveguide remains single mode for the entire modulation of the propagation constant. All in all, the proposed scheme is not limited to the cases displayed in this work, as its only requirement is that the target mode displays a gap in the spectrum. Consequently, the technique can be extended to other physical platforms or geometries that exhibit gapped topological modes, or other modes of interest.

---

## Exciting topological modes with single-waveguide injection via discrete Supersymmetry transformations

---

Making use of the isospectrality of Supersymmetry (SUSY) transformations, we propose a general and high-fidelity method to prepare gapped topological states in discrete systems from a single-site injection [214]. Through the usage of the discrete Supersymmetry (DSUSY) formalism [72], we generate a superpartner lattice to the topological chain of interest, which contains exactly the same modal content divided in two blocks: a decoupled site containing a single eigenstate, and a chain that contains the rest of the spectrum. The state that gets isolated can be chosen by the transformation, a fact that we exploit by targeting the topological state. The method to excite it then consists of adiabatically connecting the two structures along the propagation direction of the device which, as explained in Sec. 2.1.6, is analogous to time evolution in other physical platforms. The initial lattice corresponds to the superpartner chain, while the output coincides with the original one. In doing so, a single-site excitation on the isolated site is adiabatically deformed into the topological state at the output facet. Hence, from the simplest possible input, we generate the complete structure of amplitudes and phases of an eigenstate of the structure. The method is demonstrated by exciting topological states of the Su-Schrieffer-Heeger (SSH) model [95] in different configurations on an optical waveguide array, where the adiabatic deformation is performed along the propagation direction.

The chapter is organized as follows. In Section 4.1, we motivate the importance of developing a method to faithfully prepare topological modes in lattices of optical waveguides. In Section 4.2, we briefly recall the necessary theoretical elements: the SSH

model and the QR factorization method, introduced in Secs. 2.3.2 and 2.2.3, respectively. After that, we describe the physical system and the excitation method in Section 4.3. Then, we present our main results in Section 4.4, focusing on the excitation of various types of modes, namely edge, interface and bulk modes. We end the chapter by laying our conclusions in Section 4.5.

## 4.1 Introduction

Due to their general robustness against defects and disorder, topological states have gathered widespread attention in several fields [92, 139, 142, 380, 381]. For optical devices, harnessing the unique properties of these states could lead to a variety of applications, such as unidirectional propagation, lossless information transfer and general immunity to imperfections during fabrication [143]. Hence, in order to fully exploit the advantages that these topological states provide, it is of great experimental interest to devise a method to excite them efficiently. To this end, in this chapter we introduce the idea of adiabatically modifying the geometry and parameters of a discrete system, so that input and output profiles are supersymmetric partners of each other [214]. The framework of Supersymmetry (SUSY) [70–72], has been exploited in optics in recent years, finding applications in modal control [76, 77, 82, 300–303] and Mode-Division Multiplexing [212, 306, 307], control of the scattering properties of a system [79–81, 299, 308] and its topology [78], among others. One can employ discrete SUSY transformations to obtain a superpartner lattice in which the chosen state is confined in an isolated waveguide. Performing an injection on this waveguide, and then a subsequent adiabatic deformation into the original lattice, leads to a faithful excitation of the desired state with minimal leaking to any others. This method can in principle be used to prepare any state of a one-dimensional system, including topological modes, from a single-site excitation, a feat that would otherwise imply simultaneous excitation of multiple sites with the right amplitudes and relative phases.

Indeed, selective excitation of modes in waveguide lattices requires very precise input conditions. Techniques based on the usage of spatial light modulators (SLMs) allow to shape the input beam so as to achieve a high overlap with specific modes in the lattice [102, 106, 355–357]. However, the precision of SLMs may not be able to keep up as one makes the devices smaller. Our proposal attempts to go in a different direction by keeping the complexity of the input beam to the bare minimum and letting the photonic device take care of the excitation. Compared to the method described in Chapter 3 for discrete waveguide lattices, in here the propagation constants do not need to be modulated to perform the excitation when targeting zero-energy modes. After our work, an experimental implementation of our theoretical proposal was performed in Ref. [382]. On a similar note, a different experimental proposal was made in the

direction of simplifying the input, where an appropriately designed waveguide is made to radiate into the lattice with the necessary quasimomentum to excite a specific state [383].

The method described in this chapter is completely general and does not depend on a particular kind of structure. However, to demonstrate its performance we choose to focus on the geometry of the SSH model [95]. The SSH chain can host topological edge states, and modified chains with a central defect can also host a topological interface state confined around it. The topological states of the SSH chain have already found applications mainly in contexts like quantum state transfer [336, 364, 365, 368] and lasing [244, 366, 367].

## 4.2 Theoretical background

As detailed in Sec. 2.2.3, DSUSY transformations [72] can be built between two discrete superpartner Hamiltonians  $\mathcal{H}^{(1)}$  and  $\mathcal{H}^{(2)}$ . Applying these transformations to a discrete system, in general, leads to another system that has a modified geometry – and thus a different coupling structure – but shares the same spectrum of energies as the former. When the symmetry is unbroken, the superpartner  $\mathcal{H}^{(2)}$  displays an isolated site within which the mode with eigenvalue  $\mu_m$  targeted by the transformation is confined. To obtain the superpartner structure, we employ the QR factorization method [326], which allows to express the Hamiltonian  $\mathcal{H}^{(1)}$  in terms of an orthogonal matrix  $Q$  and an upper triangular matrix  $R$ . Then, inverting the relation leads to the superpartner Hamiltonian:

$$\mathcal{H}_m^{(1)} - \mu_m^{(1)} I = QR \quad \text{and} \quad \mathcal{H}_m^{(2)} - \mu_m^{(1)} I = RQ, \quad (4.1)$$

where  $I$  is the identity matrix. To perform this factorization, we use the Householder transformation method [326], which is based on applying successive reflections on the column vectors of a matrix to obtain the triangular shape of  $R$ .

To test the excitation method, we focus on the SSH model [95], see Sec. 2.3.2, which is characterized by two one-dimensional (1D) sublattices with staggered weak and strong couplings, labelled here as  $t_w$  and  $t_s$  respectively. We display this geometry and the coupling distribution in the left panels of Figs. 4.1(a) and (b), where the larger (smaller) the distance between sites, the weaker (stronger) the coupling strength between them. The SSH chain can host topological edge states in one or both of its ends, depending on whether it has an odd or even number of sites, if the outermost coupling is the weak one. The chiral symmetry of the SSH model ensures that the edge states only have nonzero projections in one of the sublattices [101], although for finite chains with two edge states some degree of hybridization occurs between them. Although an SSH chain cannot host a topological interface state, a way to make it appear naturally is to include

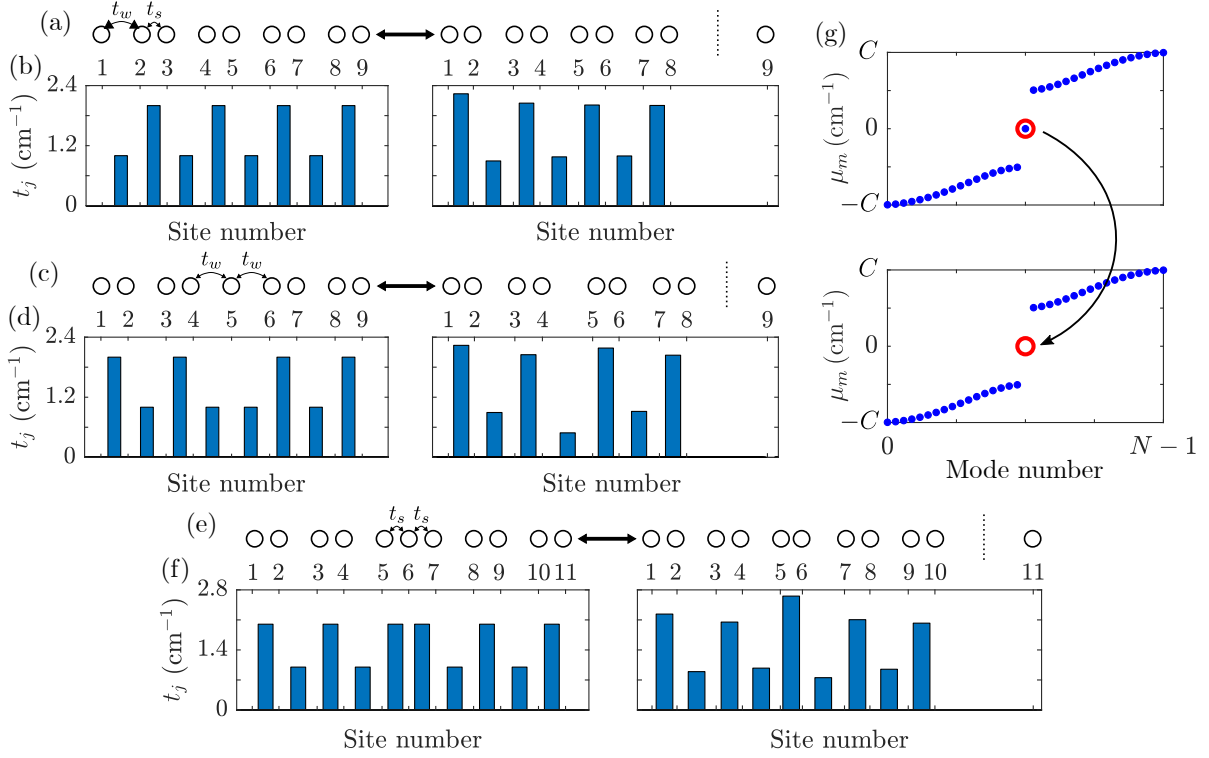


Figure 4.1: (a), (c), (e) Sketches of the configurations of SSH chains (left) and their superpartners (right). The strength of the coupling is represented by the closeness of the sites. The SSH chains can host (a) an edge state localized in the left edge or (c), (e) an interface state localized around the dimer defect. The supersymmetric partner of these modes is localized in the isolated site on the rightmost part in each case. (b), (d), (f) Structure of the coupling strengths for the chains in (a), (c) and (e), respectively. (g) Spectrum of energies of the SSH chain hosting a single edge state (top) and of the superpartner structure, barring the isolated site, where the eigenvalue is missing (bottom).

a dimer defect in a specific position of the chain [165, 334–336]. This kind of defect can be implemented by repeating one of the couplings at a certain position of the staggered configuration, see the left panels of Figs. 4.1(c) and (d), as well as Figs. 4.1(e) and (f). These dimer defects are equivalent to connecting two chains with different topological order. The interface state is thus closely confined around the boundary between the different domains.

We now apply the DSUSY formalism to the SSH Hamiltonian for the case with an edge state, an interface state of a weak dimer defect, and an interface of a strong dimer defect. The superpartner structures in each case are shown in the right side of Figs. 4.1(a), 4.1(c) and 4.1(e), respectively. The effect of this transformation on the

spectrum is displayed in Fig. 4.1(g), where we showcase the removal of the edge state eigenvalue that is contained in the isolated site of the superpartner.

## 4.3 Physical system

The proposed device is based on arrays of  $N$  coupled optical waveguides. As discussed in Sec. 2.1.3, when waveguides are in close proximity to each other, they are coupled due to the overlap of their evanescent fields. If this coupling is not strong enough to affect the mode profiles in each of the waveguides, one can describe arrays of single-mode waveguides using the coupled-mode formalism [256]. In this scenario, light propagation is determined by Eq. (2.71) and described via a tridiagonal Hamiltonian  $\mathcal{H}$  featuring the propagation constants  $\beta_j$  in each waveguide (diagonal) and the couplings  $t_{j,j\pm 1}$  between them (off-diagonal). As explained in Sec. 2.2.3, the superpartner lattice has supermodes that are phase-matched to the originals and have the same eigenvalues, but where the mode corresponding to the removed eigenvalue is localized in an isolated waveguide. By exciting this localized mode at the input, and adiabatically deforming the SUSY lattice into the SSH one, we can obtain the mode that was targeted by the transformation with high fidelity, starting from a single-waveguide excitation. The adiabatic connection between the SUSY and SSH structures can be performed in multiple ways, as many different paths can be followed in the hyperspace of parameters. We choose to follow paths in which every parameter evolves with the same type of transformation function,  $g(z)$ :

$$\mathbf{t}(z) = \mathbf{t}_{\text{SUSY}} + g(z) (\mathbf{t}_{\text{SSH}} - \mathbf{t}_{\text{SUSY}}), \quad (4.2)$$

where  $\mathbf{t}_i = (t_{i,1}, \dots, t_{i,N})$  with  $i = \text{SSH}, \text{SUSY}$  are the couplings in the input and output structures, respectively. For each case in question, one could engineer the transformation function that optimizes the adiabatic excitation. However, a single function will not optimize the method for all parameters. Since the method itself does not depend on the particular path along coupling space, we choose to use a simple linear function in  $z$  for all cases in this work. Despite that, one should keep in mind that results can be further improved by performing this optimization process.

Recall that the coupling between waveguides is proportional to the overlap of their modes, which depends exponentially on the distance  $d$  between them,  $t(d) = t_0 \exp(-\kappa d)$ . Thus, a linear transformation in the couplings implies the following dependence for the distance between waveguides  $j$  and  $j+1$ :

$$d_j(\tilde{z}) = \frac{1}{\kappa} \log \left( \frac{t_0}{(1 - \tilde{z}) t_{\text{SUSY},j} + \tilde{z} t_{\text{SSH},j}} \right), \quad (4.3)$$

where  $\tilde{z} = z/L$  is the coordinate along the propagation direction scaled to the length of the device,  $L$ . To compute the distances we have considered state-of-the-art experimen-

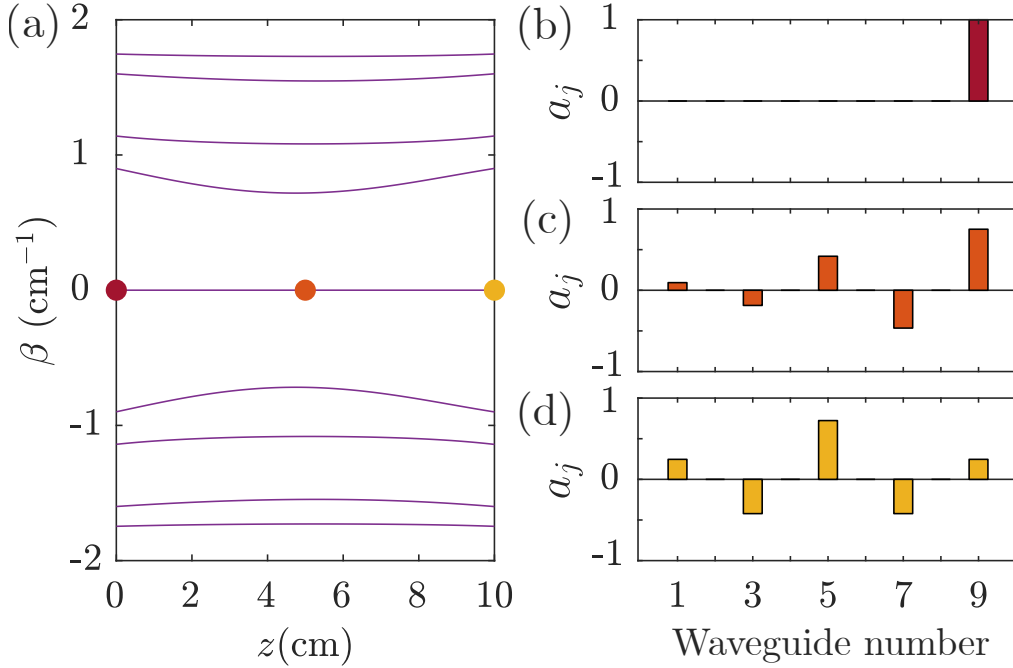


Figure 4.2: (a) Spectrum of propagation constants along the propagation direction of the device displayed in Fig. 4.3(b). (b)–(d) Amplitude profile of the target mode at (b)  $z = 0$ , (c)  $z = L/2$ , (d)  $z = L$ . The positions and propagation constants corresponding to plots (b), (c) and (d) are marked in (a) using dots with the same colors.

tal parameters for a wavelength of  $\lambda = 633$  nm for laser-written waveguides [42, 78, 220]. Then, if the distances are tuned according to (4.3) along  $z$ , the mode adiabatically follows the instantaneous eigenstate during propagation, continuously morphing into the final mode. An example of this is shown in Fig. 4.2(a), where the variation of the spectrum when exciting one of the interface states is shown. In Figs. 4.2(b)–(d), the amplitudes in the different waveguides at the input, central point and output are shown. The method relies on the adiabaticity of the transformation, implying that the following condition when following the state  $\psi_m$  has to be fulfilled:

$$|\langle \psi_p | \partial_z \psi_m \rangle| \ll |\beta_m - \beta_p| \quad (4.4)$$

for all  $p$ , that is, the coupling between the instantaneous eigenstates  $\psi_p$  and  $\psi_m$  has to be small compared to the difference between their eigenvalues,  $\beta_m - \beta_p$ . In other words, to keep nonadiabatic effects to a minimum, the length of the device has to be large enough for the coupling between eigenstates to be much smaller than the minimum eigenvalue gap. In experimental setups, the minimum length of the device will depend on how closely one can fabricate the waveguides without deviating from the tight-binding approximation or without causing distortions due to e.g. optical stress fields [268, 269].

As mentioned above, we note that DSUSY transformations targeting zero-energy

modes do not alter the propagation constants of the waveguides in the superpartner lattice. Hence, when attempting to excite edge or interface modes in the SSH model, the diagonal elements of the Hamiltonian will be zero at both input and output facets. This simplifies the devices, since only the coupling strengths need to be adiabatically modified along  $z$ , and it is sufficient to ensure that all waveguides have equal propagation constants. In contrast, in Sec. 4.4.3 we target a bulk mode of the SSH model, for which the variation of propagation constants plays a role. In that case, for simplicity, we also choose to employ a linear transformation function  $g(z)$  for the propagation constants of each individual waveguide.

## 4.4 Results

We now analyze the proposed photonic devices for the excitation of the different states. For the topological states, we connect the configurations displayed in the left and right panels of Fig. 4.1(a), 4.1(c) and 4.1(e), respectively, by adiabatically deforming one waveguide lattice into the other along the propagation direction. For the bulk state, we obtain the partner of the left panel in Fig. 4.1(a) by using the corresponding eigenvalue  $\mu_m^{(1)}$  in the transformation. In each of the cases, the input configuration is the SUSY partner and the output configuration is the corresponding SSH chain. In all of them, we excite the isolated waveguide of the input configuration, and we obtain the corresponding mode in the output chain. Throughout the rest of the chapter, we refer to these devices as adiabatic SUSY (aSUSY) devices. To characterize their efficiency, we define the fidelity:

$$F = |\langle \psi_p | \psi(z_f) \rangle|^2, \quad (4.5)$$

where  $\psi_p$  is the SSH state we aim to produce and  $\psi(z_f)$  is the output state obtained from the numerical simulations.

### 4.4.1 Edge state

We first focus on the excitation of the left edge state of the SSH lattice corresponding to the left panel of Fig. 4.1(a), with distances between waveguides being determined by Eq. (4.3). We display in Fig. 4.3(a) the propagation of the excitation along the device, and the intensity of the mode at the output facet. The obtained mode clearly resembles the edge state, being localized around the leftmost waveguide and having non-zero amplitude only in one of the sublattices of the chain. We note that light has to cross the entire lattice to reach the other edge in this setup, which is a conscious choice to demonstrate the power of the technique. If the edge mode was placed in the same side as the isolated waveguide, the excitation would be much easier comparatively, and could then be achieved with much shorter devices [382].



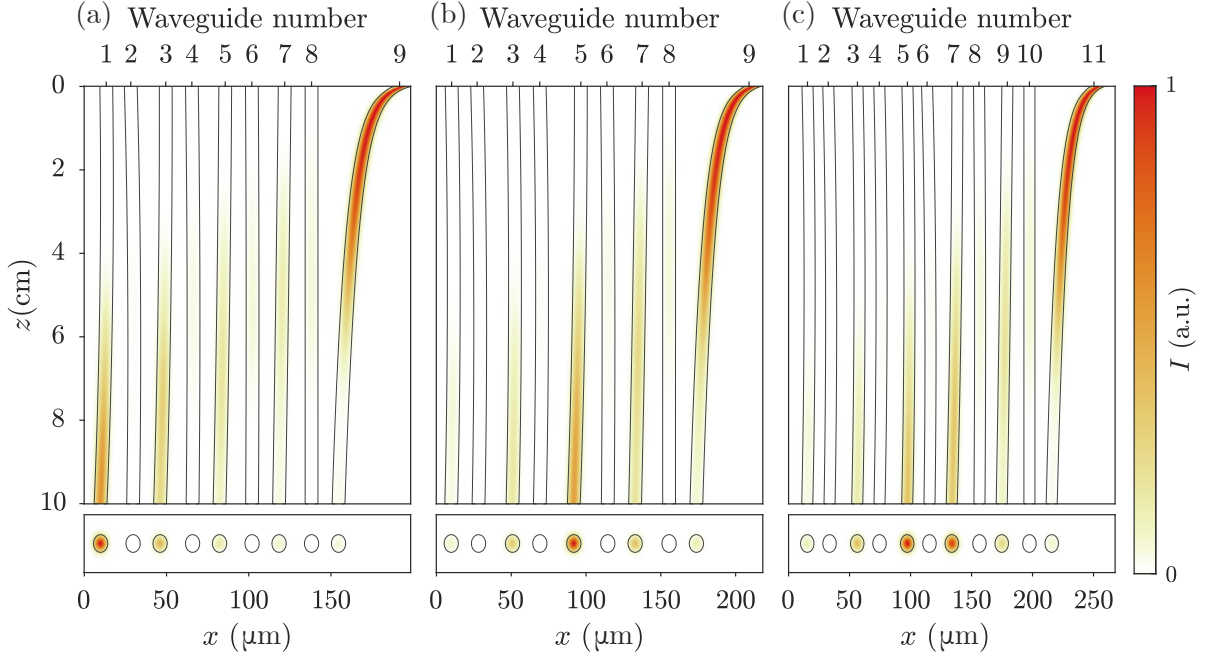


Figure 4.3: Numerical simulation of the light intensity propagation (top) and final intensity pattern (bottom) in the excitation of (a) the left edge state, (b) the interface state of the weak defect and (c) of the strong defect. Light is injected into the rightmost waveguide, waveguide 9 in (a) and (b), and waveguide 11 in (c) of the SUSY structures.

Let us now characterize how efficiently we obtain the edge state in the aSUSY device. In Fig. 4.4 we scan the two-dimensional (2D) space of couplings, maintaining  $t_s > t_w$  so that we do not change the topological order of the chain, and we plot the fidelity for a device of length  $L = 10$  cm. We observe that as long as  $t_w \gtrsim 0.8 \text{ cm}^{-1}$ , the fidelities we obtain are remarkably good, with values surpassing  $F = 0.9$  for most parameters values and with a wide region where  $F > 0.99$ . In contrast, if  $t_w$  is smaller than that value, the injected mode requires longer devices to be efficiently transformed into the edge state at the other end of the chain. Energy-wise, this decrease in efficiency is due to a reduction of the energy gap, which implies that slower deformations are required to maintain the adiabaticity of the transformation, as the appearance of nonadiabatic couplings implies the loss of power to other modes. The fidelity of the aSUSY device should be compared with the standard injection of light at the outermost waveguide – position at which the edge state has the largest amplitude – of an SSH lattice with parallel waveguides of the same length as the aSUSY device. We refer to the device with this input as the *straight waveguides* (SW) device. For this case, the input will in general have a large projection over the edge state, but will also excite other nonlocalized modes. This projection will be larger on edge modes that are strongly confined, which occurs for large dimerizations in the couplings.

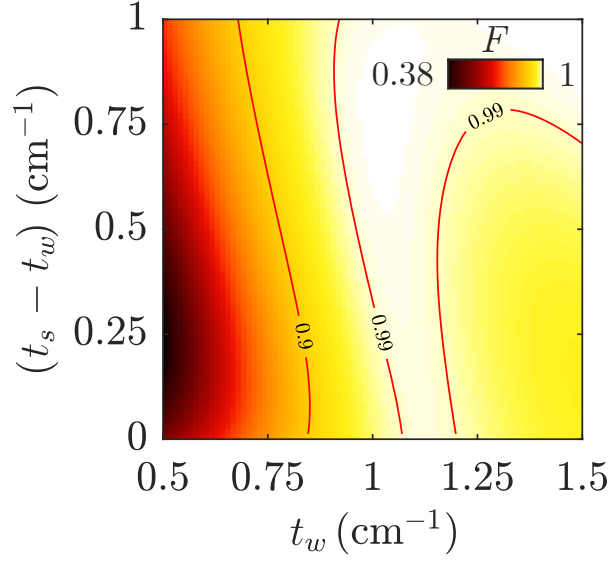


Figure 4.4: Fidelity of the excitation of the left edge state, for an aSUSY device of length  $L = 10$  cm and different values of the SSH couplings. We maintain  $t_s > t_w$  for all considered values, and indicate the regions where the fidelity exceeds  $F = 0.9$  and  $F = 0.99$  with solid red lines.

In Fig. 4.5(a) we plot  $\Delta F = F - F_s$ , where  $F$  is the fidelity of the aSUSY device and  $F_s$  is that of the SW device. The improvement of the former with respect to the latter then depends on the ratio between couplings, which determines the confinement of the edge mode. When the ratio  $t_s/t_w$  is close to one, as long as  $t_w \gtrsim 0.8 \text{ cm}^{-1}$ , our technique allows us to reach the edge state almost perfectly, whereas the SW output has only a small projection over it and thus reaches low values for the fidelity. In Fig. 4.5(b) we show the comparison between the intensity profiles of the real edge state and both the state generated by the adiabatic deformation of the structure and the state achieved by letting the input propagate through the SW device. From this comparison, we see that the adiabatic modification of the lattice allows to correctly capture the decaying amplitude of the mode. If we extend the device while maintaining the final geometry, the intensity pattern of the mode that we obtain with the aSUSY device remains mostly unaltered after a certain propagation distance, while the input in the SW device disperses due to the excitation of nonlocalized modes. The high values for the fidelity also indicate that the phase structure of the mode is correctly reproduced by the aSUSY device.

We can now ask questions regarding the size of the devices, both how small in length and how big in number of waveguides can we make them whilst keeping a high fidelity, or at least an advantage over the SW device. The answers of course depend on the choice of parameters of the system and the mode we are trying to excite. We show in Fig. 4.5(c) the increase in fidelity as we increase the length of the aSUSY device

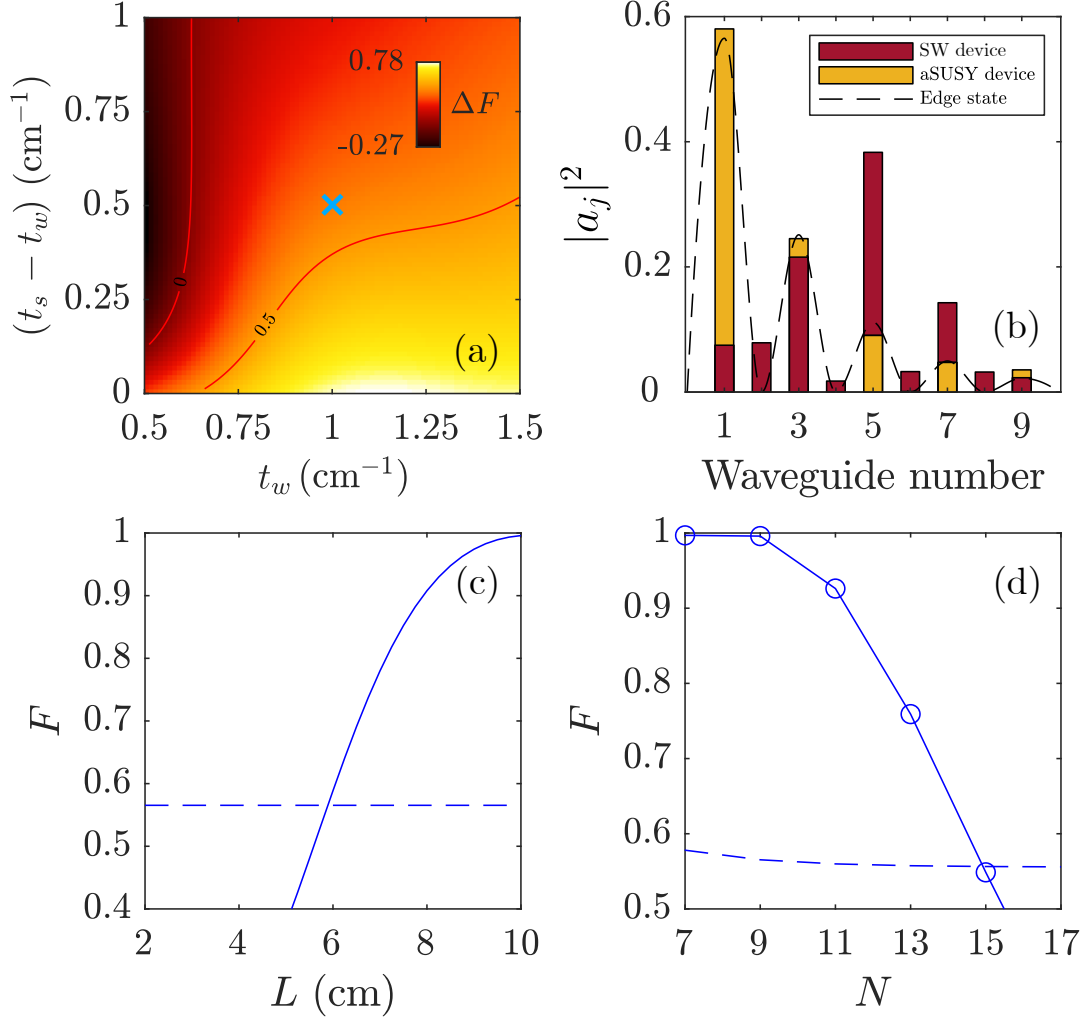


Figure 4.5: (a) Difference in fidelity  $\Delta F = F - F_s$  between the aSUSY device of length  $L = 10$  cm and the SW device. (b) Comparison between the profile of the state generated using the aSUSY device in yellow and the SW device in red for  $L = 10$  cm. The profile of the actual edge state is depicted with a dashed line. (c) Fidelity of the aSUSY (solid) and of the SW (dashed) devices of  $N = 9$  for increasing device length. (d) Fidelity of the aSUSY (circles) and of the SW (dashed line) devices of length  $L = 10$  cm for increasing number of waveguides. The value of the couplings for (b), (c) and (d) corresponds to the light blue cross in (a),  $t_w = 1 \text{ cm}^{-1}$  and  $t_s = 1.5 \text{ cm}^{-1}$ .

(solid line). Comparing it with the SW device (dashed line), we see that the adiabatic modification starts being more efficient after the device length reaches a few centimeters for our choice in parameter values, around  $L = 6$  cm. On the other hand, we see in Fig. 4.5(d) that the device has higher fidelities for lower number of waveguides, due to the energy gap getting smaller as  $N$  increases. Comparing with the SW device, for  $L = 10$  cm our method to obtain the edge state stops being efficient at around  $N = 15$  for this set of couplings. Logically, the device would need larger couplings or longer distances for light intensity to traverse more waveguides. This effect would be greatly reduced when attempting to excite the opposite edge, as we mentioned at the beginning of the section.

#### 4.4.2 Interface state

We now focus on the interface states generated by dimer defects in otherwise topologically trivial SSH chains [left panels of Figs. 4.1(c) and 4.1(e)]. The excitation again starts from a single-waveguide excitation of the isolated waveguide of their SUSY partners. The propagation of these excitations through the devices and the respective output states are shown in Figs. 4.3(b) and 4.3(c). In the first case, where the defect is spawned by the weak coupling, we see that the interface state is mostly confined within the central waveguide [waveguide 5 in Fig. 4.3(b)]. Conversely, the maximum of light intensity splits into two waveguides [waveguides 5 and 7 in Fig. 4.3(c)] when the defect is formed by repeating the strong coupling.

The efficiencies when exciting these two states are notably solid, as can be observed from Figs. 4.6(a) and 4.6(b), respectively. In both figures, the fidelity surpasses  $F = 0.99$  in most of the parameter space that we consider. Even though both results are fairly similar, some differences can be spotted in the map of fidelities. The overall values are slightly smaller in Fig. 4.6(b), and the patterns are displaced. These differences are mainly due to the different total number of waveguides considered for each case. Each device needs to have a different number of waveguides if we want to maintain the topological order of the rest of the SSH chain when adding the two different defects at the center.

As before, we compare these results with the respective SW devices. For the excitation of the interface state formed by the weak coupling defect displayed in Fig. 4.3(b), the input of the SW device will consist in the injection of light in waveguide 5 of the chain of straight waveguides. We display the difference in fidelity between the devices in Fig. 4.7(a), where we see that the biggest improvement achieved by the aSUSY device is obtained in regions where the dimerization  $|t_s - t_w|$  is small, especially around  $|t_s - t_w| \leq 0.5 \text{ cm}^{-1}$ . In a similar way as for the case of the edge state, the adiabatic procedure remains efficient even if the interface state is not strongly confined, while the

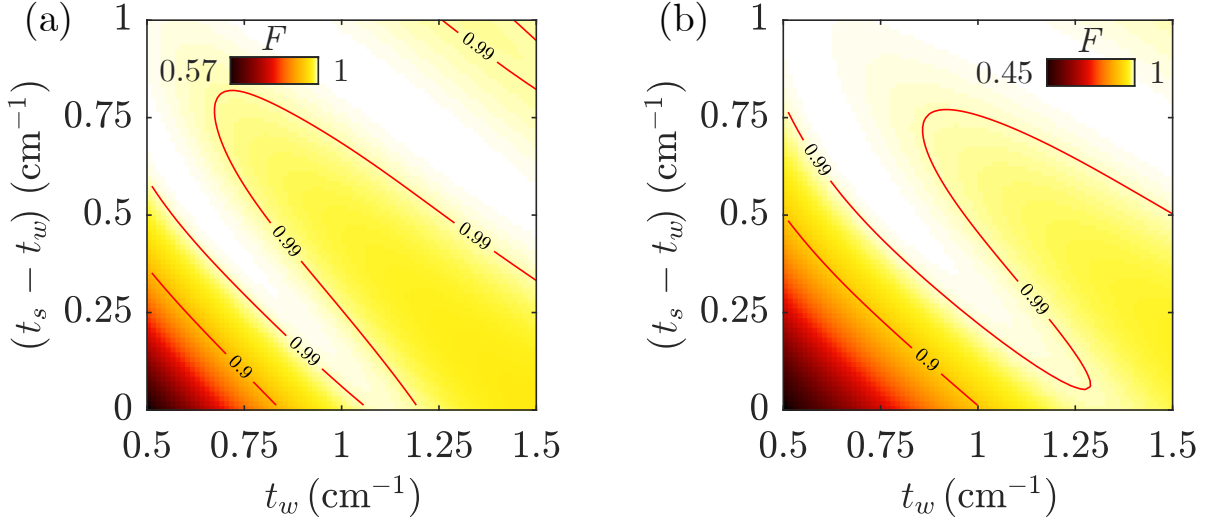


Figure 4.6: Fidelity of the excitation of the interface state in the defect formed by repeating (a) the weak coupling and (b) the strong coupling for an aSUSY device of length  $L = 10$  cm. We maintain  $t_s > t_w$  for all considered values, and indicate the regions where the fidelity exceeds  $F = 0.9$  and  $F = 0.99$  with solid red lines.

SW device fails to precisely reproduce the state. The comparison between the intensity patterns of the output state of both devices with the actual interface state is shown in Fig. 4.7(b). As for the case in Fig. 4.3(c), corresponding to the defect formed by the strong coupling, there is no simple way to obtain a state that is similar to the interface state in the SW device. Its maximum of intensity is split into two waveguides, and there is a phase difference between them. The output of the aSUSY device correctly captures these properties, while a SW device with a single-waveguide excitation simply cannot. To make a fair comparison, we assume that we can perfectly produce the split amplitudes with the right phases beforehand, with e.g. a beam splitter and a retardation plate, and that we use it as the input of the SW device. This corresponds to the excitation of waveguides 5 and 7 in the device. We make the comparison of fidelities and of intensity profiles with this device in Figs. 4.8(a) and 4.8(b), respectively. In those, we readily see that the results are similar to the ones for the previous interface state, which is remarkable considering the increased complexity of the input in the SW device.

Finally, we compare the fidelity of the aSUSY and SW devices for increasing device length and number of waveguides for each case. For the first interface state, as shown in Figs. 4.7(c) and 4.7(d), the device starts being efficient when its length is close to  $L = 5$  cm, and maintains higher efficiencies for  $L = 10$  cm until the number of waveguides reaches  $N = 21$ . The results for the second interface state plotted in Figs. 4.8(c) and 4.8(d) are similar. In this case, the aSUSY device outperforms the SW device shortly after reaching  $L = 6$  cm, and keeps being superior for any number of waveguides below

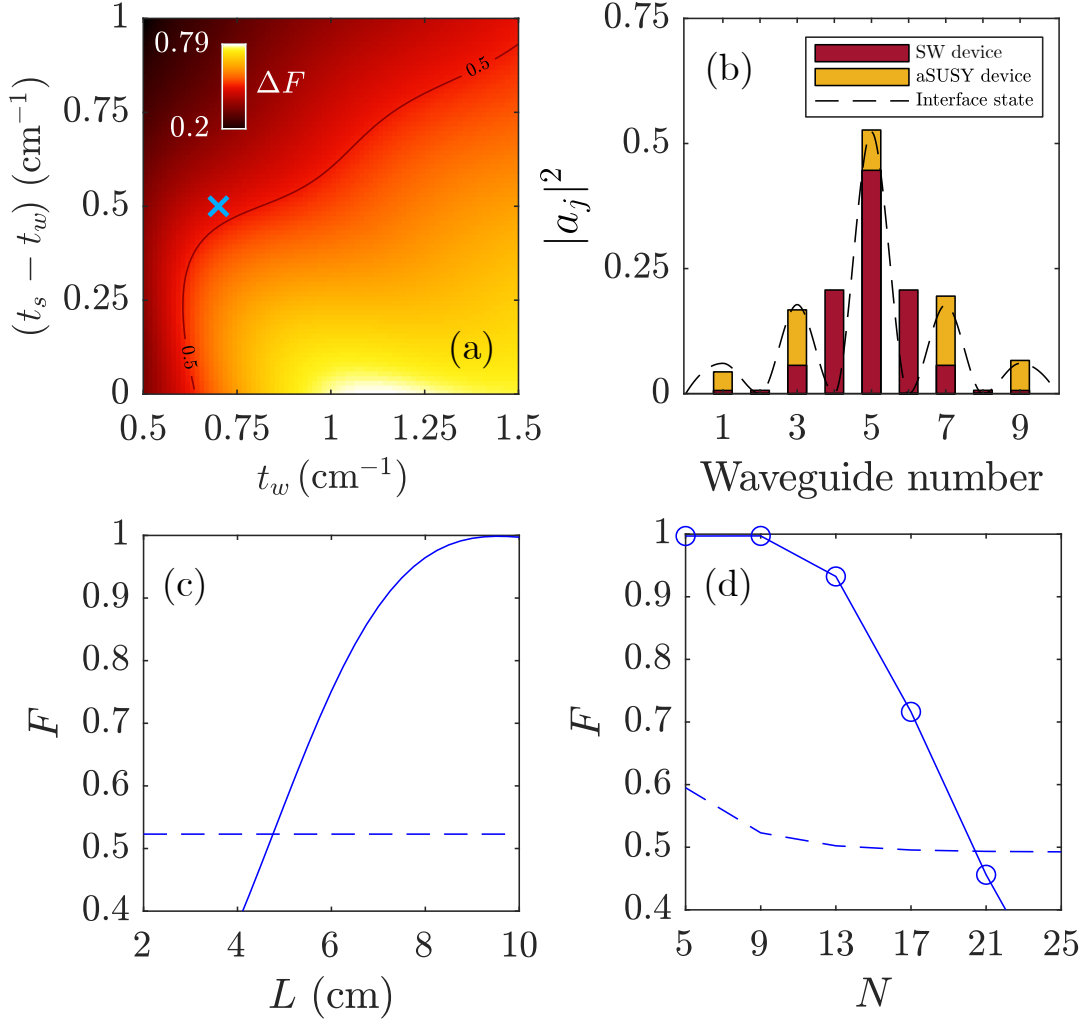


Figure 4.7: (a) Difference in fidelity  $\Delta F = F - F_s$  between the aSUSY device of length  $L = 10$  cm and the SW device when exciting the interface state corresponding to the weak coupling defect. (b) Comparison between the profile of the state generated by the aSUSY device in yellow and the SW device in red for  $L = 10$  cm. The profile of the actual interface state is depicted with a dashed line. (c) Fidelity of the aSUSY (solid) and of the SW (dashed) devices of  $N = 9$  for increasing device length. (d) Fidelity of the aSUSY (circles) and of the SW (dashed line) devices of length  $L = 10$  cm for increasing number of waveguides. The value of the couplings for (b), (c) and (d) corresponds to the light blue cross in (a),  $t_w = 0.7 \text{ cm}^{-1}$  and  $t_s = 1.2 \text{ cm}^{-1}$ .

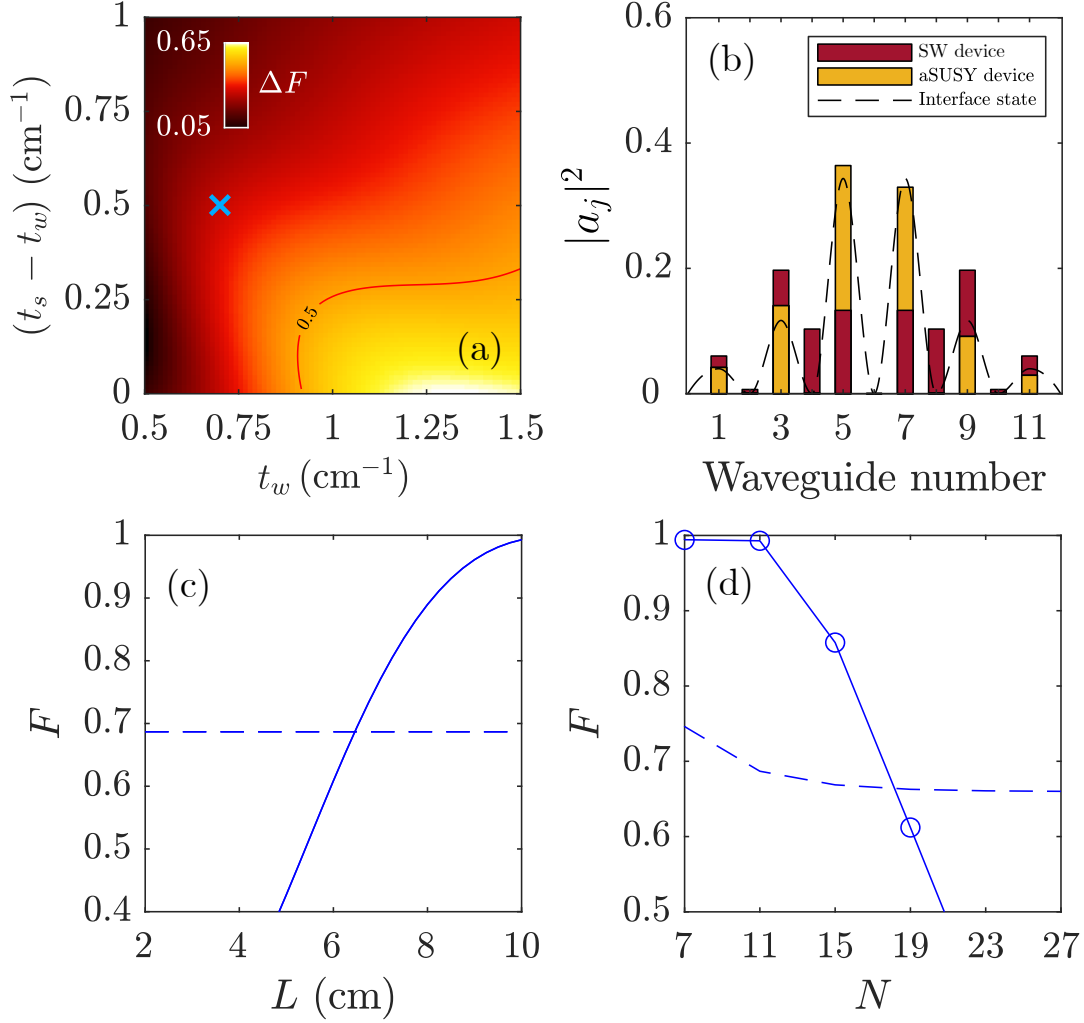


Figure 4.8: (a) Difference in fidelity  $\Delta F = F - F_s$  between the aSUSY device of length  $L = 10$  cm and the SW device when exciting the interface state generated by the strong coupling defect. (b) Comparison between the profile of the state generated by the aSUSY device in yellow and the SW device in red for  $L = 10$  cm. The profile of the actual interface state is depicted with a dashed line. (c) Fidelity of the aSUSY (solid) and of the SW (dashed) devices of  $N = 11$  for increasing device length. (d) Fidelity of the aSUSY (circles) and of the SW (dashed line) devices of length  $L = 10$  cm for increasing number of waveguides. The value of the couplings for (b), (c) and (d) corresponds to the light blue cross in (a),  $t_w = 0.7 \text{ cm}^{-1}$  and  $t_s = 1.2 \text{ cm}^{-1}$ .

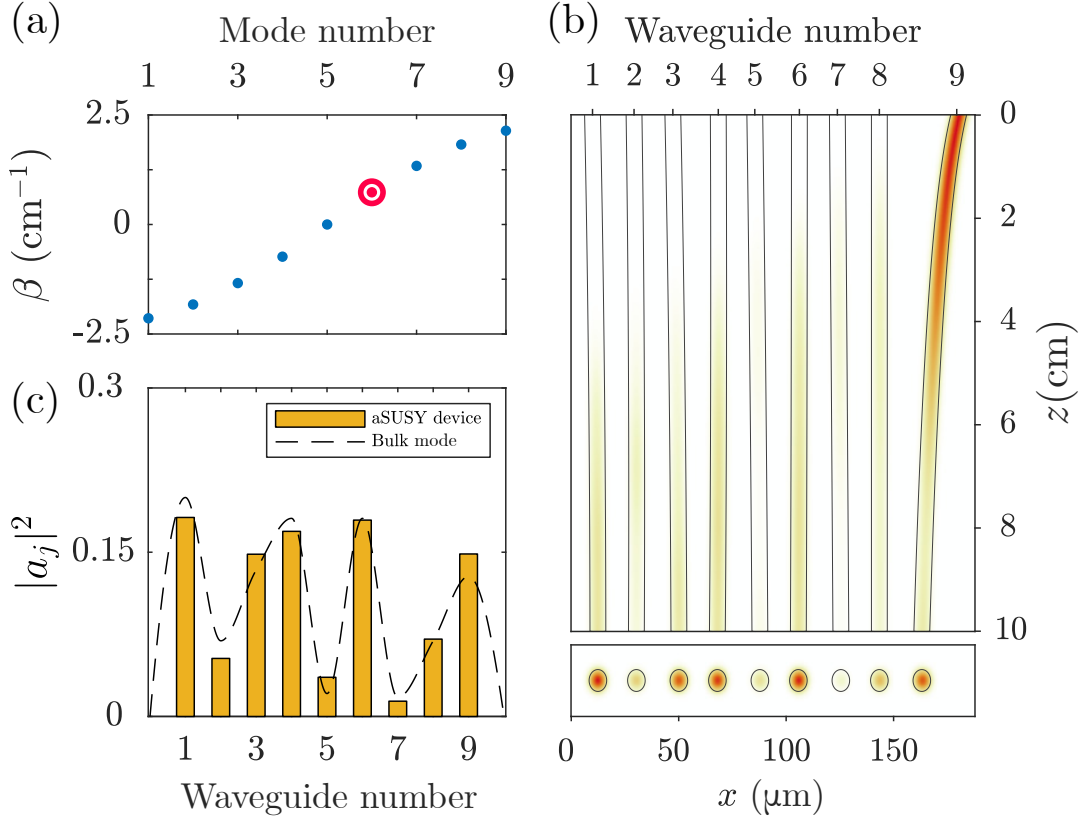


Figure 4.9: (a) Spectrum of propagation constants of the SSH model with one edge mode. The bulk mode under consideration is highlighted in red. (b) Intensity propagation for the excitation of the considered bulk state in the SSH model. (c) Output profile (yellow blocks) and target mode (dashed line) for the device in (b). The values for the couplings for (a), (b) and (c) are  $t_w = 1 \text{ cm}^{-1}$  and  $t_s = 1.5 \text{ cm}^{-1}$ .

$N = 29$  for the same set of couplings as in the previous case. Comparing both of them with the results for the edge state displayed in Fig. 4.5 in the previous section, we see a sizable improvement in this case, as the aSUSY devices excite the desired modes efficiently in shorter lengths and with larger  $N$ .

#### 4.4.3 Quasi-degenerate and bulk states

We emphasize that the presented method can be used to excite any mode of the original lattice, not only localized topological modes. As an example, we can consider the bulk modes of the SSH model. We see in Fig. 4.1(g) that the gap between bulk modes is smaller than the gap between edge and bulk. As one increases the size of the system, the dispersive bands get populated by new bulk states, rendering this gap even weaker. In essence, this means that generally longer devices are needed to achieve



efficient excitations for bulk states. Nonetheless, if we limit the application for low number of waveguides, bulk modes can be reached within the lengths considered in this chapter. Let us consider a SSH chain of  $N = 9$ , whose spectra is shown in Fig. 4.9(a), and attempt to excite the bulk mode that is highlighted in red. We show in Fig. 4.9(b) the light intensity propagation through the device. From there, it is clear that the output mode is completely delocalized. In Fig. 4.9(c) we compare the squared amplitudes of the output mode with the target bulk mode, and see that they are remarkably similar. For the parameters used in the simulation, we compute the fidelity to be  $F = 0.992$ . The downside to exciting bulk modes is that the input structure no longer displays zero detunings. As such, control over the propagation constants of the individual waveguides along the propagation direction is required. This can be achieved in laser-writing setups by controlling the relative speed of the writing laser and the laser [257].

For degenerate or quasi-degenerate states, there is no way to guarantee the absence of nonadiabatic couplings. Therefore, in general, the output mode will be a superposition of the degenerate modes and not a single mode of the lattice. This effect can be readily seen in an SSH chain with two edge modes, corresponding to symmetric and antisymmetric combinations of left and right edges. These are nearly degenerate, so when trying to obtain one of them, a certain fraction of power will inevitably be transferred to the other. This can be somewhat exploited to obtain a certain proportion of both edges as the output state, which will depend on the length of the device and the couplings that are chosen.

## 4.5 Conclusions

In this chapter, we have shown that by adiabatically connecting a structure with its SUSY partner, we can efficiently transform a single-site excitation into any gapped mode of the structure under investigation. We have focused on the topological modes of the SSH model and we have proposed the implementation of the method using optical waveguide lattices as the physical system. This allows us to perform the adiabatic deformation in space, along the propagation direction of the waveguides. However, the method can be extended to discrete systems with gapped energy levels in any physical platform.

For both the edge state of an SSH lattice and the interface states of SSH lattices featuring a dimer defect, we have obtained fidelities above  $F = 0.99$  for a wide range of parameter values of the system, with optical devices of the order of  $L = 10$  cm of length. These fidelities are much larger than the ones obtained by direct excitation of the waveguides where the target modes have the largest amplitude, implying a more precise excitation of the relevant mode and a reduction of intensity beatings. The adiabatic modification proposed here is specially useful if the desired output state is not strongly

confined, as direct excitation of such states can be hard to accomplish. In fact, the method can be applied to excite modes that have no degree of localization whatsoever, a fact that we have proven by exciting one of the bulk modes of the SSH model with a high degree of precision. The energy gap between the target mode and the rest directly determines the fidelity of the method. As such, devices with larger number of waveguides need to be longer to remain accurate.

The strength of the proposed method lies both in the generality of the modes that can be engineered and the simplicity of the input that is required to excite them. Although some of the modes displayed in this work could be prepared with other adiabatic schemes, the DSUSY formalism allows to obtain both localized and nonlocalized modes in general lattices without needing any complexity in the input beam. Additionally, DSUSY can be used to build other kinds of devices. One could for instance build a device converting an edge mode to an interface mode. This is based on the fact that the QR factorization is not unique, and thus there can exist more than one supersymmetric partner for the same mode of the SSH chain: one supporting an edge state, and one supporting an interface state [78]. The device could be built by connecting these two structures adiabatically. DSUSY transformations can also be used in 2D systems [298, 301, 320]. This opens new possibilities to generalize the high-efficiency topological excitation method discussed here to higher-dimensional settings. Although the superpartner structure of a 2D lattice may host nonlocal couplings, which are more challenging to implement physically, one may build the required structure through non-geometrical means by using synthetic dimensions [184].



---

## Effective topological impurity systems in a diamond chain of optical waveguides guiding orbital angular momentum modes

---

In flat-band (FB) systems [109, 160] with non-orthogonal compact localized states (CLSs) [111], onsite perturbations couple neighboring CLSs and generate exponentially-decaying impurity states, whose degree of localization depends on lattice parameters. In this chapter, a diamond chain with constant magnetic flux per plaquette is decorated with several controlled onsite impurities in a patterned arrangement on its top and bottom sites, generating an effective system that emerges from the FB [215, 216]. The coupling distribution of the effective system is determined by the relative distance between impurities and the value of the flux, which can be chosen to engineer a wide variety of models. We first develop the framework to describe the effective impurity states [215], and determine the coupling between them. We then employ a staggered distribution of impurities that effectively produces the well-known Su-Schrieffer-Heeger (SSH) model, and show that the topological edge states display an enhanced robustness to non-chiral disorder due to an averaging effect over their extension. Finally, we provide a route to implement the system experimentally using optical waveguides that guide orbital angular momentum (OAM) modes [216]. The work displayed in this chapter opens the way for the design of topologically protected impurity states in other flat-band systems or physical platforms with non-orthogonal bases.

The chapter is organized as follows: In Section 5.1, we contextualize and provide the motivation for generating effective topological models within FB systems. After that, we briefly depict the system under consideration in Section 5.2, a diamond chain with finite flux per plaquette. Then, we present the main theoretical elements that are necessary

to describe the effective impurity systems in Section 5.3, including brief introductions to dual bases and orthogonalization procedures. Moreover, we discuss three different cases for different impurity values, as well as how to compute the coupling between different impurity states. Having introduced the framework, we jump to the description of an effective SSH model in a tight-binding diamond chain in Section 5.4, including a complete analysis of how different kinds of disorder affect it. Then, we provide a route for experimental implementation in optical waveguides in Section 5.5. To end the chapter, we lay out our conclusions in Section 5.6.

## 5.1 Introduction

Compact localized states (CLSs) [111] are eigenstates of tight-binding models which possess strictly zero amplitude beyond a finite number of unit cells. These states cannot freely expand throughout the lattice due to destructive interference over different hopping paths, and thus are associated with the absence of transport that occurs in flat-bands (FBs) [109, 160]. FB systems possess at least one completely dispersionless band that can arise due to the protection provided by a particular symmetry of the system or the fine-tuning of the parameters of the lattice [110]. The CLSs forming the FB are degenerate and generally have nonzero overlap with the adjacent ones [118]. Since FBs lack any transport of their own, any perturbation affecting them will have strong effects on the transport properties of the lattice [110]. In some FB models, the effects of weak perturbations have been studied by projecting the perturbation operator onto one of the FBs [384–386]. For instance, projecting weak modulated interactions onto gapped FBs can lead to the emergence of effective topological two-body subspaces [387, 388]. Both CLSs, and FB systems in general, have garnered significant attention over the last few years, having been implemented in several physical platforms [102–108, 389, 390].

We aim to build an effective system with nontrivial topology within a larger system that hosts CLSs [215, 216], which we take to be the diamond chain with a finite magnetic flux per plaquette [115–117, 122, 158], a system that has a gapped zero-energy FB in the energy spectrum. By introducing small onsite impurities in a plaquette of the chain, we shift the energies of the CLSs with finite amplitude in the perturbed sites. For finite fluxes, adjacent CLSs become coupled and generate a set of exponentially decaying states whose localization length depends on the flux, and whose shape and phase structure depend on the distribution of impurities [215]. By decorating the larger lattice with these onsite perturbations, we can build a wide range of effective systems with effective coupling parameters that can be controlled by tuning the value of the flux and the distance between impurities. To benchmark the method, in this work we imprint a Su-Schrieffer-Heeger (SSH) [95] model onto a diamond chain lattice with constant flux per plaquette [216]. We first briefly describe the theoretical method behind

the formation of the effective system, and then focus on the characteristics of the effective system itself, including the appearance of edge states localized around the end of the chain of impurities. Additionally, we study the robustness of the effective system against different types of disorder, and show how it displays enhanced protection, even against disorder that breaks its chiral symmetry, due to the extension of the impurity states. This extension provides an averaging effect of the disorder over their characteristic length [217]. The effect is numerically quantified, and the effective number of sites covered by the state is related to its robustness against disorder.

Finally, we provide a possible route to implement the described system. We require a way to imprint a finite flux per plaquette onto a diamond chain, as well as a way to decorate this chain with controlled onsite impurities at certain sites. In photonics alone, several platforms have been shown to provide a controllable way to introduce these fluxes, such as ring resonators with different optical paths [151, 152, 167, 168, 220, 284, 391], microwave cavity arrays [392, 393], fiber loops [182, 394, 395] and time-multiplexed resonators [183], twisted or modulated lattices [153–156, 158, 396–399] and optical waveguides with multipolar components [400–403] or guiding orbital angular momentum (OAM) modes [159, 218]. We focus on the latter, which additionally allows for a simple method to add the impurities experimentally by slightly modifying parameters such as the writing speed in laser-writing setups [42], or the waveguide width in beam lithography setups [37]. The coupling between OAM modes carries a phase that can be used to imprint an artificial gauge field on the system [159]. To build the diamond, we propose to couple modes with different OAM order  $l$  in a zig-zag pattern. Namely, modes with  $l = 0$  will correspond to the spinal nodes, while modes with  $l = 1$  will be split in a synthetic dimension and play the role of top and bottom nodes [181]. In this setup, the relative angle between waveguide pairs will determine the value of the flux, which can be tuned to any desired value.

## 5.2 Diamond chain

For this chapter, we consider the system in Fig. 5.1(a), consisting of a diamond chain with a  $\phi = 2\pi \frac{\Phi}{\Phi_0}$  reduced magnetic flux per plaquette, with  $\Phi$  the magnetic flux and  $\Phi_0$  the magnetic flux quantum. Setting the lattice constant to unity, the bulk Hamiltonian of the clean system is given by

$$H(k) = t \begin{pmatrix} 0 & e^{-i\tilde{\phi}} + e^{-i(k-\tilde{\phi})} & e^{i\tilde{\phi}} + e^{-i(k+\tilde{\phi})} \\ e^{i\tilde{\phi}} + e^{i(k-\tilde{\phi})} & 0 & 0 \\ e^{-i\tilde{\phi}} + e^{i(k+\tilde{\phi})} & 0 & 0 \end{pmatrix}, \quad (5.1)$$

where  $t$  is the magnitude of the hopping term and  $k$  is the quasimomentum. We choose the flux to be spread across all couplings in the plaquette, as indicated in Fig. 5.1(a),

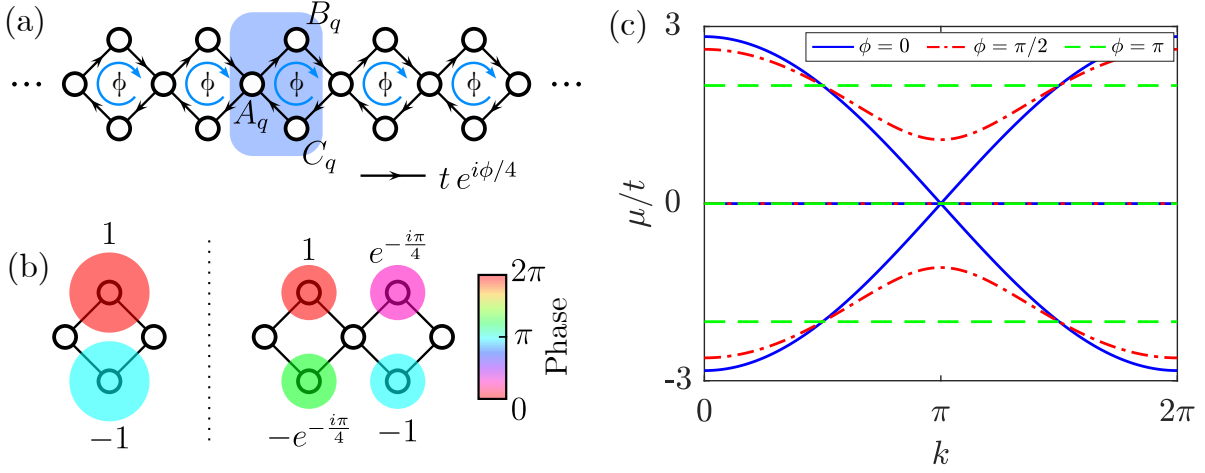


Figure 5.1: (a) Diamond chain with  $\phi$  flux per plaquette, distributed uniformly by the four hopping terms of each plaquette, with positive phase accumulated in the clockwise direction. The shaded region represents the  $q$ -th unit cell with sites  $A_q$  (center),  $B_q$  (top) and  $C_q$  (bottom). (b) Representation of the CLS of the system for  $\phi = 0$  (left) and  $\phi = \pi/2$  (right). The circle size represents the amplitude, and the color the phase. Note that, as long as  $\phi \neq 0$ , the CLS  $m$  occupies two plaquettes and overlaps with the CLSs  $m \pm 1$ . The normalization factor in each case is not included. (c) Bulk energy spectrum, in units of  $t$ , of the diamond chain for three representative values of the  $\phi$  flux per plaquette. The zero-energy flat band is common to all  $\phi$  values.

such that each coupling has a phase  $\tilde{\phi} = \phi/4$ . Diagonalization of this Hamiltonian yields three energy bands,

$$\mu_0 = 0, \quad (5.2)$$

$$\mu_{\pm}(k) = \pm 2t \sqrt{1 + \cos k \cos \frac{\phi}{2}}. \quad (5.3)$$

Note that  $\mu_{\pm}(k)$  are dispersive for all  $\phi$  except for  $\phi = \pi$ , where all bands are flat, as can be seen in Fig. 5.1(b). As the flux grows from  $\phi = 0$ , an energy gap between the zero-energy FB  $\mu_0$  and  $\mu_{\pm}(k)$  opens at  $k = \pi$ , with a value of  $\mu_{\text{gap}} = 2t \sqrt{1 + \cos \frac{\phi}{2}}$ . Moreover, when the diamond chain is threaded by a flux, there exists a basis of non-orthogonal CLSs in the zero-energy FB, with each CLS spanning two plaquettes, see Fig. 5.2(a). Considering the  $A$ ,  $B$  and  $C$  sites consecutively at plaquettes  $m$  and  $m + 1$ , the  $m$ -th normalized CLS has the form

$$|\text{Loc}, m\rangle = \frac{1}{2} (\cdots, 0, 1, -e^{-i\frac{\phi}{2}}, 0, e^{-i\frac{\phi}{2}}, -1, \cdots)^T, \quad (5.4)$$

and is zero elsewhere. Since  $|\text{Loc}, m\rangle$  has zero contribution on sites  $A$ , we speak of unit cells and plaquettes indifferently. As is obvious from expression (5.4), this CLS will only

overlap with the ones at plaquettes  $m \pm 1$ , with strength

$$S_{m m \pm 1} = S_{m \pm 1 m} = \langle \text{Loc}, m | \text{Loc}, m + 1 \rangle = \frac{1}{2} \cos \frac{\phi}{2}, \quad (5.5)$$

and thus the overlap matrix  $S$  of all localized states will be tridiagonal, with main diagonal elements  $S_{m m} = 1$  from normalization, and also real and symmetric.

### 5.3 Effective impurity systems

We now summarize the theoretical description of the formation of effective impurity systems in our FB model, whose main steps are indicated in Fig. 5.2. A more thorough mathematical description can be found in Ref. [215], while for this chapter we choose to place the focus on its applications and potential implementations.

We consider an open diamond chain with  $N_c + 1$  unit cells, with constant coupling  $t$  and flux  $\phi$ , where we add onsite impurities to the top and bottom sites  $B$  and  $C$  of a single plaquette. This chain contains  $N_c$  CLSs in its zero-energy FB. We add the impurities at unit cell  $q + 1$ , with  $q = N_c/2$  and  $N_c$  assumed even. In this scenario, the corresponding impurity operator has the general form

$$\hat{V} = \epsilon_B |B_{q+1}\rangle \langle B_{q+1}| + \epsilon_C |C_{q+1}\rangle \langle C_{q+1}|, \quad (5.6)$$

where  $\epsilon_B$  and  $\epsilon_C$  are local impurity potentials, left as free parameters. From here, one may think of building an effective dimer model out of the two CLSs directly affected by the impurity potentials, i.e.,  $|\text{Loc}, q\rangle$  and  $|\text{Loc}, q + 1\rangle$ . However, even though those are the only CLSs that have nonzero weight on the impurity sites, one has to note that the basis of CLSs is not orthogonal. Orthogonalizing it leads to a set of states that remain localized, but that now span across several plaquettes and not just the two adjacent ones. As a consequence, after orthogonalization, several other states also have nonzero weight on the impurity sites, and thus the effective model is not restricted to two states.

As we will justify shortly, to avoid this scenario and simplify the description, one might work in the dual basis of localized states [215, 216, 404, 405]. Given a non-orthogonal basis of states  $\{|m\rangle\}$  with corresponding overlap matrix elements  $S_{nm} = \langle n|m\rangle$ , also called the direct basis, a dual basis  $\{|m^*\rangle\}$  can be defined based on the property that  $\langle n|m^*\rangle = \delta_{nm}$ , with  $\delta_{nm}$  the Kronecker delta. Note that for orthogonal basis where  $S_{nm} = \delta_{nm}$ , dual and direct bases are equivalent. One might transform states between the direct and dual bases in the following way:

$$|n\rangle = \sum_m S_{nm} |m^*\rangle, \quad |n^*\rangle = \sum_m S_{nm}^{-1} |m\rangle, \quad (5.7)$$

where  $S_{nm}^{-1} \equiv [S^{-1}]_{nm}$  are the elements of the inverse overlap matrix, which fulfill

$$\sum_k S_{nk}^{-1} S_{km} = \delta_{nm}. \quad (5.8)$$



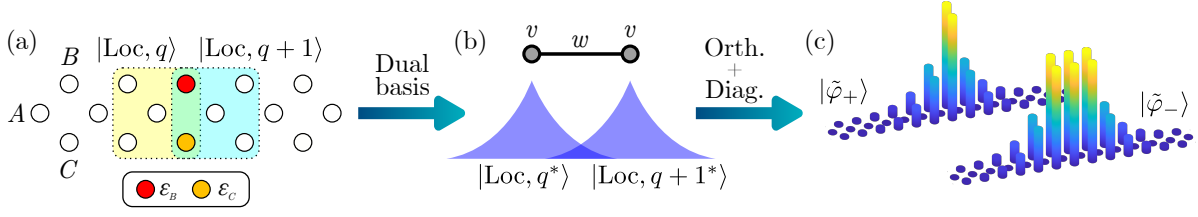


Figure 5.2: Summary of the theoretical description of the effective impurity system. (a) The CLSs of the diamond chain located in the two neighboring plaquettes to the one with onsite impurities  $\epsilon_B$  and  $\epsilon_C$  (yellow and blue shaded regions) have a direct overlap on these sites. However, the CLSs do not constitute an orthogonal basis, so other states of the FB besides the two CLSs shown in (a) will also have such an overlap when orthogonalizing. To restrict the effective system to two states only, we switch to a dual basis (b) where the impurity operator affects only two localized states that can then be orthogonalized independently to all other states. Finally, diagonalization of the impurity sub-system leads, when reverted back to the site basis of the chain, to the two exponentially-decaying states in (c), whose amplitude distribution depends on the impurity values and the flux per plaquette.

Therefore, knowing all the elements of the overlap matrix for the localized states of the diamond chain (5.5), the dual basis can be found via  $|\text{Loc}, n^*\rangle = \sum_m S_{nm}^{-1} |\text{Loc}, m\rangle$  [215]. Now one can define projection operators onto the FB subspace spanned by these localized states [404]:

$$\hat{P}_{\text{FB}} = \sum_{m=1}^{N_c} |\text{Loc}, m\rangle \langle \text{Loc}, m^*| = \sum_{n,m=1}^{N_c} |\text{Loc}, m\rangle S_{nm}^{-1} \langle \text{Loc}, n|, \quad (5.9)$$

$$\hat{P}_{\text{FB}}^\dagger = \sum_{m=1}^{N_c} |\text{Loc}, m^*\rangle \langle \text{Loc}, m| = \sum_{n,m=1}^{N_c} |\text{Loc}, n\rangle S_{nm}^{-1} \langle \text{Loc}, m|, \quad (5.10)$$

where orthogonality between the FB subspace and the rest has been used. The summations thus run over the  $N_c$  CLSs, which are orthogonal to the rest of the eigenstates in the diamond chain. Also, note that  $\hat{P}_{\text{FB}} = \hat{P}_{\text{FB}}^\dagger$ . These projectors allow one to express any operator in terms of the dual basis of localized states:

$$\hat{A}_{\text{FB}} = \hat{P}_{\text{FB}}^\dagger \hat{A} \hat{P}_{\text{FB}} = \sum_{n,m=1}^{N_c} |\text{Loc}, n^*\rangle A_{nm} \langle \text{Loc}, m^*|, \quad (5.11)$$

with  $A_{nm} = \langle \text{Loc}, n | \hat{A} | \text{Loc}, m \rangle$ . We replicate (5.11) for the impurity operator in (5.6):

$$\begin{aligned} \hat{V}_{\text{FB}} &= \sum_{n,m=q}^{q+1} |\text{Loc}, n^*\rangle V_{nm} \langle \text{Loc}, m^*| \\ &= v \sum_{n=q}^{q+1} |n^*\rangle \langle n^*| + \left[ w |q+1^*\rangle \langle q^*| + \text{H.c.} \right], \end{aligned} \quad (5.12)$$

where  $V_{nm} = \langle \text{Loc}, n | \hat{V} | \text{Loc}, m \rangle$  and we skip the “Loc” indicator in the second line for brevity. This time, the summation only runs over  $q$  and  $q+1$ . So, when expressed in the dual basis, the impurity operator only involves the two corresponding CLSs. This is true as long as the impurities are small compared to the gap between flat and dispersive bands,  $\epsilon_B, \epsilon_C \ll \mu_{\text{gap}}$ , so that higher-order couplings mediated through the dispersive bands can be neglected. Therefore, for large impurities or for fluxes close to zero where the gap closes [see Fig. 5.1(c)], this description ceases to be valid. Taking another look at (5.12), we see that in the dual basis  $v = \frac{\epsilon_B + \epsilon_C}{4}$  behaves as a local potential on the dual CLSs at  $q$  and  $q+1$ , and  $w = (\epsilon_B e^{-i\frac{\phi}{2}} + \epsilon_C e^{i\frac{\phi}{2}})/4$  is a hopping term that acts *exclusively* between these two states, see Fig. 5.2(b). Therefore, we have succeeded in reducing the problem to that of only two CLSs, which one can now orthogonalize independently of the rest and work on a reduced subspace of impurity states.

There exist multiple methods to perform this orthogonalization. A well-known option is the Gram-Schmidt method [326], which relies on a recursive state-by-state orthogonalization procedure where the final set of vectors depends on the order chosen for orthogonalization. However, this method can be computationally demanding and is prone to numerical instabilities. A more efficient alternative consists of using the Löwdin transformation [262, 263, 406, 407] to perform a symmetrical orthogonalization based on a linear transformation of the original basis set. With this transformation, from our original non-orthogonal basis  $\{|m\rangle\}$ , the orthogonal basis states may be found with the help of the overlap matrix as

$$|\tilde{n}\rangle = \sum_m S_{nm}^{-\frac{1}{2}} |m\rangle, \quad (5.13)$$

where  $S_{nm}^{-\frac{1}{2}} \equiv (S^{-\frac{1}{2}})_{nm}$ . To prove this statement, let us consider a general linear transformation for our basis [406]:

$$|\tilde{n}\rangle = \sum_m A_{mn} |m\rangle, \quad (5.14)$$

where we require that the new basis is orthonormal:

$$\delta_{mn} = \langle \tilde{m} | \tilde{n} \rangle = \sum_{kj} A_{mk} \langle k | j \rangle A_{jn} = \sum_{kj} A_{mk} S_{kj} A_{jn}. \quad (5.15)$$

In matrix form, Eq. (5.15) reads:

$$A^\dagger S A = I. \quad (5.16)$$

A general solution to this equation can be found for  $A = S^{-1/2}B$  for any matrix  $B$ , as long as  $B^\dagger B = I$ . Choosing the simplest case of  $B = I$  leads to  $A = S^{-1/2}$ , which when substituted in (5.14), recalling that  $S$  is real and symmetric, leads to the transformation in (5.13). Based on this transformation, we can now project the impurity operator (5.12) from the dual basis onto the new orthonormal basis:

$$\mathcal{V}_{\text{FB}} = S_*^{-\frac{1}{2}} \hat{V}_{\text{FB}} S_*^{-\frac{1}{2}}, \quad (5.17)$$

with  $S_*$  being the overlap matrix in the dual basis of localized states with elements  $S_{*,nm} = \langle \text{Loc}, n^* | \text{Loc}, m^* \rangle$ . Using the expression of the dual basis states (5.7) and the property in (5.8), it is easy to show that  $S_{*,nm} = S_{nm}^{-1}$  [215]. The method for inverting tridiagonal matrices is known [408], and as such an analytical computation of (5.17) is achievable. The somewhat lengthy procedure is explained in detail in Ref. [215], but we mention the key points here. An approximate expression for  $S_{nm}^{-1}$  can be computed in the thermodynamic limit  $N_c \rightarrow \infty$ , for an impurity in  $q = N_c/2$ :

$$\begin{cases} S_{q+\Delta, q+\Delta}^{-1} = \coth \theta \\ S_{q+\Delta, q}^{-1} = (-1)^\Delta \coth \theta e^{-\Delta \theta} \end{cases}, \quad \Delta = 0, 1, 2, \dots, \quad (5.18)$$

with  $S_{q+\Delta, q+\Delta}^{-1} = S_{q+\Delta, q+\Delta}^{-1}$ . With the expressions in (5.18), the  $S_*^{-\frac{1}{2}}$  matrix can be constructed. From there, using (5.17) and (5.12), the following expression is reached [215]:

$$\mathcal{V}_{\text{FB}} = \begin{pmatrix} \frac{\epsilon_B + \epsilon_C}{4} e^{-\chi} - i \frac{\epsilon_B - \epsilon_C}{4} \sqrt{1 - e^{-2\chi}} & \frac{\epsilon_B + \epsilon_C}{4} e^{-\chi} + i \frac{\epsilon_B - \epsilon_C}{4} \sqrt{1 - e^{-2\chi}} \\ \frac{\epsilon_B + \epsilon_C}{4} e^{-\chi} + i \frac{\epsilon_B - \epsilon_C}{4} \sqrt{1 - e^{-2\chi}} & \frac{\epsilon_B + \epsilon_C}{4} e^{-\chi} - i \frac{\epsilon_B - \epsilon_C}{4} \sqrt{1 - e^{-2\chi}} \end{pmatrix}, \quad (5.19)$$

where  $\chi = \cosh^{-1}(\sec \frac{\phi}{2})$  contains the flux dependence. All that remains is diagonalizing this matrix, which allows to obtain the exponentially decaying impurity states showcased in Fig. 5.2(c), and in more detail in Fig. 5.3. These states are pulled from the FB, obtaining nonzero energy, and will behave as the main sites of an effective system when decorating the lattice with more impurities. We now explore three cases of interest, depending on the value of the impurities.

### 5.3.1 Opposite impurities

For opposite impurities,  $\epsilon_B = -\epsilon_C = \epsilon$ , where the impurity strength  $\epsilon$  is given in units of the hopping parameter  $t$ , the effective impurity matrix in (5.19) reduces to

$$\mathcal{V}_{\text{FB}} = -\frac{\epsilon}{2} \sqrt{1 - e^{-2\chi}} \sigma_y, \quad (5.20)$$

with  $\sigma_y$  the  $y$  Pauli matrix. The respective eigenvalues and eigenvectors read as

$$\mu_{\pm} = \pm \frac{\epsilon}{2} \sqrt{1 - e^{-2\chi}}, \quad (5.21)$$

$$\begin{pmatrix} |\tilde{\varphi}_+\rangle \\ |\tilde{\varphi}_-\rangle \end{pmatrix} = \frac{1}{\sqrt{2}} \begin{pmatrix} i & 1 \\ -i & 1 \end{pmatrix} \begin{pmatrix} |\tilde{\varphi}_q\rangle \\ |\tilde{\varphi}_{q+1}\rangle \end{pmatrix}, \quad (5.22)$$

which are written in terms of the orthogonal two-state basis  $\{|\tilde{\varphi}_q\rangle, |\tilde{\varphi}_{q+1}\rangle\}$  with:

$$|\tilde{\varphi}_q\rangle = \sum_{m=q}^{q+1} S_{*,q}^{-\frac{1}{2}} |\text{Loc}, m^*\rangle, \quad |\tilde{\varphi}_{q+1}\rangle = \sum_{m=q}^{q+1} S_{*,q+1}^{-\frac{1}{2}} |\text{Loc}, m^*\rangle. \quad (5.23)$$

In Figs. 5.3(a) and (b), we plot the spatial profile of the eigenstate with positive and negative energy, respectively, for a diamond chain with 53 plaquettes and constant flux  $\phi = \frac{\pi}{2}$ , where we add opposite local impurities  $\epsilon = 0.1t$  at the top and bottom sites of the midchain plaquette [depicted in the right inset of Fig. 5.3(a)]. We see that, aside from the central plaquette, the spatial distribution of both states are identical. In both cases, amplitudes decay exponentially with the plaquette separation from the two neighboring plaquettes. This can be further checked by looking at the plots in the left insets of both figures, plotted in a semi-logarithmic scale. Analytical expressions for the eigenstates in (5.22), as well as for the following two cases below (Secs. 5.3.2 and 5.3.3), are also shown in Fig. 5.3. Both numerical and analytical results present a near-perfect agreement. A small difference can be observed in  $A$  sites, where analytically the amplitudes are exactly zero. Even though the numerical amplitude is nonzero, it is at least an order of magnitude smaller than the one at adjacent  $B$  and  $C$  sites. Furthermore, we can compare the eigenvalues in (5.21) with the numerical values obtained in the full tight-binding matrix. We plot both quantities in Fig. 5.4(a), and do the same in (b)–(c) for the following two cases, again for  $\epsilon = 0.1t$ . In all cases, despite the fact that  $\epsilon$  is far away from the condition of  $\epsilon \ll \mu_{\text{gap}}$ , the numerical values closely follow the analytical expressions. However, for Figs. 5.4(b) and (c), a deviation appears when  $\phi \rightarrow 0, 2\pi$ . This is expected, as in those regions the gap between flat and dispersive bands goes to zero, so higher-order couplings to the dispersive bands can no longer be neglected and the analytical treatment breaks down. Nevertheless, the region of discrepancy is very limited, and becomes even smaller with decreasing  $\epsilon$ .

### 5.3.2 Equal impurities

For equal impurities,  $\epsilon_B = \epsilon_C = \epsilon$ , the effective impurity matrix in (5.19) takes the form:

$$\mathcal{V}_{\text{FB}} = \frac{\epsilon}{2} (I + e^{-\chi} \sigma_x), \quad (5.24)$$

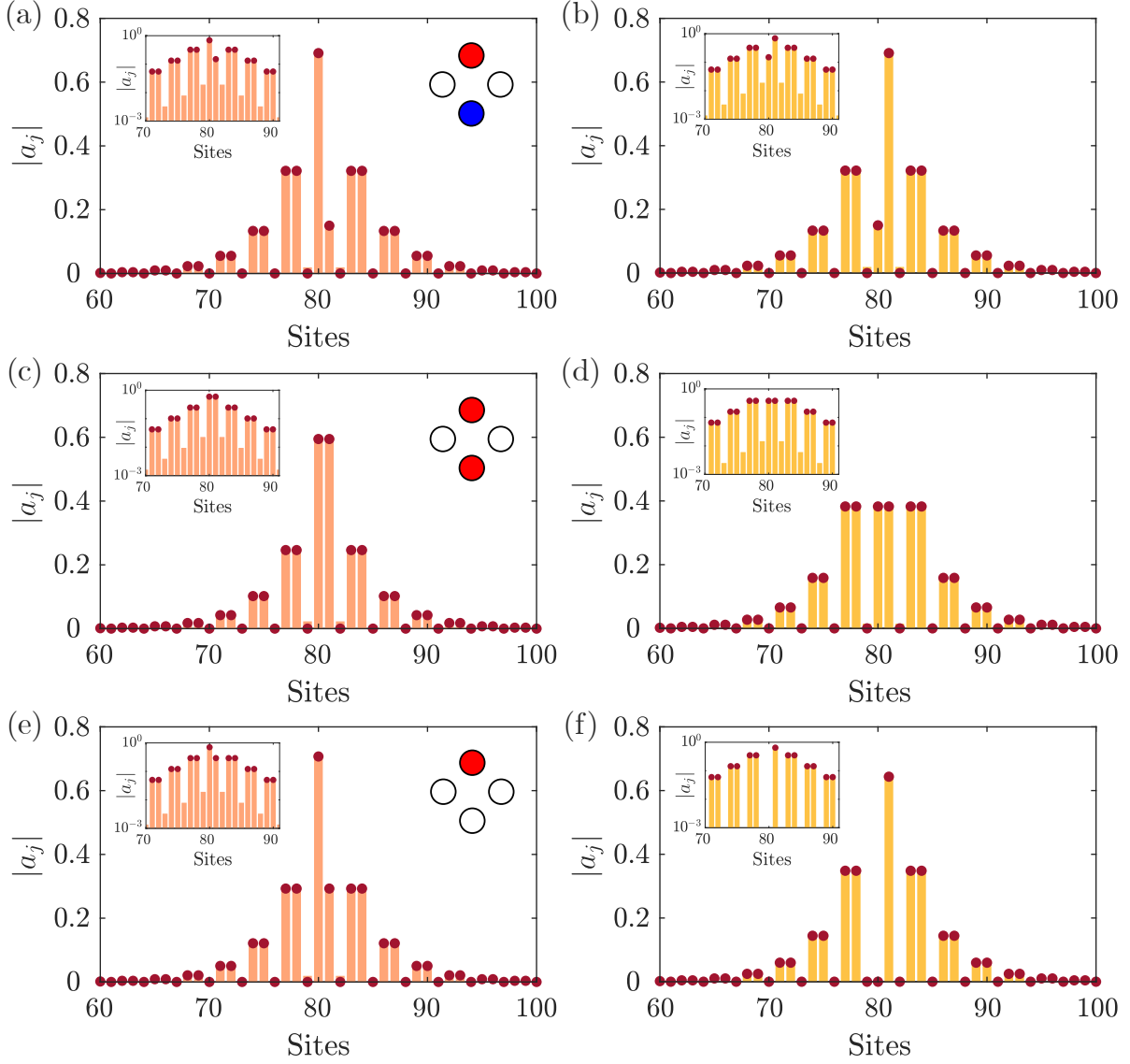


Figure 5.3: Probability amplitudes of the eigenstates of the impurity subsystem in a diamond chain with 53 plaquettes pierced by a  $\pi/2$  flux, for (a)–(b) opposite  $\epsilon_B = -\epsilon_C = \epsilon$  impurities, (c)–(d) equal  $\epsilon_B = \epsilon_C = \epsilon$  impurities, and (e)–(f) a single impurity  $\epsilon_B = \epsilon$  with  $\epsilon_C = 0$ .  $\epsilon = 0.1t$  in all cases. Orange and yellow bars (dark red dots) correspond to numerical (analytical) results. We sketch each case in the right insets of the left column, with red (blue) representing positive (negative) impurities. In all cases, figures in the left (right) column correspond to the state with higher (lower) energy. The insets to the left show the same results in a semi-logarithmic scale and for a smaller portion of the chain, where the exponential decay of the amplitudes can be observed to start from the two neighboring plaquettes of the impurity sites. Sites without red dots are  $A$  sites where the CLSs forming the analytical subspace have zero weight.

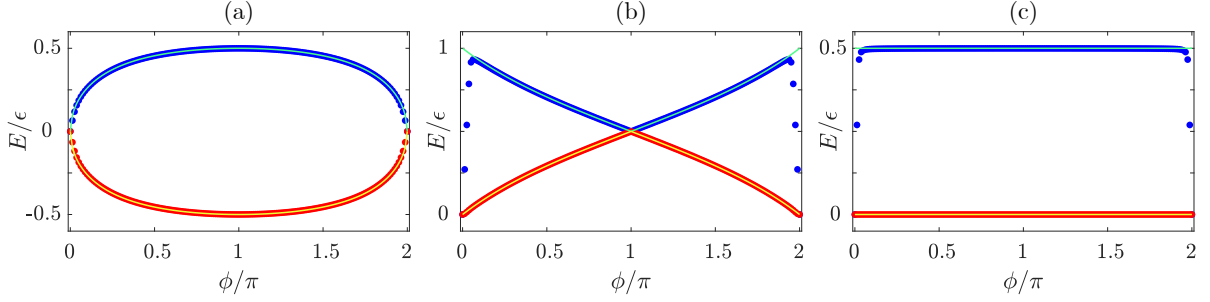


Figure 5.4: Analytical energy curves (light green and yellow solid lines) obtained from the diagonalization of the effective impurity matrix, as a function of the magnetic flux  $\phi$  for (a) opposite impurities, (b) equal impurities, and (c) a single impurity, with  $\epsilon = 0.1t$ . Blue and red dots correspond to the numerically obtained energies in the equivalent diamond chain with impurities in the  $B$  and  $C$  sites of the midchain plaquette.

where  $\sigma_x$  is the  $x$  Pauli matrix. The eigenvalues and eigenvectors now become:

$$\mu_{\pm} = \frac{\epsilon}{2}(1 \pm e^{-\chi}), \quad (5.25)$$

$$\begin{pmatrix} |\tilde{\varphi}_+\rangle \\ |\tilde{\varphi}_-\rangle \end{pmatrix} = \frac{1}{\sqrt{2}} \begin{pmatrix} 1 & 1 \\ 1 & -1 \end{pmatrix} \begin{pmatrix} |\tilde{\varphi}_q\rangle \\ |\tilde{\varphi}_{q+1}\rangle \end{pmatrix}. \quad (5.26)$$

As before, we plot in Figs. 5.3(c) and (d) the amplitudes for the higher- and lower-energy eigenstate, respectively. In this case, two clear differences can be spotted. First, the state in Fig. 5.3(c) has a higher central peak, compared to the one in Fig. 5.3(d). In contrast, the latter state has a larger spatial extension compared to the former, a fact that will prove to be important when we discuss the disordered lattices in the next sections. Despite these differences, both states decay exponentially with the distance to the central plaquette. We will focus on this specific case for the rest of the results of this chapter. However, we first present a last case of interest.

### 5.3.3 Single impurity

Finally, let us address the case where a single impurity,  $\epsilon_B = \epsilon$ , is placed at the top site of the  $q + 1$  plaquette. The effective impurity matrix in (5.19) now reads

$$\mathcal{V}_{\text{FB}} = \frac{\epsilon}{4}(\sigma_0 + e^{-\chi}\sigma_x - \sqrt{1 - e^{-2\chi}}\sigma_y), \quad (5.27)$$

and the eigenvalues and eigenvectors take the form

$$\mu_{\pm} = \frac{\epsilon}{4}(1 \pm 1), \quad (5.28)$$

$$\begin{pmatrix} |\tilde{\varphi}_+\rangle \\ |\tilde{\varphi}_-\rangle \end{pmatrix} = \frac{1}{\sqrt{2}} \begin{pmatrix} 1 & e^{-i\xi} \\ 1 & -e^{-i\xi} \end{pmatrix} \begin{pmatrix} |\tilde{\varphi}_q\rangle \\ |\tilde{\varphi}_{q+1}\rangle \end{pmatrix}, \quad (5.29)$$

where  $\xi$  is defined as  $\cos \xi \equiv e^{-\chi}$ . There is now no flux dependence on the energies in (5.28), and most notably one eigenvector has zero energy. This has important implications with regards to the impurity system. When a single impurity is present, the system can always rotate the subspace of dual localized states in order to generate a state, namely  $|\tilde{\varphi}_-\rangle$  in (5.29), with zero weight at the impurity site and thus zero energy, such that it remains degenerate with the other FB states. Hence, even though the methodology points to the appearance of two exponentially decaying impurity states, only one of them actually emerges from the FB. This is illustrated in Fig. 5.5, where a partial profile of the  $|\tilde{\varphi}_+\rangle$  and  $|\tilde{\varphi}_-\rangle$  eigenstates is depicted. It can be readily seen that the weight of the state at the impurity site, marked in both cases with an arrow, is maximum for  $|\tilde{\varphi}_+\rangle$  and zero for  $|\tilde{\varphi}_-\rangle$ .

The single impurity case has an interesting topological characterization that is treated in detail in Ref. [215]. Although we do not fully delve into its details in this thesis, we do present the most remarkable result. In essence, the Zak phase, as defined in Sec. 2.3.1, can be computed as

$$\gamma = i \oint dR \langle \tilde{\varphi}(R)_- | \frac{d}{dR} | \tilde{\varphi}(R)_- \rangle, \quad (5.30)$$

where the integral path is usually taken along the Brillouin zone such that the parameter  $R$  corresponds to the quasimomentum  $k$ . However, the relevant parameter of integration in our case is not the quasimomentum, but rather the reduced magnetic flux  $\phi$  as it changes by one flux quantum, that is, from  $\phi = 0$  to  $\phi = 2\pi$ . Recall that the flux

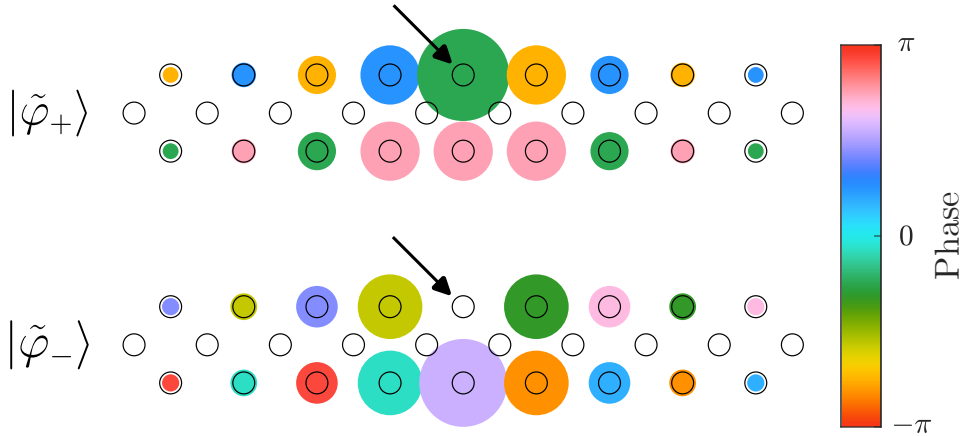


Figure 5.5: Partial profile of the  $|\tilde{\varphi}_+\rangle$  and  $|\tilde{\varphi}_-\rangle$  eigenstates in (5.29), respectively, and where the radius of each circle represents the amplitude of the wavefunction at the respective site and the color represents its phase, coded by the color bar at the right. The arrow indicates the  $B_{q+1}$  site where the  $\epsilon_B = \epsilon = 0.1 t$  impurity is placed, and where  $|\tilde{\varphi}_+\rangle$  ( $|\tilde{\varphi}_-\rangle$ ) has maximum (zero) amplitude.

appears in the expression of the eigenstates (5.29) through the definition of  $\xi$ . Therefore, we can introduce (5.29) in (5.30) and integrate taking  $R = \phi$ , which leads to a Zak phase having a *half-integer* value  $\gamma = \frac{\pi}{2}$ . Equivalently, the winding number can also be shown to take a half-integer value [215]. We can compare this with the value of the Zak phase for the SSH model, whose value is  $\gamma = 0$  in the trivial phase and  $\gamma = \pi$  in the nontrivial phase. In this latter case, two edge states appear in the gap [101]. Analogously, for the half-integer value in our case, one would expect a single edge state to show up under OBC. However, in contrast to the usual scenario where boundaries are opened in real space, complementary to momentum space where the Zak phase is computed, here it is not evident how to open the boundaries on the complementary space of the flux. In Ref. [215], it is detailed how this pivotal issue can be circumvented by employing an exact mapping onto a 2D lattice where the  $y$ -momentum plays the role of the flux in the diamond chain. In the mapped lattice the boundaries can be opened, and therefore the anticipated single edge state can be observed.

### 5.3.4 Coupling between impurity states

Before jumping to the fully decorated diamond chain, let us first consider the simpler case where only two plaquettes contain onsite impurities. In particular, we consider the case of equal impurities just described in Sec. 5.3.2, with values  $\epsilon_B = \epsilon_C = 0.1 t$ . In this scenario, four states emerge from the FB with energies following the expression in (5.25).

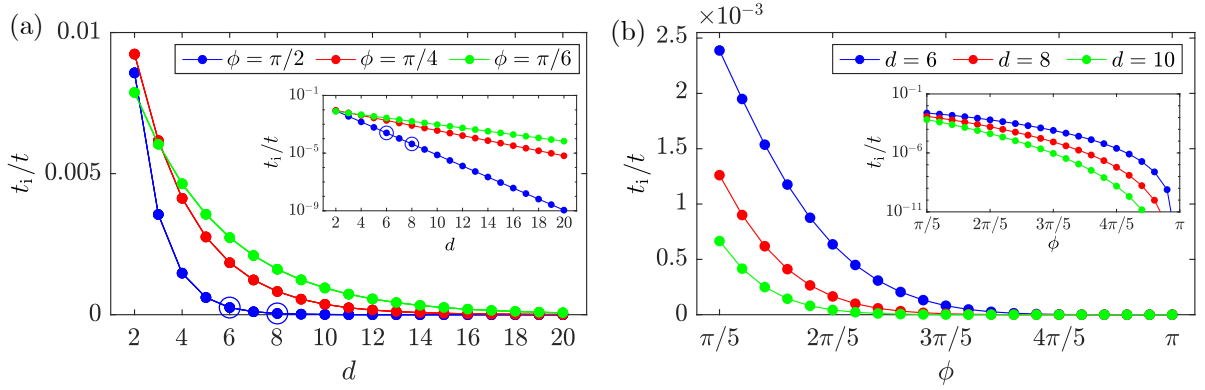


Figure 5.6: (a) Coupling strength between two sets of impurities with  $\epsilon_B = \epsilon_C = 0.1 t$  with respect to the distance between impurities for different flux values. The inset shows the same curves in a logarithmic scale. The coupling values chosen for Fig. 5.8(b) in the next section, namely those for  $d_1 = 6$  and  $d_2 = 8$  for  $\phi = \frac{\pi}{2}$ , are highlighted with blue circles. (b) Coupling strength for the same impurity values, this time for varying fluxes and fixed impurity distances. The higher extension of the states for lower fluxes is reflected by the increased coupling strengths.



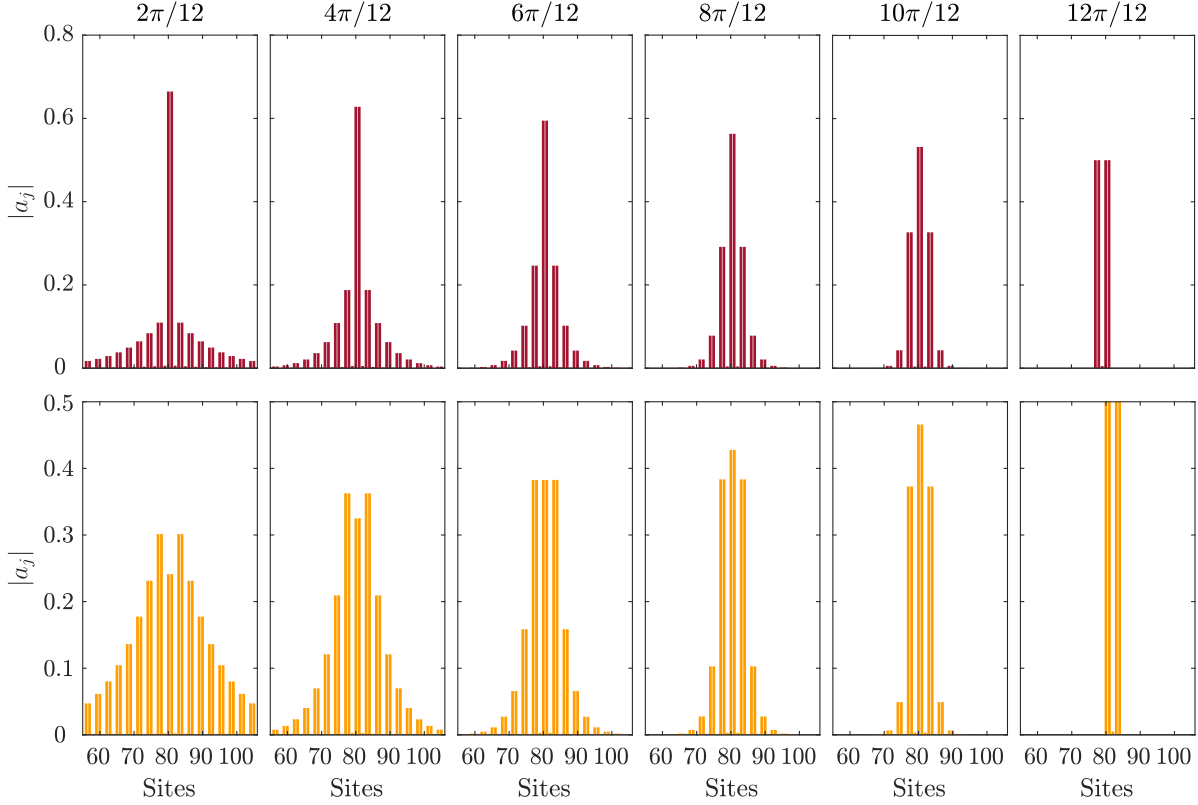


Figure 5.7: Snapshots of the absolute value of the amplitudes of the higher (lower) impurity state at the top (bottom) panel at different flux values, indicated on the top of the figure. We show a partial section of an open diamond chain with 53 complete plaquettes, centered around the central plaquette where equal impurities  $\epsilon = 0.1 t$  are added.

Although these states will overlap with one another, they will couple independently in two groups due to the significant energy difference between them. Thus, two effective systems are formed, with energies around  $\mu_+$  and  $\mu_-$ , respectively. To extract the value of the coupling between impurity states, we check the energy gap that is induced between the two of them as we change the relative distance between impurities. We focus on the lower-energy block, thus defining the coupling as:

$$t_i = \frac{1}{2} (\tilde{\mu}_a - \tilde{\mu}_b), \quad (5.31)$$

with  $\tilde{\mu}_a$  ( $\tilde{\mu}_b$ ) the energy of the higher (lower) state in the coupled set. We plot the obtained coupling dependence with the distance between impurities in Fig. 5.6(a), where we observe that it displays an exponential dependence on their separation, confirmed also by the inset. We also see that the decaying of the curves is slower for smaller fluxes. This is further proved in Fig. 5.6(b), where we now plot the coupling with respect to the

flux for different separations. Since the coupling is larger for lower fluxes, the extension of the states is necessarily larger as well.

Further proof can be found in Fig. 5.7, where snapshots of the spatial extension of both impurity states are shown for different flux values. Although the lower-energy state is considerably more extended at all flux values, we can observe that the exponential tails grow longer as the flux decreases in both instances. Note that this does not imply that the effective number of sites covered by the state, as defined later on in Sec. 5.4.1 based on the effects of disorder, grows for both states. This aspect will be treated below. Going back to Fig. 5.6, the curves there allow us to build a map between couplings and distances, which can also be tuned by controlling the flux on the lattice. Based on it, any coupling distribution can be engineered. The couplings for the set of higher-energy impurity states presents very similar values as those depicted here. This may seem counter-intuitive, specially considering the fact that the lower energy states possess a comparatively larger extension as we just showed in Fig. 5.7. Nevertheless, when numerically computing the coupling, the different behavior of the central peak at the plaquette hosting the impurities as well as the exponential amplitude tails in both cases seems to compensate each other and lead to approximately equal results.

## 5.4 Effective SSH impurity chains

We now consider a larger diamond chain of  $N_c = 101$  unit cells with nearest-neighbor coupling  $t$  and nonzero flux per plaquette  $\phi$ , decorated with a series of thirteen impurity pairs in the top and bottom sites, following a staggered pattern as sketched in Fig. 5.8(a). In particular, we use  $d_1 = 8$  and  $d_2 = 6$  plaquettes of separation between impurities, ending with  $d_1$  at the left and  $d_2$  at the right end of the chain. The induced impurity states couple among themselves forming an effective system described by a Hamiltonian  $H_{\text{eff}}$ . As we just described in the previous section, the coupling between the impurity states depends exponentially on their separation. Therefore, the effective system displays the staggered coupling distribution that is characteristic to the SSH model [95]. We consider the case of equal impurities with values  $\epsilon = 0.1t$  and a flux of  $\phi = \pi/2$ . To avoid cutting the exponentially decaying tails of the edgemost impurity states, which would perturb the ends of the effective system, 13 plaquettes before the first impurity pair and after the last one are left impurity-free at both ends of the chain.

As we showcase in Fig. 5.8(b), two SSH-like sub-spectra emerge above the FB (orange and green dots). For the other possible choices for the impurity distribution, which were discussed previously, one or two impurity spectra are similarly produced. In this manuscript, we focus on the spectrum of lower energy (orange dots) in Fig. 5.8(c). The highlighted state in the middle of the gap corresponds to the edge state of the effective system, whose amplitudes are shown in Fig. 5.8(d). Interestingly, this edge state is

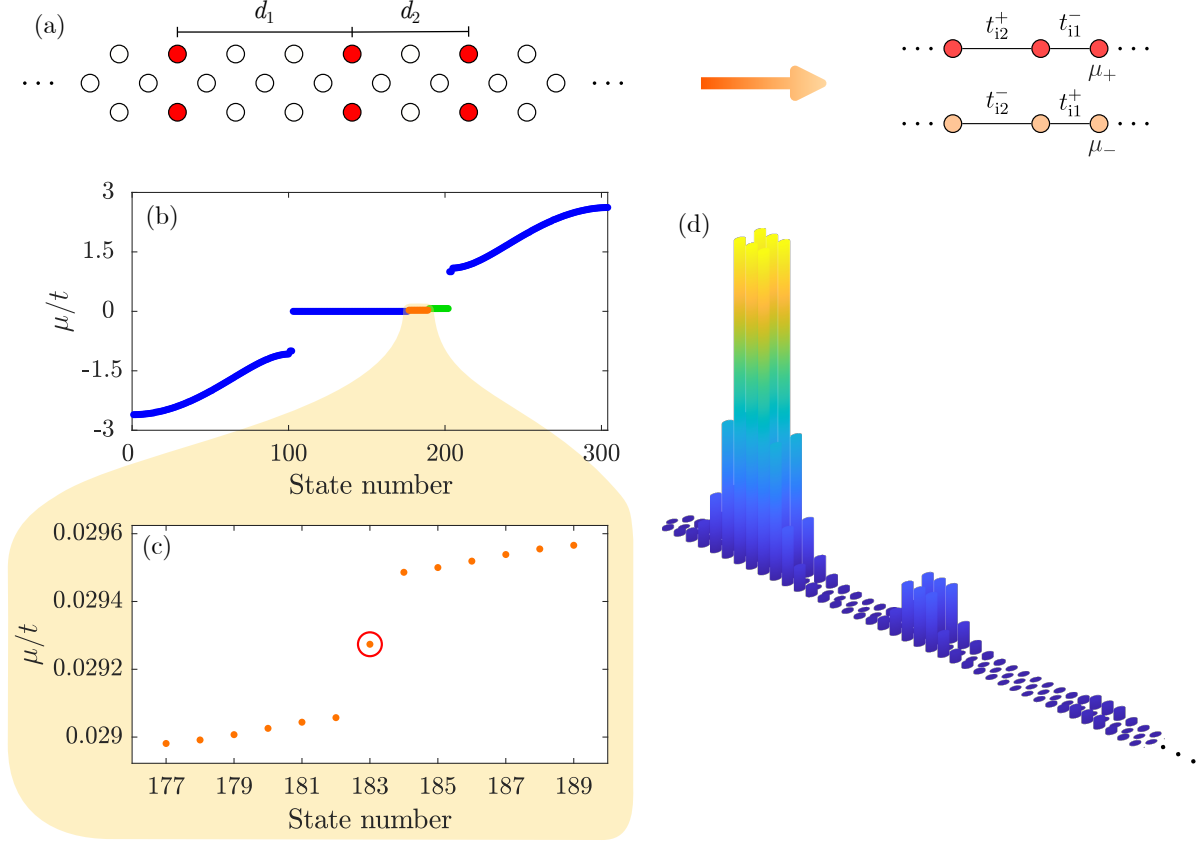


Figure 5.8: (a) A diamond chain decorated with a staggered impurity distribution in the top and bottom sites hosts two effective low-energy SSH sub-systems. (b) Energy spectrum for a diamond chain of  $N_c = 101$  unit cells and thirteen impurities  $\epsilon_B = \epsilon_C = \epsilon = 0.1t$ , with  $\phi = \pi/2$  and relative distances  $d_1 = 8$  and  $d_2 = 6$  that yield a coupling ratio of  $t_{i1}^-/t_{i2}^- = 0.17$ . From the FB, two effective SSH systems centered around different energies (orange and green dots) emerge as a consequence of the coupling of impurity states. (c) Spectrum of the lower-energy SSH system (orange dots) highlighted in (b). The state marked with a red circle is its topological edge state. We show in (d) the absolute value of its amplitudes on each site for a segment of the chain.

not localized around the edge of the diamond chain, but rather around the edge of the impurity sub-system. The features of the effective system may be controlled by tuning the parameter values of the diamond chain. Therefore, choosing an appropriate distribution for the impurities allows to design a wide range of one-dimensional (1D) models. Nonetheless, the flux through each plaquette remains a key property, as it affects both the energies and the couplings of the effective system, as can be seen from (5.24) and (5.25). In particular, the extension of the impurity states grows for weaker flux, see Fig. 5.7, as does the coupling between states localized around adjacent impurity pairs and the gap of the effective system.

Most remarkably, the coupling between impurity states is not limited only to real values, and can be pushed into the complex plane by including complex onsite potentials. Namely, one can impose  $\epsilon = |\epsilon|e^{i\rho}$ , which has two main consequences in the spectrum, as we showcase in Fig. 5.9 for  $\rho = \pi/4$ . Firstly, all eigenstates in the conductive bands with finite weight on the impurity sites pick up a small imaginary component in their energies. This effect, however, is nullified when the impurities are balanced, i.e.  $\epsilon_B = -\epsilon_C$ . Secondly, and more interestingly, the spectra of the effective SSH systems rotate along the complex plane according to the angle  $\rho$ , as can be seen in the inset in Fig. 5.9.

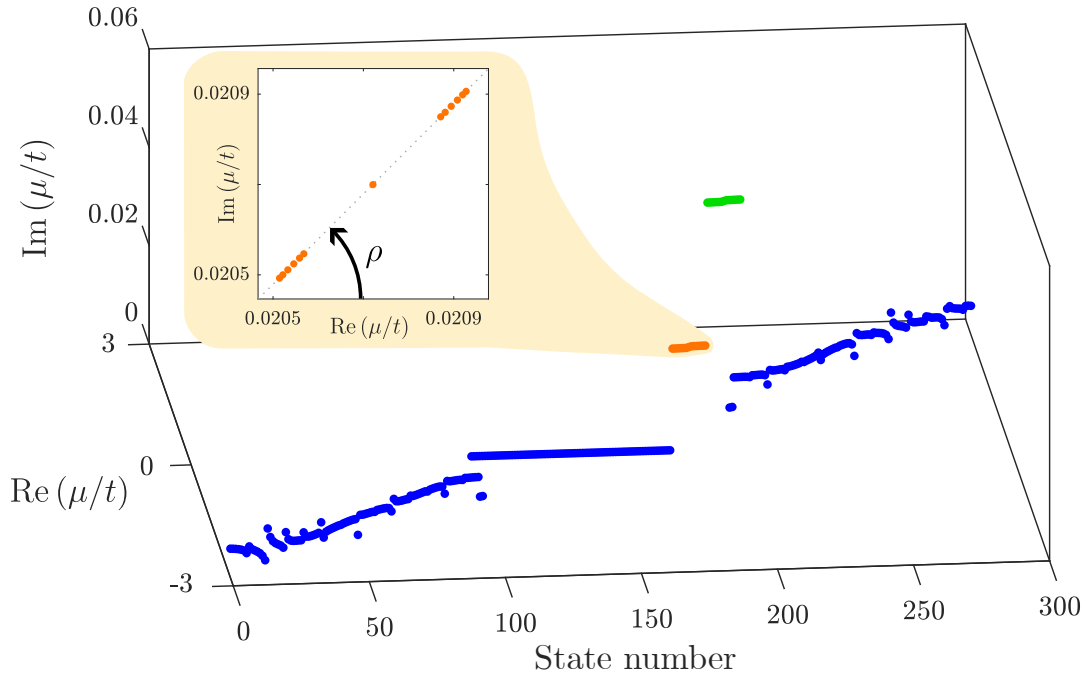


Figure 5.9: Complex energy spectrum for the diamond chain with complex onsite impurities  $\epsilon_B = \epsilon_C = \epsilon e^{i\rho}$ , with  $\rho = \pi/4$ , and the same lattice parameter values as in Fig. 5.8. The spectra of the effective SSH systems rotate along the complex plane by an angle  $\rho$ , as can be observed in the inset.

By virtue of this rotation, one can readily deduce that the effective Hamiltonian of each SSH becomes  $\tilde{H}_{\text{eff}} = e^{i\rho} H_{\text{eff}}$  compared to the cases in Fig. 5.8, implying that they are now *non-Hermitian*. This effect could open up the possibility of experimentally exploring non-Hermitian couplings in FB systems by employing lossy impurities, where the coupling strength is determined by the flux per plaquette and the angle of rotation  $\rho$  by the included losses.

### 5.4.1 Disorder

Due to the dependence of the extension of the impurity states on the flux, a disorder on the flux translates into disorder in both the onsite energies and the couplings of the effective system, and thus breaks the chiral symmetry of the effective SSH model. We introduce a random flux disorder of strength  $\eta$  in each plaquette,  $\phi_q = \phi + \eta_q$ , sampled from a uniform distribution  $\eta_q \in [-\eta/2, \eta/2]$  as sketched in Fig. 5.10(a). We explore the consequences of this disorder by checking the variation of the edge state gap  $\Delta = \min(|\mu_m - \mu_{m\pm 1}|)$  for the edge state  $m$  of the SSH system in Fig. 5.8(c) as the perturbation is increased. We plot in Fig. 5.10(b) the size of this gap and its standard deviation for different values of the central flux  $\phi$ , averaged over 1000 random realizations for each  $\eta$ , in steps of  $\Delta\eta = 0.01$  rad. We see that disorder distorts the effective system, reducing the gap on average for increasing flux disorder. In general, however, for a weak  $\phi$  the system displays a larger gap that is also more resilient to disorder compared to fluxes closer to  $\pi$ . This is made evident in Fig. 5.10(c), where the average gap in each case is compared to the one for the pristine system,  $\Delta_0$ . The plot shows how weaker fluxes display a slower decay, even for values of disorder of the same order as  $\phi$  itself. This behavior is closely related to the extension of the impurity states. Although flux disorder breaks chiral symmetry, the impurity states feel the effects of an averaged disorder over their whole characteristic length [217], which tends to the effective restoration of chiral symmetry. This average effect becomes stronger for longer extensions, implying an overall weaker effect of the disorder. The flux-dependent extension of the impurity states thus becomes a pivotal property of the system, as it is directly related to their robustness against disorder [215, 216].

We justify this averaging effect further below, but we first describe the effects of coupling disorder on the system. The chiral symmetry of the SSH model protects it against off-diagonal disorder. However, coupling disorder in the parent diamond chain does not necessarily translate into such a disorder for the effective system. Uncorrelated coupling disorder, as sketched in Fig. 5.10(d), affects the amplitude distribution of the CLSs themselves as well as their overlap, thus affecting the effective impurity system in a similar manner to flux disorder. We prove this fact by including a random coupling disorder in each link such that  $t_j = t + \tilde{t}_j$ , for  $\tilde{t}_j \in [-\tilde{t}/2, \tilde{t}/2]$ . In Figs. 5.10(e) and

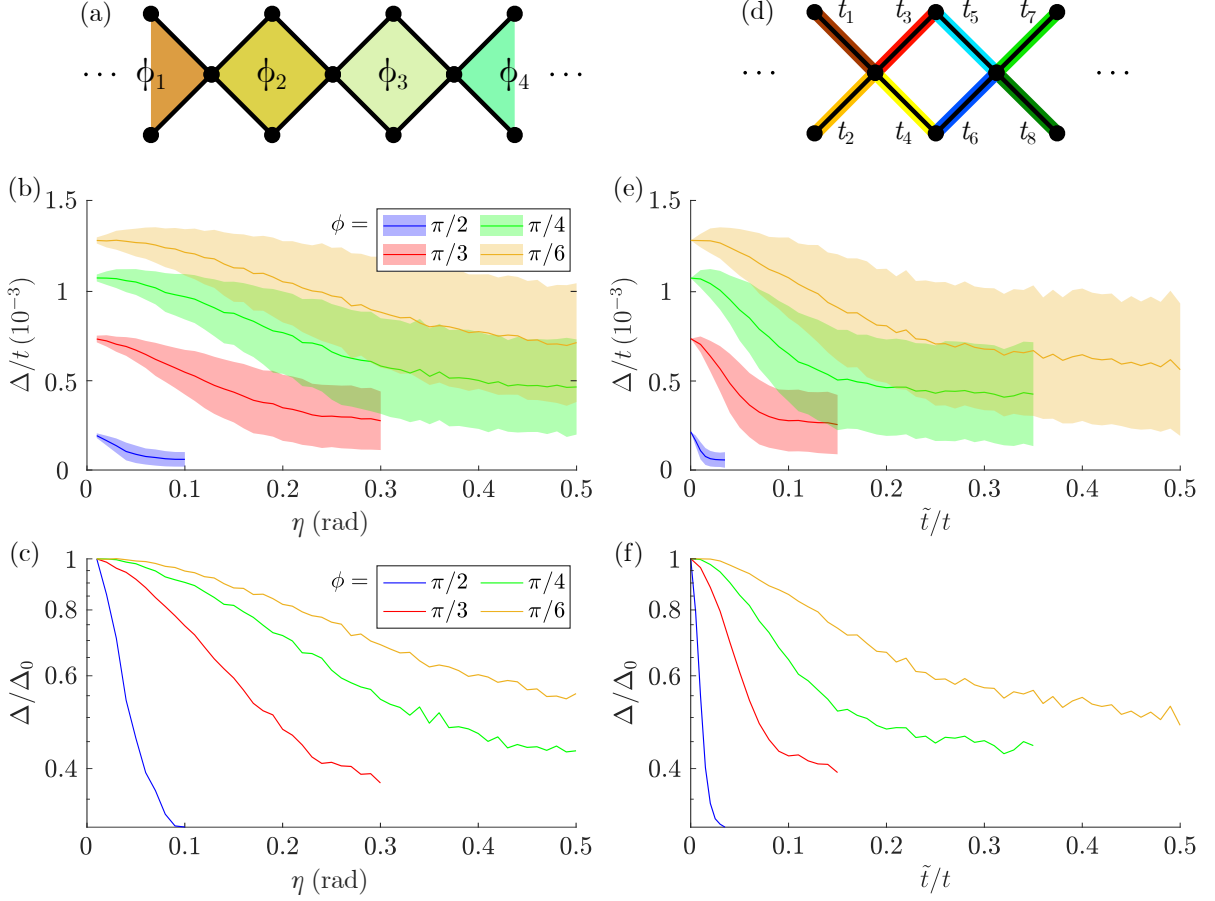


Figure 5.10: Effects of disorder on the spectrum of the effective system of Fig. 5.8(a). (a) Sketch of flux disorder, where each plaquette is threaded by a random flux centered around  $\phi$ . (b) Average gap size  $\Delta$  of the edge state of the effective SSH model (solid lines) and standard deviation (shaded region) for increasing flux disorder strengths and different values of  $\phi$ . (c) Disordered average gap size  $\Delta$  relative to the clean system's gap  $\Delta_0$  for the same flux values as in (b). (d) Sketch of uncorrelated coupling disorder, where each link displays a random coupling sampled uniformly around  $t$ . (e) Average gap size (solid lines) and standard deviation (shaded regions) for uncorrelated coupling disorder, for the same central flux values  $\phi$  as in (b). (f) Average gap size relative to the clean system's gap for uncorrelated coupling disorder. In all cases, we employ 1000 different realizations of disorder.

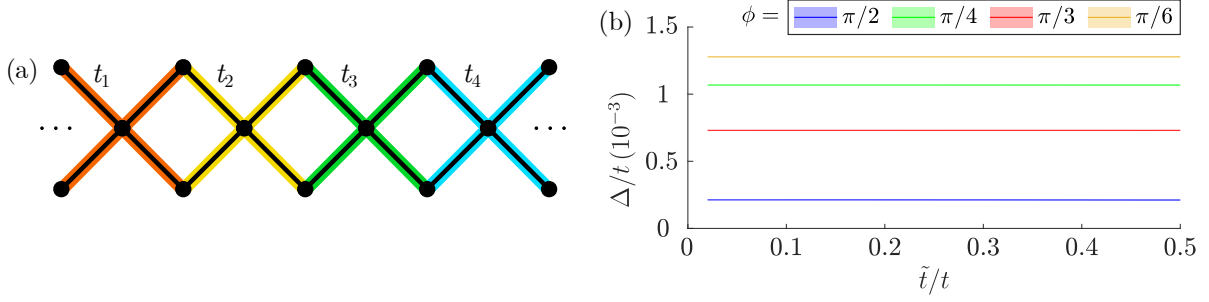


Figure 5.11: Effects of correlated coupling disorder on the spectrum of the effective system. (a) Sketch of the considered disorder, introduced in quartets as indicated by the different link colors. (b) Average gap size  $\Delta$  of the edge state of the effective SSH model (solid lines) and standard deviation (shaded region) for different flux values. In this scale, the shaded regions are too thin to be observed.

(f), we plot the average gap size and its standard deviation for different values of  $\phi$  and its comparison with the one on the pristine system, respectively. Following the trend depicted in Figs. 5.10(b) and (c) for flux disorder, we observe how uncorrelated coupling disorder heavily affects the spectrum and the gap of the effective system, but is partially resisted on average for low fluxes even for disorder strengths up to 50% of the value of  $t$ .

On the other hand, for coupling disorder to translate into off-diagonal disorder in the effective system, it must be introduced in a correlated manner. As CLSs occupy two plaquettes for fluxes between 0 and  $\pi$ , any coupling disorder within the span of each CLS will affect their amplitudes and energies, hence breaking the chiral symmetry of the effective system. For the disorder to be chiral, it has to be introduced in hopping quartets [220] as highlighted in Fig. 5.11(a), so that it may affect the coupling between impurity states without distorting the CLSs themselves. We plot in Fig. 5.11(b) the effects of this disorder on the gap size of the effective system. Comparing with Fig. 5.10, we observe that the edge state gap is immune to correlated disorder even for  $\phi = \pi/2$ . Both for flux as well as coupling disorder, results for the other non-highlighted subsystem are similar to those depicted here. Nonetheless, when comparing the two systems, the lower-energy one displays a higher robustness to disorder owing to the higher extension of its states that enhances the disorder averaging effect, which we now delve into.

### Averaging effect of disorder

To prove the existence of this averaging effect of disorder in our system, we introduce diagonal disorder by setting the onsite potential at each site to a random value taken from a uniform distribution in the interval  $[-\delta/2, \delta/2]$ , with  $\delta = 0.02$  as the disorder strength. Note that the standard deviation of such a distribution is given by  $\sigma_{\text{ud}} =$

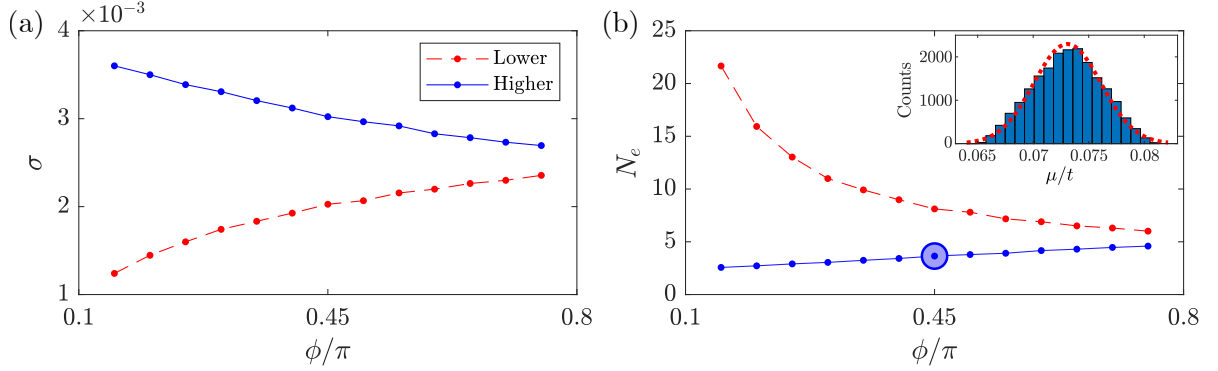


Figure 5.12: (a) Standard deviation, as a function of the flux, of the energy of both impurity states for an open diamond chain with 101 plaquettes with equal impurities  $\epsilon = 0.1t$  in the middle one. For each point, we have performed 20000 realizations of diagonal disorder with disorder strength  $\delta = 0.02$ . (b) Effective number of sites involved in the disorder averaging effect, computed from the corresponding standard deviation values in (a) in accordance with the CLT. The inset shows the energy histogram for the encircled higher-energy state at  $\phi = 0.45\pi$ , with the red dotted curve corresponding to the Gaussian fit from which the standard deviation is extracted.

$\frac{\delta}{\sqrt{12}} \approx 5.8 \times 10^{-3}$  [409]. We remark that for the sites at the midchain plaquette hosting the impurities, the disorder is added on top of  $\epsilon = 0.1t$ . We perform 20000 disorder realizations for each flux value and track the energies of the impurity states. The distributions of energies are used to construct histograms, as exemplified in the inset of Fig. 5.12(b) for the higher-energy state at  $\phi = \frac{9\pi}{20}$ . Remarkably, the underlying uniform distribution of the disorder generates a normal distribution for the energies of the impurity states, whose mean approaches their disorder-free values given in Eq. (5.25) as we increase the number of realizations. This result is consistent with the central limit theorem (CLT) [409, 410], which states that, given a sample of random variables, the average value of the sample tends to follow a normal distribution if the sample size is large enough. In other words, the average effect of many random variables tends to a Gaussian distribution as we increase the number of realizations. Therefore, considering again the Gaussian distribution for the energy of the impurity states in the inset of Fig. 5.12(b), we can conclude that these states effectively feel the effect of an *averaged disorder* in each realization. The averaged effect is in turn related to their localization length or, equivalently, to their spatial extension.

In Fig. 5.12(a), we plot the standard deviation of the Gaussian fits, which are applied to the energy distributions of both impurity states, as a function of the flux. The flux was taken in increments of  $\frac{\pi}{20}$  and restricted to the  $[\frac{3\pi}{20}, \frac{15\pi}{20}]$  interval, since near  $\phi = 0, \pi$  the energy separation of the states is of the order of  $\delta$ . This leads to a reordering of the states and to an overlap of their corresponding energy distributions, preventing their



independent analysis. According to the CLT [410], the standard deviation of the normal distribution is related to the sample size, which in our case corresponds to the effective number of sites  $N_e$  over which the disorder is averaged for each impurity state, through  $\sigma = \frac{\sigma_{\text{ud}}}{\sqrt{N_e}}$ , with  $\sigma_{\text{ud}}$  given above. With this formula, and from the  $\sigma$  values given in Fig. 5.12(a), we plot in Fig. 5.12(b) the flux dependence of  $N_e$  for both impurity states. Interestingly, it can be seen that they follow opposite tendencies with decreasing flux: while  $N_e$  increases exponentially for the lower state, it decreases monotonously for the higher state.

The dependence of the spatial profile of the impurity states with flux, shown in Fig. 5.7, can be used to explain their different response to disorder. The lower state becomes globally less localized as flux decreases, starting from the profile of a regular CLS at  $\phi = \pi$ . This agrees with its increasing  $N_e$  in Fig. 5.12(b), since the disorder is being averaged over more sites, thus generating a lower effective disorder. The higher state, on the other hand, has dominant contributions from the central peaks located at the impurity sites, which become more prominent as the flux decreases. Despite the fact that its exponential tails at sites other than the central ones become increasingly delocalized for lower flux, the main contributors to the number of effective sites  $N_e$  of the averaged disorder remain the central peaks. This effect, which tends to decrease  $N_e$  as the flux decreases, overpowers the delocalization of the exponential tails, leading to the behavior observed in Fig. 5.12(b). While, strictly speaking, the normal distribution of the sample means expected from CLT is only exact in the limit of infinite sample size,  $N_e \rightarrow \infty$ , we have checked numerically that a Gaussian fit is in very good agreement with the energy histogram of all points in Fig. 5.12(b). This includes the higher-energy state, as exemplified in the inset, where the effective number of sites responsible for the averaged disorder is small, ranging from  $N_e \approx 2.5$  to  $N_e \approx 5$ . As for the cases of opposite impurities in Sec. 5.3.1 and of a single impurity in Sec. 5.3.3, we have checked numerically that this averaging effect is less pronounced. Under the same kind of diagonal disorder and for different flux values, the energy histogram of these other impurity states yields in general a mix between Gaussian and uniform distributions, signaling a number of effective sites involved in the averaging effect close to one, such that the CLT cannot be used to determine this number. This can be explained from the dominant weight that these states always have at one of the impurity sites [see the central peak in Figs. 5.3(a) and (e)], which is where the perturbative effects of disorder are felt the most.

The averaging of diagonal disorder on the impurity states, conjectured to be the mechanism behind the enhanced robustness to disorder displayed by certain domain wall states with similar localization properties [217], is quantitatively confirmed here by the numerical results of Fig. 5.12. For the case studied in this section, this enhanced robustness to disorder is greater for the lower impurity state at low flux values where, according to Fig. 5.12(b),  $N_e$  is maximized.

## 5.5 Implementation in optical waveguides

In this section, we discuss a proposal for experimentally implementing the effective impurity systems studied in this chapter in lattices of cylindrical optical waveguides. In particular, we consider a zig-zag chain of optical waveguides with a relative distance of  $d$  and a staggered relative angle of  $\theta$ , as depicted in Fig. 5.13(a). As shown in Sec. 2.1.2, these will guide orbital angular momentum (OAM) modes of the form

$$E^{\pm l}(r, \varphi, z) = e^{\pm l}(r) e^{\pm i l (\varphi - \varphi_0)} e^{-i \beta_l z}, \quad (5.32)$$

where  $l$  is the OAM charge,  $(r, \varphi, z)$  are the cylindrical coordinates centered at each waveguide,  $e^{\pm l}(r)$  the radial mode profile,  $\varphi_0$  an arbitrary phase origin and  $\beta_l$  the propagation constant of the mode. According to the modes that are guided in each case, we will consider two types of waveguides. The first set [lower row in Fig. 5.13(a)] will guide only the fundamental  $l = 0$  mode, while the second set [upper row in Fig. 5.13(a)] will also guide the  $l = 1$  modes. By tuning the refractive index contrast of both sets, one can achieve phase matching between the aforementioned  $l = 0$  and  $l = 1$  modes. In such a scenario, this subset of modes forms an effective diamond chain model by considering the mode circulations as a synthetic dimension. The  $l = 0$  modes become the central sites, while the  $\mathcal{K} = \pm$  circulations of the  $l = 1$  modes become the top and bottom sites of the diamond, respectively, as shown in the right-hand side of Fig. 5.13(a). Furthermore, it is known that the coupling between OAM modes picks up a phase according to their momentum charge and their circulation, as well as the coupling angle  $\theta$  with respect to an arbitrary direction  $\varphi_0$  [115, 116, 265] [see Fig. 5.13(a)]. In other words:

$$\tau_{l_1, l_2} = |\tau_{l_1, l_2}| e^{i(\mathcal{K}_1 l_1 - \mathcal{K}_2 l_2) \theta}. \quad (5.33)$$

The different possible couplings between the OAM modes that we consider in this chapter were detailed in Sec. 2.1.4, and in particular in Fig. 2.6. As we will show later, for the considered range of parameter values, the system is well-described by a nearest-neighbor (NN) coupling  $\tau$  as given in (2.83) between  $l = 0$  and  $l = 1$  modes. Considering our geometry, the synthetic dimension formed by  $l = 1$  modes and the expression in (5.33), this implies a flux per plaquette of twice the geometric angle  $2\theta$  throughout the diamond chain. Therefore, any arbitrary value for the flux can be generated by tuning this angle. The implementation of the system in Fig. 5.8(a) is completed by perturbing the refractive index of the  $l = 1$  waveguides. Since the two OAM components that form the top and bottom sites in the diamond come from the same physical waveguide, we are limited to the case of equal impurities  $\epsilon_B = \epsilon_C = \epsilon$  in the effective system.

For our numerical simulations, we consider cylindrical waveguides of radius  $R = 12 \mu\text{m}$  separated by a relative distance  $d = 55 \mu\text{m}$  and with a cladding refractive index of  $n = 1.48$ . The  $l = 0$  waveguides display a contrast of  $\Delta n_0 = 1 \times 10^{-4}$  and the

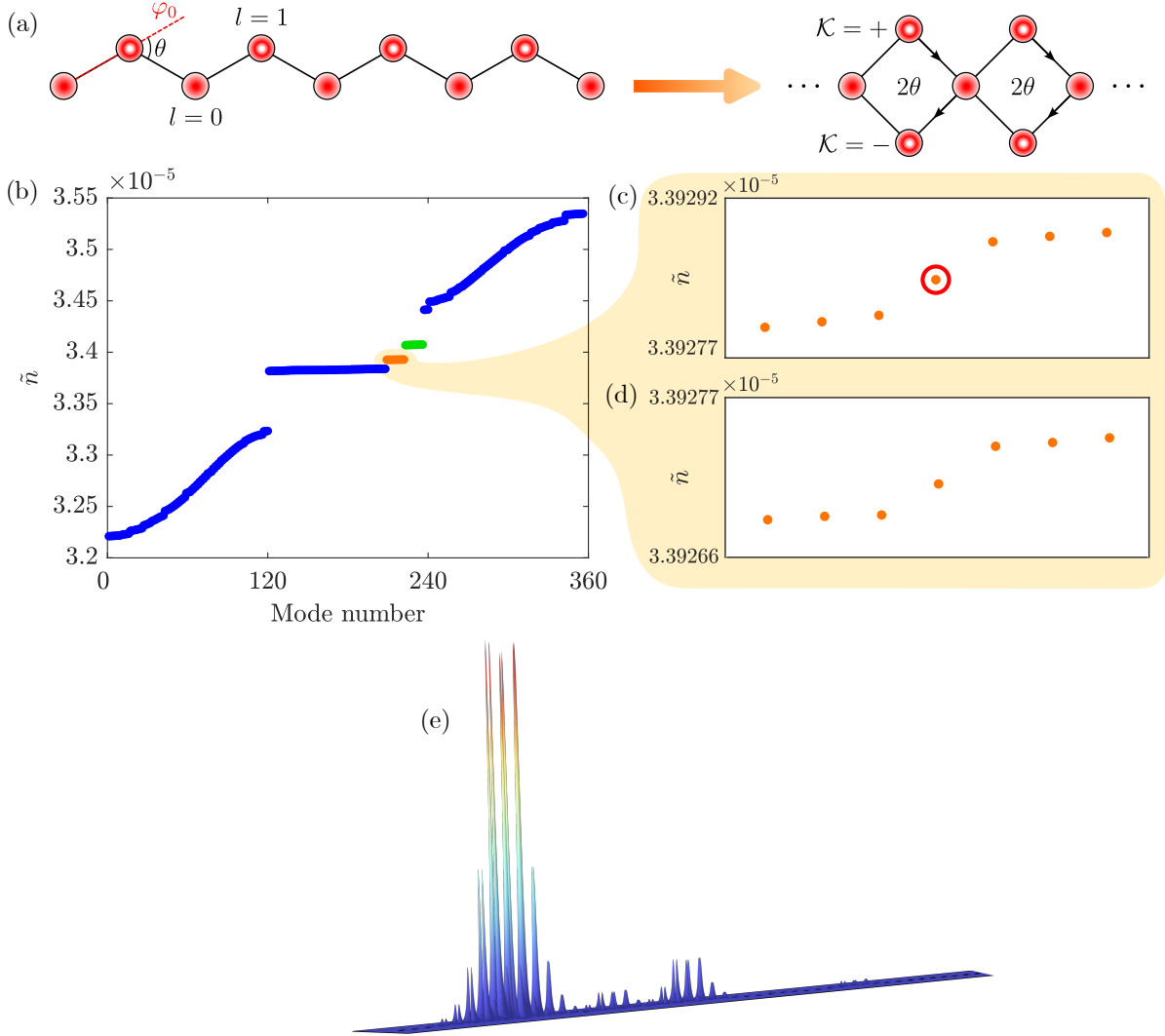


Figure 5.13: Implementation of the effective SSH model in a lattice of waveguides hosting OAM modes. (a) Coupled optical waveguides forming a zig-zag chain with alternating  $l = 0$  and  $l = 1$  OAM charges and a staggered relative angle  $\theta$  with respect to the reference axis  $\varphi_0$ , which behaves as diamond chain lattice with a flux per plaquette of  $2\theta$ . The circulations of the  $l = 1$  modes can be split in a synthetic dimension that forms the top and bottom sites of the diamond. (b) Spectrum of effective mode indices with respect to the cladding index,  $\tilde{n} = n_{\text{eff}} - n_0$ , for a waveguide lattice of  $N_c = 59$  unit cells, a relative angle of  $\theta = \pi/4$  ( $\phi = \pi/2$ ) and 13 impurity pairs in a staggered pattern  $d_1 = 8$  and  $d_2 = 6$ . (c)–(d) Highlights of the lower-energy SSH sub-system (orange dots). Since each waveguide can host two orthogonal mode polarizations, the eigensolver picks up two orthogonal spectra for each SSH system and the spectrum appears doubled. (e) Electric field norms on each waveguide for the edge state circled in red in (c).

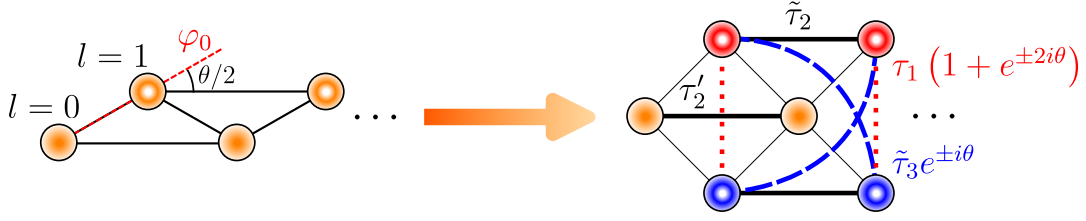


Figure 5.14: Full coupling scheme in the diamond chain featured in Fig. 5.13(a), including the phases induced by the geometrical angle. The NN couplings are also sketched for clarity. Cross-circulation couplings in the  $l = 1$  waveguides due to the nearest  $l = 1$  waveguides,  $\tilde{\tau}_1$ , are much smaller than  $\tau_1$  and are thus not included in the picture.

matching contrast for  $l = 1$  waveguides is computed to be  $\Delta n_1 = 2.579 \times 10^{-4}$  for a wavelength of  $\lambda = 730$  nm. We impose small impurities on top of some  $l = 1$  waveguides by adding an additional contrast of  $\Delta n_{\text{imp}} = 6 \times 10^{-7}$  at alternating distances of 8 and 6 unit cells to achieve the staggering, and choose a relative angle of  $\theta = \pi/4$  equivalent to a flux value of  $\phi = \pi/2$ . Using these parameter values, we simulate a chain of  $N = 59$  unit cells using the commercial finite-element solver COMSOL Multiphysics. As depicted in Fig. 5.13(b), we obtain the eigenmodes of the structure, closely matching those obtained in the tight-binding model described in Sec. 5.4. The insets of the figure show that we obtain a doubled spectrum, which is due to the orthogonal mode polarizations that can be guided by the waveguide structure. These have similar mode profiles but different projections  $(E_x, E_y, E_z)$ , and are both picked up by the eigensolver. We showcase in Fig. 5.13(c) the electric field norms  $|E|$  in the waveguide system of the highlighted edge state in the bottom right inset of Fig. 5.13(b).

The simulations display a remarkable agreement with the theoretical results. However, there exist possible sources of discrepancy with the original model in the form of additional couplings. In Fig. 5.14, we show the complete coupling scheme in our system up to next-nearest neighbor (NNN) couplings. To estimate the importance of each one, we simulate three sets of two coupled waveguides containing the following OAM modes: (a)  $l = 0 \leftrightarrow l = 0$ , (b)  $l = 1 \leftrightarrow l = 1$  and (c)  $l = 0 \leftrightarrow l = 1$ . Then, we compute each coupling through the expressions (2.77), (2.80) and (2.83) in Sec. 2.1.4, respectively, and display them in Fig. 5.15. For our considered relative distance of  $d = 55 \mu\text{m}$ , the NN coupling has a value of  $\tau = 5.08 \text{ m}^{-1}$ . First, the cross-circulation coupling, which emerges due to the breaking of the cylindrical symmetry of the modes caused by the presence of other waveguides [265], is valued at  $\tau_1 = -0.12 \text{ m}^{-1} = -0.024 \tau$  at the same distance. Being around two orders of magnitude lower than  $\tau$ , we can safely neglect it. On the other hand, the distance  $d'$  corresponding to NNN couplings will vary depending on the angle  $\theta$ . For the limiting case of  $\theta = \pi/2$ , and thus a flux of  $\pi$ , the NNN distance between waveguides becomes as short as  $d' = \sqrt{2}d$ . We summarize the NNN

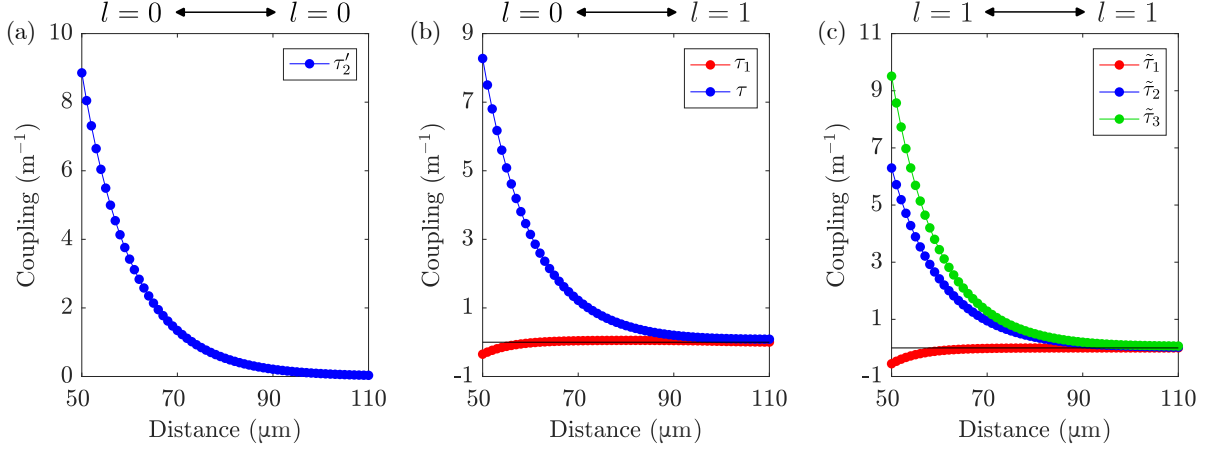


Figure 5.15: Coupling strengths between waveguides with different OAM modal content at increasing relative distances, for the waveguide parameter values included in the text. The  $\tau_1$  coupling is at least an order of magnitude lower than the rest at all distances, both in (b) and (c).

	$\phi = \pi$	$\phi = \pi/2$
$\tau_2' (l = 0, \quad 0 \leftrightarrow 0)$	12.82%	2.58%
$\tilde{\tau}_2 (l = 1, \quad \pm \leftrightarrow \pm)$	9.04%	1.82%
$\tilde{\tau}_3 (l = 1, \quad \pm \leftrightarrow \mp)$	12%	2.58%

Table 5.1: NNN coupling strength values for different fluxes, relative to the value for the NN coupling at  $d = 55 \mu\text{m}$ .

couplings at this limit of  $\theta = \pi/2$  ( $d' = 77.8 \mu\text{m}$ ), as well as for a lower angle of  $\theta = \pi/4$  ( $d' = 101.64 \mu\text{m}$ ) in Table 5.1. We do not include the NNN cross-circulation coupling  $\tilde{\tau}_1$  as it is at least an order of magnitude lower than the others at all distances.

We can observe how the exponential nature of the couplings quickly makes these couplings negligible as the angle decreases. Even though these are at least an order of magnitude lower than the main coupling  $\tau$ , they can nonetheless perturb the bands of the system and cause some states to deviate from the FB. With the coupling strengths in Table 5.1, we simulate the tight-binding model of a diamond chain model with NNN and cross-circulation couplings, see Fig. 5.14, and compare the obtained spectrum with a system with only NN couplings in Fig. 5.16. For fluxes close to  $\pi$ , where the geometrical angle is large and thus the NNN distances relatively small, the deformation of the bands is evident. In Fig. 5.16(a), one can observe that the top and bottom bands are not flat as they should be, but rather dispersive. The same effect happens to a sizeable portion of the central band, which significantly tilts to lower energies. Conversely, for  $\phi = \pi/2$  and lower fluxes, the deviations caused by these couplings become much smaller

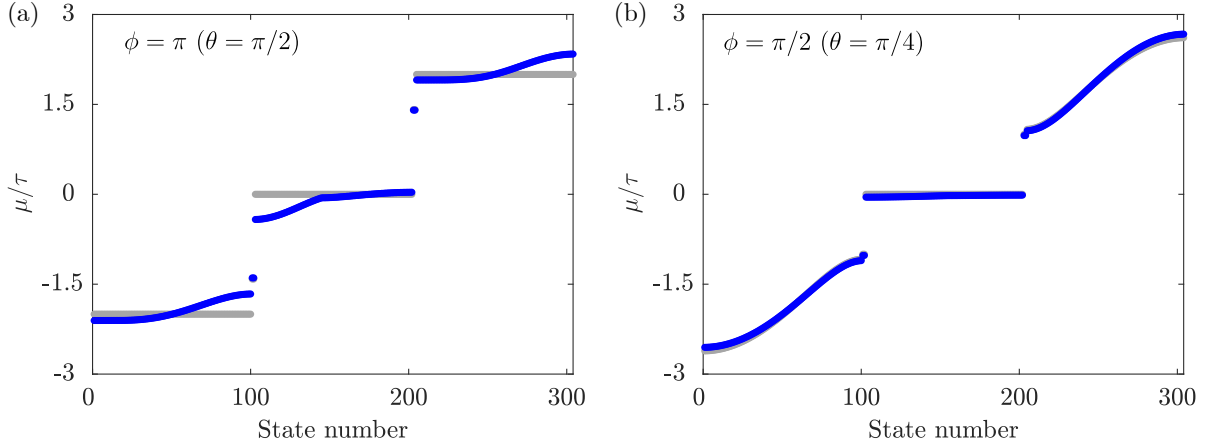


Figure 5.16: Energy spectrum of the diamond chain for (a)  $\phi = \pi$  ( $\theta = \pi/2$ ) and (b)  $\phi = \pi/2$  ( $\theta = \pi/4$ ), using the coupling strengths obtained from the waveguide simulations in Fig. 5.15 at  $d = 55\mu\text{m}$  and for  $N_c = 101$  plaquettes. The spectrum in blue corresponds to a system with both a cross-circulation coupling and the NNN couplings included in Table 5.1, whereas the gray spectrum corresponds to a system with only NN couplings.

and increasingly negligible as can be observed in Fig. 5.16(b). Therefore, limiting the study to  $0 < \theta \leq \frac{\pi}{4}$  (corresponding to  $0 < \phi \leq \frac{\pi}{2}$ ), as was done for the results in Fig. 5.13, guarantees that only the considered NN coupling plays a significant role in the system. One way to safely surpass this limit could be to employ higher-order OAM modes [219]. From the expression in (5.33) we gather that the induced phase in the coupling increases for higher OAM charges, which could allow to imprint higher fluxes with smaller geometrical angles, corresponding to larger  $d'$ . Note, however, that these higher-order modes are more spatially extended [234], so the NNN couplings in that case would be larger as a consequence.

## 5.6 Conclusions

We have demonstrated a method to engineer an arbitrary system from the CLSs of a FB lattice, and whose parameters are controlled via the flux that threads the plaquettes of the original system. By decorating the FB lattice with onsite impurities, CLSs can be made to couple, giving rise to an effective system in the subspace of exponentially decaying impurity states. An appropriate choice for the impurity positions leads to a manifestation of non-trivial topology and the appearance of edge states. To exemplify the method, we have imprinted an SSH model on top of a diamond chain lattice with nonzero flux per plaquette. By alternating the relative distance between impurities, the

characteristic staggered coupling distribution of the SSH model is achieved. We have then studied the behavior of the effective system when disorder of two kinds is introduced in the system. When correlated coupling disorder is applied, and thus chiral symmetry is preserved, the effective system is immune to it. On the other hand, when flux disorder or uncorrelated coupling disorder is introduced, chiral symmetry is no longer satisfied. Nonetheless, the system presents an increased robustness to non-chiral disorder owing to the large spatial extension of the impurity states. Effectively, the disorder is averaged out over their characteristic lengths, which in turn implies a lower distortion of the energy spectrum of the effective system [217]. This effect is also amplified at lower fluxes, where the extension of the states is larger. Moreover, we have provided quantitative evidence of this enhanced robustness for the case of random onsite disorder. By applying diagonal disorder following a uniform distribution to the diamond chain, the energy histogram of both impurity states is seen to follow a normal distribution for a wide range of flux values. By relating the standard deviations of the normal and uniform distributions, the effective number of sites involved in the disorder averaging effect can be computed. For larger effective sizes, the robustness to disorder is enhanced.

Additionally, we have provided a route for an experimental implementation of the proposed system using optical waveguides guiding light with OAM [159, 216, 218, 219]. The coupling of different OAM modes introduces a phase component in the couplings by controlling the geometric angle between waveguides. This phase serves as an artificial gauge field that provides the necessary flux to the system. Moreover, the different circulations of  $l = 1$  OAM modes are used as a synthetic dimension and translated as the top and bottom sites of the diamond chain, while  $l = 0$  modes form the central sites. The onsite impurities can be included by manipulating the propagation constant of the corresponding waveguides by changing their size or refractive index. The proposed platform gives complete freedom over the choice of the flux per plaquette. The energy bands have been shown to closely replicate those of the diamond chain for fluxes lower than  $\pi/2$ , with only minor band distortions appearing for fluxes nearing  $\pi$ .

Our work lays the groundwork for future studies involving impurity-decorated systems and FB models with non-orthogonal CLSs. The method for generating effective models by impurity decorating flat band systems with non-orthogonal bases can be readily generalized to higher-dimensional systems, such as the Lieb lattice [102–105, 356], where higher-order TIs may be explored. Furthermore, and as exemplified here, non-Hermitian couplings are also easily achievable by including onsite gains and losses, opening a new FB-based venue for the study of non-Hermitian physics. Aside from optical waveguides guiding OAM, other platforms capable of controlling the phase of the couplings could be well suited for an alternative experimental implementation. Still within the frame of photonic waveguides, arrays of coupled multiorbital waveguides [401, 402, 411] have been used to produce negative couplings and thus allow to introduce

$\pi$  fluxes in the system, but they lack the freedom of arbitrary flux that OAM provides. Alternatively, in waveguide arrays an arbitrary synthetic flux may also be generated by an appropriate bending of the lattice along its longitudinal direction combined with modulations of the propagation constants of different waveguides [158]. On the other hand, in photonic resonator arrays the synthetic flux can be controlled by modifying the optical paths of the auxiliary rings, which generate the coupling between main rings, in an asymmetric manner [152, 167, 220, 284, 391, 412], e.g. by displacing them from the line that joins the center of the main rings. In this case, the impurities can be introduced by slightly perturbing the resonance condition of the main lattice rings locally [199]. Outside of photonics, electrical circuits [136, 195, 196] can also provide an appropriate venue for implementation, as they have a remarkable flexibility and allow to recreate most tight-binding models by connecting nodes with capacitors or inductors. It has also been shown that arbitrary phase factors can be added to the couplings in this platform [413].





---

## Root topological insulators of arbitrary order in Non-Hermitian photonic ring resonators

---

Square-root topology [119] is one of the newest additions to the ever expanding field of topological insulators (TIs). It characterizes systems that relate to their parent TI through the squaring of their Hamiltonians. Extensions to  $2^n$ -root topology, where  $n$  is the number of squaring operations involved in retrieving the parent TI, were quick to follow [128]. Here, we go one step further and develop the framework for designing general  $n$ -root TIs, with  $n$  any positive integer, using the Su-Schrieffer-Heeger (SSH) model as the parent TI from which the higher-root versions are constructed [220]. The method relies on using loops of unidirectional couplings as building blocks, such that the resulting model is non-Hermitian and embedded with a generalized chiral symmetry. Edge states are observed at the  $n$  branches of the complex energy spectrum, appearing within a ring gap in the complex plane, which is a novel type of gap that is shown to be irreducible to the usual point or line gaps. We further detail on how such an  $n$ -root model can be realistically implemented in photonic ring systems. Near perfect unidirectional effective couplings between the main rings can be generated via mediating link rings with modulated gains and losses [199]. These induce high imaginary gauge fields that strongly suppress couplings in one direction, while enhancing them in the other. We use these photonic lattices to validate and benchmark the analytical predictions. Our results introduce a new class of high-root topological models, as well as a route for their experimental realization.

The chapter is organized as follows. In Section 6.1, we motivate the interest in developing a method to produce root TIs of arbitrary order, as well as briefly describe

its implementation. Then, we begin the description of the  $\sqrt[3]{\text{SSH}}$  model and its main features in Section 6.2, including a discussion of its symmetries, a characterization of its topology in comparison with the SSH model, and a study of the robustness against disorder of its edge states. This is followed by the generalization to roots of any order in Section 6.3. After establishing the framework, we describe in detail the method to obtain quasi-unidirectional couplings using ring resonators in Section 6.4, where we also present the results of our simulations for the roots of order 3, 4 and 5. Finally, we lay our conclusions and outlook in Section 6.5.

## 6.1 Introduction

High-root topology has emerged as a rich new branch within the field of TIs. Square-root TIs ( $\sqrt{\text{TIs}}$ ) [119] were first proposed to characterize lattice models whose parent TI, from which its topological features are inherited, manifests itself as one of the diagonal blocks of the squared Hamiltonian [115, 120–122, 200, 248, 414–419]. Experimental realization of these models in different platforms followed soon [123–126, 420–424]. Subsequently, these systems were further generalized to  $2^n$ -root TIs ( $\sqrt[2^n]{\text{TIs}}$ ) [127–130], meaning models that connect to their parent TI through a sequence of  $n$  squaring operations. The first experimental demonstrations of quartic-root topology ( $n = 2$ ) appeared in the context of acoustic [131] and photonic [132] lattices. Studies on related topics, such as those of fractionally twisted models [425] or multiplicative topological phases [426], have also started to appear recently. The mathematical description of  $\sqrt{\text{TIs}}$  was carried out in Sec. 2.3.3 and exemplified through the calculation of the square root of the SSH model. In there, it is established that a key ingredient is the subdivision of the model into a bipartite graph. Although not explicitly computed, the generalization to  $2^n$  roots by further root partitions of the chain also appears in a relatively straightforward way.

As a direct follow-up, the question of whether general  $n$ -root TIs ( $\sqrt[n]{\text{TIs}}$ ) can be devised, with  $n \in \mathbb{N}$ , naturally arises. This has already been affirmatively answered for Floquet systems [427, 428], through a method based on subdividing the driving period into  $n$  subperiods, each with its own associated Hamiltonian. However, for non-driven systems, a natural generalization of  $\sqrt[2^n]{\text{TIs}}$  to  $\sqrt[n]{\text{TIs}}$  has been lacking so far. Here, we bridge this gap in the literature, and consider the SSH model [95] as the parent TI from which its higher-root versions ( $\sqrt[n]{\text{SSH}}$ ) are derived, following a novel procedure [220]. Specifically, instead of constructing bipartite chains to obtain the square root, the procedure involves constructing  $n$ -partite chains from loop modules of unidirectional couplings as the building blocks. Under open boundary conditions (OBC),  $n$  edge states, all decaying from the same edge [128], are seen to appear in the complex energy spectrum when in the topological phase.

The main challenge regarding the experimental design of the  $\sqrt[n]{\text{SSH}}$  model relates to the implementation of the unidirectional couplings in the loops. Although seemingly exotic, non-Hermitian couplings have been a matter of intense discussion in recent years, with theoretical proposals and experimental implementations appearing in many different platforms, including optical and acoustic ring resonators [199–204, 429–433], optical fibers and waveguides [205–208], ultracold atoms [189–192, 434], electrical circuits [138, 193–196], photonic crystals [209–211], synthetic dimensions [435–437], micropillar arrays [438, 439], mechanical lattices [197, 198], active particles [440], quantum walks of single photons [441, 442] and even robotic metamaterials [443]. In particular, we focus on optical ring resonators, which allow to obtain non-Hermitian couplings through the usage of adequately engineered link rings. The link rings feature a split gain/loss distribution, in which the upper half of the ring has optical gain while the lower half suffers losses. Through the presence of the link rings, and due to their balanced gain and loss distribution, an effective asymmetric coupling is enabled between the main rings [199], which is akin to an imaginary gauge field acting on the system. Additionally, a real flux of any desired value can also be generated by modifying the optical path of the upper and lower arms of the link rings, either by orthogonally displacing them from the line connecting the centers of the corresponding main rings [152], changing the lengths of each arm [151], or locally modifying them with external elements [167]. In each case, a phase is generated in the coupling between them that allows for the implementation of the synthetic flux.

## 6.2 Cubic-root SSH

Here we extend the methodology presented in Sec. 2.3.3 for square-root Hamiltonians to cubic-root [220], and beyond to any root order  $n \geq 3$  later on. Recall that for square roots, the technique to obtain the root Hamiltonian is based on subdividing the graph representation of the original system so as to obtain a bipartite model as the root. This, in turn, guaranteed that squaring the root Hamiltonian resulted in decoupled diagonal blocks, one of which was equal to the original Hamiltonian up to an identity term. This time, we wish to obtain a tripartite system that yields three decoupled blocks when taking the cube of the Hamiltonian. To achieve this, we employ unidirectional coupling loops of length 3 as linking elements, instead of single sites, leaving a simple path for the generalization by extending the length of the hopping loop. For cubic roots, and any root of higher order, the unidirectionality of the couplings renders the system non-Hermitian.

We thus start from the SSH model in Fig. 6.1(a) and substitute each link with three-hopping loops with rescaled couplings  $t_j \rightarrow \sqrt[3]{t_j}$ , arriving at the graph displayed in Fig. 6.1(b). To achieve the desired tripartite nature, we require three consecutive hoppings to lead back to the same sublattice [128, 129, 131, 221]. Note how this justifies

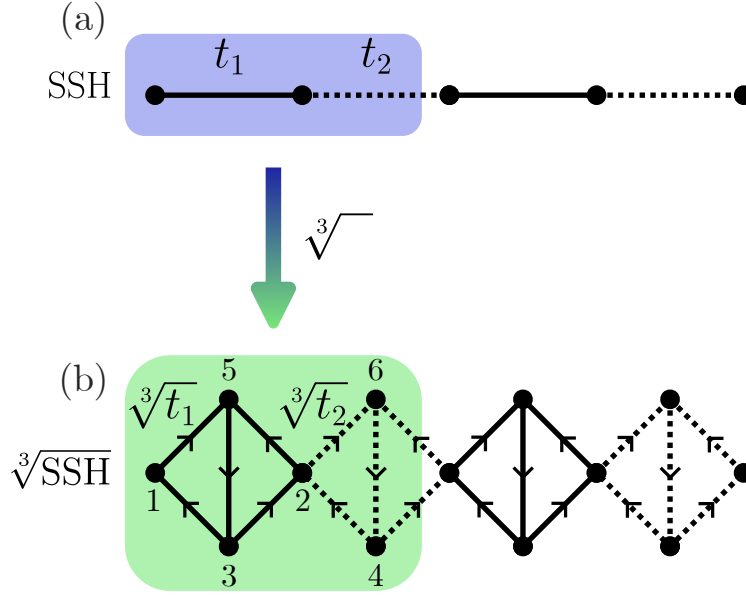


Figure 6.1: (a) Graph representation of the SSH model, with the blue shaded region indicating the unit cell of two sites. (b) Graph representation of the cubic root of the SSH model, with its unit cell shaded in green. To obtain it, each link is substituted by an unidirectional coupling loop consisting of three hoppings and two additional sites. The couplings are renormalized to  $\sqrt[3]{t_j}$ .

the need for unidirectionality: with Hermitian couplings, different paths could lead to different sublattices e.g. by going back and forth between two adjacent sites, and the model would not be tripartite. To recover the original SSH, one needs to compute the cubed graph. To do this, two types of paths need to be considered: those joining different sites as sketched in Fig. 6.2(a) and those leading to the same site as seen in Fig. 6.2(b), which represent the coupling and self-energy terms, respectively. Since forward and backward couplings are equal in the cubed graph, one can readily observe in Fig. 6.2(c) that we indeed recover the SSH model.

Let us now describe the root Hamiltonian. We consider the ordered  $\{|u(k)\rangle\}$  basis, with  $u = 1, 2, \dots, 6$ , as indicated in Fig. 6.1(b). The bulk Hamiltonian of the  $\sqrt[3]{\text{SSH}}$  model can then be written as

$$H_{\sqrt[3]{\text{SSH}}}(k) = \begin{pmatrix} 0 & h_1 & 0 \\ 0 & 0 & h_2 \\ h_3 & 0 & 0 \end{pmatrix}, \quad (6.1)$$

$$h_1 = h_3^\dagger = - \begin{pmatrix} \sqrt[3]{t_1} & \sqrt[3]{t_2} e^{-ik} \\ \sqrt[3]{t_1} & \sqrt[3]{t_2} \end{pmatrix}, \quad (6.2)$$

$$h_2 = - \begin{pmatrix} \sqrt[3]{t_1} & 0 \\ 0 & \sqrt[3]{t_2} \end{pmatrix}, \quad (6.3)$$

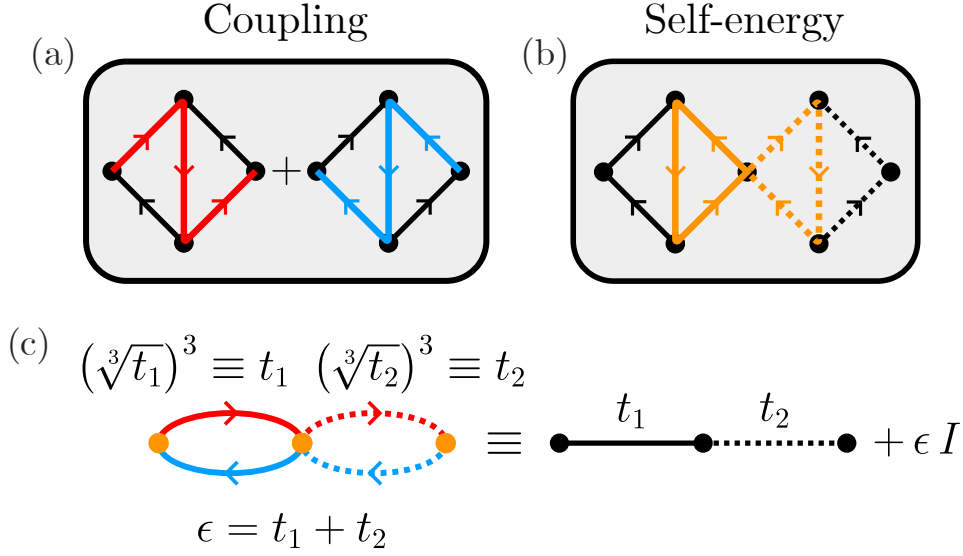


Figure 6.2: Sketch explaining how to recover the parent system by cubing the root graph. (a) The forward (red) and backward (blue) parent couplings are the result of taking three consecutive hoppings between the relevant sites. (b) The self energy is the result of the set of three-hopping paths that lead to the same site. (c) The result is a 1D lattice where forward and backward couplings are equal, i.e. Hermitian, and with a global onsite energy term that can be extracted as an identity term.

where the lattice spacing was set to unity. Note that the conjugate of (6.1) corresponding to a global inversion of all couplings,  $H(k) \rightarrow H^\dagger(k)$ , can also play the role of the root model. Due to its tripartite nature, defined by the sublattices (1, 2), (3, 4) and (5, 6) [221], this Hamiltonian obeys a generalized chiral symmetry,

$$\mathcal{C}_3 : \Gamma_3 H_{\sqrt[3]{\text{SSH}}}(k) \Gamma_3^{-1} = \eta_3^{-1} H_{\sqrt[3]{\text{SSH}}}(k), \quad (6.4)$$

$$\Gamma_3 = \text{diag}(I, \eta_3 I, \eta_3^{-1} I), \quad (6.5)$$

with  $\eta_3 = e^{i\frac{2\pi}{3}}$  and  $I$  the  $2 \times 2$  identity matrix. After cubing the Hamiltonian in (6.1) we obtain

$$[H_{\sqrt[3]{\text{SSH}}}]^3(k) = \begin{pmatrix} H_{\text{SSH}'}(k) & 0 & 0 \\ 0 & H_2(k) & 0 \\ 0 & 0 & H_3(k) \end{pmatrix}, \quad (6.6)$$

with the first block being

$$H_{\text{SSH}'}(k) = h_1 h_2 h_3 = H_{\text{SSH}}(k) - (t_1 + t_2)I. \quad (6.7)$$

The other diagonal blocks,  $H_2$  and  $H_3$ , are cyclic permutations of  $H_{\text{SSH}'}$ :

$$H_2(k) = h_2 h_3 h_1 = - \begin{pmatrix} 2t_1 & t_1^{\frac{2}{3}} t_2^{\frac{1}{3}} (1 + e^{-ik}) \\ t_1^{\frac{1}{3}} t_2^{\frac{2}{3}} (1 + e^{ik}) & 2t_2 \end{pmatrix}, \quad (6.8)$$

$$H_3(k) = h_3 h_1 h_2 = H_2^\dagger. \quad (6.9)$$

The eigenvalues and eigenvectors of  $H_{\text{SSH}'}$  can be readily determined to be

$$\mu_\pm(k) = -(t_1 + t_2) \pm \sqrt{t_1^2 + t_2^2 + 2t_1 t_2 \cos k}, \quad (6.10)$$

$$|u_{\text{SSH}}^\pm(k)\rangle = \frac{1}{\sqrt{2}} \begin{pmatrix} 1 \\ \mp e^{i\phi(k)} \end{pmatrix}, \quad (6.11)$$

$$\cot \phi(k) = \frac{t_1}{t_2 \sin k} + \cot k, \quad (6.12)$$

and one can easily show that the other diagonal blocks are isospectral to  $H_{\text{SSH}'}$  by realizing that  $h_3 H_{\text{SSH}'} = H_3 h_3$  and  $h_2 H_3 = H_2 h_2$ , according to (6.7)–(6.9). Hence, if one has  $H_{\text{SSH}'} |u_{\text{SSH}}^\pm\rangle = \mu_\pm |u_{\text{SSH}}^\pm\rangle$  and applies  $h_3$  from the left, one obtains:

$$h_3 H_{\text{SSH}'} |u_{\text{SSH}}^\pm\rangle = \mu_\pm h_3 |u_{\text{SSH}}^\pm\rangle \longrightarrow H_3 (h_3 |u_{\text{SSH}}^\pm\rangle) = \mu_\pm (h_3 |u_{\text{SSH}}^\pm\rangle), \quad (6.13)$$

and a similar procedure can be applied for  $H_2$ . The fact that  $H_2$  and  $H_3$  have real energies despite being non-Hermitian implies that they are *pseudo-Hermitian* [444], as defined by

$$\tilde{\eta} H_2(k) \tilde{\eta}^{-1} = H_2^\dagger(k) = H_3(k), \quad (6.14)$$

$$\tilde{\eta} = \text{diag}(t_1^{-\frac{1}{3}}, t_2^{-\frac{1}{3}}), \quad (6.15)$$

where  $t_1, t_2 > 0$  is assumed. The eigenvectors of the  $H_2(k)$  and  $H_3(k)$  blocks can be expressed in terms of the  $|u_{\text{SSH}}^\pm(k)\rangle$  in (6.11),

$$|u_{2,R}^\pm(k)\rangle = \frac{1}{\mathcal{N}_{2,R}^\pm(k)} h_2 h_3 |u_{\text{SSH}}^\pm(k)\rangle, \quad (6.16)$$

$$|u_{3,R}^\pm(k)\rangle = \frac{1}{\mathcal{N}_{3,R}^\pm(k)} h_3 |u_{\text{SSH}}^\pm(k)\rangle, \quad (6.17)$$

where  $\mathcal{N}_{o,R}^{\pm(k)}$ , with  $o = 2, 3$ , are normalization constants, and  $R$  stands for right eigenvector. Recall that the non-Hermiticity of  $H_o(k)$  implies that its left ( $L$ ) and right ( $R$ ) eigenstates are not the same in general. To determine the normalization constants one must impose a *biorthogonal* normalization for the eigenstates:

$$\langle u_{o,L}^\sigma(k) | u_{o,R}^{\sigma'}(k) \rangle = \delta_{\sigma,\sigma'}, \quad \sigma, \sigma' = \pm, \quad (6.18)$$

which, joined with relation (6.9) and the pseudo-Hermiticity condition (6.14) leads to

$$\mathcal{N}_{2,R}^{\pm}(k)\mathcal{N}_{3,R}^{\pm}(k) = \mu_{\pm}(k). \quad (6.19)$$

Finally, we can fix the values of the normalization constants by relating the problem back to the starting  $\sqrt[3]{\text{SSH}}$  model, whose eigenstates can be grouped in three pairs of bands. One of these pairs has the form

$$|\psi_1^{\pm}(k)\rangle = \frac{1}{\sqrt{3}} \begin{pmatrix} |u_{\text{SSH}}^{\pm}(k)\rangle \\ |u_{2,R}^{\pm}(k)\rangle \\ |u_{3,R}^{\pm}(k)\rangle \end{pmatrix}, \quad (6.20)$$

whose corresponding eigenvalue equation reads as

$$H_{\sqrt[3]{\text{SSH}}}(k) |\psi_1^{\pm}(k)\rangle = \mu_{\pm}^{\frac{1}{3}}(k) |\psi_1^{\pm}(k)\rangle, \quad (6.21)$$

with the eigenvalues being the cubic root of the eigenvalues of the cubed system in (6.10). Then, by introducing (6.20) in (6.21), one finally obtains the values of the normalization constants,

$$\mathcal{N}_{2,R}^{\pm}(k) = \mu_{\pm}^{\frac{2}{3}}(k), \quad \mathcal{N}_{3,R}^{\pm}(k) = \mu_{\pm}^{\frac{1}{3}}(k). \quad (6.22)$$

The other two pairs of eigenvalues and eigenstates can be obtained by making use of the generalized chiral symmetry of the system [221], as expressed in (6.4). The eigenstates have the following form

$$|\psi_2^{\pm}(k)\rangle = \Gamma_3 |\psi_1^{\pm}(k)\rangle = \frac{1}{\sqrt{3}} \begin{pmatrix} |u_{\text{SSH}}^{\pm}(k)\rangle \\ \eta_3 |u_{2,R}^{\pm}(k)\rangle \\ \eta_3^{-1} |u_{3,R}^{\pm}(k)\rangle \end{pmatrix}, \quad (6.23)$$

$$|\psi_3^{\pm}(k)\rangle = \Gamma_3^2 |\psi_1^{\pm}(k)\rangle = \frac{1}{\sqrt{3}} \begin{pmatrix} |u_{\text{SSH}}^{\pm}(k)\rangle \\ \eta_3^{-1} |u_{2,R}^{\pm}(k)\rangle \\ \eta_3 |u_{3,R}^{\pm}(k)\rangle \end{pmatrix}, \quad (6.24)$$

with energies  $\eta_3 \mu_{\pm}^{\frac{1}{3}}(k)$  and  $\eta_3^{-1} \mu_{\pm}^{\frac{1}{3}}(k)$ , respectively, forming three energy branches in total. We show the bulk spectrum of the  $H_{\sqrt[3]{\text{SSH}}}$  model in Fig. 6.3(a), where it is clear that the bands are indeed split in three separate branches along the complex plane. From one of the branches, one may obtain the others by applying  $\pm \frac{2\pi}{3}$  rotations on the complex plane. Furthermore, all three branches converge and become degenerate at  $\mu = 0$  for  $k = 0$ , which constitutes an exceptional point of the spectrum [445]. This point is associated only to two eigenstates: one with weight only on the first sublattice,  $|\psi_1^-(0)\rangle = \frac{1}{\sqrt{2}}(1, -1, 0, 0, 0, 0)^T$ ; and a doubly degenerate state with weight only on the



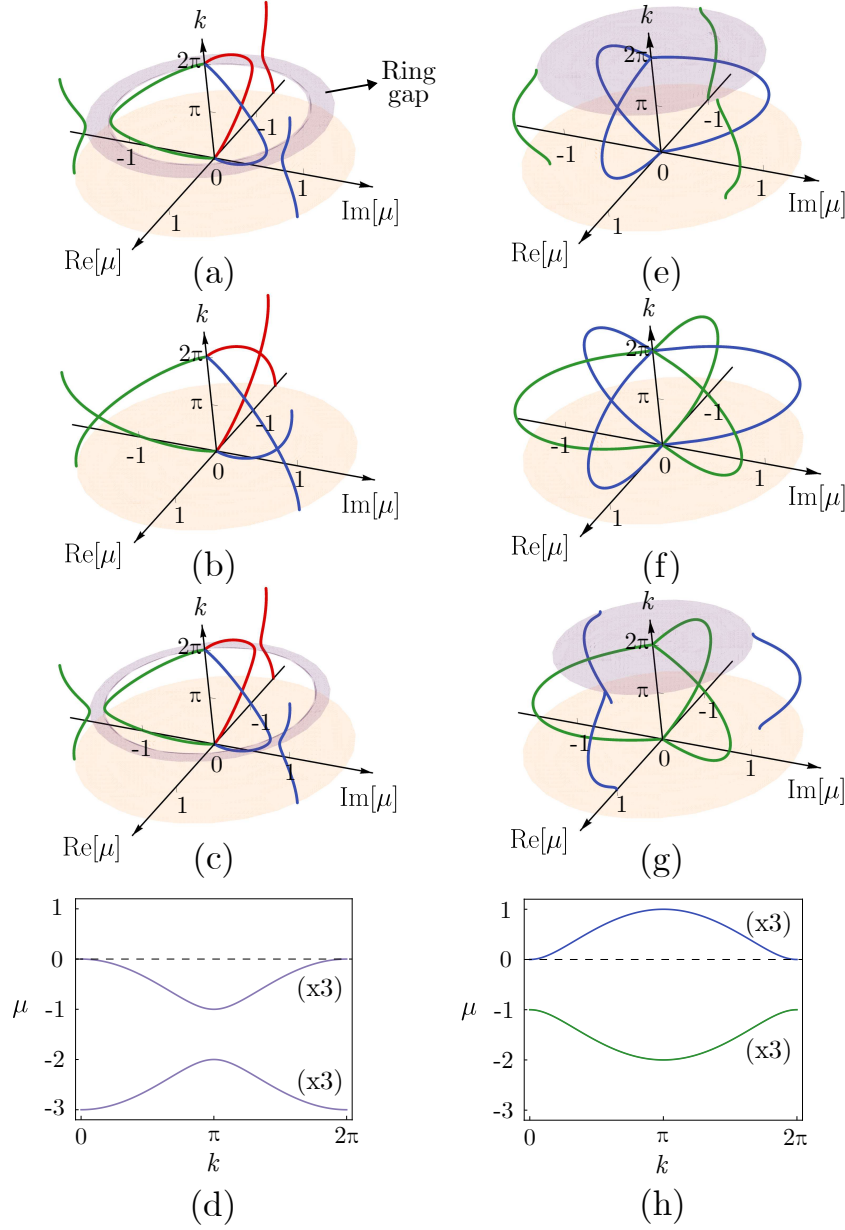


Figure 6.3: Complex energy spectrum, in units of  $\sqrt[3]{t_2} = 1$ , as a function of the momentum for the  $\sqrt[3]{\text{SSH}}$  model with (a)  $\sqrt[3]{t_1} = \sqrt[3]{0.5}$ , (b)  $\sqrt[3]{t_1} = 1$ , and (c)  $\sqrt[3]{t_1} = \sqrt[3]{1.5}$ . Different energy branches are indicated with different colors. (d) Cubed energy spectrum of the model in (a), which is purely real and with each band three-fold degenerate. (e)-(h) Same as the corresponding cases above, but for  $\sqrt[3]{t_1} \rightarrow e^{i\frac{\pi}{3}} \sqrt[3]{t_1}$ , leading to the  $\sqrt[3]{\text{SSH}}_{\pi/3}$  model. Different colors in (e)-(g) now distinguish the groups of three bands that become degenerate upon cubing the spectrum. The ring gaps are depicted in light purple and appear at  $k = \pi$  in (a) and (c), and at  $k = 2\pi$  in (e) and (g), where the inner circumference of the ring reduces to a point at  $\mu = 0$ .

second sublattice,  $|\psi_2^-(0)\rangle = (t_1^{\frac{2}{3}} + t_2^{\frac{2}{3}})^{-\frac{1}{2}}(0, 0, \sqrt[3]{t_2}, -\sqrt[3]{t_1}, 0, 0)^T$ . In the spectrum of the root model, the complex energy branches are balanced. That is, for every complex  $\mu$ , there exists a conjugate pair  $\mu^*$  on the opposite complex branch. This implies that  $H_{\sqrt[3]{\text{SSH}}}$  is also pseudo-Hermitian [444], as the spectrum of pseudo-Hermitian matrices is either real or comes in complex-conjugate pairs. Similarly to the definitions for  $H_2$  and  $H_3$  in Eqs. (6.14)–(6.15), we detail the form of the  $\tilde{\eta}$  matrix for  $H_{\sqrt[3]{\text{SSH}}}$  below, in Sec. 6.2.1. Most notably, on a different note, the bulk spectrum presents a novel spectral gap that cannot be described as the point or line gaps that are present in the literature on non-Hermitian systems [445, 446], and that we label as a *ring gap*. Through Figs. 6.3(a)–(c), where  $\sqrt[3]{t_1}$  is swept across the topological transition point, one can observe how the ring gap closes at  $\sqrt[3]{t_1} = \sqrt[3]{t_2}$  and opens when the couplings are unequal. Its magnitude is given by:

$$\Delta = |\sqrt[3]{2t_1} - \sqrt[3]{2t_2}| \quad (6.25)$$

In Fig. 6.3(d), where the cubed spectrum is computed for  $\sqrt[3]{t_1} < \sqrt[3]{t_2}$ , we show how a gap is also present in the parent system, which can be thought of as the origin of the ring gap. For open systems in the nontrivial phase, the ring gap will host three sets of edge states, one set for each branch.

It is interesting to study the effect of introducing a real flux in the system. We consider the case where a  $\pi$  flux is evenly distributed along the loops of one coupling term only, i.e., the equivalent of performing a Peierls substitution  $\sqrt[3]{t_1} \rightarrow e^{i\frac{\pi}{3}}\sqrt[3]{t_1}$ . We label such a root system as the  $\sqrt[3]{\text{SSH}}_{\frac{\pi}{3}}$  model. This change induces a  $\frac{\pi}{3}$  rotation of the three inner bands, as well as a flipping of the three outer bands. Furthermore, due to the relative rotation, now we lack a one-to-one correspondence between inner and outer bands each branch. This is shown in Figs. 6.3(e)–(g), where one can also notice how inner and outer bands change their designation at the topological transition point. When considering the cubed system, the Peierls substitution leads to a change of  $t_1 \rightarrow -t_1$  in the parent SSH, which changes the energy of its bands to:

$$\mu_{\pm}(k) = t_1 - t_2 \pm \sqrt{t_1^2 + t_2^2 - 2t_1t_2 \cos k}, \quad (6.26)$$

as illustrated in Fig. 6.3(h). In other words, we obtain a  $k \rightarrow k + \pi$  sliding of both energy bands and push the overall energy up by a factor of  $2t_1$ . Notice how the energy gap is now open at  $k = 0$  in the cubed spectrum. As a consequence, the spectral gap of the corresponding  $\sqrt[3]{\text{SSH}}_{\frac{\pi}{3}}$  model in Fig. 6.3(e) is also defined as a ring gap at the  $k = 0$  point. This is the gap closing point in Fig. 6.3(f), with the inner circumference of the ring reduced to a single degenerate point at zero energy. Nevertheless, if we employ the usual projection of the whole spectrum onto the complex energy plane, the ring gap gets obscured and appears to have zero width. Hence, the three-dimensional (3D)

representation of the spectrum, as in Figs. 6.3(e)-(g), is required for the manifestation of the ring gap in the  $\sqrt[3]{\text{SSH}}_{\frac{\pi}{3}}$  model.

Finally, we remark that we do not consider general distributions of Peierls phases at the hopping terms as, even though a similar description can be found for general distributions, one does not recover the purely real energy spectrum of an SSH-like model upon cubing the system, which instead leads to a different non-Hermitian model.

### 6.2.1 Symmetries of the system

As discussed in the previous section, the spectrum of the  $\sqrt[3]{\text{SSH}}$  model has a deep connection with the generalized chiral symmetry that is defined in (6.4), which explains its splitting in energy branches and the relative angle that separates them. Nevertheless, the model possesses additional symmetries that we believe to be worth describing. As later on in Sec. 6.4 we propose to use a photonic ring system as an implementation, with the main ring resonators supporting two opposite circulations  $\mathcal{K} = \pm$ , we ought to consider an enlarged Hilbert space when compared to the tight-binding Hamiltonian. Namely, the Hilbert space is enlarged as  $\{|\mathcal{K}, u(k)\rangle\} = \{|\mathcal{K}\rangle\} \otimes \{|u(k)\rangle\}$ , with  $|u(k)\rangle$  defined above Eq. (6.1). As such, instead of only considering the tight-binding model, in this section we extend the discussion of the symmetries to the *full*  $\sqrt[3]{\text{SSH}}$  model, constructed with the photonic ring system depicted in Fig. 6.12, when working with both circulations on the new Hilbert space.

As can be understood from Fig. 6.9, a switch in the circulations in the main rings,  $\mathcal{K} = - \rightarrow \mathcal{K} = +$ , amounts to a switch in the direction over which they connect with the losses and gains of the auxiliary rings (a connection through gains between main rings in one circulation becomes a connection through losses for the other circulation, and vice-versa). Consequently, all hopping directions are swapped when  $\mathcal{K} = - \rightarrow \mathcal{K} = +$ , and the corresponding Hamiltonian becomes

$$H_{\sqrt[3]{\text{SSH}}}^{\mathcal{K}=-}(k) = H_{\sqrt[3]{\text{SSH}}}(k) \rightarrow H_{\sqrt[3]{\text{SSH}}}^{\mathcal{K}=+}(k) = H_{\sqrt[3]{\text{SSH}}}^{\dagger}(k). \quad (6.27)$$

The total Hamiltonian, written in the enlarged Hilbert space, has the following block diagonal form

$$H_t = \begin{pmatrix} H_{\sqrt[3]{\text{SSH}}}(k) & O_6 \\ O_6 & H_{\sqrt[3]{\text{SSH}}}^{\dagger}(k) \end{pmatrix}, \quad (6.28)$$

where  $O_6$  is the zero square-matrix of size 6. For the parameter values used in our numerical simulations, inter-circulation couplings between  $\mathcal{K} = +$  and  $\mathcal{K} = -$  can be safely neglected, as we discuss in Sec. 6.4. For much smaller rings, or when using sharper transitions between regions with strong gain and loss, small off-diagonal blocks should be considered in place of the  $O_6$  matrix. In Table 6.1, we summarize the symmetries of  $H_t(k)$ , indicating the matrix representation of their respective operators. Non-Hermitian

Operator	Representation	Action on $H_t(k)$
$y$ -mirror	$M_y = \bar{\sigma}_x \otimes R_y$	$M_y H_t(k) M_y^{-1} = H_t(k)$
Parity <sup>†</sup>	$P_t(k) = \bar{\sigma}_x \otimes P(k)$	$P_t(k) H_t(k) P_t(k)^{-1} = H_t^\dagger(-k)$
Flip <sup>†</sup>	$F = \bar{\sigma}_x \otimes I_6$	$F H_t(k) F^{-1} = H_t^\dagger(k)$
Time-reversal <sup>†</sup>	$T = FK$	$T H_t(k) T^{-1} = H_t^\dagger(-k)$
Flip-time	$FT = (\bar{I}_2 \otimes I_6)K$	$FT H_t(k) T^{-1} F^{-1} = H_t(-k)$
Flip-inversion	$FP_t(k) = \bar{I}_2 \otimes P(k)$	$FP_t(k) H_t(k) P_t(k)^{-1} F^{-1} = H_t(-k)$
Parity-time	$P_t(k)T = (\bar{I}_2 \otimes P(k))K$	$P_t(k)T H_t(k) T^{-1} P_t(k)^{-1} = H_t(k)$
G. Chiral	$\Gamma_3^t = \Gamma_3 \oplus \Gamma_3^\dagger$	$\Gamma_3^t H_t(k) (\Gamma_3^t)^{-1} = \omega_3^{-1} H_t(k)$
G. Particle-hole	$S_3^t = \Gamma_3^t FT$	$S_3^t H_t(k) (S_3^t)^{-1} = \omega_3^{-1} H_t(-k)$

Table 6.1: Operators and symmetries of  $H_t(k)$  in (6.28), defined as  $\{|u(k)\rangle\}$ , with  $u = 1, 2, \dots, 6$  labeling the corresponding site within the unit cell.  $\bar{I}_2$  is the  $2 \times 2$  identity matrix and  $\bar{\sigma}_x$  the  $x$  Pauli matrix, both acting on the space of circulations.  $\Gamma_3$  was defined previously in (6.5).

symmetries [446] are labeled with the “†” symbol, with the parity<sup>†</sup> symmetry being the same as the pseudo-inversion symmetry defined in [447]. This notation is adopted since the result of applying a non-Hermitian symmetry (†) to the Hamiltonian is its Hermitian conjugate.

The  $y$ -mirror operation  $M_y$ , performed about the central horizontal axis of the ring system in Fig. 6.12, acts as a  $y$ -reflection<sup>†</sup> operation  $R_y$ , on the position space,

$$R_y H_{\sqrt[3]{\text{SSH}}}(k) R_y^{-1} = H_{\sqrt[3]{\text{SSH}}}^\dagger(k), \quad (6.29)$$

$$R_y = \begin{pmatrix} I_2 & 0 & 0 \\ 0 & 0 & I_2 \\ 0 & I_2 & 0 \end{pmatrix} \quad (6.30)$$

while simultaneously flipping the circulations in their respective space. In (6.30),  $I_2$  is the  $2 \times 2$  identity matrix in the position space. Note that Eq. (6.29) serves as proof that  $H_{\sqrt[3]{\text{SSH}}}$  is pseudo-Hermitian, as mentioned earlier, since taking  $\tilde{\eta} = R_y$  leads to the same definition as (6.14) for  $H_2$ . Both the reflection as well as the flipping of the circulations generate a global swap of all hopping directions, such that the two together act as a double negative that keeps the system invariant under  $M_y$ , as shown in Table 6.1.

The parity<sup>†</sup> symmetry involves an inversion operation in the position space, defined

about the vertical axis crossing sites 3 and 5 in the unit cell at the bottom of Fig. 6.1,

$$P(k)H_{\sqrt[3]{\text{SSH}}}(k)P^{-1}(k) = H_{\sqrt[3]{\text{SSH}}}(-k), \quad (6.31)$$

$$P(k) = \begin{pmatrix} 0 & 1 & 0 & 0 & 0 & 0 \\ 1 & 0 & 0 & 0 & 0 & 0 \\ 0 & 0 & 1 & 0 & 0 & 0 \\ 0 & 0 & 0 & e^{-ik} & 0 & 0 \\ 0 & 0 & 0 & 0 & 1 & 0 \\ 0 & 0 & 0 & 0 & 0 & e^{-ik} \end{pmatrix}. \quad (6.32)$$

Note that the inversion operator  $P(k)$  is  $k$ -dependent, reflecting the fact that the inversion axis is shifted from the center of the unit cell. This has been shown to lead, in Hermitian systems, to nonquantized Zak's phases for the energy bands [333, 448]. When the complete ring system in Fig. 6.12 is considered, it is clear that the inversion operation switches the gain and loss regions of the link rings, leading to a global flip of the hopping directions. Or, equivalently, to a global flip of the circulations (an  $x$  Pauli matrix,  $\bar{\sigma}_x$ , in the circulation space). The operator  $P_t(k)$  of the  $k$ -dependent parity<sup>†</sup> symmetry is obtained by combining both effects, and its action on  $H_t(k)$  is given in Table 6.1.

We additionally define in Table 6.1 a flip<sup>†</sup> symmetry which acts non-trivially only in the circulation space, that is, the  $\mathcal{K} = \pm$  circulations are flipped under the action of its operator,  $F = \bar{\sigma}_x \otimes I_6$ . This can be understood both as a global reversal of the hopping directions, or as a global swap of the gain and loss regions within each link ring, and appears due to considering the enlarged Hilbert space in our proposed implementation.

Some care is needed for deriving the time-reversal operator. It is defined in general as an anti-unitary operator of the form  $\mathcal{T} = \mathcal{U}K$ , where  $K$  is the complex conjugation operator obeying  $KO = O^*K$  and  $KK^{-1} = I$ , while  $\mathcal{U}$  is a unitary operator that, for a general angular momentum, and up to a global phase factor, can be written as

$$\mathcal{U} = -e^{-i\pi J_y/\hbar}, \quad (6.33)$$

where  $\hbar$  is the reduced Planck's constant and  $J_y$  is the  $y$ -component of the angular momentum operator. Assuming a pseudospin-1 system, the basis spans  $\{|1, 1\rangle = (1, 0, 0)^T, |1, 0\rangle = (0, 1, 0)^T, |1, -1\rangle = (0, 0, 1)^T\}$ , where the states are written in the form  $|l, \mathcal{K}\rangle$ , and one has

$$J_y = \frac{i\hbar}{\sqrt{2}} \begin{pmatrix} 0 & -1 & 0 \\ 1 & 0 & -1 \\ 0 & 1 & 0 \end{pmatrix}, \quad (6.34)$$

$$\mathcal{U} = \begin{pmatrix} 0 & 0 & 1 \\ 0 & -1 & 0 \\ 1 & 0 & 0 \end{pmatrix}. \quad (6.35)$$

$\mathcal{U}$  reverses the circulations, that is,  $\mathcal{U}|l, \mathcal{K}\rangle = (-1)^{\mathcal{K}l+1}|l, -\mathcal{K}\rangle$ . In our ring system, the accessible states are the ones with opposite circulations,  $\mathcal{K} = \pm$ . The  $l = 0$  mode ( $\mathcal{K} = 0$  circulation) does not correspond to a whispering gallery resonant mode in the ring system and, as such, can be dropped to get, in the  $\{|1, 1\rangle, |1, -1\rangle\}$  subspace,  $\mathcal{U} = \bar{\sigma}_x$ . When the entire Hilbert space is considered, the time-reversal operator can be defined in terms of the flip operator as  $\mathcal{T} = FK$  (see Table 6.1), so that apart from the usual conjugation, the circulations are also flipped under the time-reversal operation. We employ this pseudospin-1 formalism and drop the  $\mathcal{K} = 0$  state, instead of directly working with a two-state pseudospin- $\frac{1}{2}$  system, to properly reach the expected  $\mathcal{T}^2 = 1$  condition in our model. For pseudospin- $\frac{1}{2}$ , where  $J_y \sim \sigma_y$ , we would instead obtain  $\mathcal{T}^2 = -1$ . Table 6.1 shows that the total system has the non-Hermitian time-reversal<sup>†</sup> symmetry. When it is combined with the flip operation (which duplicates the one already contained in  $\mathcal{T} = FK$ ), we obtain a new kind of symmetry for the full model that we label *flip-time* symmetry, and whose operator is given by the product  $F\mathcal{T}$ . Considering that  $F^2 = I$ , we see that the flip-time symmetry in our system plays the role that is generally assigned to time-reversal in other scenarios [221].

The generalized chiral symmetry  $\mathcal{C}_3$  is also present in the full model of (6.28), and its operator,  $\Gamma_3^t$ , is given by the direct sum of the  $\mathcal{C}_3$  symmetry operators of each circulation (see Table 6.1), with each being the Hermitian conjugated version of the other. Finally, we also define in Table 6.1 a generalized particle-hole symmetry [221], whose operator can be written as a product of three operators,  $S_3^t = \Gamma_3^t F \mathcal{T}$ .

### 6.2.2 Topological characterization

The choice of a topological invariant that allows to distinguish the topological phases of the root system and relate them to the SSH parent is not evident. By looking at Fig. 6.1(b), one can deduce that the axis of inversion of the system is located along the coupling line of sites 3 and 5 (or, equivalently, sites 4 and 6). In other words, performing an inversion along the  $x$ -axis only yields the same system  $H_{\sqrt[3]{\text{SSH}}}(k) \rightarrow H_{\sqrt[3]{\text{SSH}}}(-k)$  when the center of inversion is located in this axis. One can easily observe that this axis is always shifted from the center of the unit cell, no matter the specific choice that one makes for the cell itself. As a consequence, the inversion operator is  $k$ -dependent, which has been shown to lead to nonquantized Zak's phases in other systems [333, 448].

Instead, we will exploit the existence of the ring gap in our system to define a new type of polarization for complex spectra, which will serve as our topological invariant. Typically, the polarization of a system, which is related to the Berry phase [101] as we showed in Sec. 2.3.1, is computed by filling all states below a certain Fermi level. However, this is ill-defined in our case. Alternatively, we define a *ring Fermi level* at a radius  $|\mu_F|$  within the ring gap which determines the states we deem to be occupied.

Do note, however, that in order to obtain a direct comparison with the polarization in the parent SSH model, we will occupy the states *outside* the Fermi level. This is justified by comparing Figs. 6.3(a) and (d), where one readily notices that the inner bands correspond to the higher-energy band in the cubed system. The *biorthogonal polarization* [449, 450] in our case is thus defined as [220]

$$\mathcal{P} := \sum_{m=m_F+1}^{6N_c} \langle \psi_m^L | \hat{\mathcal{P}} | \psi_m^R \rangle, \quad (6.36)$$

where  $|\psi_m^{L,R}\rangle$  are the left/right eigenstates of the  $\sqrt[3]{\text{SSH}}$  model,  $N_c$  the number of unit cells,  $m$  the eigenstate index and  $m_F$  is the index of the state with highest  $|\mu| \leq |\mu_F|$ , corresponding to  $m_F = 3N_c$  at half-filling. The polarization operator  $\hat{\mathcal{P}}$  in turn is

$$\hat{\mathcal{P}} = \frac{e}{N_c} \sum_{q=1}^{N_c} q \hat{\Pi}_q, \quad \hat{\Pi}_q = \sum_{u=1}^6 |q, u\rangle \langle q, u|, \quad (6.37)$$

with  $e$  being the electron charge and  $|q, u\rangle$  is the basis state at site  $u$  of unit cell  $q$ . Note that we simplify the expression by assuming that all sites in a cell occupy the same spatial position  $q$ . The polarization is then defined by the following expression:

$$\mathcal{P} = \frac{e}{N_c} \sum_{q=-\frac{N_c-1}{2}}^{\frac{N_c-1}{2}} \sum_{u=1}^6 \sum_{m=3N_c+1}^{6N_c} q (\Psi_{q,u,m}^L)^* \Psi_{q,u,m}^R, \quad (6.38)$$

where  $\Psi_{q,u,m}^{L(R)}$  denotes the amplitude of the left (right) eigenstate  $m$  of the root model at the corresponding position. We plot the spectrum of an open  $\sqrt[3]{\text{SSH}}$  chain of  $N_c = 121$  unit cells at half-filling and the equivalent SSH chain with the same  $N_c$  in Figs. 6.4(a) and (b), respectively. In those, the corresponding gaps are indicated by the pink shaded region and the Fermi levels by the red solid lines, separating unoccupied (blue) from occupied (red) states. Then, in Fig. 6.4(c), the polarization for the root system (blue solid line) is plotted as a function of  $t_2$  for  $t_1 = 1$ . We see that the polarization displays a sharp transition at the critical gap closing point  $t_2 = 1$ , but that it is only quantized at the atomic limits,  $\mathcal{P}(t_2 = 0) = 0$  and  $\mathcal{P}(t_2 \rightarrow \infty) = 1/2$  in units of  $e$ , while being nonquantized away from them. This is in agreement with the behavior that was observed for the  $\sqrt{\text{SSH}}$  model [333]. The difference between these quantized values serves as a topological invariant of our root systems. To give physical meaning to these limits, in Fig. 6.5(a) and (b) we plot an open  $\sqrt[3]{\text{SSH}}$  chain with the lowest-energy states occupied for  $t_2 = 0$  and  $t_1 = 0$ , respectively. Note that this reverses the results for the polarization  $\mathcal{P} \rightarrow -\mathcal{P}$  when compared to Fig. 6.4(c), but we do so for ease of visualization since the states of the outer bands are harder to depict. In Fig. 6.5(a), when  $t_2 = 0$ , the particle density is balanced for all unit cells, such that  $\mathcal{P} = 0$ . On the other hand, when  $t_1 = 0$



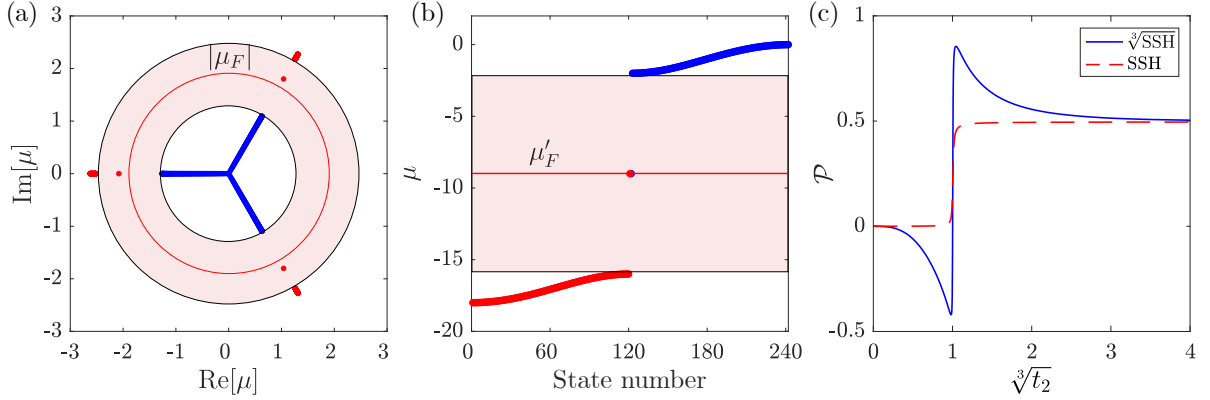


Figure 6.4: (a) Complex energy spectrum of the open  $\sqrt[3]{\text{SSH}}$  chain with  $N_c = 121$  unit cells, for  $\sqrt[3]{t_1} = 1$  and  $\sqrt[3]{t_2} = 2$ , with the ring gap highlighted in pink. The ring Fermi level of radius  $|\mu_F|$  is marked with a solid red line. (b) Energy spectrum of an open SSH chain of the same size  $N_c$ , with lattice parameters extracted from the corresponding diagonal block of the cubed Hamiltonian of the model in (a), with the Fermi level  $\mu'_F$  placed at half-filling, where small edge perturbations were included to place the right (left) in-gap edge state below (above) the Fermi level. (c) Polarization in the  $\sqrt[3]{\text{SSH}}$  (blue solid line) and the SSH (red dashed line) models, as a function of  $\sqrt[3]{t_2}$  for  $\sqrt[3]{t_1} = 1$ , computed by filling the states marked in red in (a) and (b), respectively.

in Fig. 6.5(b), there is an excess of one particle at the first unit cell in relation to the last one, which leads to  $\mathcal{P} = -\frac{\epsilon}{2}$ . Considering the complementary filling from before, this perfectly agrees with the results in Fig. 6.4(c). For comparison, we plot in the same Fig. 6.4(c) the polarization for the parent SSH chain of the same size  $N_c$  at half-filling (red dashed line), by using the expression (6.36). Note that, unlike what occurs in the root system, right and left eigenstates are equivalent in the SSH chain. This time, the usual quantized plateaus at  $\mathcal{P} = 0$  ( $\mathcal{P} = 1/2$ ) appear for the (non-)trivial region, also with a sharp transition from one to the other at the gap closing point. This once more demonstrates that the parent SSH model is indeed the source of the topological features of the root models.

### 6.2.3 Disorder and dilution of the topological protection

We now focus on the topological edge states that can be found within the ring gap. As described in other works [128, 129], the root model inherits the topological protection from the parent system, which in our case is the Hermitian SSH model. In that sense, the edge states of the  $\sqrt[3]{\text{SSH}}$  model are protected against any disorder that preserves the chiral symmetry of the parent SSH model, which is the protecting symmetry. As is well known, the SSH model is protected against chiral disorder such as off-diagonal



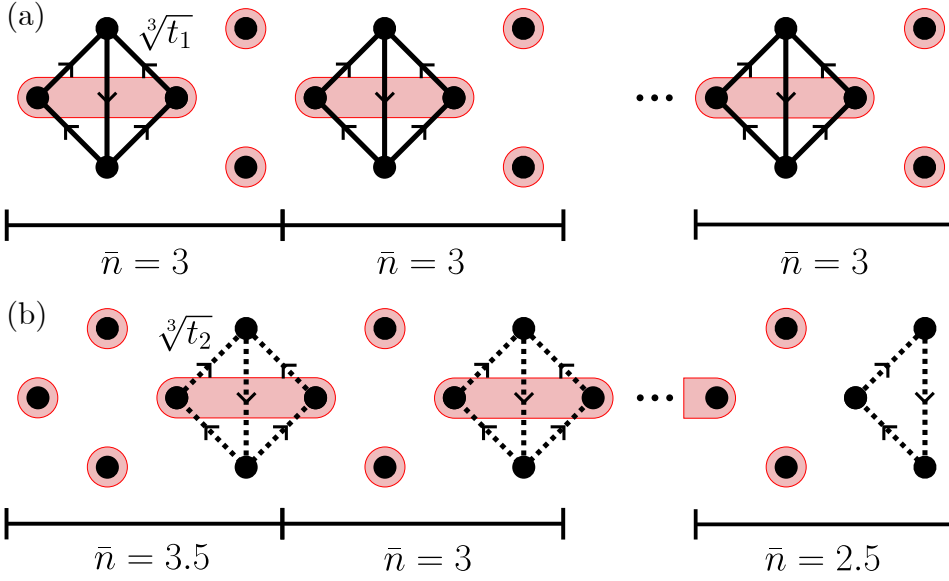


Figure 6.5: Illustration of an open  $\sqrt[3]{\text{SSH}}$  chain at half-filling (filling the states within the ring Fermi level) in the atomic limit (a)  $t_1 > 0$  and  $t_2 = 0$ , and (b)  $t_1 = 0$  and  $t_2 > 0$ . The occupied states are colored in red and all have zero energy at these limits, with the ones spanning two sites corresponding to antisymmetric linear combinations with the same weight at each site. The average number of particles  $\bar{n}$  at each unit cell is indicated at the bottom of each plot.

disorder. As a consequence, we expect our edge states to be protected against the types of disorder in the  $\sqrt[n]{\text{SSH}}$  systems that, when raised to the  $n$ th-power, translate as chiral disorder for the parent SSH block. This constitutes a smaller subset of allowed disorders when compared to those of the parent SSH model, which can be thought of as a dilution of the topological protection [128]. An example of such disorder in a open chain is provided in Fig. 6.6(a), where we have added two extra sites to the left of the chain to impose inversion symmetry. In there, we consider disorder around  $\sqrt[3]{t_1} = \cos \theta_c$  and  $\sqrt[3]{t_2} = \sin \theta_c$ , where  $\theta_c$  is defined so that  $\sqrt[3]{t_2}/\sqrt[3]{t_1} = 2$  and two edge states per branch appear, located at opposite edges. As indicated in Fig. 6.6(a), the disorder is sampled from a uniform distribution in quartets of hopping terms, and is thus correlated. When cubing this system, the SSH block takes the form sketched in Fig. 6.6(b), where the onsite energies are  $\sin^2 \theta_q + \cos^2 \theta_q = 1$  and the disorder is entirely off-diagonal. The spectrum of the clean  $\sqrt[3]{\text{SSH}}$  model is presented in Fig. 6.6(c). The response of the edge and closest bulk states to the described disorder in the real branch is presented in Fig. 6.6(d), where it is clear that the edge states remain unaltered until the disorder is strong enough to close the gap. As a direct comparison, we provide the same plot for uncorrelated disorder where each  $\theta_q$  is sampled independently in Fig. 6.6(e), which corresponds to both diagonal and off-diagonal disorder for the SSH block when cubed.

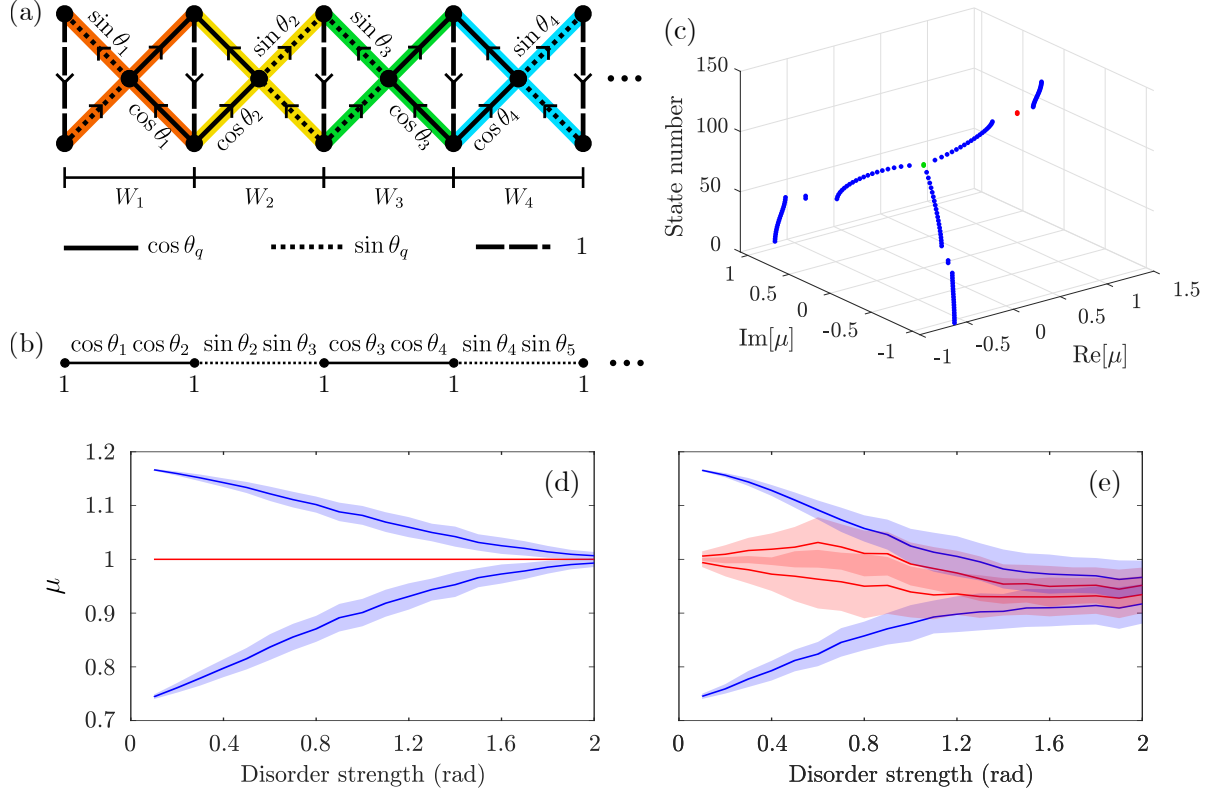


Figure 6.6: Correlated and uncorrelated disorder. (a) Sketch of a  $\sqrt[3]{\text{SSH}}$  model with correlated disorder  $\theta_q = \theta_c + W_q$  sampled in quartets of hopping terms, as indicated by the lower segments and the different shaded colors in the hoppings, from a uniform distribution  $W_q \in [-W/2, W/2]$ , and with the vertical couplings being disorder free. (b) Sketch of the Hermitian SSH system obtained for the decoupled spinal sublattice when cubing the Hamiltonian corresponding to (a). Due to the correlated disorder in (a), this system displays only off-diagonal disorder. (c) Spectrum of the clean  $\sqrt[3]{\text{SSH}}$  model. (d), (e) Mean value (solid lines) and standard deviation (shaded region) for the edge states (red) and the closest bulk states (blue) in the real branch of the disordered root system for increasing strengths of (d) correlated and (e) uncorrelated disorder, taken over 200 different realizations. The corresponding edge states are marked in red in (c).

For this case, it can be seen that the robustness of the edge states is lost. This proves that the topological protection in our model is related to the preservation of the chiral symmetry of the parent SSH model.

Finally, one might also consider the protection granted by the generalized chiral symmetry of the root system, that stems from the tripartite nature of the system and is not directly inherited from the parent. In Fig. 6.6(c), attention might be drawn to the states at the center of the spectrum, marked in green, which originate from the sublattice imbalance caused by the extra sites at the left of the chain [221]. These zero-energy states are unaffected by either kind of disorder, since neither of them breaks the chiral symmetry. It could be interesting to explore in further works the degree of protection that this symmetry provides, and whether the spectrum can be engineered so that states of interest are placed under that protection. For instance, one might attempt to displace the bands in each of the branches towards the zero of energies by adding extra sites to the lattice, so that the topological edge states, now placed at the center of the spectrum, could be doubly protected by the symmetries of both parent and root systems.

### 6.3 Generalization to $n$ -root systems

The above method to generate cubic roots of any TI can easily be generalized to roots of any order  $n > 3$  by increasing the amount of unidirectional hoppings in a loop, so that the root system will be  $n$ -partite. For the SSH model, this can be easily achieved by including additional sites in the vertical link, as sketched in Fig. 6.7(a). For  $\mathcal{M}$  sites within the vertical link, a root of order  $n = \mathcal{M} + 3$  is produced. The Hamiltonian of the  $\sqrt[n]{\text{SSH}}$  model then becomes:

$$H_{\sqrt[n]{\text{SSH}}}(k) = \begin{pmatrix} h_1 & & & \\ & h_2 & & \\ & & \ddots & \\ & & & h_{n-1} \\ h_n & & & \end{pmatrix}, \quad (6.39)$$

$$h_1 = h_n^\dagger = - \begin{pmatrix} \sqrt[n]{t'_1} & \sqrt[n]{t'_2} e^{-ik} \\ \sqrt[n]{t_1} & \sqrt[n]{t_2} \end{pmatrix}, \quad (6.40)$$

$$h_s = - \begin{pmatrix} \sqrt[n]{t_1} & 0 \\ 0 & \sqrt[n]{t_2} \end{pmatrix}, \quad s = 2, 3, \dots, n-1, \quad (6.41)$$

which again obeys a generalized chiral symmetry,

$$\mathcal{C}_n : \Gamma_n H_{\sqrt[n]{\text{SSH}}}(k) \Gamma_n^{-1} = \eta_n^{-1} H_{\sqrt[n]{\text{SSH}}}(k), \quad (6.42)$$

$$\Gamma_n = \text{diag}(I, \eta_n I, \eta_n^2 I, \dots, \eta_n^{n-1} I), \quad (6.43)$$

with  $\eta_n = e^{i\frac{2\pi}{n}}$ . Note that  $\sqrt[n]{t_1}$ ,  $\sqrt[n]{t_2}$  need not be equal to  $\sqrt[n]{t'_1}$ ,  $\sqrt[n]{t'_2}$  to produce the root system. Even if one chooses them to be different, one may renormalize the couplings when taking the  $n$ -th power so that  $\bar{t}_j \equiv t_j'^{\frac{2}{n}} t_j^{\frac{n-2}{n}}$ . Following what was stated in the previous section, this Hamiltonian presents  $n$  branches, each with two bands, related by a rotation of  $\frac{2\pi}{n}$  in the complex plane. We present in Figs. 6.7(b) and (c) the spectra of the roots of order 4 and 5 of the SSH model, as determined by the graph in (a) for  $\mathcal{M} = 1$  and  $\mathcal{M} = 2$ , respectively. In there, we observe the increased amount of bands, and perhaps more interestingly of band gaps that can host edge states in open systems, when compared to Fig. 6.3. One can readily observe that the concept of ring gap persists even when increasing the root order. Indeed, we present the more ‘extreme’ case of the 20-th order root in Fig. 6.8. One can infer that in the limit of  $n \rightarrow \infty$  the ring gap becomes continuous since the separation between branches tends to zero, as we sketch on the right side of the figure. Once again, raising the root Hamiltonian in (6.39) to the  $n$ -th power yields:

$$[H_{\sqrt[n]{\text{SSH}}}]^n(k) = \text{diag}(H_{\text{SSH}'}(k), H_2(k), \dots, H_n(k)), \quad (6.44)$$

where the first block is an energy shifted SSH Hamiltonian,

$$H_{\text{SSH}'}(k) = h_1 h_2 \dots h_n = -(\bar{t}_1 + \bar{t}_2)I + H_{\text{SSH}}(k), \quad (6.45)$$

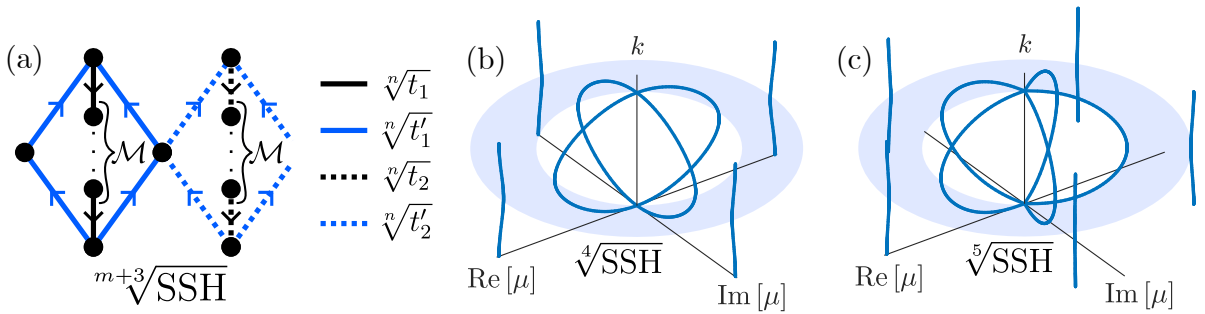


Figure 6.7: (a) Graph of the root of order  $n = \mathcal{M} + 3$  the SSH model, which contains  $\mathcal{M}$  sites within the vertical link. The most general form of the root does not require the vertical hopping terms in black to be equal to the ones in blue. (b)–(c) Bulk spectra for the (b)  $\sqrt[4]{\text{SSH}}$  and (c)  $\sqrt[5]{\text{SSH}}$  models. It is clear that the root order corresponds with the amount of band branches, which is also related to the angle that separates them along the complex plane. The ring gap, shaded in blue, appears in both cases.

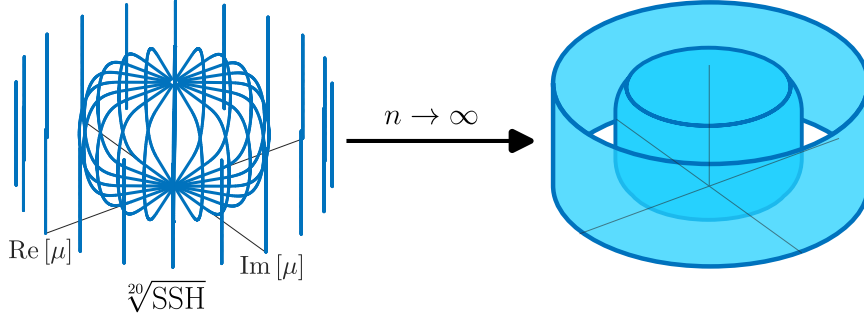


Figure 6.8: Left: Bulk spectrum of the  $\sqrt[n]{\text{SSH}}$  model, where one can observe that the relative angle between band branches tends to zero for high  $n$ . Right: In the limit where  $n \rightarrow \infty$ , one can expect two continuous blocks of inner and outer bands as  $2\pi/n \rightarrow 0$ , with the now continuous ring gap being the clear separation between both of them.

and all other diagonal blocks are cyclic permutations of (6.45) and therefore isospectral to it. Following the development showcased in Sec. 6.2, the generalization of the expressions for the eigenstates and their energies to the  $n$ -th root is [220]:

$$H_{\sqrt[n]{\text{SSH}}}(k) |\psi_1^\pm(k)\rangle = \mu_\pm^{\frac{1}{n}}(k) |\psi_1^\pm(k)\rangle, \quad (6.46)$$

$$|\psi_1^\pm(k)\rangle = \frac{1}{\sqrt{n}} \begin{pmatrix} |u_{\text{SSH}}^\pm(k)\rangle \\ \mu_\pm^{-\frac{n-1}{n}}(k) h_2 h_3 \dots h_n |u_{\text{SSH}}^\pm(k)\rangle \\ \mu_\pm^{-\frac{n-2}{n}}(k) h_3 \dots h_n |u_{\text{SSH}}^\pm(k)\rangle \\ \vdots \\ \mu_\pm^{-\frac{1}{n}}(k) h_n |u_{\text{SSH}}^\pm(k)\rangle \end{pmatrix}, \quad (6.47)$$

and with the rest of the eigenstates being

$$|\psi_m^\pm(k)\rangle = \Gamma_n^{m-1} |\psi_1^\pm(k)\rangle, \quad (6.48)$$

with energies  $\eta_n^{m-1} \mu_\pm^{\frac{1}{n}}(k)$ . As we have seen before for the  $\sqrt[3]{\text{SSH}}$  model, there will now be an  $n$ -fold degenerate zero-energy point at  $k = 0$  that corresponds to an exceptional point of the spectrum, with the same two associated eigenstates. One of them,  $|\psi_1^-(0)\rangle = \frac{1}{\sqrt{2}}(1, -1, 0, 0, \vec{O}_{2n-4})^T$ , with  $\vec{O}_{2n-4}$  a zero vector of size  $2n - 4$ , only has weight on the first sublattice, while the other,  $(n - 1)$ -fold degenerate,  $|\psi_2^-(0)\rangle = (t_1^{\frac{2}{n}} + t_2^{\frac{2}{n}})^{-\frac{1}{2}}(0, 0, \sqrt[n]{t_2}, -\sqrt[n]{t_1}, \vec{O}_{2n-4})^T$ , only has weight on the second. Finally, we also explore below the consequences of adding a Peierls phase  $\sqrt[n]{t_j^{(l)}} \rightarrow \sqrt[n]{t_j^{(l)}} e^{i\frac{\pi}{n}}$  for higher-order roots in Sec. 6.4.2.

It should also be stressed that our scheme of generating  $\sqrt[n]{\text{TIs}}$  is fundamentally different from the one recently proposed in [451]. There, the  $n$ -root of a lattice is obtained

by a direct extension of the split graph [452] structure of several  $\sqrt{\text{TI}}$ s [120, 121, 339, 453–455]. Namely, each link/hopping of the TI is subdivided into  $n$  equal parts by adding  $n - 1$  sites between the two original ones. The resulting model is always bipartite, regardless of  $n$ . Upon raising its Hamiltonian to the  $n$ -th power, the parent TI and topologically equivalent models are obtained as diagonal blocks. However, a global off-diagonal term, labeled enhanced Hamiltonian, couples the diagonal blocks among each other in non-trivial ways, and it is not yet clear how this mixing ultimately affects the clean topological characterization of the diagonal blocks. Our scheme for constructing  $\sqrt[n]{\text{TI}}$ s, on the other hand, relies on substituting the links of the parent TI with loop modules composed of unidirectional links. The resulting system is automatically  $n$ -partite, according to the definition of [221], and therefore has a built-in generalized chiral symmetry  $\mathcal{C}_n$ . Furthermore, when the Hamiltonian is raised to the  $n$ th-power, all off-diagonal blocks vanish, and a direct hierarchical relation, free of ambiguity, can be established between the  $\sqrt[n]{\text{TI}}$  and the parent TI.

## 6.4 Implementation in ring resonator lattices

We focus here on photonic ring systems, and show that they are a well suited candidate for the realization of the models described in the previous sections. We consider an array made up of a set of resonant optical ring resonators, which constitute the main rings of the lattice, coupled through smaller antiresonant link rings, as illustrated in Fig. 6.9. The link rings feature a split gain/loss distribution, in which the upper half of the ring has gain characterized by a parameter  $h$  while the lower half has an equal amount of loss. To avoid reflection effects, we use a sine-like distribution for the imaginary part of the refractive index, as shown below in Fig. 6.12. The antiresonant condition for a ring mode with propagation constant  $\beta$  reads:  $\beta(L_L - L_M) = (2m+1)\pi$ , for an integer  $m$ , where  $L_M$  and  $L_L$  are the lengths of main and link rings, respectively. Through the presence of the link rings, and due to their balanced gain and loss distribution, an effective asymmetric coupling is enabled between the same circulation  $\mathcal{K}$  in the main rings  $t_{\pm} = t e^{\pm h}$  [199], which depends exponentially on the gain and loss parameters and is analogous to an imaginary gauge field acting on the system. We represent the forward coupling direction by  $+$  and the backward direction by  $-$ . Unidirectionality in the couplings is obtained in the limit  $h \rightarrow \infty$ , while Hermiticity is restored for  $h = 0$ . For a finite  $h$  value, one is in the intermediate situation where the hoppings occur in both directions, but with the predominance of one over the other. For a strong enough gauge field, nearly perfect unidirectionality can be achieved, as we propose below. The coupling  $t$ , which from now on we label as  $\sqrt[3]{t}$  to follow the previous notation in the chapter, is determined by the relative distance between the main rings, which for the roots of the SSH model alternates between two values in different plaquettes to achieve

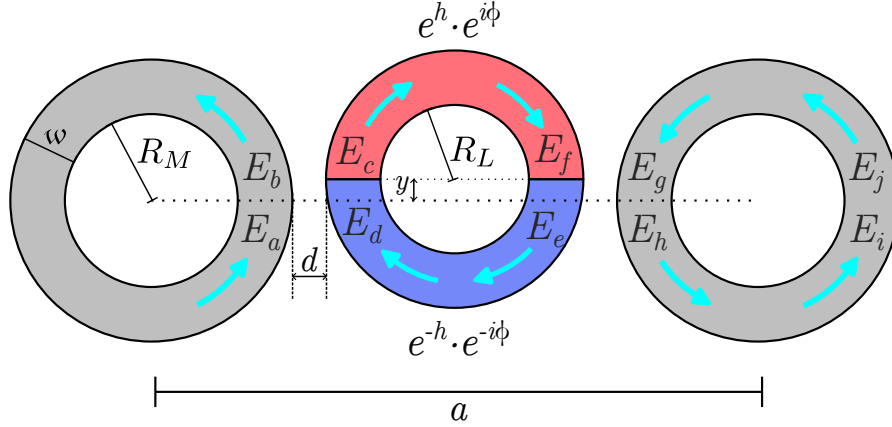


Figure 6.9: Sketch of a set of two main rings in grey, coupled through a link ring with a split gain and loss distribution, which yields a  $e^{\pm h}$  term in the coupling depending on the direction. The blue arrows signal the circulations and the field amplitudes that are coupled in each ring are also indicated. A vertical displacement of the link ring from the coupling line leads to a real phase  $\phi$  in the coupling.

$\sqrt[3]{t_1} \neq \sqrt[3]{t_2}$ . A key characteristic in this system is that for each pair of rings, only opposite circulations may be coupled between them. That is, we consider that the coupling of the (counter-)clockwise circulation of a main ring with the (counter-)clockwise of a link ring is negligible. In that sense, we can separate the system in clockwise and counter-clockwise components for all main rings. This assumption is valid as long as the coupling region between main and link rings is long compared to the wavelength of light [151], which is fulfilled for the sizes considered in this work and is reflected in the numerical results. Additionally, as we detail below, a real flux of desired value can be established in ring systems by orthogonally displacing a link ring from the line connecting the centers of the corresponding main rings, and thus generating a phase in the coupling between them [152].

For our simulations, we consider rings of planar waveguides with a radius of  $4.5 \mu\text{m}$  and a width of  $250 \text{ nm}$ . For simplicity, the cores (with refractive index  $\tilde{n}_{\text{co}} = 3$ ) are surrounded by air, leading to an overall high contrast, and the considered resonant frequency is  $195.225 \text{ THz}$ . The asymmetric effective coupling is established through smaller antiresonant link rings of radius  $3.24 \mu\text{m}$  and core refractive index  $\tilde{n}_{\text{link}} = 3 + 0.1i \sin \varphi$ , where  $\varphi$  is the angle of the polar coordinates with origin at the center of the link ring. For these parameter values, the loss factor in  $t_{\pm} = t e^{\pm h}$  is computed to be  $h = 2.07$ , implying a coupling asymmetry ratio of  $\nu \equiv t_-/t_+ = 0.016$ , very close to perfect unidirectionality. Below, we detail how to compute these coupling parameters.

### 6.4.1 Mathematical description of the ring system

As sketched in Fig. 6.9, we consider a set of main rings of radius  $R_M$  coupled through an antiresonant link ring of radius  $R_L$  with nonreciprocity parameter  $h$ , which is displaced a small distance  $y$  from the line between the center of the two neighboring main rings so that each arm picks up a phase factor of  $\phi$ . All rings have a width of  $\omega$  and we consider a separation of  $d$  between their outer radii. In such a system, we can relate the field amplitudes in neighboring rings by using the transfer matrix formulation introduced in Section 2.1.3. This yields:

$$\begin{pmatrix} E_c \\ E_d \end{pmatrix} = \frac{1}{i\kappa} \begin{pmatrix} \mathcal{T} & -1 \\ 1 & -\mathcal{T} \end{pmatrix} \begin{pmatrix} E_b \\ E_a \end{pmatrix} = M_1 \begin{pmatrix} E_b \\ E_a \end{pmatrix}, \quad (6.49)$$

$$\begin{pmatrix} E_f \\ E_e \end{pmatrix} = \begin{pmatrix} e^{i(\beta L_L/2+\phi)} e^h & 0 \\ 0 & e^{i(-\beta L_L/2+\phi)} e^h \end{pmatrix} \begin{pmatrix} E_c \\ E_d \end{pmatrix} = M_2 \begin{pmatrix} E_c \\ E_d \end{pmatrix}, \quad (6.50)$$

$$\begin{pmatrix} E_g \\ E_h \end{pmatrix} = \frac{-1}{i\kappa} \begin{pmatrix} \mathcal{T} & -1 \\ 1 & -\mathcal{T} \end{pmatrix} \begin{pmatrix} E_f \\ E_e \end{pmatrix} = M_3 \begin{pmatrix} E_f \\ E_e \end{pmatrix}, \quad (6.51)$$

$$\begin{pmatrix} E_j \\ E_i \end{pmatrix} = \begin{pmatrix} e^{-i\beta L_M/2} & 0 \\ 0 & e^{i\beta L_M/2} \end{pmatrix} \begin{pmatrix} E_g \\ E_h \end{pmatrix} = M_4 \begin{pmatrix} E_g \\ E_h \end{pmatrix}, \quad (6.52)$$

where  $\mathcal{T}$  and  $\kappa$  are the transmission and coupling coefficients,  $\beta$  is the propagation constant in the rings,  $L_M = 2\pi[R_M + \omega/2]$  ( $L_L = 2\pi[R_L + \omega/2]$ ) is the circumference length of the main (link) rings and  $E_s$  are the field amplitudes as labelled in Fig. 6.9. Note that Eqs. (6.49) and (6.51) relate amplitudes in different rings due to their coupling, while (6.50) and (6.52) relate amplitudes before/after propagating through each ring, which can also be expressed in matrix form. In a periodic system we can apply Bloch's theorem,

$$\begin{pmatrix} E_j \\ E_i \end{pmatrix} = e^{ik} \begin{pmatrix} E_b \\ E_a \end{pmatrix}, \quad (6.53)$$

where the lattice spacing is set to  $a \equiv 1$ . Notice how the relation between amplitudes in (6.53) should also be reached by sequentially following relations (6.49)-(6.52). We can then impose  $|M_4 M_3 M_2 M_1 - e^{ik} I| = 0$ , with  $I$  the identity matrix, and solve for the dispersion relation. Close to resonance of the main rings, we can apply the following substitution:  $\sin(\beta L_M) \approx (\omega - \omega_0)L_M/v_g$  [152, 200, 220], where  $\omega_0$  is the resonant frequency and  $v_g$  the group velocity. Using this approximation, in addition to the antiresonant condition for the link rings, results in the following solution for the dispersion relation:

$$\omega(k) = \omega_0 + t \left[ e^h e^{i(\phi-k)} + e^{-h} e^{-i(\phi-k)} \right], \quad (6.54)$$

where  $t = v_g \kappa^2 / L_M$  is the coupling strength between main rings. This dispersion relation is exactly the same as the one for a system with asymmetric coupling  $t_{\pm} = t e^{\pm h} e^{\pm i\phi}$ ,



thus proving that the considered ring setup can generate such a coupling. Alternatively, one might also prove this fact by obtaining the set of coupled-mode equations for the main rings as done in Ref. [199], and compare it with the asymmetric system.

To determine the value of the coupling  $t$  in a real system, we consider the Hamiltonian describing a set of two main rings coupled through a link ring with an effective asymmetric coupling but no phase:

$$H = \begin{pmatrix} \omega_0 & te^h \\ te^{-h} & \omega_0 \end{pmatrix} \quad (6.55)$$

The eigenvalues of this Hamiltonian are  $\omega_{\pm} = \omega_0 \pm t$ . Therefore, by numerically computing the eigenfrequencies of the ring block, we can obtain the coupling between main rings by doing

$$t = \frac{1}{2} (\omega_+ - \omega_-). \quad (6.56)$$

In Fig. 6.10(a) and (b), we show the eigenvalues of the basic ring block and the coupling computed from them as a function of the distance between main and link rings, respectively, for our chosen ring parameter values.

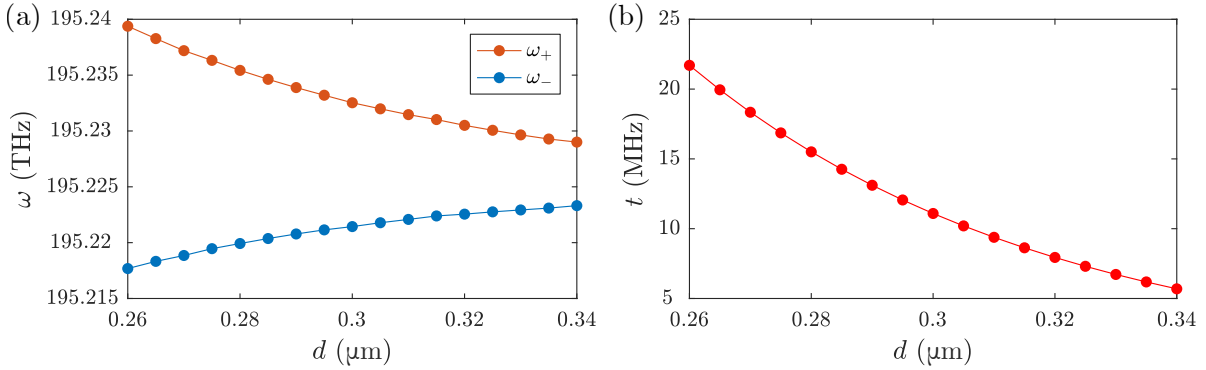


Figure 6.10: (a) Eigenfrequencies of the set depicted in Fig. 6.9, composed of two main rings coupled through a link ring, and (b) coupling between main rings computed through (6.56) using the eigenfrequencies in (a), with respect to the relative distance between main and link rings.

The description of the real and imaginary fluxes can be done by rearranging the dispersion relation (6.54) in the following way:

$$\omega(k) = \omega_0 + 2t \cos(k - \phi) \cosh h - 2it \sin(k - \phi) \sinh h, \quad (6.57)$$

where each effect can be treated separately. Real flux parameterized by  $\phi$  is introduced by displacing the link ring a certain distance  $y$  orthogonally with respect to the line between the center of the main rings, see Fig. 6.9. In essence, this modifies the optical

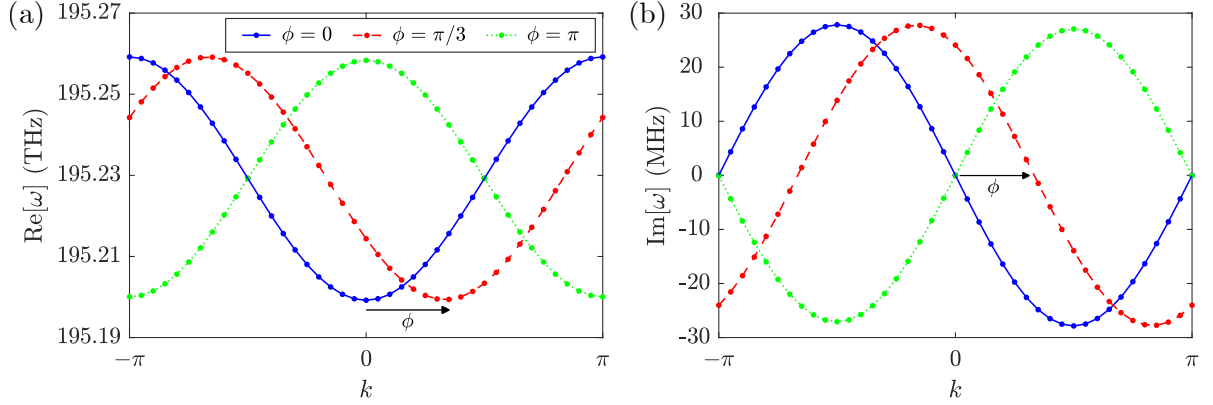


Figure 6.11: Effect of the real flux on the real part (a) and imaginary part (b) of the eigenfrequencies of the basic ring block (see Fig. 6.9) for the counterclockwise circulation. The reverse circulation will experience the effect of an equal but opposite flux.

path length of the upper and lower arms of the link ring, and thus induces a phase mismatch between both geometrical paths that approximately amounts to  $2\beta y$ , with  $\beta$  being the propagation constant of the link ring mode, which translates into a real phase  $\phi$  in the coupling. From (6.57), one can see that the real flux shifts both the real and imaginary parts of the spectrum along the  $k$  axis, as we showcase in Fig. 6.11(a) and (b), respectively. Therefore, this shift allows to properly establish a relation between the flux intensity and the displacement  $y$  of the link rings. Namely, for the fluxes shown in the figure, we employ a displacement of  $y = 0.169 \mu\text{m}$  ( $\pi$  phase) and  $y = 0.169/3 \mu\text{m}$  ( $\pi/3$  phase).

As for the imaginary flux, to quantify the asymmetry with respect to the gain and loss, we set  $\phi = 0$  and check that the imaginary part of (6.57) has a maximum (minimum) at  $k = -\pi/2$  ( $k = \pi/2$ ). Comparing  $\text{Im}(\omega)$  at these two points yields  $\Delta\omega \equiv \text{Im}(\omega(-\pi/2)) - \text{Im}(\omega(\pi/2)) = 4t \sinh h$ . Therefore, if we already computed the coupling  $t$  according to (6.56), we can extract the parameter  $h$  from

$$h = \text{asinh} \left( \frac{\Delta\omega}{4t} \right). \quad (6.58)$$

Alternatively, by knowing that the reverse circulation experiences opposite fluxes, we can apply  $h \rightarrow -h$  and  $\phi \rightarrow -\phi$  to (6.57). After doing this, we see that the position of the maximum and minimum for the imaginary part are reversed, so we can obtain the same result by comparing  $\text{Im}(\omega)$  of both circulations at  $k = \pi/2$ . From (6.58), it is straightforward to compute the asymmetry ratio of couplings  $\nu \equiv t_-/t_+ = e^{-2h}$ .

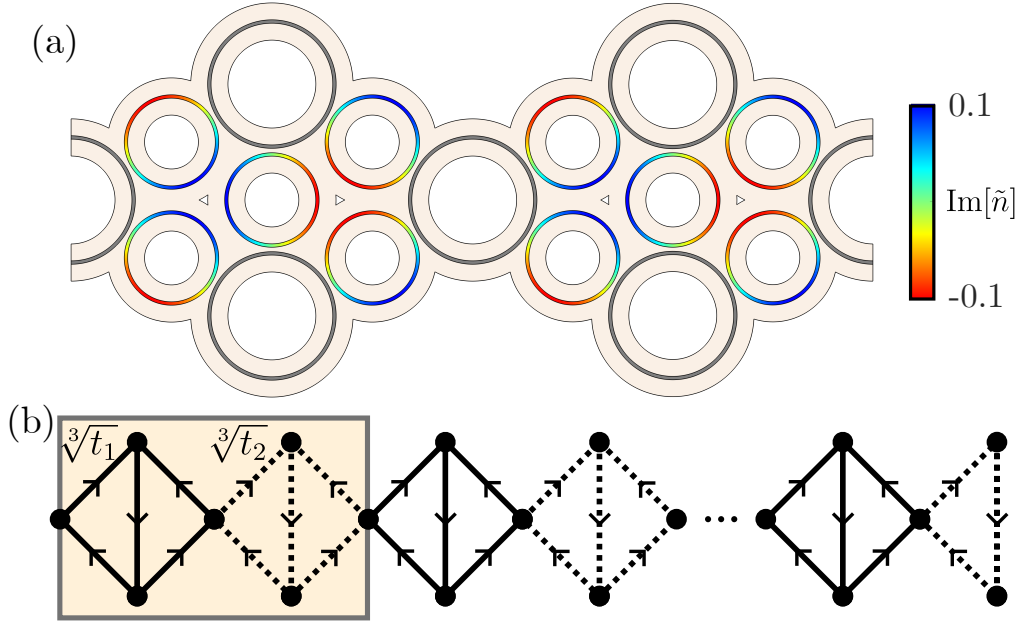


Figure 6.12: (a) Unit cell geometry of the photonic ring implementation of the  $\sqrt[3]{\text{SSH}}$  model. The grey rings constitute the main rings of the effective lattice, without gain or loss. The smaller link rings are antiresonant to the former, and display a sine-like distribution of the imaginary component of the refractive index  $\tilde{n}$ , as represented by the color bar on the right. The distance between rings is different in each plaquette so that  $\sqrt[3]{t_1} \neq \sqrt[3]{t_2}$ . (b) Graph of a lattice of the  $\sqrt[3]{\text{SSH}}$  model with OBC, with the shaded region indicating the unit cell in (a). The arrows indicate the direction of the couplings, corresponding to an effective description of the counter-clockwise ( $\mathcal{K} = -1$ ) circulation of the photonic system above. For the opposite clockwise ( $\mathcal{K} = 1$ ) circulation, an equivalent model is obtained, but with all coupling directions flipped.

### 6.4.2 Implementation of $n = 3, 4$ and 5 roots

The unit cell of the  $\sqrt[3]{\text{SSH}}$  model in the ring system takes the form displayed in Fig. 6.12(a), where the gain and loss sine-like distribution in the link rings is indicated by the color palette. This structure is then replicated several times to form the full lattice sketched in Fig. 6.12(b). To achieve the staggering of coupling, the structure displays alternating relative ring distances  $d_1 = 0.33 \mu\text{m}$  and  $d_2 = 0.3 \mu\text{m}$  in each plaquette spanning half of the unit cell, which corresponds to a coupling ratio of  $\sqrt[3]{t_1}/\sqrt[3]{t_2} \simeq 0.6$  according to Fig. 6.10(b). These distances are drawn between the outer radii of the rings. Using this structure, we perform our finite-element simulations and compute the bulk spectrum of eigenfrequencies for a periodic ring system in Fig. 6.13(a), which play the role of the energy in our system. The spectrum agrees exceptionally well with the theoretical results shown in Fig. 6.3(a). This time, the band gap for this system can

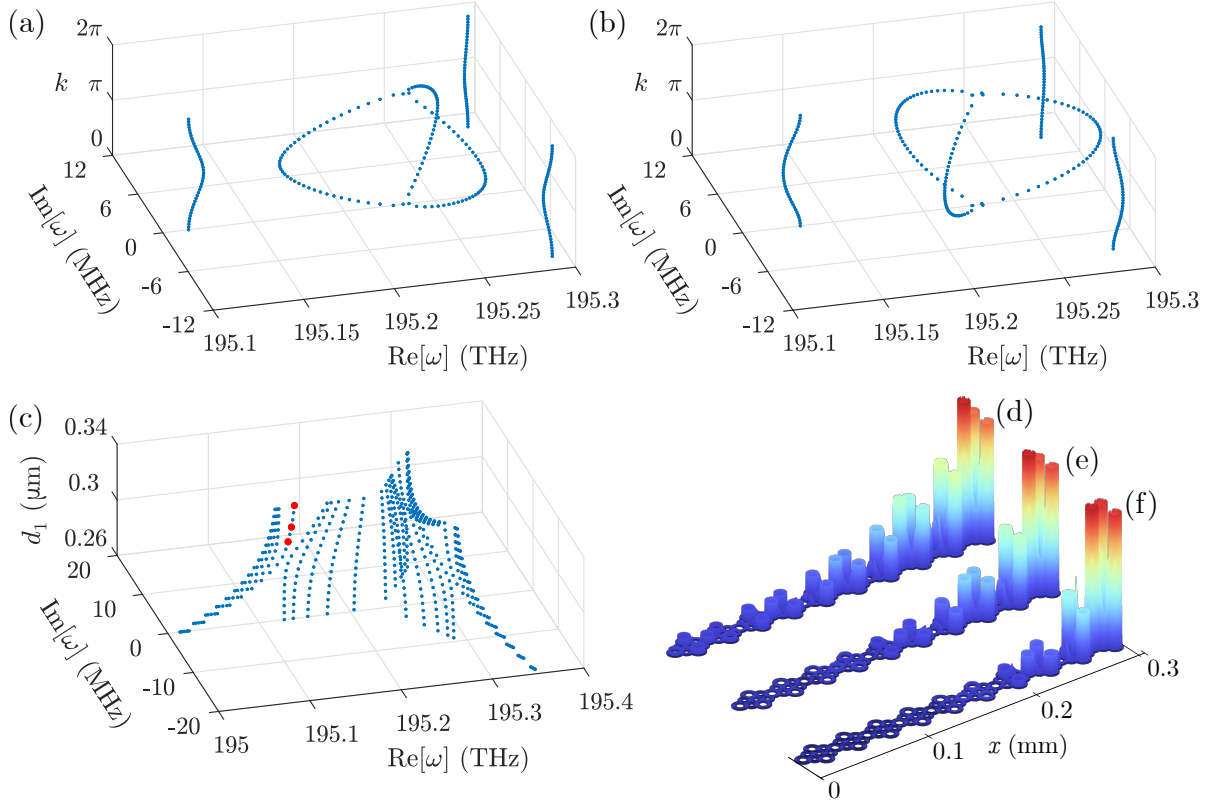


Figure 6.13: Eigenfrequencies of the photonic (a)  $\sqrt[3]{\text{SSH}}$  model and (b)  $\sqrt[3]{\text{SSH}}_{\pi/3}$  model with PBC at steps of  $\Delta k = 0.05\pi$ . The three-fold splitting along the complex plane can be readily observed. (c) Eigenspectrum of the photonic  $\sqrt[3]{\text{SSH}}$  chain with OBC and  $N_c = 5$  unit cells, with  $d_2 = 0.3 \mu\text{m}$  and  $d_1$  spanning both the topologically trivial and nontrivial phases, i.e.,  $d_1 \in [0.26 \mu\text{m}, 0.34 \mu\text{m}]$ . (d)–(f) Electric field norms for the three edge modes appearing along the ring gap for (d)  $d_1 = 0.315 \mu\text{m}$ , (e)  $d_1 = 0.325 \mu\text{m}$  and (f)  $d_1 = 0.34 \mu\text{m}$ , which are marked in red in (c).

be defined by an interval in  $|\omega|$ . On a separate note, the spectra for both clockwise and counter-clockwise circulations in the main rings are obtained in the simulations. Nonetheless, we only observe a doubly-degenerate joint spectrum instead of two separate ones. Reversing the circulation in the rings corresponds to a change of all coupling directions, but as we mentioned in Section 6.2, the system in that case is still the root of the SSH model. We now add a real flux to the system by displacing the link rings orthogonally to the coupling line [152]. We are particularly interested in realizing the  $\sqrt[3]{\text{SSH}}_{\pi/3}$  model by considering a  $\pi$  flux around the loops involving one type of hopping terms. As detailed in previous sections, this implies a sign change for one of the bands of the parent SSH model. Relative to the  $\sqrt[3]{\text{SSH}}$  model of Fig. 6.13(a), we can see in Fig. 6.13(b) that the flux causes a  $\pi$ -sliding of the outer bands and a  $\pi/3$  rotation of

the inner ones, again in perfect agreement with the theoretical results of Fig. 6.3(e).

As one would expect from a root TI, the existence of edge states in the  $\sqrt[3]{\text{SSH}}$  model under OBC is inherited from the parent system. One of the remarkable features of the cubic-root system is that, since it possesses three times as many bands as the parent one, it will host three times as many in-gap states at one of the edges, in this case the right one. The absence of topological states at the left edge can be understood as follows: upon cubing the lattice, the resulting SSH chain at the first sublattice will have an onsite energy offset at the leftmost site, due to its lower coordination number at the cubic-root level (two missing connections at its left). This onsite energy shift converts the left edge state into a bulk state. The converse reasoning can be applied to the right edge, as well as to the other two pseudo-Hermitian residual chains of the cubed model. This mechanism of single-edge locking of the topological modes is typical of high-root TIs, as demonstrated, e.g., for the diamond chain (a square-root model) in [128]. For a lattice of  $N_c = 5$  unit cells, keeping the relative distances in one sublattice fixed at  $d_2 = 0.3 \mu\text{m}$  and sweeping  $d_1$  across the topological transition point yields the spectrum showcased in Fig. 6.13(c). The edge states are exponentially localized around one of the ends of the lattice, with the localization length growing as  $d_1$  gets closer to  $d_2$  and the states evolving into bulk states after crossing the critical point  $d_1 = d_2$ , that is, after crossing to the topologically trivial regime. Three examples for different  $d_1$  are shown in Figs. 6.13(d)-(f), corresponding to the eigenfrequencies marked in red in Fig. 6.13(c). Note that the maximum of amplitudes are not to scale, but still the different localization lengths can be observed. The edge states from the other two branches are also localized around the same end of the chain, albeit with different phase distributions in the main rings.

In the case of the  $\sqrt[4]{\text{SSH}}$  model, the unit cell has the shape displayed in Fig. 6.14(a), where the long link rings are of elliptical shape with semiaxis lengths  $R_{a1} = 6.85 \mu\text{m}$  and  $R_{b1} = 2.5 \mu\text{m}$  and maximum loss value of  $\text{Im}(\tilde{n}_{\text{link}}) = 0.072$ . The short ring has semiaxis lengths  $R_{a2} = 3.2 \mu\text{m}$  and  $R_{b2} = 1.81 \mu\text{m}$  and maximum loss value of  $\text{Im}(\tilde{n}_{\text{link}}) = 0.12$ . We use  $d_1 = 0.33 \mu\text{m}$  and  $d_2 = 0.3 \mu\text{m}$  as alternating distances for both kinds of link rings in each plaquette. This leads to the following coupling values, using the notation indicated in Fig. 6.7 and in units of  $\sqrt[4]{t_2}$ :  $\sqrt[4]{t_1} = 0.615$ ,  $\sqrt[4]{t'_1} = 0.566$  and  $\sqrt[4]{t'_2} = 0.918$ . All these couplings have a nonreciprocity ratio of around  $\nu = 0.032$ . With these parameters, we simulate the system both under PBC and OBC. In Fig. 6.14(b), we show that the bulk spectrum of the photonic implementation of the  $\sqrt[4]{\text{SSH}}$  model correctly captures the four-fold splitting of the bands along the complex plane, as well as the ring gap between the inner and outer bands. A similar agreement with the theoretical result is seen in Fig. 6.14(c), where the bulk spectrum of the photonic  $\sqrt[4]{\text{SSH}}_{\frac{\pi}{4}}$  is plotted. Finally, the spectrum for OBC of the photonic  $\sqrt[4]{\text{SSH}}$  model with  $N_c = 4$  unit cells is shown in Fig. 6.14(d), where four edge modes are present, as expected. The highlighted

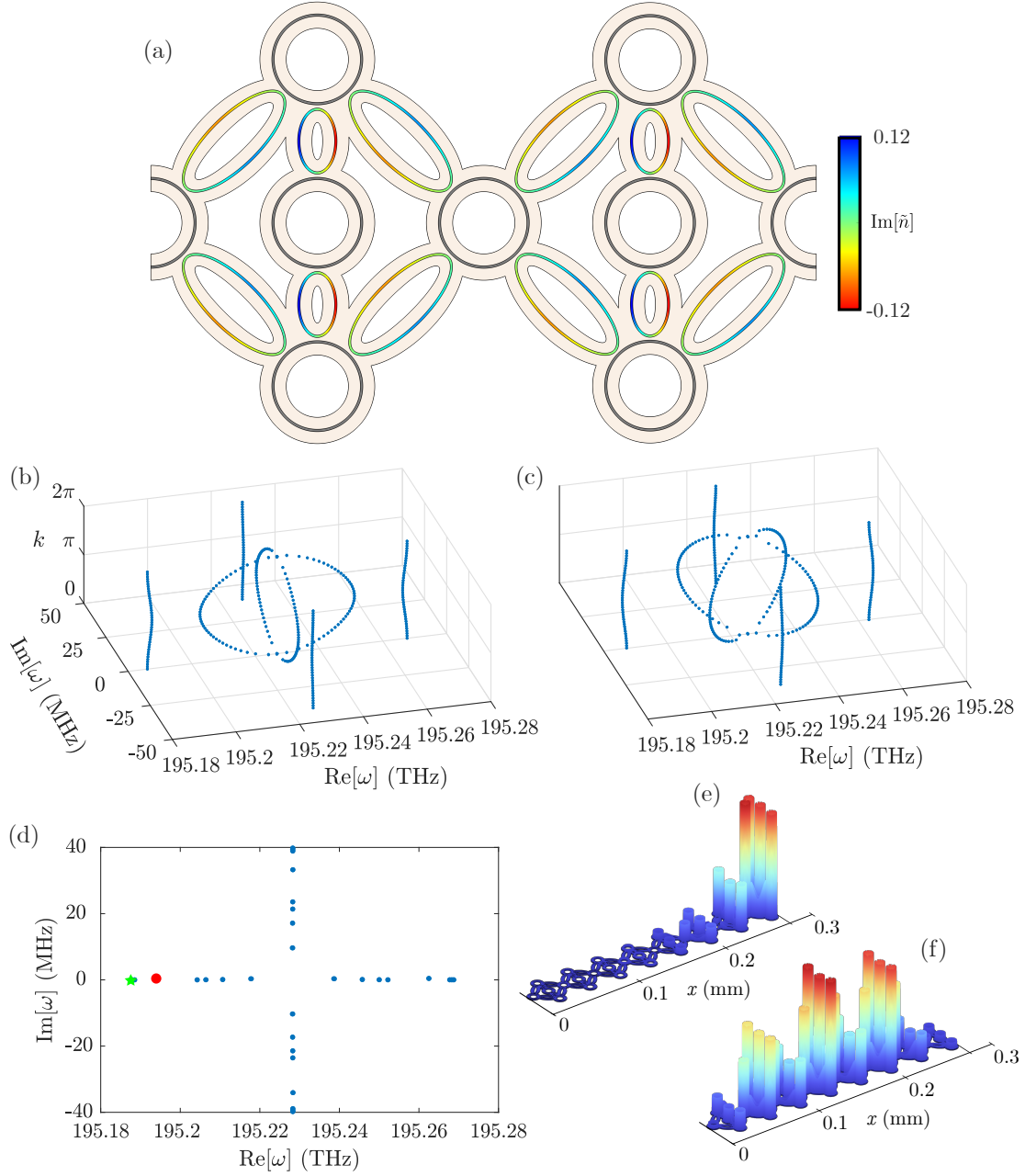


Figure 6.14: (a) Unit cell for the  $\sqrt[4]{\text{SSH}}$  model. Shorter (longer) link resonators display stronger (weaker) gain and loss modulations. Eigenfrequencies of the photonic (b)  $\sqrt[4]{\text{SSH}}$  model and (c)  $\sqrt[4]{\text{SSH}}_{\frac{\pi}{4}}$  model with PBC at steps of  $\Delta k = 0.05\pi$ . (d) Eigenfrequencies of the photonic  $\sqrt[4]{\text{SSH}}$  chain with OBC and  $N_c = 4$  unit cells, for  $d_1 = 0.33\mu\text{m}$  and  $d_2 = 0.3\mu\text{m}$ , where the four-fold splitting of the bands can be readily observed. (e)–(f) Electric field norms for the (e) edge and (f) bulk modes of the system indicated by the red point and green star, respectively, in (d).

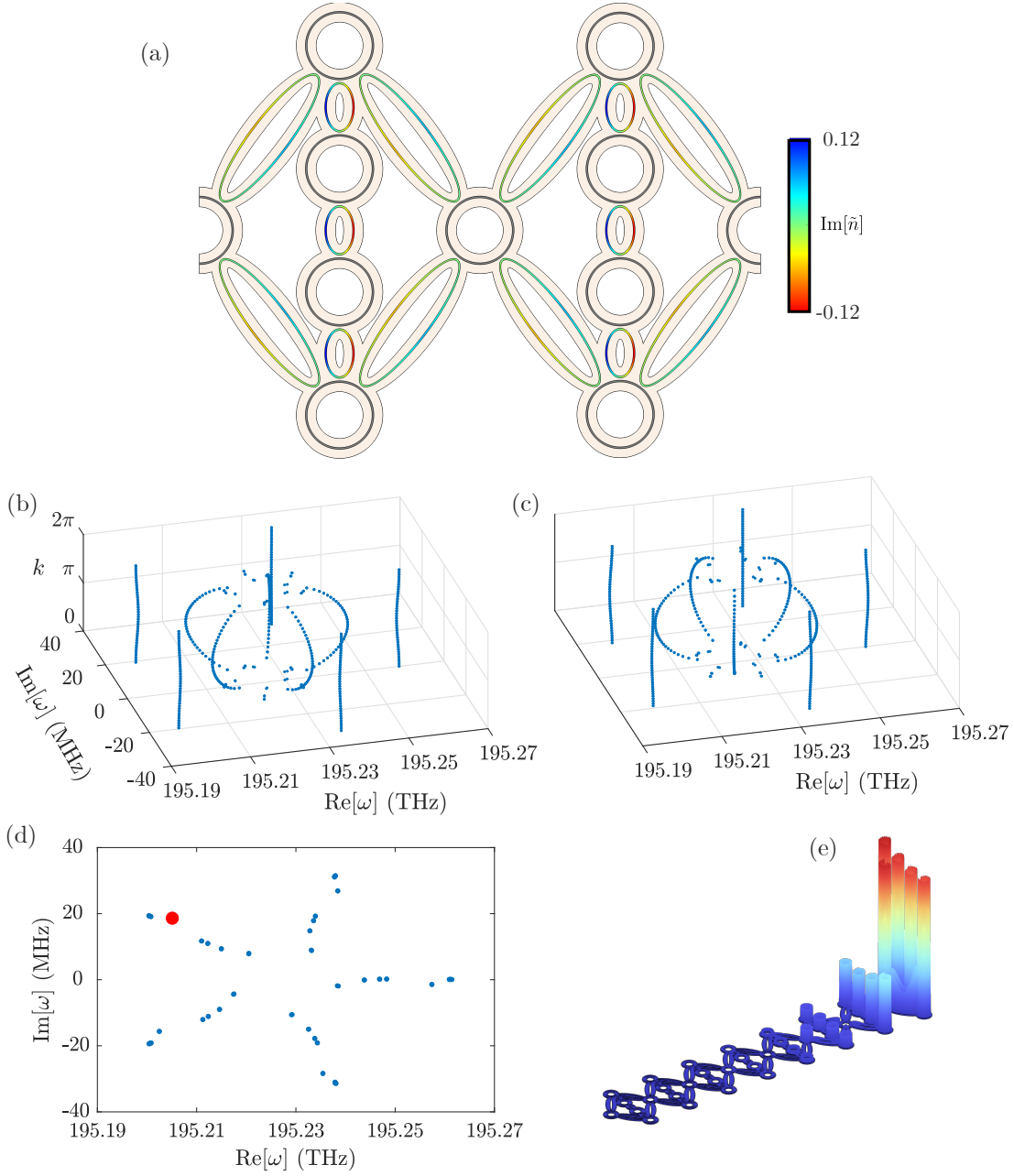


Figure 6.15: (a) Unit cell for the  $\sqrt[5]{\text{SSH}}$  model. Shorter (longer) link resonators display stronger (weaker) gain and loss values. Eigenfrequencies of the photonic (b)  $\sqrt[5]{\text{SSH}}$  model and (c)  $\sqrt[5]{\text{SSH}}_{\frac{\pi}{5}}$  model with PBC at steps of  $\Delta k = 0.05\pi$ . (d) Eigenfrequencies of the photonic  $\sqrt[5]{\text{SSH}}$  chain with OBC and  $N_c = 4$  unit cells, for  $d_1 = 0.33\mu\text{m}$  and  $d_2 = 0.3\mu\text{m}$ , where the five-fold splitting of the bands can be readily observed. (e) Electric field norms for the edge mode of the system indicated by the red point in (d).



edge mode in red is showcased in Fig. 6.14(e), together with a bulk mode in Fig. 6.14(f) for comparison.

Finally, we build the  $\sqrt[5]{\text{SSH}}$  model with the unit cell displayed in Fig. 6.15(a). For this case, the long link ring has semiaxis lengths of  $R_{a1} = 10.74 \mu\text{m}$  and  $R_{b1} = 2.5 \mu\text{m}$  and a maximum loss value of  $\text{Im}(\tilde{n}_{\text{link}}) = 0.058$ , whereas the short rings are the same as the ones used in the previous case. In Fig. 6.15(b)-(e), the same pattern of results is repeated, now showcasing the five-fold splitting characteristic of a five-partite system. In principle, any  $n$ -root model can be constructed in this manner, at the cost of increasing the system size. Comparing these figures with Fig. 6.13 and Fig. 6.14, corresponding to the cubic- and quartic-root models, one might note some deviations, particularly in the  $k = 0$  points of Figs. 6.15(b) and (c) and in the edge modes of Fig. 6.15(d) which are slightly displaced from their expected position. This is mainly caused by the elongated nature of the link rings with sharp bends, which are inherently lossier than the circular rings. By virtue of the geometrical constraints, the ellipticity in this case is made large enough for distortions to appear in the spectrum. Although these are expected to increase for higher-order roots, one may move away from the elliptic design and use different shapes for the linking elements to mitigate these effects.

### 6.4.3 Deviation from unidirectionality

Throughout the chapter, we have assumed that the ring system with modulated gains and losses produced a strong enough imaginary gauge field for the couplings to be approximately unidirectional. Now, we study how the results change as we deviate from this limit. From the Hamiltonian of the  $\sqrt[3]{\text{SSH}}$  model in (6.1), we parameterize the deviation from perfect unidirectionality as follows,

$$H'_{\sqrt[3]{\text{SSH}}}(k) = H_{\sqrt[3]{\text{SSH}}}(k) + \nu H_{\sqrt[3]{\text{SSH}}}^\dagger(k). \quad (6.59)$$

Assuming the same  $\nu$  parameterization under OBC, we show in Fig. 6.16 the energy spectrum of an  $\sqrt[3]{\text{SSH}}$  chain with  $N_c = 40$  unit cells as a function of the coupling ratio  $\sqrt[3]{t_1}/\sqrt[3]{t_2}$ , for different  $\nu$  values. As  $\nu$  is increased, little effect is observed on the real branch of the spectrum, except for some low-energy states. The two imaginary branches, in contrast, start bending more and more towards the real energy axis, eventually collapsing on it when Hermiticity is restored for  $\nu = 1$  in Fig. 6.16(e). From the system parameters indicated at the beginning of Section 6.4, we obtain the same imaginary gauge field of  $h = 2.07$  for both hopping terms  $\sqrt[3]{t_1}$  and  $\sqrt[3]{t_2}$ , translating to  $\nu = 0.016$ , which is very close to unidirectionality as can be seen, e.g., by comparing the numerical results of Fig. 6.13(a) with the analytical ones of Fig. 6.3(a). We emphasize that even for deviations as large as  $\nu = 0.25$  [see Fig. 6.16(c)], the main qualitative features survive: (i) the presence of three distinct energy branches, except at the low-energy region of



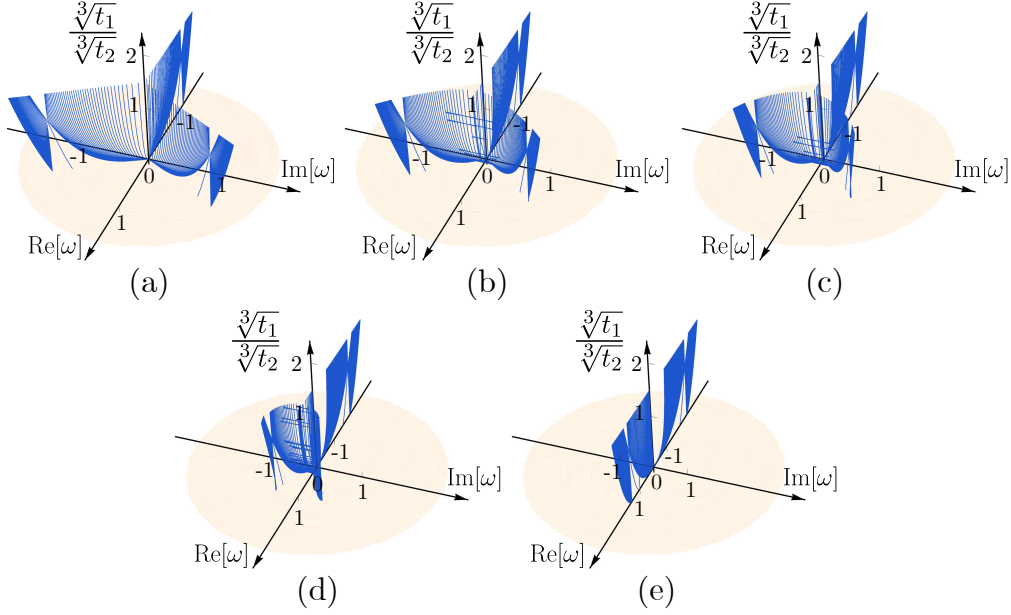


Figure 6.16: Complex energy spectrum, in units of  $\sqrt[3]{t_2} \equiv 1$ , as a function of the hopping ratio obtained from diagonalization of the Hamiltonian in (6.59) for an open chain with  $N_c = 40$  unit cells and (a)  $\nu = 0$ , (b)  $\nu = 0.13$ , (c)  $\nu = 0.25$ , (d)  $\nu = 0.5$ , and (e)  $\nu = 1$ , where  $\nu \equiv t_-/t_+ = e^{-2h}$  is a global measure of the non-reciprocity of the hopping terms.

the spectrum, since the states near zero energy are the first ones to hybridize; (ii) the persistence of a ring gap away from the gap closing point  $\sqrt[3]{t_1} = \sqrt[3]{t_2}$ , harboring three in-gap edge states for the topological phase  $\sqrt[3]{t_1} < \sqrt[3]{t_2}$ , but with small deformations with respect to the circular form that one finds for  $\nu = 0$ .

#### 6.4.4 Lossy ring resonators

Alternatively to the split gain and loss distribution in the link rings, one may also obtain an asymmetric coupling by employing only lossy rings. The main idea is similar: the upper half of the link ring allows light to propagate and couple to the other rings, this time without enhancing it with optical gain, while the lower half suppresses this propagation with losses. In this situation one must note that, instead of (6.50), now that relation becomes

$$\begin{pmatrix} E_f \\ E_e \end{pmatrix} = \begin{pmatrix} e^{i(\beta\pi R_2 + \phi)} & 0 \\ 0 & e^{i(-\beta\pi R_2 + \phi)} e^h \end{pmatrix} \begin{pmatrix} E_c \\ E_d \end{pmatrix} = M_2 \begin{pmatrix} E_c \\ E_d \end{pmatrix}, \quad (6.60)$$

to properly describe the lack of gain in the upper path. Repeating the calculation of the dispersion relation described in Section 6.4.1 now yields

$$\omega(k) = (\omega_0 - iA) + \frac{t}{\cosh(h/2)} [e^{h/2} e^{i(\phi-k)} + e^{-h/2} e^{-i(\phi-k)}], \quad (6.61)$$

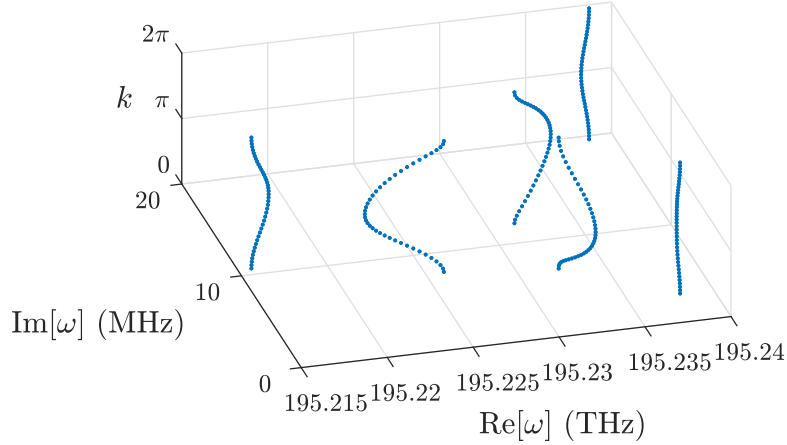


Figure 6.17: Bulk eigenfrequencies for a periodic chain of the  $\sqrt[3]{\text{SSH}}$  model using only losses in the link rings. Compared to the results in Fig. 6.13(a), the bands are distorted and shifted along the complex plane, but the main qualitative features of the three-branch spectrum are still present.

where  $A = 2t \tanh(h/2)$ . It is implicit in (6.61) that, aside from the appearance of a lower coupling  $t/\cosh(h/2)$ , compared to the case with balanced gains and losses, the effective system also displays onsite losses in the rings with a strength that is proportional to the coupling. As we see in Fig. 6.17, this distorts the bands along the complex plane and the inner bands no longer connect at  $k = 0$ . This can be explained by the fact that not all main rings are connected with the same number of link rings, so there are different sets of losses in the effective system. However, in the same figure we also observe that this is not enough to break the three-fold splitting of the bands, which is still maintained. For small gain/loss imbalance in the original implementation, only a small distortion of the bands is expected to occur.

## 6.5 Conclusions

We have demonstrated a method to obtain general  $n$ -root systems of the SSH model. We have analyzed the symmetries of the root model, and characterized the parent SSH model as the origin of the nontrivial topology of the different roots by comparing the behavior of a topological invariant in both models. Moreover, we have studied the behavior of the edge states in the root model when subject to correlated and uncorrelated disorder. We have proved that the root system is robust against any disorder that preserves the chiral symmetry of the parent SSH model, which serves as further proof that it is indeed the protecting symmetry. In addition, the root model also has the protection of its generalized chiral symmetry, which applies to the non-topological states

at the center of the spectrum.

The root procedure requires the usage of unidirectional couplings to be implemented. This poses a challenge, as non-Hermitian systems have proven to be elusive to experimental efforts until recently, where major advances have been achieved [138, 189, 190, 193, 195, 196, 199–203, 205–207, 431, 432, 435, 437, 456]. Among different possible platforms, we focused on a system of photonic ring resonators, showing it to be a very viable candidate for the implementation of  $n$ -root TIs, since quasi-unidirectional couplings can be realized by means of auxiliary link rings with a non-uniform imaginary component of the refractive index. Additionally, the high versatility of this platform makes it ideal for designing  $n$ -root systems, as it also allows, e.g., for a very precise control over the effective magnetic flux piercing the loops of these systems by simply adjusting the position of the link rings. Furthermore, we have shown how even relatively large deviations from perfect unidirectionality, up to 25%, only slightly modify the energy bands with the system maintaining its most representative properties: the  $n$ -branch splitting and the existence of a ring gap.

Implementation of systems similar to the one in this work has been accomplished with waveguide technology [152], where the positioning of the link rings is precise enough to allow introducing real phases in the couplings between main rings. The key challenge in our case is the correct engineering of the link rings. Non-Hermitian couplings in ring systems have already been achieved in lossy acoustic setups [201, 202, 432]. If no gain is considered in our system, or if gain and loss are not perfectly balanced, the effective Hamiltonian picks up imaginary diagonal elements that again only distort the bands but not the main features of the model. More recently, the split gain and loss has been implemented using optically pumped waveguides, where the lasing of different modes has been exploited [203]. The effective coupling generated in that case is analogous to the one employed here, and could allow to build the root systems in an experiment. Note that the gain/loss function need not be sine-like to achieve the results in this work, although sharp transitions from gain to loss within the same ring may cause reflection effects leading to small cross-circulation couplings. This effect can cause small band splitting, but it does not distort the properties of the whole system. Instead, one might separate the gain and loss regions into different link rings instead of within a single ring [432], or consider elongated waveguides as couplers over which the available gain can be maximized [203, 456]. Some experimental efforts to shape the pumping region have focused on the usage of spatial light modulators (SLMs), which allows to control the sections of the lattice that receive optical gain [185, 456], or alternatively limit the extent of the pump by using absorbing metal plates on top of the lattice [203, 287]. Another option is the usage of nonlinearities in the lattice to produce gain via four-wave mixing [204], where the gain region is determined by the propagation of the pumping beam through the lattice itself.

---

On the theoretical side, the method for the construction of  $n$ -root TIs, based on coupling loop modules of unidirectional couplings, is completely general and therefore not limited to the SSH model. As such, our work paves the way for further studies generalizing the applicability of the method to other emblematic topological and flat-band systems, and is expected to significantly broaden the scope of high-root topology from the  $2^n$ -root models [127–130] studied thus far.



## CHAPTER 7

---

### Conclusions and outlook

---

In this final chapter, we provide a summary of the main results presented in this thesis, as well as comment on possible extensions or future lines of research that can stem from our work. In this thesis, we have explored the role of topology in photonic systems. First, in Chapters 3 and 4, we have shown how topology can be combined with techniques originating from different fields, such as Stark-Chirped Rapid-Adiabatic-Passage (SCRAP) [212, 213] and Supersymmetry (SUSY) [212, 214], to design efficient photonic devices. Then, in Chapters 5 and 6, we have reversed the point of view and proved how photonics provides a highly versatile platform to study the fundamental properties of topological models. Namely, we have proposed experimental implementations of topological impurity systems within flat-band (FB) lattices [215, 216] in waveguide chains guiding orbital angular momentum (OAM) modes, as well as high-root topological insulators (TIs) in systems of non-Hermitian ring resonators [220]. We now delve into the results in each separate chapter.

In Chapter 2, we have set the theoretical framework for the rest of the thesis. The chapter starts by introducing Maxwell's equations and the electromagnetic theory of light, which serves to explain light propagation in optical waveguides, the physical platform on which all applications in this dissertation are based, and the concept of optical modes. We have also given a detailed analysis of the considered geometries – namely planar, cylindrical and ring resonator waveguides – and a description of how the different modes in these waveguides couple to one another. Then, we have commented on how these structures can be fabricated, and their potential as simulators for other physical systems. After this, we have dedicated a section to the description of SUSY in the context of optical waveguides. This technique can be employed to find super-

partner structures from a given waveguide or waveguide lattice, which share the same modal content as the original structure except for a single mode that is removed by the transformation. We have described the continuous formalism, which establishes a relation between spatial refractive index profiles and only allows to remove the fundamental mode; and the discrete formalism, which does the same for matrix Hamiltonians describing coupled waveguides under the tight-binding approximation, while also allowing to target any guided supermode. Finally, we have given an introduction to the ideas from the field of topology that can be applied in photonics, leading up to the concept of a TI. These striking systems serve as one of the main focus points of our works. We have introduced their key concepts, including topological invariants and protected states, through the Su-Schrieffer-Heeger (SSH) model, the quintessential one-dimensional (1D) TI. We have ended the chapter by briefly addressing the more recent field of root topology.

Our contributions begin in Chapter 3, where we have employed the SCRAP technique [53] to design a variety of photonic devices both for sets of two multimode waveguides [212] as well as lattices of single-mode waveguides [213]. To begin the chapter, we have provided a mathematical description of the technique and the particularities of the implementation in waveguide systems. Then, we have started the proposed applications by showing how SCRAP can be used for mode division (de)multiplexing in coupled two-mode waveguides, by exploiting the different transverse extension of fundamental and excited modes. Light on the excited mode is efficiently transferred between waveguides by virtue of SCRAP, while the fundamental mode remains mostly confined for the same parameter values. We have then proved how SUSY [72] can be naturally added to the scheme. Substituting one of the waveguides with its SUSY partner removes the possibility of transfer for the fundamental mode and thus enhances the efficiency of the device. After that, we have demonstrated how this geometry can be used to transform fundamental-mode injections on the SUSY waveguide into excited mode outputs on the multimode waveguide. Adding mode layers of SUSY allows to extend this for higher order optical modes as well. The second main set of applications have been based on discrete lattices of single-mode waveguides, in which transfer occurs to a supermode of the structure rather than an individual waveguide mode. We have proposed an efficient way to excite gapped topological modes of a structure, or in general any gapped mode, by appropriately engineering the propagation constant of an auxiliary waveguide and its coupling to the lattice. As a result, a single-mode injection into the auxiliary waveguide transforms into the desired supermode at the output of the device. We have proved this by exciting the topological edge modes and the bulk modes of the SSH model [95] in various configurations. By employing an entire auxiliary lattice, we have also shown how the technique can also be utilized to transfer light between the same supermode or even different supermodes in different waveguide lattices. In all cases, the transfer has been proved to be robust to geometrical inaccuracies with minimal leaking

to unwanted modes, with disorder or imperfections only reducing the total intensity that is transferred. All in all, the technique allows to efficiently excite or transfer light into any target mode as long as this mode displays a gap, and as such can be extended to systems with higher dimensionality. The interest in the topological protection of edge and interface states makes a technique that can faithfully excite them highly desirable. Both standalone SCRAP and its combination with SUSY could be employed in other physical platforms, such as in ultracold atoms [457] by controlling the position and shape of the optical traps along time.

In Chapter 4, we have focused solely on SUSY and shown how it allows to excite any gapped mode of a waveguide lattice [214]. The proposed scheme is based on using discrete SUSY (DSUSY) to design the superpartner of a given lattice by targeting a mode of interest with the transformation. In the superpartner, this mode is confined in a waveguide that is isolated from the rest of the lattice. Then, adiabatically connecting the two lattices along the propagation direction allows to efficiently transform a single-waveguide excitation into any gapped mode of the structure under investigation. To validate the proposal, we have focused on topological modes of the SSH model, both the edge state and two interface states generated by dimer defects, as well as its bulk modes. In all cases, the modes are obtained with high accuracy, yielding a significant increase in fidelity when compared to a direct excitation on the highest-amplitude waveguide. Indeed, the adiabatic modification that we have proposed in this chapter is specially useful if the desired output state is not strongly confined, as direct excitation of such states can be hard to accomplish. Compared with other more complex injection methods, such as those employing spatial light modulators (SLM) [102, 106], our proposal reduces the complexity of the input beam to the minimum. Furthermore, the strength of the method relies on the generality of the modes that can be engineered, which only require the existence of a gap. Additionally, DSUSY can be used to build other devices, such as a mode converter between edge and interface modes. This would utilize the fact that DSUSY transformations are not unique, so one could connect a lattice supporting an edge state, and one supporting an interface state adiabatically. DSUSY transformations can also be employed in two-dimensional (2D) systems [301, 320], thus opening new possibilities to generalize the high-efficiency topological excitation method discussed here to higher-dimensional settings. In general, applying DSUSY to 2D causes the appearance of nonlocal couplings that are challenging to implement physically. Some proposals relying on synthetic dimensions to engineer long range couplings [184] could be useful to overcome that obstacle. Moreover, SUSY has also been applied to non-Hermitian Hamiltonians [300, 323] and extended into what has been labeled as second- or higher-order SUSY [294, 297], where multiple modes can be targeted by the transformation. In both cases, possible scenarios in which to apply the idea of adiabatically connecting different structures could arise. Although some limited efforts to apply SUSY



to many-body systems have been proposed [298], how to implement it in general interacting systems remains an open question to be explored. Also, applications of SUSY to nonlinear optics may also appear, as it has already been shown that the superpartner of a nonlinear equation can be computed [458]. Finally, we note that although here we have used optical waveguide lattices as the physical platform and thus the adiabatic deformation is performed in space, the quantum-optical analogy [49] that we mention throughout the thesis can be reversed, and the technique could be applied to atomic, condensed-matter or quantum systems where the deformation would be performed along time.

In Chapter 5, we have demonstrated a method to engineer arbitrary systems in FB lattices by decorating them with onsite impurities [215, 216]. The method is based on the non-orthogonal compact localized states (CLSs) that inhabit the FB [111], which become coupled under the presence of impurities and generate exponentially decaying impurity states. These states form the main sites of the effective system, and their localization length depends on the flux that threads the original system, which in turn directly controls the coupling between separate impurity states. To prove the potential of the method, we have imprinted a nontrivial topological model, the SSH model, on top of a diamond chain lattice with nonzero flux per plaquette by staggering the relative distance between impurities. In the nontrivial phase, edge states have been shown to appear at the end of the impurity chain. We have conducted thorough studies on the resistance of these states to various kinds of disorders, and established that the effective system presents an increased robustness to diagonal disorder, even though it does not preserve the chiral symmetry of the SSH model. The origin of this effect has been attributed to an averaging effect that occurs over the characteristic spatial extension of the impurity states [217], and thus the resistance to disorder has been quantitatively related to the flux in the system. Moreover, we have demonstrated how non-Hermitian couplings can also be generated in the effective system by using complex-valued impurities. For a viable experimental implementation of the system, we have proposed waveguide lattices guiding light with OAM [159, 218]. The OAM modes serve both as a synthetic dimension to realize the diamond chain, as well as provide a mechanism to introduce a phase into the couplings. This works as an artificial gauge field (AGF) [154, 160] in the lattice, which reproduces the flux. Then, the value of the flux can be controlled through geometrical means simply by choosing a relative angle between the lines that unite successive waveguides. In addition, onsite impurities can be readily included by manipulating the size or refractive index of individual waveguides. The proposed platform closely replicates the theoretical results for fluxes lower than  $\pi/2$ , and shows only minor band distortions for fluxes nearing  $\pi$ . The work in this chapter lays the bases for future studies involving FB models with non-orthogonal CLSs and impurity-decorated systems. First, the method for generating effective impurity systems can be readily

extended to higher dimensional models, such as the 2D Lieb lattice [102–104], which enables the exploration of higher-order TIs. Second, non-Hermitian physics [187, 189] are also within reach in the system, as non-Hermitian couplings can be generated by the usage of onsite gains and losses in the impurity sites. This gives experimentally-available access to non-Hermitian effects in FBs. Lastly, aside from our proposed platform, modulated waveguides [158], ring resonators [152, 167], electrical circuits [136, 196], and electronic or cold atom setups [109] are promising platforms wherein FBs and impurity systems could be explored.

Finally, in Chapter 6 we have designed a method to obtain root systems of arbitrary order of the SSH model [220]. Square-root topology [119] relates a parent TI to a root TI via a square-root operation on its Hamiltonian, with the root model inheriting the topological properties from the parent whilst displaying new phenomena. In contrast to the limited extensions to  $2^n$ -th order roots that appeared shortly after [128], in this chapter we have provided a complete generalization to any order  $n$ . The method relies on the usage of unidirectional coupling loops between sublattices, making the model  $n$ -partite but also non-Hermitian. This endows the root model with a generalized chiral symmetry [221], which causes the spectrum to be split among  $n$  branches along the complex energy space, each separated by a relative angle of  $2\pi/n$ . To benchmark the procedure, we have calculated the roots of the SSH model. We have shown how, across all energy branches, a common energy gap appears with a ring shape in the complex plane. This is a novel type of gap, not reducible to line or point gaps. Within the gap,  $n$  topologically protected edge states appear. By studying the behavior of these edge states under different disorders, as well as the topological invariant in root and parent models, we have unambiguously identified the parent SSH as the source for the topology of the roots. Furthermore, we have detailed how such models can be implemented in systems of non-Hermitian photonic ring resonators [199–201]. We have shown how the required unidirectionality in the couplings can be achieved by engineering a distribution of gain and loss in the linking resonators, which effectively enhances coupling in one direction and suppresses it in the other for any given mode circulation. Also, ring resonators allow for precise implementation of a real phase in the couplings [152], which further hints at their great versatility. Using this ring system, we have presented results for the roots of orders 3, 4 and 5 of the SSH model, and analyzed how their main properties survive deviations from perfect unidirectionality and from perfect balance of gain and loss in the link rings. The split gain and loss regions have been previously implemented in optically pumped elongated waveguides [203, 456], which are used as couplers to maximize the pumped region and thus the gain. Alternatively, separating the gain and loss regions into different link rings [432], or employing nonlinearities to produce the gain via four-wave mixing [204] are also viable alternatives. Other platforms such as optical fibers [205, 206], ultracold atoms [189–192] or electrical circuits [138, 193–196] have also

shown great promise for the study of non-Hermitian effects and could allow for a similar implementation. On the theoretical side, the method for the construction of  $n$ -root TIs is completely general and therefore not limited to the SSH model. Future studies generalizing the applicability of the method to other FB systems and higher-order TIs could stem from the work presented here.

---

## Bibliography

---

- [1] J. C. Maxwell, *A Treatise on Electricity and Magnetism*, Vol. 1 (Clarendon press, 1873).
- [2] T. H. Maiman, “Stimulated Optical Radiation in Ruby,” *Nature* **187**, 493 (1960).
- [3] M. Bertolotti, *The history of the laser* (CRC press, 2004).
- [4] T. Li, “Advances in Optical Fiber Communications: An Historical Perspective,” *IEEE Journal on Selected Areas in Communications* **1**, 356 (1983).
- [5] K. Kao and G. Hockham, “Dielectric-fibre surface waveguides for optical frequencies,” *Proceedings of the Institution of Electrical Engineers* **113**, 1151 (1966).
- [6] F. P. Kapron, D. B. Keck, and R. D. Maurer, “Radiation losses in glass optical waveguides,” *Applied Physics Letters* **17**, 423 (1970).
- [7] S. E. Miller, “Integrated optics: An introduction,” *The Bell System Technical Journal* **48**, 2059 (1969).
- [8] M. A. Powell and A. O. Donnell, “What integrated optics is really used for,” *Opt. Photon. News* **8**, 23 (1997).
- [9] Z. I. Alferov, “The history and future of semiconductor heterostructures from the point of view of a Russian scientist,” *Physica Scripta* **1996**, 32 (1996).
- [10] H. Kroemer, “Band offsets and chemical bonding: the basis for heterostructure applications,” *Physica Scripta* **1996**, 10 (1996).

- [11] W. S. Boyle and G. E. Smith, “Charge Coupled Semiconductor Devices,” [Bell System Technical Journal](#) **49**, 587 (1970).
- [12] L. Ginés, *Integrated photonics: fundamentals* (J. Wiley, 2003).
- [13] P. J. Winzer, “Making spatial multiplexing a reality,” [Nature Photonics](#) **8**, 345 (2014).
- [14] D. Dai and J. E. Bowers, “Silicon-based on-chip multiplexing technologies and devices for Peta-bit optical interconnects,” [Nanophotonics](#) **3**, 283 (2014).
- [15] D. J. Richardson, J. M. Fini, and L. E. Nelson, “Space-division multiplexing in optical fibres,” [Nature Photonics](#) **7**, 354 (2013).
- [16] B. J. Puttnam, G. Rademacher, and R. S. Luís, “Space-division multiplexing for optical fiber communications,” [Optica](#) **8**, 1186 (2021).
- [17] N. Bozinovic, Y. Yue, Y. Ren, M. Tur, *et al.*, “Terabit-Scale Orbital Angular Momentum Mode Division Multiplexing in Fibers,” [Science](#) **340**, 1545 (2013).
- [18] G. Li, N. Bai, N. Zhao, and C. Xia, “Space-division multiplexing: the next frontier in optical communication,” [Adv. Opt. Photon.](#) **6**, 413 (2014).
- [19] C. Brackett, “Dense wavelength division multiplexing networks: principles and applications,” [IEEE Journal on Selected Areas in Communications](#) **8**, 948 (1990).
- [20] A. Banerjee, Y. Park, F. Clarke, H. Song, *et al.*, “Wavelength-division-multiplexed passive optical network (WDM-PON) technologies for broadband access: a review,” [J. Opt. Netw.](#) **4**, 737 (2005).
- [21] P. J. Winzer, “High-Spectral-Efficiency Optical Modulation Formats,” [J. Light-wave Technol.](#) **30**, 3824 (2012).
- [22] X. Liu, S. Chandrasekhar, and P. J. Winzer, “Digital Signal Processing Techniques Enabling Multi-Tbs Superchannel Transmission: An overview of recent advances in DSP-enabled superchannels,” [IEEE Signal Processing Magazine](#) **31**, 16 (2014).
- [23] L. Thylén and L. Wosinski, “Integrated photonics in the 21st century,” [Photonics Research](#) **2**, 75 (2014).
- [24] E. Agrell, M. Karlsson, A. R. Chraplyvy, D. J. Richardson, *et al.*, “Roadmap of optical communications,” [Journal of Optics](#) **18**, 063002 (2016).
- [25] J. Wang and Y. Long, “On-chip silicon photonic signaling and processing: a review,” [Science Bulletin](#) **63**, 1267 (2018).

- [26] N. Thomas-Peter, N. K. Langford, A. Datta, L. Zhang, *et al.*, “Integrated photonic sensing,” [New Journal of Physics](#) **13**, 055024 (2011).
- [27] P. Kozma, F. Kehl, E. Ehrentreich-Förster, C. Stamm, *et al.*, “Integrated planar optical waveguide interferometer biosensors: A comparative review,” [Biosensors and Bioelectronics](#) **58**, 287 (2014).
- [28] C. Xiang, J. Guo, W. Jin, L. Wu, *et al.*, “High-performance lasers for fully integrated silicon nitride photonics,” [Nature Communications](#) **12**, 6650 (2021).
- [29] J. Yang, M. Tang, S. Chen, and H. Liu, “From past to future: on-chip laser sources for photonic integrated circuits,” [Light: Science & Applications](#) **12**, 16 (2023).
- [30] J. S. Fandiño, P. Muñoz, D. Doménech, and J. Capmany, “A monolithic integrated photonic microwave filter,” [Nature Photonics](#) **11**, 124 (2017).
- [31] Y. Liu, A. Choudhary, D. Marpaung, and B. J. Eggleton, “Integrated microwave photonic filters,” [Adv. Opt. Photon.](#) **12**, 485 (2020).
- [32] E. Knill, R. Laflamme, and G. J. Milburn, “A scheme for efficient quantum computation with linear optics,” [Nature](#) **409**, 46 (2001).
- [33] P. Kok, W. J. Munro, K. Nemoto, T. C. Ralph, *et al.*, “Linear optical quantum computing with photonic qubits,” [Rev. Mod. Phys.](#) **79**, 135 (2007).
- [34] M. Thompson, A. Politi, J. Matthews, and J. O’Brien, “Integrated waveguide circuits for optical quantum computing,” [IET Circuits, Devices & Systems](#) **5**, 94 (2011).
- [35] G. I. Stegeman and C. T. Seaton, “Nonlinear integrated optics,” [Journal of Applied Physics](#) **58**, R57 (1985).
- [36] L. Chang, S. Liu, and J. E. Bowers, “Integrated optical frequency comb technologies,” [Nature Photonics](#) **16**, 95 (2022).
- [37] Y. Chen, “Nanofabrication by electron beam lithography and its applications: A review,” [Microelectronic Engineering](#) **135**, 57 (2015).
- [38] N. K. Efremidis, J. Hudock, D. N. Christodoulides, J. W. Fleischer, *et al.*, “Two-Dimensional Optical Lattice Solitons,” [Phys. Rev. Lett.](#) **91**, 213906 (2003).
- [39] J. W. Fleischer, M. Segev, N. K. Efremidis, and D. N. Christodoulides, “Observation of two-dimensional discrete solitons in optically induced nonlinear photonic lattices,” [Nature](#) **422**, 147 (2003).

- [40] T. Pertsch, U. Peschel, F. Lederer, J. Burghoff, *et al.*, “Discrete diffraction in two-dimensional arrays of coupled waveguides in silica,” *Opt. Lett.* **29**, 468 (2004).
- [41] K. Itoh, W. Watanabe, S. Nolte, and C. B. Schaffer, “Ultrafast Processes for Bulk Modification of Transparent Materials,” *MRS Bulletin* **31**, 620 (2006).
- [42] A. Szameit and S. Nolte, “Discrete optics in femtosecond-laser-written photonic structures,” *Journal of Physics B: Atomic, Molecular and Optical Physics* **43**, 163001 (2010).
- [43] G. C. Righini and A. Chiappini, “Glass optical waveguides: a review of fabrication techniques,” *Optical Engineering* **53**, 071819 (2014).
- [44] M. Bazzan and C. Sada, “Optical waveguides in lithium niobate: Recent developments and applications,” *Applied Physics Reviews* **2**, 040603 (2015).
- [45] S. Bogdanov, M. Y. Shalaginov, A. Boltasseva, and V. M. Shalaev, “Material platforms for integrated quantum photonics,” *Optical Materials Express* **7**, 111 (2017).
- [46] I. Buluta and F. Nori, “Quantum Simulators,” *Science* **326**, 108 (2009).
- [47] A. Aspuru-Guzik and P. Walther, “Photonic quantum simulators,” *Nature Physics* **8**, 285 (2012).
- [48] I. M. Georgescu, S. Ashhab, and F. Nori, “Quantum simulation,” *Rev. Mod. Phys.* **86**, 153 (2014).
- [49] S. Longhi, “Quantum-optical analogies using photonic structures,” *Laser & Photonics Reviews* **3**, 243 (2009).
- [50] N. Chiodo, G. D. Valle, R. Osellame, S. Longhi, *et al.*, “Imaging of Bloch oscillations in erbium-doped curved waveguide arrays,” *Optics Letters* **31**, 1651 (2006).
- [51] G. D. Valle, S. Longhi, P. Laporta, P. Biagioni, *et al.*, “Discrete diffraction in waveguide arrays: A quantitative analysis by tunneling optical microscopy,” *Applied Physics Letters* **90**, 261118 (2007).
- [52] A. Szameit, F. Dreisow, H. Hartung, S. Nolte, *et al.*, “Quasi-incoherent propagation in waveguide arrays,” *Applied Physics Letters* **90**, 241113 (2007).
- [53] L. P. Yatsenko, B. W. Shore, T. Halfmann, K. Bergmann, *et al.*, “Source of metastable  $H(2s)$  atoms using the Stark chirped rapid-adiabatic-passage technique,” *Physical Review A* **60**, R4237 (1999).

- [54] B. W. Shore, “Picturing stimulated Raman adiabatic passage: a STIRAP tutorial,” [Adv. Opt. Photon.](#) **9**, 563 (2017).
- [55] T. Rickes, L. P. Yatsenko, S. Steuerwald, T. Halfmann, *et al.*, “Efficient adiabatic population transfer by two-photon excitation assisted by a laser-induced Stark shift,” [Journal of Chemical Physics](#) **113**, 534 (2000).
- [56] S. Myslivets, A. Popov, T. Halfmann, J. Marangos, *et al.*, “Nonlinear-optical vacuum ultraviolet generation at maximum atomic coherence controlled by a laser-induced Stark chirp of two-photon resonance,” [Optics Communications](#) **209**, 335 (2002).
- [57] T. Rickes, J. Marangos, and T. Halfmann, “Enhancement of third-harmonic generation by Stark-chirped rapid adiabatic passage,” [Optics Communications](#) **227**, 133 (2003).
- [58] A. A. Rangelov, N. V. Vitanov, L. P. Yatsenko, B. W. Shore, *et al.*, “Stark-shift-chirped rapid-adiabatic-passage technique among three states,” [Physical Review A](#) **72**, 053403 (2005).
- [59] B. Y. Chang, H. Choi, S. Shin, and I. R. Sola, “Quantum-state-selective two-photon excitation of multilevel systems assisted by the Stark shift,” [Physical Review A](#) **75**, 063405 (2007).
- [60] M. Oberst, H. Münch, and T. Halfmann, “Efficient Coherent Population Transfer among Three States in NO Molecules by Stark-Chirped Rapid Adiabatic Passage,” [Physical Review Letters](#) **99**, 173001 (2007).
- [61] N. Shirkhanghah, M. Saadati-Niari, and S. Ahadpour, “Fractional population transfer among three-level systems in a cavity by Stark-shift-chirped rapid adiabatic passage,” [Quantum Information Processing](#) **19**, 128 (2020).
- [62] T. Wan, T. Wang, W. Zhou, and C. Chen, “Coupling modulation for efficient wavelength conversion with the Stark-chirped rapid adiabatic passage,” [Results in Physics](#) **19**, 103387 (2020).
- [63] H. Zhang, X. Zhang, T. Wan, D. Cheng, *et al.*, “Efficient cascaded wavelength conversion under two-peak modulated Stark-chirped rapid adiabatic passage via grating structures,” [Results in Physics](#) **27**, 104524 (2021).
- [64] P. Ramond, “Dual Theory for Free Fermions,” [Phys. Rev. D](#) **3**, 2415 (1971).
- [65] A. Neveu and J. Schwarz, “Factorizable dual model of pions,” [Nuclear Physics B](#) **31**, 86 (1971).



- [66] Y. A. Gelfand and E. P. Likhtman, “Extension of the algebra of Poincare group generators and violation of P invariance,” [JETP Lett. \*\*13\*\*, 323 \(1971\)](#).
- [67] J. Wess and B. Zumino, “Supergauge transformations in four dimensions,” [Nuclear Physics B \*\*70\*\*, 39 \(1974\)](#).
- [68] G. L. Kane and M. A. Shifman, *The supersymmetric world: the beginnings of the theory* (World Scientific Publishing, 2001).
- [69] N. Surlas, “Introduction to supersymmetry in condensed matter physics,” [Physica D: Nonlinear Phenomena \*\*15\*\*, 115 \(1985\)](#).
- [70] S. M. Chumakov and K. B. Wolf, “Supersymmetry in Helmholtz optics,” [Physics Letters A \*\*193\*\*, 51 \(1994\)](#).
- [71] S. Longhi, “Bloch oscillations in tight-binding lattices with defects,” [Physical Review B \*\*81\*\*, 195118 \(2010\)](#).
- [72] M.-A. Miri, M. Heinrich, R. El-Ganainy, and D. N. Christodoulides, “Supersymmetric Optical Structures,” [Phys. Rev. Lett. \*\*110\*\*, 233902 \(2013\)](#).
- [73] F. Cooper, A. Khare, and U. Sukhatme, “Supersymmetry and quantum mechanics,” [Physics Reports \*\*251\*\*, 267 \(1995\)](#).
- [74] G. Junker, *Supersymmetric methods in quantum and statistical physics* (Springer-Verlag, 1996).
- [75] M. Dine, *Supersymmetry and string theory - beyond the standard model* (Cambridge University Press, 2007).
- [76] M.-A. Miri, M. Heinrich, and D. N. Christodoulides, “Supersymmetry-generated complex optical potentials with real spectra,” [Phys. Rev. A \*\*87\*\*, 43819 \(2013\)](#).
- [77] M. Heinrich, M.-A. Miri, S. Stützer, R. El-Ganainy, *et al.*, “Supersymmetric mode converters,” [Nature Communications \*\*5\*\*, 3698 \(2014\)](#).
- [78] G. Queraltó, M. Kremer, L. J. Maczewsky, M. Heinrich, *et al.*, “Topological state engineering via supersymmetric transformations,” [Communications Physics \*\*3\*\*, 49 \(2020\)](#).
- [79] S. Longhi, “Invisibility in non-Hermitian tight-binding lattices,” [Phys. Rev. A \*\*82\*\*, 32111 \(2010\)](#).
- [80] M. Heinrich, M.-A. Miri, S. Stützer, S. Nolte, *et al.*, “Observation of supersymmetric scattering in photonic lattices,” [Opt. Lett. \*\*39\*\*, 6130 \(2014\)](#).

- [81] M.-A. Miri, M. Heinrich, and D. N. Christodoulides, “SUSY-inspired one-dimensional transformation optics,” *Optica* **1**, 89 (2014).
- [82] G. Queraltó, V. Ahufinger, and J. Mompart, “Integrated photonic devices based on adiabatic transitions between supersymmetric structures,” *Optics Express* **26**, 33797 (2018).
- [83] I. James, *History of Topology* (Elsevier Science, 1999).
- [84] P. A. M. Dirac, “Quantised singularities in the electromagnetic field,” *Proceedings of the Royal Society of London A* **133**, 60 (1931).
- [85] Y. Aharonov and D. Bohm, “Significance of Electromagnetic Potentials in the Quantum Theory,” *Physical Review* **115**, 485 (1959).
- [86] R. G. Chambers, “Shift of an Electron Interference Pattern by Enclosed Magnetic Flux,” *Phys. Rev. Lett.* **5**, 3 (1960).
- [87] K. v. Klitzing, G. Dorda, and M. Pepper, “New Method for High-Accuracy Determination of the Fine-Structure Constant Based on Quantized Hall Resistance,” *Phys. Rev. Lett.* **45**, 494 (1980).
- [88] D. S. Simon, *Tying Light in Knots*, 2053-2571 (Morgan & Claypool Publishers, 2018).
- [89] R. B. Laughlin, “Quantized Hall conductivity in two dimensions,” *Phys. Rev. B* **23**, 5632 (1981).
- [90] D. J. Thouless, M. Kohmoto, M. P. Nightingale, and M. den Nijs, “Quantized Hall Conductance in a Two-Dimensional Periodic Potential,” *Phys. Rev. Lett.* **49**, 405 (1982).
- [91] F. D. M. Haldane, “Model for a Quantum Hall Effect without Landau Levels: Condensed-Matter Realization of the "Parity Anomaly",” *Phys. Rev. Lett.* **61**, 2015 (1988).
- [92] M. Z. Hasan and C. L. Kane, “Colloquium : Topological insulators,” *Reviews of Modern Physics* **82**, 3045 (2010).
- [93] X.-L. Qi and S.-C. Zhang, “Topological insulators and superconductors,” *Rev. Mod. Phys.* **83**, 1057 (2011).
- [94] A. P. Schnyder, S. Ryu, A. Furusaki, and A. W. W. Ludwig, “Classification of topological insulators and superconductors in three spatial dimensions,” *Phys. Rev. B* **78**, 195125 (2008).

- [95] W. P. Su, J. R. Schrieffer, and A. J. Heeger, “Solitons in Polyacetylene,” [Phys. Rev. Lett. \*\*42\*\*, 1698 \(1979\)](#).
- [96] M. V. Berry, “Quantal Phase Factors Accompanying Adiabatic Changes,” [Proceedings of the Royal Society of London. Series A, Mathematical and Physical Sciences \*\*392\*\*, 45 \(1984\)](#).
- [97] E. Cohen, H. Larocque, F. Bouchard, F. Nejadsattari, *et al.*, “Geometric phase from Aharonov–Bohm to Pancharatnam–Berry and beyond,” [Nature Reviews Physics \*\*1\*\*, 437 \(2019\)](#).
- [98] S. Pancharatnam, “Generalized theory of interference, and its applications,” [Proceedings of the Indian Academy of Sciences - Section A \*\*44\*\*, 247 \(1956\)](#).
- [99] J. Zak, “Berry’s phase for energy bands in solids,” [Phys. Rev. Lett. \*\*62\*\*, 2747 \(1989\)](#).
- [100] D. Vanderbilt, [\*Berry Phases in Electronic Structure Theory: Electric Polarization, Orbital Magnetization and Topological Insulators\*](#) (Cambridge University Press, 2018).
- [101] J. K. Asbóth, L. Oroszlány, and A. P. Pályi, *A Short Course on Topological Insulators: Band Structure and Edge States in One and Two Dimensions* (Springer International Publishing, 2016).
- [102] R. A. Vicencio, C. Cantillano, L. Morales-Inostroza, B. Real, *et al.*, “Observation of Localized States in Lieb Photonic Lattices,” [Physical Review Letters \*\*114\*\*, 245503 \(2015\)](#).
- [103] S. Mukherjee, A. Spracklen, D. Choudhury, N. Goldman, *et al.*, “Observation of a Localized Flat-Band State in a Photonic Lieb Lattice,” [Physical Review Letters \*\*114\*\*, 245504 \(2015\)](#).
- [104] S. Taie, H. Ozawa, T. Ichinose, T. Nishio, *et al.*, “Coherent driving and freezing of bosonic matter wave in an optical Lieb lattice,” [Science Advances \*\*1\*\*, e1500854 \(2015\)](#).
- [105] S. Xia, Y. Hu, D. Song, Y. Zong, *et al.*, “Demonstration of flat-band image transmission in optically induced Lieb photonic lattices,” [Optics Letters \*\*41\*\*, 1435 \(2016\)](#).
- [106] Y. Zong, S. Xia, L. Tang, D. Song, *et al.*, “Observation of localized flat-band states in Kagome photonic lattices,” [Optics Express \*\*24\*\*, 8877 \(2016\)](#).

- [107] R. Drost, T. Ojanen, A. Harju, and P. Liljeroth, “Topological states in engineered atomic lattices,” [Nature Physics](#) **13**, 668 (2017).
- [108] M. R. Slot, T. S. Gardenier, P. H. Jacobse, G. C. Van Miert, *et al.*, “Experimental realization and characterization of an electronic Lieb lattice,” [Nature Physics](#) **13**, 672 (2017).
- [109] A. A. Daniel Leykam and S. Flach, “Artificial flat band systems: from lattice models to experiments,” [Advances in Physics: X](#) **3**, 1473052 (2018).
- [110] C. Danieli, A. Andreanov, D. Leykam, and S. Flach, Flat band fine-tuning and its photonic applications (2024), [arXiv:2403.17578 \[physics.optics\]](#) .
- [111] W. Maimaiti, A. Andreanov, H. C. Park, O. Gendelman, *et al.*, “Compact localized states and flat-band generators in one dimension,” [Physical Review B](#) **95**, 115135 (2017).
- [112] J. Vidal, R. Mosseri, and B. Douçot, “Aharonov-Bohm Cages in Two-Dimensional Structures,” [Phys. Rev. Lett.](#) **81**, 5888 (1998).
- [113] K. Fang, Z. Yu, and S. Fan, “Photonic Aharonov-Bohm Effect Based on Dynamic Modulation,” [Phys. Rev. Lett.](#) **108**, 153901 (2012).
- [114] S. Longhi, “Aharonov–Bohm photonic cages in waveguide and coupled resonator lattices by synthetic magnetic fields,” [Optics Letters](#) **39**, 5892 (2014).
- [115] G. Pelegrí, A. M. Marques, R. G. Dias, A. J. Daley, *et al.*, “Topological edge states with ultracold atoms carrying orbital angular momentum in a diamond chain,” [Physical Review A](#) **99**, 023612 (2019).
- [116] G. Pelegrí, A. M. Marques, R. G. Dias, A. J. Daley, *et al.*, “Topological edge states and Aharonov-Bohm caging with ultracold atoms carrying orbital angular momentum,” [Phys. Rev. A](#) **99**, 023613 (2019).
- [117] M. D. Liberto, S. Mukherjee, and N. Goldman, “Nonlinear dynamics of Aharonov-Bohm cages,” [Physical Review A](#) **100**, 043829 (2019).
- [118] A. A. Lopes, B. A. Z. António, and R. G. Dias, “Conductance through geometrically frustrated itinerant electronic systems,” [Physical Review B](#) **89**, 235418 (2014).
- [119] J. Arkinstall, M. H. Teimourpour, L. Feng, R. El-Ganainy, *et al.*, “Topological tight-binding models from nontrivial square roots,” [Physical Review B](#) **95**, 165109 (2017).

- [120] T. Mizoguchi, Y. Kuno, and Y. Hatsugai, “Square-root higher-order topological insulator on a decorated honeycomb lattice,” [Physical Review A \*\*102\*\*, 033527 \(2020\)](#).
- [121] M. Ezawa, “Systematic construction of square-root topological insulators and superconductors,” [Physical Review Research \*\*2\*\*, 033397 \(2020\)](#).
- [122] M. Kremer, I. Petrides, E. Meyer, M. Heinrich, *et al.*, “A square-root topological insulator with non-quantized indices realized with photonic Aharonov-Bohm cages,” [Nature Communications \*\*11\*\*, 907 \(2020\)](#).
- [123] M. Yan, X. Huang, L. Luo, J. Lu, *et al.*, “Acoustic square-root topological states,” [Physical Review B \*\*102\*\*, 180102 \(2020\)](#).
- [124] L. Song, H. Yang, Y. Cao, and P. Yan, “Realization of the Square-Root Higher-Order Topological Insulator in Electric Circuits,” [Nano Letters \*\*20\*\*, 7566 \(2020\)](#).
- [125] W. Yan, D. Song, S. Xia, J. Xie, *et al.*, “Realization of Second-Order Photonic Square-Root Topological Insulators,” [ACS Photonics \*\*8\*\*, 3308 \(2021\)](#).
- [126] L. Song, H. Yang, Y. Cao, and P. Yan, “Square-root higher-order Weyl semimetals,” [Nature Communications \*\*13\*\*, 5601 \(2022\)](#).
- [127] R. G. Dias and A. M. Marques, “Matryoshka approach to sine-cosine topological models,” [Physical Review B \*\*103\*\*, 245112 \(2021\)](#).
- [128] A. M. Marques, L. Madail, and R. G. Dias, “One-dimensional  $2^n$ -root topological insulators and superconductors,” [Physical Review B \*\*103\*\*, 235425 \(2021\)](#).
- [129] A. M. Marques and R. G. Dias, “ $2^n$ -root weak, Chern, and higher-order topological insulators, and  $2^n$ -root topological semimetals,” [Physical Review B \*\*104\*\*, 165410 \(2021\)](#).
- [130] A. M. Marques, J. Mögerle, G. Pelegrí, S. Flannigan, *et al.*, “Kaleidoscopes of Hofstadter butterflies and Aharonov-Bohm caging from  $2^n$ -root topology in decorated square lattices,” [Physical Review Research \*\*5\*\*, 023110 \(2023\)](#).
- [131] Z. Cui, M. Peng, X. Zhang, Q. Wei, *et al.*, “Realization of multiple topological boundary states in phononic crystals,” [Physical Review B \*\*107\*\*, 165414 \(2023\)](#).
- [132] R. Wei, Q. Zhang, D. Yang, X. Huang, *et al.*, “Realization of one-dimensional  $2^n$ -root topological states in photonic lattices,” [Science China Technological Sciences \*\*67\*\*, 98 \(2024\)](#).

- [133] M. Aidelsburger, M. Atala, M. Lohse, J. T. Barreiro, *et al.*, “Realization of the Hofstadter Hamiltonian with Ultracold Atoms in Optical Lattices,” [Phys. Rev. Lett.](#) **111**, 185301 (2013).
- [134] N. Goldman, J. C. Budich, and P. Zoller, “Topological quantum matter with ultracold gases in optical lattices,” [Nature Physics](#) **12**, 639 (2016).
- [135] N. R. Cooper, J. Dalibard, and I. B. Spielman, “Topological bands for ultracold atoms,” [Rev. Mod. Phys.](#) **91**, 015005 (2019).
- [136] C. H. Lee, S. Imhof, C. Berger, F. Bayer, *et al.*, “Topoelectrical Circuits,” [Communications Physics](#) **1**, 39 (2018).
- [137] S. Imhof, C. Berger, F. Bayer, J. Brehm, *et al.*, “Topoelectrical-circuit realization of topological corner modes,” [Nature Physics](#) **14**, 925 (2018).
- [138] T. Helbig, T. Hofmann, S. Imhof, M. Abdelghany, *et al.*, “Generalized bulk–boundary correspondence in non-Hermitian topoelectrical circuits,” [Nature Physics](#) **16**, 747 (2020).
- [139] Z. Yang, F. Gao, X. Shi, X. Lin, *et al.*, “Topological Acoustics,” [Physical Review Letters](#) **114**, 114301 (2015).
- [140] X. Zhang, M. Xiao, Y. Cheng, M.-H. Lu, *et al.*, “Topological sound,” [Communications Physics](#) **1**, 97 (2018).
- [141] H. Xue, Y. Yang, and B. Zhang, “Topological acoustics,” [Nature Reviews Materials](#) **7**, 974 (2022).
- [142] L. Lu, J. D. Joannopoulos, and M. Soljačić, “Topological photonics,” [Nature Photonics](#) **8**, 821 (2014).
- [143] T. Ozawa, H. M. Price, A. Amo, N. Goldman, *et al.*, “Topological photonics,” [Reviews of Modern Physics](#) **91**, 015006 (2019).
- [144] D. Leykam and L. Yuan, “Topological phases in ring resonators: recent progress and future prospects,” [Nanophotonics](#) **9**, 4473 (2020).
- [145] J. Kang, R. Wei, Q. Zhang, and G. Dong, “Topological Photonic States in Waveguide Arrays,” [Advanced Physics Research](#) **2**, 2200053 (2023).
- [146] F. D. M. Haldane and S. Raghu, “Possible Realization of Directional Optical Waveguides in Photonic Crystals with Broken Time-Reversal Symmetry,” [Phys. Rev. Lett.](#) **100**, 013904 (2008).

- [147] S. Raghu and F. D. M. Haldane, “Analogues of quantum-Hall-effect edge states in photonic crystals,” [Phys. Rev. A](#) **78**, 033834 (2008).
- [148] J. Joannopoulos, P. R. Villeneuve, and S. Fan, “Photonic crystals,” [Solid State Communications](#) **102**, 165 (1997), highlights in Condensed Matter Physics and Materials Science.
- [149] Z. Wang, Y. D. Chong, J. D. Joannopoulos, and M. Soljačić, “Reflection-Free One-Way Edge Modes in a Gyromagnetic Photonic Crystal,” [Phys. Rev. Lett.](#) **100**, 013905 (2008).
- [150] Z. Wang, Y. Chong, J. D. Joannopoulos, and M. Soljačić, “Observation of unidirectional backscattering-immune topological electromagnetic states,” [Nature](#) **461**, 772 (2009).
- [151] M. Hafezi, E. A. Demler, M. D. Lukin, and J. M. Taylor, “Robust optical delay lines with topological protection,” [Nature Physics](#) **7**, 907 (2011).
- [152] M. Hafezi, S. Mittal, J. Fan, A. Migdall, *et al.*, “Imaging topological edge states in silicon photonics,” [Nature Photonics](#) **7**, 1001 (2013).
- [153] M. C. Rechtsman, J. M. Zeuner, A. Tünnermann, S. Nolte, *et al.*, “Strain-induced pseudomagnetic field and photonic Landau levels in dielectric structures,” [Nature Photonics](#) **7**, 153 (2013).
- [154] Y. Lumer, M. A. Bandres, M. Heinrich, L. J. Maczewsky, *et al.*, “Light guiding by artificial gauge fields,” [Nature Photonics](#) **13**, 339 (2019).
- [155] K. Fang, Z. Yu, and S. Fan, “Realizing effective magnetic field for photons by controlling the phase of dynamic modulation,” [Nature Photonics](#) **6**, 782 (2012).
- [156] M. C. Rechtsman, J. M. Zeuner, Y. Plotnik, Y. Lumer, *et al.*, “Photonic Floquet topological insulators,” [Nature](#) **496**, 196 (2013).
- [157] S. Mukherjee, A. Spracklen, M. Valiente, E. Andersson, *et al.*, “Experimental observation of anomalous topological edge modes in a slowly driven photonic lattice,” [Nature Communications](#) **8**, 13918 (2017).
- [158] S. Mukherjee, M. D. Liberto, P. Öhberg, R. R. Thomson, *et al.*, “Experimental Observation of Aharonov-Bohm Cages in Photonic Lattices,” [Physical Review Letters](#) **121**, 075502 (2018).
- [159] C. Jörg, G. Queraltó, M. Kremer, G. Pelegrí, *et al.*, “Artificial gauge field switching using orbital angular momentum modes in optical waveguides,” [Light: Science & Applications](#) **9**, 150 (2020).

- [160] R. A. Vicencio, “Photonic flat band dynamics,” [Advances in Physics: X](#) **6**, 1878057 (2021).
- [161] N. Malkova, I. Hromada, X. Wang, G. Bryant, *et al.*, “Observation of optical Shockley-like surface states in photonic superlattices,” [Opt. Lett.](#) **34**, 1633 (2009).
- [162] Y. E. Kraus, Y. Lahini, Z. Ringel, M. Verbin, *et al.*, “Topological States and Adiabatic Pumping in Quasicrystals,” [Phys. Rev. Lett.](#) **109**, 106402 (2012).
- [163] M. Verbin, O. Zilberberg, Y. E. Kraus, Y. Lahini, *et al.*, “Observation of Topological Phase Transitions in Photonic Quasicrystals,” [Phys. Rev. Lett.](#) **110**, 076403 (2013).
- [164] M. Xiao, Z. Q. Zhang, and C. T. Chan, “Surface Impedance and Bulk Band Geometric Phases in One-Dimensional Systems,” [Physical Review X](#) **4**, 021017 (2014).
- [165] C. Poli, M. Bellec, U. Kuhl, F. Mortessagne, *et al.*, “Selective enhancement of topologically induced interface states in a dielectric resonator chain,” [Nature Communications](#) **6**, 6710 (2015).
- [166] A. Blanco-Redondo, I. Andonegui, M. J. Collins, G. Harari, *et al.*, “Topological Optical Waveguiding in Silicon and the Transition between Topological and Trivial Defect States,” [Phys. Rev. Lett.](#) **116**, 163901 (2016).
- [167] S. Mittal, J. Fan, S. Faez, A. Migdall, *et al.*, “Topologically Robust Transport of Photons in a Synthetic Gauge Field,” [Physical Review Letters](#) **113**, 087403 (2014).
- [168] S. Mittal, S. Ganeshan, J. Fan, A. Vaezi, *et al.*, “Measurement of topological invariants in a 2D photonic system,” [Nature Photonics](#) **10**, 180 (2016).
- [169] M. A. Bandres, S. Wittek, G. Harari, M. Parto, *et al.*, “Topological insulator laser: Experiments,” [Science](#) **359**, eaar4005 (2018).
- [170] C. W. Peterson, W. A. Benalcazar, T. L. Hughes, and G. Bahl, “A quantized microwave quadrupole insulator with topologically protected corner states,” [Nature](#) **555**, 346 (2018).
- [171] S. Mittal, V. V. Orre, G. Zhu, M. A. Gorlach, *et al.*, “Photonic quadrupole topological phases,” [Nature Photonics](#) **13**, 692 (2019).
- [172] A. El Hassan, F. K. Kunst, A. Moritz, G. Andler, *et al.*, “Corner states of light in photonic waveguides,” [Nature Photonics](#) **13**, 697 (2019).



- [173] W. A. Benalcazar, B. A. Bernevig, and T. L. Hughes, “Quantized electric multipole insulators,” [Science](#) **357**, 61 (2017).
- [174] F. Schindler, A. M. Cook, M. G. Vergniory, Z. Wang, *et al.*, “Higher-order topological insulators,” [Science Advances](#) **4**, eaat0346 (2018).
- [175] A. Celi, P. Massignan, J. Ruseckas, N. Goldman, *et al.*, “Synthetic Gauge Fields in Synthetic Dimensions,” [Physical Review Letters](#) **112**, 043001 (2014).
- [176] T. Ozawa, H. M. Price, N. Goldman, O. Zilberberg, *et al.*, “Synthetic dimensions in integrated photonics: From optical isolation to four-dimensional quantum Hall physics,” [Physical Review A](#) **93**, 043827 (2016).
- [177] L. Yuan, Q. Lin, M. Xiao, and S. Fan, “Synthetic dimension in photonics,” [Optica](#) **5**, 1396 (2018).
- [178] A. Dutt, M. Minkov, I. A. D. Williamson, and S. Fan, “Higher-order topological insulators in synthetic dimensions,” [Light: Science & Applications](#) **9**, 131 (2020).
- [179] M. Ehrhardt, S. Weidemann, L. J. Maczewsky, M. Heinrich, *et al.*, “A Perspective on Synthetic Dimensions in Photonics,” [Laser & Photonics Reviews](#) **17**, 2200518 (2023).
- [180] E. Lustig, S. Weimann, Y. Plotnik, Y. Lumer, *et al.*, “Photonic topological insulator in synthetic dimensions,” [Nature](#) **567**, 356 (2019).
- [181] E. Nicolau, A. M. Marques, R. G. Dias, J. Mompart, *et al.*, “Many-body Aharonov-Bohm caging in a lattice of rings,” [Physical Review A](#) **107**, 023305 (2023).
- [182] M. Wimmer, H. M. Price, I. Carusotto, and U. Peschel, “Experimental measurement of the Berry curvature from anomalous transport,” [Nature Physics](#) **13**, 545 (2017).
- [183] C. Leefmans, A. Dutt, J. Williams, L. Yuan, *et al.*, “Topological dissipation in a time-multiplexed photonic resonator network,” [Nature Physics](#) **18**, 442 (2022).
- [184] B. A. Bell, K. Wang, A. S. Solntsev, D. N. Neshev, *et al.*, “Spectral photonic lattices with complex long-range coupling,” [Optica](#) **4**, 1433 (2017).
- [185] H. Zhao, X. Qiao, T. Wu, B. Midya, *et al.*, “Non-Hermitian topological light steering,” [Science](#) **365**, 1163 (2019).
- [186] D.-W. Zhang, L.-Z. Tang, L.-J. Lang, H. Yan, *et al.*, “Non-Hermitian topological Anderson insulators,” [Science China Physics, Mechanics & Astronomy](#) **63**, 267062 (2020).

- [187] M. M. Denner, A. Skurativska, F. Schindler, M. H. Fischer, *et al.*, “Exceptional topological insulators,” [Nature Communications](#) **12**, 5681 (2021).
- [188] N. Okuma and M. Sato, “Non-Hermitian Topological Phenomena: A Review,” [Annual Review of Condensed Matter Physics](#) **14**, 83 (2023).
- [189] Z. Gong, Y. Ashida, K. Kawabata, K. Takasan, *et al.*, “Topological Phases of Non-Hermitian Systems,” [Physical Review X](#) **8**, 031079 (2018).
- [190] T. Liu, Y.-R. Zhang, Q. Ai, Z. Gong, *et al.*, “Second-Order Topological Phases in Non-Hermitian Systems,” [Physical Review Letters](#) **122**, 076801 (2019).
- [191] Q. Liang, D. Xie, Z. Dong, H. Li, *et al.*, “Dynamic Signatures of Non-Hermitian Skin Effect and Topology in Ultracold Atoms,” [Physical Review Letters](#) **129**, 070401 (2022).
- [192] S. Guo, C. Dong, F. Zhang, J. Hu, *et al.*, “Theoretical prediction of a non-Hermitian skin effect in ultracold-atom systems,” [Physical Review A](#) **106**, L061302 (2022).
- [193] T. Hofmann, T. Helbig, C. H. Lee, M. Greiter, *et al.*, “Chiral Voltage Propagation and Calibration in a Topoelectrical Chern Circuit,” [Physical Review Letters](#) **122**, 247702 (2019).
- [194] L. Li, C. H. Lee, S. Mu, and J. Gong, “Critical non-Hermitian skin effect,” [Nature Communications](#) **11**, 5491 (2020).
- [195] S. Liu, R. Shao, S. Ma, L. Zhang, *et al.*, “Non-Hermitian Skin Effect in a Non-Hermitian Electrical Circuit,” [Research](#) **2021**, 5608038 (2021).
- [196] D. Zou, T. Chen, W. He, J. Bao, *et al.*, “Observation of hybrid higher-order skin-topological effect in non-Hermitian topoelectrical circuits,” [Nature Communications](#) **12**, 7201 (2021).
- [197] A. Ghatak, M. Brandenbourger, J. van Wezel, and C. Coullais, “Observation of non-Hermitian topology and its bulk–edge correspondence in an active mechanical metamaterial,” [Proceedings of the National Academy of Sciences](#) **117**, 29561 (2020).
- [198] W. Wang, X. Wang, and G. Ma, “Non-Hermitian morphing of topological modes,” [Nature](#) **608**, 50 (2022).
- [199] S. Longhi, D. Gatti, and G. D. Valle, “Robust light transport in non-Hermitian photonic lattices,” [Scientific Reports](#) **5**, 13376 (2015).

- [200] Z. Lin, S. Ke, X. Zhu, and X. Li, “Square-root non-Bloch topological insulators in non-Hermitian ring resonators,” [Optics Express](#) **29**, 8462 (2021).
- [201] X. Zhang, Y. Tian, J.-H. Jiang, M.-H. Lu, *et al.*, “Observation of higher-order non-Hermitian skin effect,” [Nature Communications](#) **12**, 5377 (2021).
- [202] Z. Gu, H. Gao, H. Xue, J. Li, *et al.*, “Transient non-Hermitian skin effect,” [Nature Communications](#) **13**, 7668 (2022).
- [203] Y. G. N. Liu, Y. Wei, O. Hemmatyar, G. G. Pyrialakos, *et al.*, “Complex skin modes in non-Hermitian coupled laser arrays,” [Light: Science & Applications](#) **11**, 336 (2022).
- [204] T. Dai, Y. Ao, J. Mao, Y. Yang, *et al.*, “Non-Hermitian topological phase transitions controlled by nonlinearity,” [Nature Physics](#) **20**, 101 (2024).
- [205] S. Weidemann, M. Kremer, T. Helbig, T. Hofmann, *et al.*, “Topological funneling of light,” [Science](#) **368**, 311 (2020).
- [206] S. Weidemann, M. Kremer, S. Longhi, and A. Szameit, “Topological triple phase transition in non-Hermitian Floquet quasicrystals,” [Nature](#) **601**, 354 (2022).
- [207] S. Ke, W. Wen, D. Zhao, and Y. Wang, “Floquet engineering of the non-Hermitian skin effect in photonic waveguide arrays,” [Physical Review A](#) **107**, 053508 (2023).
- [208] R. A. Vicencio, D. Román-Cortés, M. Rubio-Saldías, P. Vildoso, *et al.*, Non-reciprocal coupling in photonics (2024), [arXiv:2407.18174 \[physics.optics\]](#) .
- [209] J. Zhong, K. Wang, Y. Park, V. Asadchy, *et al.*, “Nontrivial point-gap topology and non-Hermitian skin effect in photonic crystals,” [Physical Review B](#) **104**, 125416 (2021).
- [210] K. Yokomizo, T. Yoda, and S. Murakami, “Non-Hermitian waves in a continuous periodic model and application to photonic crystals,” [Physical Review Research](#) **4**, 023089 (2022).
- [211] Z. Fang, M. Hu, L. Zhou, and K. Ding, “Geometry-dependent skin effects in reciprocal photonic crystals,” [Nanophotonics](#) **11**, 3447 (2022).
- [212] D. Viedma, V. Ahufinger, and J. Mompart, “Supersymmetry-enhanced stark-chirped rapid-adiabatic-passage in multimode optical waveguides,” [Optics Express](#) **29**, 39200 (2021).
- [213] D. Viedma, J. Mompart, and V. Ahufinger, “Mode pumping in photonic lattices using a single tailored auxiliary waveguide,” [Physical Review A](#) **107**, 023506 (2023).

- [214] D. Viedma, G. Queraltó, J. Mompart, and V. Ahufinger, “High-efficiency topological pumping with discrete supersymmetry transformations,” *Optics Express* **30**, 23531 (2022).
- [215] A. M. Marques, D. Viedma, V. Ahufinger, and R. G. Dias, Impurity flat band states in the diamond chain (2024), [arXiv:2407.14405 \[cond-mat.str-el\]](#) .
- [216] D. Viedma, A. M. Marques, R. G. Dias, and V. Ahufinger, Flux-mediated effective su-schrieffer-heeger model in an impurity decorated diamond chain (2024), [arXiv:2407.15789 \[cond-mat.str-el\]](#) .
- [217] F. Munoz, F. Pinilla, J. Mella, and M. I. Molina, “Topological properties of a bipartite lattice of domain wall states,” *Scientific Reports* **8**, 17330 (2018).
- [218] C. Jiang, Y. Wu, M. Qin, and S. Ke, “Topological Bound Modes With Orbital Angular Momentum in Optical Waveguide Arrays,” *Journal of Lightwave Technology* **41**, 2205 (2023).
- [219] Y. Wang, C. Jiang, M. Zhao, D. Zhao, *et al.*, “Compact topological edge modes through hybrid coupling of orbital angular momentum modes,” *Phys. Rev. A* **109**, 063516 (2024).
- [220] D. Viedma, A. M. Marques, R. G. Dias, and V. Ahufinger, “Topological n-root Su-Schrieffer-Heeger model in a non-Hermitian photonic ring system,” *Nanophotonics* **13**, 51 (2024).
- [221] A. M. Marques and R. G. Dias, “Generalized Lieb’s theorem for noninteracting non-Hermitian n-partite tight-binding lattices,” *Physical Review B* **106**, 205146 (2022).
- [222] B. E. A. Saleh and M. C. Teich, *Fundamentals of photonics*, 2nd ed. (Wiley-Interscience, 2007).
- [223] C.-L. Chen, *Foundations for guided-wave optics* (Wiley-Interscience, 2007).
- [224] R. Burden, J. Faires, and A. Burden, *Numerical Analysis* (Cengage Learning, 2015).
- [225] R. Olshansky, “Propagation in glass optical waveguides,” *Reviews of Modern Physics* **51**, 341 (1979).
- [226] W.-P. Huang, “Coupled-mode theory for optical waveguides: an overview,” *Journal of the Optical Society of America A* **11**, 963 (1994).

- [227] L. Allen, M. W. Beijersbergen, R. J. C. Spreeuw, and J. P. Woerdman, “Orbital angular momentum of light and the transformation of Laguerre-Gaussian laser modes,” [Physical Review A](#) **45**, 8185 (1992).
- [228] G. Gibson, J. Courtial, M. J. Padgett, M. Vasnetsov, *et al.*, “Free-space information transfer using light beams carrying orbital angular momentum,” [Optics Express](#) **12**, 5448 (2004).
- [229] Z. Bouchal and R. Celechovský, “Mixed vortex states of light as information carriers,” [New Journal of Physics](#) **6**, 131 (2004).
- [230] Z.-K. Su, F.-Q. Wang, R.-B. Jin, R.-S. Liang, *et al.*, “A simple scheme for quantum networks based on orbital angular momentum states of photons,” [Optics Communications](#) **281**, 5063 (2008).
- [231] J. Wang, J.-Y. Yang, I. M. Fazal, N. Ahmed, *et al.*, “Terabit free-space data transmission employing orbital angular momentum multiplexing,” [Nature Photonics](#) **6**, 488 (2012).
- [232] J. Zhang, G. Zhu, J. Liu, X. Wu, *et al.*, “Orbital-angular-momentum mode-group multiplexed transmission over a graded-index ring-core fiber based on receive diversity and maximal ratio combining,” [Optics Express](#) **26**, 4243 (2018).
- [233] L. Gong, Q. Zhao, H. Zhang, X.-Y. Hu, *et al.*, “Optical orbital-angular-momentum-multiplexed data transmission under high scattering,” [Light: Science & Applications](#) **8**, 27 (2019).
- [234] J. Wang and X. Zhang, “Orbital Angular Momentum in Fibers,” [Journal of Light-wave Technology](#) **41**, 1934 (2023).
- [235] Y. Chen, J. Gao, Z.-Q. Jiao, K. Sun, *et al.*, “Mapping Twisted Light into and out of a Photonic Chip,” [Physical Review Letters](#) **121**, 233602 (2018).
- [236] J. Heebner, R. Grover, and T. Ibrahim, [Optical Microresonators: Theory, Fabrication, and Applications](#), Optical Sciences, 138 (Springer, 2008).
- [237] T. Barwicz, M. A. Popovic, P. T. Rakich, M. R. Watts, *et al.*, “Microring-resonator-based add-drop filters in SiN: fabrication and analysis,” [Optics Express](#) **12**, 1437 (2004).
- [238] F. Xia, L. Sekaric, and Y. Vlasov, “Ultracompact optical buffers on a silicon chip,” [Nature Photonics](#) **1**, 65 (2007).

- [239] H. Jayatilleka, H. Shoman, R. Boeck, N. A. F. Jaeger, *et al.*, “Automatic Configuration and Wavelength Locking of Coupled Silicon Ring Resonators,” [Journal of Lightwave Technology](#) **36**, 210 (2018).
- [240] A. M. Armani and K. J. Vahala, “Heavy water detection using ultra-high-Q microcavities,” [Optics Letters](#) **31**, 1896 (2006).
- [241] Y. Sun and X. Fan, “Optical ring resonators for biochemical and chemical sensing,” [Analytical and Bioanalytical Chemistry](#) **399**, 205 (2011).
- [242] H. Xu, M. Hafezi, J. Fan, J. M. Taylor, *et al.*, “Ultra-sensitive chip-based photonic temperature sensor using ring resonator structures,” [Optics Express](#) **22**, 3098 (2014).
- [243] P. Miao, Z. Zhang, J. Sun, W. Walasik, *et al.*, “Orbital angular momentum microlaser,” [Science](#) **353**, 464 (2016).
- [244] M. Parto, S. Wittek, H. Hodaei, G. Harari, *et al.*, “Edge-Mode Lasing in 1D Topological Active Arrays,” [Phys. Rev. Lett.](#) **120**, 113901 (2018).
- [245] B. Midya, H. Zhao, X. Qiao, P. Miao, *et al.*, “Supersymmetric microring laser arrays,” [Photonics Research](#) **7**, 363 (2019).
- [246] X. Qiao, B. Midya, Z. Gao, Z. Zhang, *et al.*, “Higher-dimensional supersymmetric microlaser arrays,” [Science](#) **372**, 403 (2021).
- [247] T. J. Kippenberg, A. L. Gaeta, M. Lipson, and M. L. Gorodetsky, “Dissipative Kerr solitons in optical microresonators,” [Science](#) **361**, eaan8083 (2018).
- [248] L. Ding, Z. Lin, S. Ke, B. Wang, *et al.*, “Non-Hermitian flat bands in rhombic microring resonator arrays,” [Optics Express](#) **29**, 24373 (2021).
- [249] L. Rayleigh, “CXII. The problem of the whispering gallery,” [The London, Edinburgh, and Dublin Philosophical Magazine and Journal of Science](#) **20**, 1001 (1910).
- [250] X. Roselló Mechó, *Whispering gallery modes: advanced photonic applications*, Ph.D. thesis, Universitat de València (2019).
- [251] J. Sarma and K. Shore, “Electromagnetic theory for optical disc resonators,” [IEEE Proceedings J Optoelectronics](#) **132**, 325 (1985).
- [252] I. Chremmos, O. Schwelb, and N. Uzunoglu, *Photonic microresonator research and applications*, Vol. 156 (Springer, 2010).

- [253] M. Heiblum and J. Harris, “Analysis of curved optical waveguides by conformal transformation,” [IEEE Journal of Quantum Electronics](#) **11**, 75 (1975).
- [254] M. Chin and S. Ho, “Design and modeling of waveguide-coupled single-mode microring resonators,” [Journal of Lightwave Technology](#) **16**, 1433 (1998).
- [255] U. Leonhardt, “Optical Conformal Mapping,” [Science](#) **312**, 1777 (2006).
- [256] A. L. Jones, “Coupling of Optical Fibers and Scattering in Fibers,” [J. Opt. Soc. Am.](#) **55**, 261 (1965).
- [257] A. Szameit, F. Dreisow, T. Pertsch, S. Nolte, *et al.*, “Control of directional evanescent coupling in fs laser written waveguides,” [Optics Express](#) **15**, 1579 (2007).
- [258] R. Keil, B. Pressl, R. Heilmann, M. Gräfe, *et al.*, “Direct measurement of second-order coupling in a waveguide lattice,” [Applied Physics Letters](#) **107**, 241104 (2015).
- [259] D. N. Christodoulides, F. Lederer, and Y. Silberberg, “Discretizing light behaviour in linear and nonlinear waveguide lattices,” [Nature](#) **424**, 817 (2003).
- [260] J. Zhou, “A non-orthogonal coupled mode theory for super-modes inside multi-core fibers,” [Optics Express](#) **22**, 10815 (2014).
- [261] H. Haus, W. Huang, S. Kawakami, and N. Whitaker, “Coupled-mode theory of optical waveguides,” [Journal of Lightwave Technology](#) **5**, 16 (1987).
- [262] B. A. McKinnon and T. C. Choy, “Significance of nonorthogonality in tight-binding models,” [Physical Review B](#) **52**, 14531 (1995).
- [263] F. Mangussi, M. Milićević, I. Sagnes, L. L. Gratiet, *et al.*, “Multi-orbital tight binding model for cavity-polariton lattices,” [Journal of Physics: Condensed Matter](#) **32**, 315402 (2020).
- [264] J. Schulz, C. Jörg, and G. von Freymann, “Geometric control of next-nearest-neighbor coupling in evanescently coupled dielectric waveguides,” [Optics Express](#) **30**, 9869 (2022).
- [265] J. Polo, J. Mompart, and V. Ahufinger, “Geometrically induced complex tunnelings for ultracold atoms carrying orbital angular momentum,” [Physical Review A](#) **93**, 033613 (2016).
- [266] M. Kremer, L. J. Maczewsky, M. Heinrich, and A. Szameit, “Topological effects in integrated photonic waveguide structures [Invited],” [Optical Materials Express](#) **11**, 1014 (2021).



- [267] L. Li, W. Kong, and F. Chen, “Femtosecond laser-inscribed optical waveguides in dielectric crystals: a concise review and recent advances,” [Advanced Photonics](#) **4**, 024002 (2022).
- [268] A. Champion, M. Beresna, P. Kazansky, and Y. Bellouard, “Stress distribution around femtosecond laser affected zones: effect of nanogratings orientation,” [Optics Express](#) **21**, 24942 (2013).
- [269] B. McMillen and Y. Bellouard, “On the anisotropy of stress-distribution induced in glasses and crystals by non-ablative femtosecond laser exposure,” [Optics Express](#) **23**, 86 (2015).
- [270] J. Burghoff, C. Grebing, S. Nolte, and A. Tünnermann, “Efficient frequency doubling in femtosecond laser-written waveguides in lithium niobate,” [Applied Physics Letters](#) **89**, 081108 (2006).
- [271] F. Chen and J. R. V. de Aldana, “Optical waveguides in crystalline dielectric materials produced by femtosecond-laser micromachining,” [Laser & Photonics Reviews](#) **8**, 251 (2014).
- [272] B. Zhang, L. Wang, and F. Chen, “Recent Advances in Femtosecond Laser Processing of LiNbO<sub>3</sub> Crystals for Photonic Applications,” [Laser and Photonics Reviews](#) **14**, 1900407 (2020).
- [273] Y. Jia, S. Wang, and F. Chen, “Femtosecond laser direct writing of flexibly configured waveguide geometries in optical crystals: fabrication and application,” [Opto-Electronic Advances](#) **3**, 190042 (2020).
- [274] A. Žukauskas, I. Matulaitienė, D. Paipulas, G. Niaura, *et al.*, “Tuning the refractive index in 3D direct laser writing lithography: towards GRIN microoptics,” [Laser & Photonics Reviews](#) **9**, 706 (2015).
- [275] C. Jörg, F. Letscher, M. Fleischhauer, and G. von Freymann, “Dynamic defects in photonic Floquet topological insulators,” [New Journal of Physics](#) **19**, 083003 (2017).
- [276] J. Schulz, S. Vaidya, and C. Jörg, “Topological photonics in 3D micro-printed systems,” [APL Photonics](#) **6**, 080901 (2021).
- [277] A. Rodenas and A. K. Kar, “High-contrast step-index waveguides in borate non-linear laser crystals by 3D laser writing,” [Optics Express](#) **19**, 17820 (2011).



- [278] G. Cheng, C. D’Amico, X. Liu, and R. Stoian, “Large mode area waveguides with polarization functions by volume ultrafast laser photoinscription of fused silica,” [Optics Letters](#) **38**, 1924 (2013).
- [279] B. Sun, F. Morozko, P. S. Salter, S. Moser, *et al.*, “On-chip beam rotators, adiabatic mode converters, and waveplates through low-loss waveguides with variable cross-sections,” [Light: Science & Applications](#) **11**, 214 (2022).
- [280] Y. Jia, C. Cheng, J. R. V. de Aldana, G. R. Castillo, *et al.*, “Monolithic crystalline cladding microstructures for efficient light guiding and beam manipulation in passive and active regimes,” [Scientific Reports](#) **4**, 5988 (2014).
- [281] J. Lv, Y. Cheng, J. R. V. de Aldana, X. Hao, *et al.*, “Femtosecond Laser Writing of Optical-Lattice-Like Cladding Structures for Three-Dimensional Waveguide Beam Splitters in LiNbO<sub>3</sub> Crystal,” [Journal of Lightwave Technology](#) **34**, 3587 (2016).
- [282] W. Sun, Y. Liu, C. Romero, J. R. V. de Aldana, *et al.*, “Q-switched vortex waveguide laser generation based on LNOI thin films with implanted Ag nanoparticles,” [Optics Express](#) **31**, 36725 (2023).
- [283] H. Hodaei, M.-A. Miri, M. Heinrich, D. N. Christodoulides, *et al.*, “Parity-time-symmetric microring lasers,” [Science](#) **346**, 975 (2014).
- [284] C. J. Flower, M. J. Mehrabad, L. Xu, G. Moille, *et al.*, “Observation of topological frequency combs,” [Science](#) **384**, 1356 (2024).
- [285] J. Ren, Y. G. N. Liu, M. Parto, W. E. Hayenga, *et al.*, “Unidirectional light emission in PT-symmetric microring lasers,” [Optics Express](#) **26**, 27153 (2018).
- [286] W. E. Hayenga, M. Parto, J. Ren, F. O. Wu, *et al.*, “Direct Generation of Tunable Orbital Angular Momentum Beams in Microring Lasers with Broadband Exceptional Points,” [ACS Photonics](#) **6**, 1895 (2019).
- [287] Y. G. N. Liu, P. S. Jung, M. Parto, D. N. Christodoulides, *et al.*, “Gain-induced topological response via tailored long-range interactions,” [Nature Physics](#) **17**, 704 (2021).
- [288] N. K. Efremidis, S. Sears, D. N. Christodoulides, J. W. Fleischer, *et al.*, “Discrete solitons in photorefractive optically induced photonic lattices,” [Physical Review E](#) **66**, 046602 (2002).
- [289] P. Wang, Y. Zheng, X. Chen, C. Huang, *et al.*, “Localization and delocalization of light in photonic moiré lattices,” [Nature](#) **577**, 42 (2020).

- [290] S. Xia, D. Song, N. Wang, X. Liu, *et al.*, “Topological phenomena demonstrated in photorefractive photonic lattices [Invited],” [Optical Materials Express](#) **11**, 1292 (2021).
- [291] M. Chamanzar, M. G. Scopelliti, J. Bloch, N. Do, *et al.*, “Ultrasonic sculpting of virtual optical waveguides in tissue,” [Nature Communications](#) **10**, 92 (2019).
- [292] A. Ishijima, U. Yagyu, K. Kitamura, A. Tsukamoto, *et al.*, “Nonlinear photoacoustic waves for light guiding to deep tissue sites,” [Optics Letters](#) **44**, 3006 (2019).
- [293] A. Goffin, I. Larkin, A. Tartaro, A. Schweinsberg, *et al.*, “Optical Guiding in 50-Meter-Scale Air Waveguides,” [Physical Review X](#) **13**, 011006 (2023).
- [294] D. J. Fernández, R. Muñoz, and A. Ramos, “Second order SUSY transformations with ‘complex energies’,” [Physics Letters A](#) **308**, 11 (2003).
- [295] A. A. Andrianov and F. Cannata, “Nonlinear supersymmetry for spectral design in quantum mechanics,” [Journal of Physics A: Mathematical and General](#) **37**, 10297 (2004).
- [296] D. J. Fernández, “Higher-order supersymmetric quantum mechanics,” [AIP Conference Proceedings](#) **744**, 236 (2004).
- [297] N. Chandra and N. M. Litchinitser, “Photonic bandgap engineering using second-order supersymmetry,” [Communications Physics](#) **4**, 59 (2021).
- [298] Q. Zhong, S. Nelson, M. Khajavikhan, D. N. Christodoulides, *et al.*, “Bosonic discrete supersymmetry for quasi-two-dimensional optical arrays,” [Photon. Res.](#) **7**, 1240 (2019).
- [299] C. García-Meca, A. M. Ortiz, and R. L. Sáez, “Supersymmetry in the time domain and its applications in optics,” [Nature Communications](#) **11**, 813 (2020).
- [300] M. Principe, G. Castaldi, M. Consales, A. Cusano, *et al.*, “Supersymmetry-Inspired Non-Hermitian Optical Couplers,” [Scientific Reports](#) **5**, 8568 (2015).
- [301] W. Walasik, B. Midya, L. Feng, and N. M. Litchinitser, “Supersymmetry-guided method for mode selection and optimization in coupled systems,” [Opt. Lett.](#) **43**, 3758 (2018).
- [302] A. Contreras-Astorga and V. Jakubský, “Photonic systems with two-dimensional landscapes of complex refractive index via time-dependent supersymmetry,” [Phys. Rev. A](#) **99**, 53812 (2019).

- [303] A. Macho, R. Llorente, and C. García-Meca, “Supersymmetric Transformations in Optical Fibers,” [Phys. Rev. Applied](#) **9**, 14024 (2018).
- [304] A. Macho, *Multi-Core Fiber and Optical Supersymmetry: Theory and Applications*, [Ph.D. thesis](#), Universitat Politècnica de València (2019).
- [305] S. Longhi, “Supersymmetric Bragg gratings,” [Journal of Optics](#) **17**, 045803 (2015).
- [306] G. Queraltó, V. Ahufinger, and J. Mompart, “Mode-division (de)multiplexing using adiabatic passage and supersymmetric waveguides,” [Optics Express](#) **25**, 27396 (2017).
- [307] W. Walasik, N. Chandra, B. Midya, L. Feng, *et al.*, “Mode-sorter design using continuous supersymmetric transformation,” [Optics Express](#) **27**, 22429 (2019).
- [308] S. Longhi, “Supersymmetric transparent optical intersections,” [Opt. Lett.](#) **40**, 463 (2015).
- [309] S. Longhi and G. D. Valle, “Invisible defects in complex crystals,” [Annals of Physics](#) **334**, 35 (2013).
- [310] B. Midya, “Supersymmetry-generated one-way-invisible PT-symmetric optical crystals,” [Physical Review A](#) **89**, 032116 (2014).
- [311] F. Correa, V. Jakubský, and M. S. Plyushchay, “PT-symmetric invisible defects and confluent Darboux-Crum transformations,” [Physical Review A](#) **92**, 023839 (2015).
- [312] J. Bai and D. S. Citrin, “Supersymmetric optimization of second-harmonic generation in mid-infrared quantum cascade lasers,” [Optics Express](#) **14**, 4043 (2006).
- [313] R. El-Ganainy, L. Ge, M. Khajavikhan, and D. N. Christodoulides, “Supersymmetric laser arrays,” [Physical Review A](#) **92**, 033818 (2015).
- [314] M. H. Teimourpour, L. Ge, D. N. Christodoulides, and R. El-Ganainy, “Non-Hermitian engineering of single mode two dimensional laser arrays,” [Scientific Reports](#) **6**, 33253 (2016).
- [315] M. P. Hokmabadi, N. S. Nye, R. El-Ganainy, D. N. Christodoulides, *et al.*, “Supersymmetric laser arrays,” [Science](#) **363**, 623 (2019).
- [316] A. D. Campo, M. G. Boshier, and A. Saxena, “Bent waveguides for matter-waves: supersymmetric potentials and reflectionless geometries,” [Scientific Reports](#) **4**, 5274 (2014).

- [317] S. Ward, R. Allahverdi, and A. Mafi, “A supersymmetric approach to the problem of micro-bending attenuation in optical waveguides,” [Optics Communications](#) **507**, 127743 (2022).
- [318] J. Yim, N. Chandra, X. Feng, Z. Gao, *et al.*, “Broadband continuous supersymmetric transformation: a new paradigm for transformation optics,” [eLight](#) **2**, 16 (2022).
- [319] B. Midya, W. Walasik, N. M. Litchinitser, and L. Feng, “Supercharge optical arrays,” [Optics Letters](#) **43**, 4927 (2018).
- [320] D. A. Smirnova, P. Padmanabhan, and D. Leykam, “Parity anomaly laser,” [Opt. Lett.](#) **44**, 1120 (2019).
- [321] P. I. M. Berumen and B. M. Rodríguez-Lara, “Isospectral and square-root Cholesky photonic lattices,” [Physical Review A](#) **102**, 043521 (2020).
- [322] R. El-Ganainy, K. G. Makris, and D. N. Christodoulides, “Local PT invariance and supersymmetric parametric oscillators,” [Physical Review A](#) **86**, 033813 (2012).
- [323] M. A. Miri, *Parity-time and supersymmetry in optics*, [Ph.D. thesis](#), Electronic Theses and Dissertations (2014).
- [324] Q. Zhong, J. Kou, Ş. K. Özdemir, and R. El-Ganainy, “Hierarchical Construction of Higher-Order Exceptional Points,” [Physical Review Letters](#) **125**, 203602 (2020).
- [325] S. Park, I. Lee, J. Kim, N. Park, *et al.*, “Hearing the shape of a drum for light: isospectrality in photonics,” [Nanophotonics](#) **11**, 2763 (2022).
- [326] L. Hogben, *Handbook of linear algebra*, 2nd ed. (Chapman & Hall/CRC, 2013).
- [327] A. S. Householder, “Unitary Triangularization of a Nonsymmetric Matrix,” [Journal of the ACM](#) **5**, 339 (1958).
- [328] S. Yu, X. Piao, J. Hong, and N. Park, “Bloch-like waves in random-walk potentials based on supersymmetry,” [Nature Communications](#) **6**, 8269 (2015).
- [329] S. Yu, X. Piao, J. Hong, and N. Park, “Interdimensional optical isospectrality inspired by graph networks,” [Optica](#) **3**, 836 (2016).
- [330] M. Born and V. Fock, “Beweis des Adiabatenatzes,” [Zeitschrift für Physik](#) **51**, 165 (1928).
- [331] S. Ramaseshan and R. Nityananda, “The interference of polarized light as an early example of Berry’s phase,” [Current Science](#) **55**, 1225 (1986).

- [332] R. Bhandari and J. Samuel, “Observation of topological phase by use of a laser interferometer,” [Physical Review Letters](#) **60**, 1211 (1988).
- [333] A. M. Marques and R. G. Dias, “One-dimensional topological insulators with non-centered inversion symmetry axis,” [Physical Review B](#) **100**, 041104 (2019).
- [334] S. Weimann, M. Kremer, Y. Plotnik, Y. Lumer, *et al.*, “Topologically protected bound states in photonic parity–time-symmetric crystals,” [Nature Materials](#) **16**, 433 (2017).
- [335] M. P. Estarellas, I. D’Amico, and T. P. Spiller, “Topologically protected localised states in spin chains,” [Scientific Reports](#) **7**, 42904 (2017).
- [336] S. Longhi, “Topological pumping of edge states via adiabatic passage,” [Phys. Rev. B](#) **99**, 155150 (2019).
- [337] J. Zurita, C. E. Creffield, and G. Platero, “Fast quantum transfer mediated by topological domain walls,” [Quantum](#) **7**, 1043 (2023).
- [338] G. O. Pérez, J. M. Dueñas, D. Guzmán-Silva, L. E. F. F. Torres, *et al.*, “Transport of non-classical light mediated by topological domain walls in a SSH photonic lattice,” [Scientific Reports](#) **14**, 12435 (2024).
- [339] K. Roychowdhury, J. Attig, S. Trebst, and M. J. Lawler, Supersymmetry on the lattice: Geometry, topology, and spin liquids (2022), [arXiv:2207.09475 \[cond-mat.str-el\]](#) .
- [340] C. L. Kane and T. C. Lubensky, “Topological boundary modes in isostatic lattices,” [Nature Physics](#) **10**, 39 (2014).
- [341] J. Attig, K. Roychowdhury, M. J. Lawler, and S. Trebst, “Topological mechanics from supersymmetry,” [Physical Review Research](#) **1**, 032047 (2019).
- [342] J. Attig and S. Trebst, “Classical spin spirals in frustrated magnets from free-fermion band topology,” [Physical Review B](#) **96**, 085145 (2017).
- [343] C. Li, D. Liu, and D. Dai, “Multimode silicon photonics,” [Nanophotonics](#) **8**, 227 (2018).
- [344] H. Xu, D. Dai, and Y. Shi, “Silicon Integrated Nanophotonic Devices for On-Chip Multi-Mode Interconnects,” [Applied Sciences](#) **10**, 6365 (2020).
- [345] Y. Su, Y. He, H. Chen, X. Li, *et al.*, “Perspective on mode-division multiplexing,” [Applied Physics Letters](#) **118**, 200502 (2021).

- [346] Y. Fazea and V. Mezhuyev, “Selective mode excitation techniques for mode-division multiplexing: A critical review,” [Optical Fiber Technology](#) **45**, 280 (2018).
- [347] D. J. Richardson, “New optical fibres for high-capacity optical communications,” [Philosophical Transactions of the Royal Society A: Mathematical, Physical and Engineering Sciences](#) **374**, 20140441 (2016).
- [348] T. Ma, A. B. Khanikaev, S. H. Mousavi, and G. Shvets, “Guiding Electromagnetic Waves around Sharp Corners: Topologically Protected Photonic Transport in Metawaveguides,” [Physical Review Letters](#) **114**, 127401 (2015).
- [349] M. I. Shalaev, W. Walasik, A. Tsukernik, Y. Xu, *et al.*, “Robust topologically protected transport in photonic crystals at telecommunication wavelengths,” [Nature Nanotechnology](#) **14**, 31 (2019).
- [350] Y. Poo, R.-x. Wu, Z. Lin, Y. Yang, *et al.*, “Experimental Realization of Self-Guiding Unidirectional Electromagnetic Edge States,” [Physical Review Letters](#) **106**, 093903 (2011).
- [351] S. Barik, A. Karasahin, C. Flower, T. Cai, *et al.*, “A topological quantum optics interface,” [Science](#) **359**, 666 (2018).
- [352] Y. Ota, K. Takata, T. Ozawa, A. Amo, *et al.*, “Active topological photonics,” [Nanophotonics](#) **9**, 547 (2020).
- [353] S. Kruk, A. Poddubny, D. Smirnova, L. Wang, *et al.*, “Nonlinear light generation in topological nanostructures,” [Nature Nanotechnology](#) **14**, 126 (2019).
- [354] Y. Wang, L.-J. Lang, C. H. Lee, B. Zhang, *et al.*, “Topologically enhanced harmonic generation in a nonlinear transmission line metamaterial,” [Nature Communications](#) **10**, 1102 (2019).
- [355] B. Real, C. Cantillano, D. López-González, A. Szameit, *et al.*, “Flat-band light dynamics in Stub photonic lattices,” [Scientific Reports](#) **7**, 15085 (2017).
- [356] S. Xia, A. Ramachandran, S. Xia, D. Li, *et al.*, “Unconventional Flatband Line States in Photonic Lieb Lattices,” [Physical Review Letters](#) **121**, 263902 (2018).
- [357] J. Ma, J.-W. Rhim, L. Tang, S. Xia, *et al.*, “Direct Observation of Flatband Loop States Arising from Nontrivial Real-Space Topology,” [Physical Review Letters](#) **124**, 183901 (2020).
- [358] T. Wang, J. Li, W. Zhou, and C. Chen, “Efficient cascaded wavelength conversion based on Stark-chirped rapid adiabatic passage,” [Applied Physics Express](#) **11**, 122202 (2018).

- [359] T. Wang, T. Wan, W. Zhou, and C. Chen, “Three-process cascaded frequency conversion based on Stark-chirped rapid adiabatic passage,” [J. Opt. Soc. Am. B](#) **36**, 1958 (2019).
- [360] T. Wan, T. Wang, H. Zhang, and C. Chen, “The synthesis of white-laser source based on the frequency conversion with the Stark-chirped rapid adiabatic passage,” [Results in Physics](#) **22**, 103871 (2021).
- [361] V. O. Nesterenko, A. N. Novikov, A. Y. Cherny, F. F. de Souza Cruz, *et al.*, “An adiabatic transport of Bose–Einstein condensates in double-well traps,” [Journal of Physics B: Atomic, Molecular and Optical Physics](#) **42**, 235303 (2009).
- [362] V. O. Nesterenko, A. N. Novikov, E. Suraud, and J. Kvasil, “Tunneling and transport dynamics of trapped Bose–Einstein condensates,” [Journal of Physics: Conference Series](#) **248**, 012033 (2010).
- [363] Y. Wang, S. Pandey, C. H. Greene, and N. Shivaram, “Attosecond entangled photons from two-photon decay of metastable atoms: A source for attosecond experiments and beyond,” [Phys. Rev. Res.](#) **4**, L032038 (2022).
- [364] G. M. A. Almeida, F. Ciccarello, T. J. G. Apollaro, and A. M. C. Souza, “Quantum-state transfer in staggered coupled-cavity arrays,” [Phys. Rev. A](#) **93**, 32310 (2016).
- [365] M. Bello, C. E. Creffield, and G. Platero, “Long-range doublon transfer in a dimer chain induced by topology and ac fields,” [Scientific Reports](#) **6**, 22562 (2016).
- [366] P. St-Jean, V. Goblot, E. Galopin, A. Lemaître, *et al.*, “Lasing in topological edge states of a one-dimensional lattice,” [Nature Photonics](#) **11**, 651 (2017).
- [367] H. Zhao, P. Miao, M. H. Teimourpour, S. Malzard, *et al.*, “Topological hybrid silicon microlasers,” [Nature Communications](#) **9**, 981 (2018).
- [368] S. Longhi, G. L. Giorgi, and R. Zambrini, “Landau–Zener Topological Quantum State Transfer,” [Advanced Quantum Technologies](#) **2**, 1800090 (2019).
- [369] Muhammad, W. Zhou, and C. Lim, “Topological edge modeling and localization of protected interface modes in 1D phononic crystals for longitudinal and bending elastic waves,” [International Journal of Mechanical Sciences](#) **159**, 359 (2019).
- [370] S. de Léséleuc, V. Lienhard, P. Scholl, D. Barredo, *et al.*, “Observation of a symmetry-protected topological phase of interacting bosons with Rydberg atoms,” [Science](#) **365**, 775 (2019).



- [371] C. Han, M. Kang, and H. Jeon, “Lasing at Multidimensional Topological States in a Two-Dimensional Photonic Crystal Structure,” [ACS Photonics](#) **7**, 2027 (2020).
- [372] G. J. Chaplain, J. M. D. Ponti, G. Aguzzi, A. Colombi, *et al.*, “Topological Rainbow Trapping for Elastic Energy Harvesting in Graded Su-Schrieffer-Heeger Systems,” [Physical Review Applied](#) **14**, 054035 (2020).
- [373] S. Roy, T. Mishra, B. Tanatar, and S. Basu, “Reentrant Localization Transition in a Quasiperiodic Chain,” [Physical Review Letters](#) **126**, 106803 (2021).
- [374] A. Saxena, Y. Chen, Z. Fang, and A. Majumdar, “Photonic Topological Baths for Quantum Simulation,” [ACS Photonics](#) **9**, 682 (2022).
- [375] A. Wójcik, T. Łuczak, P. Kurzyński, A. Grudka, *et al.*, “Unmodulated spin chains as universal quantum wires,” [Physical Review A](#) **72**, 034303 (2005).
- [376] N. Y. Yao, L. Jiang, A. V. Gorshkov, Z.-X. Gong, *et al.*, “Robust Quantum State Transfer in Random Unpolarized Spin Chains,” [Physical Review Letters](#) **106**, 040505 (2011).
- [377] K. Korzekwa, P. Machnikowski, and P. Horodecki, “Quantum-state transfer in spin chains via isolated resonance of terminal spins,” [Physical Review A](#) **89**, 062301 (2014).
- [378] A. Zwick, G. A. Álvarez, G. Bensusky, and G. Kurizki, “Optimized dynamical control of state transfer through noisy spin chains,” [New Journal of Physics](#) **16**, 065021 (2014).
- [379] M.-A. Miri, M. Heinrich, and D. N. Christodoulides, “Supersymmetric optical waveguides,” [Physics and Simulation of Optoelectronic Devices XXII](#) **8980**, 316 (2014).
- [380] S. D. Huber, “Topological mechanics,” [Nature Physics](#) **12**, 621 (2016).
- [381] M. Sato and Y. Ando, “Topological superconductors: a review,” [Reports on Progress in Physics](#) **80**, 076501 (2017).
- [382] X. Liu, Z. Lin, W. Song, J. Sun, *et al.*, “Perfect Excitation of Topological States by Supersymmetric Waveguides,” [Phys. Rev. Lett.](#) **132**, 016601 (2024).
- [383] B. Real, D. Guzmán-Silva, and R. A. Vicencio, “Radiation-based wave-packet generator in one-dimensional lattices,” [Physical Review B](#) **109**, 064308 (2024).
- [384] M. Tovmasyan, E. P. L. van Nieuwenburg, and S. D. Huber, “Geometry-induced pair condensation,” [Phys. Rev. B](#) **88**, 220510(R) (2013).



- [385] T. Čadež, Y. Kim, A. Andreanov, and S. Flach, “Metal-insulator transition in infinitesimally weakly disordered flat bands,” [Phys. Rev. B \*\*104\*\*, L180201 \(2021\)](#).
- [386] Y. Kim, T. Čadež, A. Andreanov, and S. Flach, “Flat band induced metal-insulator transitions for weak magnetic flux and spin-orbit disorder,” [Phys. Rev. B \*\*107\*\*, 174202 \(2023\)](#).
- [387] G. Pelegrí, A. M. Marques, V. Ahufinger, J. Mompart, *et al.*, “Interaction-induced topological properties of two bosons in flat-band systems,” [Phys. Rev. Research \*\*2\*\*, 033267 \(2020\)](#).
- [388] Y. Kuno, T. Mizoguchi, and Y. Hatsugai, “Interaction-induced doublons and embedded topological subspace in a complete flat-band system,” [Phys. Rev. A \*\*102\*\*, 063325 \(2020\)](#).
- [389] C. C. Abilio, P. Butaud, T. Fournier, B. Pannetier, *et al.*, “Magnetic field induced localization in a two-dimensional superconducting wire network,” [Physical Review Letters \*\*83\*\*, 5102 \(1999\)](#).
- [390] T. Jacqmin, I. Carusotto, I. Sagnes, M. Abbarchi, *et al.*, “Direct observation of Dirac cones and a flatband in a honeycomb lattice for polaritons,” [Physical Review Letters \*\*112\*\*, 116402 \(2014\)](#).
- [391] L. Huang, L. He, W. Zhang, H. Zhang, *et al.*, “Hyperbolic photonic topological insulators,” [Nature Communications \*\*15\*\*, 1647 \(2024\)](#).
- [392] B. M. Anderson, R. Ma, C. Owens, D. I. Schuster, *et al.*, “Engineering Topological Many-Body Materials in Microwave Cavity Arrays,” [Phys. Rev. X \*\*6\*\*, 041043 \(2016\)](#).
- [393] C. Owens, A. LaChapelle, B. Saxberg, B. M. Anderson, *et al.*, “Quarter-flux Hofstadter lattice in a qubit-compatible microwave cavity array,” [Phys. Rev. A \*\*97\*\*, 013818 \(2018\)](#).
- [394] A. Regensburger, C. Bersch, B. Hinrichs, G. Onishchukov, *et al.*, “Photon Propagation in a Discrete Fiber Network: An Interplay of Coherence and Losses,” [Physical Review Letters \*\*107\*\*, 233902 \(2011\)](#).
- [395] A. Regensburger, C. Bersch, M.-A. Miri, G. Onishchukov, *et al.*, “Parity-time synthetic photonic lattices,” [Nature \*\*488\*\*, 167 \(2012\)](#).
- [396] S. Longhi, “Effective magnetic fields for photons in waveguide and coupled resonator lattices,” [Optics Letters \*\*38\*\*, 3570 \(2013\)](#).

- [397] Y. Plotnik, M. A. Bandres, S. Stützer, Y. Lumer, *et al.*, “Analogue of Rashba pseudo-spin-orbit coupling in photonic lattices by gauge field engineering,” [Physical Review B](#) **94**, 020301 (2016).
- [398] M. Parto, H. Lopez-Aviles, J. E. Antonio-Lopez, M. Khajavikhan, *et al.*, “Observation of twist-induced geometric phases and inhibition of optical tunneling via Aharonov-Bohm effects,” [Science Advances](#) **5**, eaau8135 (2019).
- [399] P. S. J. Russell and Y. Chen, “Localization of Light in Multi-Helical Arrays of Discrete Coupled Waveguides,” [Laser and Photonics Reviews](#) **17**, 2200570 (2023).
- [400] G. Cáceres-Aravena, L. E. F. F. Torres, and R. A. Vicencio, “Topological and flat-band states induced by hybridized linear interactions in one-dimensional photonic lattices,” [Physical Review A](#) **102**, 023505 (2020).
- [401] G. Cáceres-Aravena, D. Guzmán-Silva, I. Salinas, and R. A. Vicencio, “Controlled Transport Based on Multiorbital Aharonov-Bohm Photonic Caging,” [Physical Review Letters](#) **128**, 256602 (2022).
- [402] J. Schulz, J. Noh, W. A. Benalcazar, G. Bahl, *et al.*, “Photonic quadrupole topological insulator using orbital-induced synthetic flux,” [Nature Communications](#) **13**, 6597 (2022).
- [403] C. Jiang, Y. Song, X. Li, P. Lu, *et al.*, “Photonic Möbius topological insulator from projective symmetry in multiorbital waveguides,” [Optics Letters](#) **48**, 2337 (2023).
- [404] M. Soriano and J. J. Palacios, “Theory of projections with nonorthogonal basis sets: Partitioning techniques and effective Hamiltonians,” [Phys. Rev. B](#) **90**, 075128 (2014).
- [405] F. D. R. Santos and R. G. Dias, “Methods for the construction of interacting many-body Hamiltonians with compact localized states in geometrically frustrated clusters,” [Scientific Reports](#) **10**, 4532 (2020).
- [406] P.-O. Löwdin, “Quantum theory of cohesive properties of solids,” [Advances in Physics](#) **5**, 1 (1956).
- [407] Y. Leschber and J. P. Draayer, “Orthogonal polynomial expansion for the Lowdin transformation,” [Journal of Physics A: Mathematical and General](#) **22**, 2675 (1989).
- [408] C. da Fonseca and J. Petronilho, “Explicit inverses of some tridiagonal matrices,” [Linear Algebra and its Applications](#) **325**, 7 (2001).

- [409] D. Montgomery and G. Runger, *Applied Statistics and Probability for Engineers* (John Wiley & Sons, 2010).
- [410] H. Fischer, *A History of the Central Limit Theorem: From Classical to Modern Probability Theory*, Sources and Studies in the History of Mathematics and Physical Sciences (Springer New York, 2010).
- [411] M. Mazanov, D. Román-Cortés, G. Cáceres-Aravena, C. Cid, *et al.*, “Photonic Molecule Approach to Multiorbital Topology,” *Nano Letters* **24**, 4595 (2024).
- [412] S. Chen, S. Ke, D. Zhao, J. Ye, *et al.*, “On-Chip Photonic Localization in Aharonov–Bohm Cages Composed of Microring Lattices,” *Nano Letters* **24**, 4810 (2024).
- [413] M. Ezawa, “Non-Abelian braiding of Majorana-like edge states and topological quantum computations in electric circuits,” *Phys. Rev. B* **102**, 075424 (2020).
- [414] S. Ke, D. Zhao, J. Fu, Q. Liao, *et al.*, “Topological Edge Modes in Non-Hermitian Photonic Aharonov-Bohm Cages,” *IEEE Journal of Selected Topics in Quantum Electronics* **26**, 1 (2020).
- [415] T. Yoshida, T. Mizoguchi, Y. Kuno, and Y. Hatsugai, “Square-root topological phase with time-reversal and particle-hole symmetry,” *Physical Review B* **103**, 235130 (2021).
- [416] H. Wu, G. Wei, Z. Liu, and J.-J. Xiao, “Square-root topological state of coupled plasmonic nanoparticles in a decorated Su–Schrieffer–Heeger lattice,” *Optics Letters* **46**, 4256 (2021).
- [417] R. L. Zhang, Q. P. Wu, M. R. Liu, X. B. Xiao, *et al.*, “Complex–Real Transformation of Eigenenergies and Topological Edge States in Square-Root Non-Hermitian Topoelectrical Circuits,” *Annalen der Physik* **534**, 2100497 (2022).
- [418] D. Matsumoto, T. Mizoguchi, and Y. Hatsugai, “Higher-Order Topological Insulator on a Martini Lattice and Its Square Root Descendant,” *Journal of the Physical Society of Japan* **92**, 034705 (2023).
- [419] Z.-G. Geng, Y.-X. Shen, L. Duan, Z. Chen, *et al.*, “Third-order square-root topological insulators on decorated diamond sonic crystals,” *Journal of Physics: Condensed Matter* **35**, 405001 (2023).
- [420] Z. Cheng, R. W. Bomantara, H. Xue, W. Zhu, *et al.*, “Observation of  $\pi/2$  Modes in an Acoustic Floquet System,” *Physical Review Letters* **129**, 254301 (2022).

- [421] J. Kang, T. Liu, M. Yan, D. Yang, *et al.*, “Observation of Square-Root Higher-Order Topological States in Photonic Waveguide Arrays,” [Laser & Photonics Reviews](#) **17**, 2200499 (2023).
- [422] S.-Q. Wu, Z.-K. Lin, Z. Xiong, B. Jiang, *et al.*, “Square-Root Higher-Order Topology in Rectangular-Lattice Acoustic Metamaterials,” [Physical Review Applied](#) **19**, 024023 (2023).
- [423] W. Yan, W. Cheng, W. Liu, Q. Liu, *et al.*, “Square-root higher-order topological insulators in a photonic decorated SSH lattice,” [Optics Letters](#) **48**, 3765 (2023).
- [424] S. Guo, G. Pan, J. Huang, R. Huang, *et al.*, “Realization of the square-root higher-order topology in decorated Su–Schrieffer–Heeger electric circuits,” [Applied Physics Letters](#) **123**, 043102 (2023).
- [425] B. Basa, G. L. Nave, and P. W. Phillips, “Kitaev chain with a fractional twist,” [Physical Review B](#) **106**, 125109 (2022).
- [426] A. M. Cook and J. E. Moore, “Multiplicative topological phases,” [Communications Physics](#) **5**, 262 (2022).
- [427] R. W. Bomantara, “Square-root Floquet topological phases and time crystals,” [Physical Review B](#) **106**, L060305 (2022).
- [428] L. Zhou, R. W. Bomantara, and S. Wu, “ $q$ th-root non-Hermitian Floquet topological insulators,” [SciPost Physics](#) **13**, 015 (2022).
- [429] S. Longhi, D. Gatti, and G. D. Valle, “Non-Hermitian transparency and one-way transport in low-dimensional lattices by an imaginary gauge field,” [Physical Review B](#) **92**, 094204 (2015).
- [430] Z. Lin, L. Ding, S. Chen, S. Li, *et al.*, “Photonic non-Bloch quadrupole topological insulators in coupled ring resonators,” [Physical Review A](#) **103**, 063507 (2021).
- [431] Z. Lin, L. Ding, S. Ke, and X. Li, “Steering non-Hermitian skin modes by synthetic gauge fields in optical ring resonators,” [Optics Letters](#) **46**, 3512 (2021).
- [432] H. Gao, H. Xue, Z. Gu, L. Li, *et al.*, “Anomalous Floquet non-Hermitian skin effect in a ring resonator lattice,” [Physical Review B](#) **106**, 134112 (2022).
- [433] H. Xin, W. Song, S. Wu, Z. Lin, *et al.*, “Manipulating the non-Hermitian skin effect in optical ring resonators,” [Physical Review B](#) **107**, 165401 (2023).
- [434] P. He, H.-T. Ding, and S.-L. Zhu, “Geometry and superfluidity of the flat band in a non-Hermitian optical lattice,” [Physical Review A](#) **103**, 043329 (2021).

- [435] C. Qin, B. Wang, Z. J. Wong, S. Longhi, *et al.*, “Discrete diffraction and Bloch oscillations in non-Hermitian frequency lattices induced by complex photonic gauge fields,” [Physical Review B](#) **101**, 064303 (2020).
- [436] Y. Song, Y. Chen, W. Xiong, and M. Wang, “Flexible light manipulation in non-Hermitian frequency Su–Schrieffer–Heeger lattice,” [Optics Letters](#) **47**, 1646 (2022).
- [437] L. Zheng, B. Wang, C. Qin, L. Zhao, *et al.*, “Chiral Zener tunneling in non-Hermitian frequency lattices,” [Optics Letters](#) **47**, 4644 (2022).
- [438] S. Mandal, R. Banerjee, E. A. Ostrovskaya, and T. C. H. Liew, “Nonreciprocal Transport of Exciton Polaritons in a Non-Hermitian Chain,” [Physical Review Letters](#) **125**, 123902 (2020).
- [439] S. Mandal, R. Banerjee, and T. C. H. Liew, “From the Topological Spin-Hall Effect to the Non-Hermitian Skin Effect in an Elliptical Micropillar Chain,” [ACS Photonics](#) **9**, 527 (2022).
- [440] L. S. Palacios, S. Tchoumakov, M. Guix, I. Pagonabarraga, *et al.*, “Guided accumulation of active particles by topological design of a second-order skin effect,” [Nature Communications](#) **12**, 4691 (2021).
- [441] L. Xiao, T. Deng, K. Wang, G. Zhu, *et al.*, “Non-Hermitian bulk–boundary correspondence in quantum dynamics,” [Nature Physics](#) **16**, 761 (2020).
- [442] K. Wang, T. Li, L. Xiao, Y. Han, *et al.*, “Detecting Non-Bloch Topological Invariants in Quantum Dynamics,” [Physical Review Letters](#) **127**, 270602 (2021).
- [443] M. Brandenbourger, X. Locsin, E. Lerner, and C. Coullais, “Non-reciprocal robotic metamaterials,” [Nature Communications](#) **10**, 4608 (2019).
- [444] A. Mostafazadeh, “Pseudo-Hermiticity versus PT symmetry: The necessary condition for the reality of the spectrum of a non-Hermitian Hamiltonian,” [Journal of Mathematical Physics](#) **43**, 205 (2002).
- [445] E. J. Bergholtz, J. C. Budich, and F. K. Kunst, “Exceptional topology of non-Hermitian systems,” [Reviews of Modern Physics](#) **93**, 015005 (2021).
- [446] K. Kawabata, K. Shiozaki, M. Ueda, and M. Sato, “Symmetry and Topology in Non-Hermitian Physics,” [Physical Review X](#) **9**, 041015 (2019).
- [447] F. Schindler, K. Gu, B. Lian, and K. Kawabata, “Hermitian Bulk – Non-Hermitian Boundary Correspondence,” [PRX Quantum](#) **4**, 030315 (2023).

- [448] L. Madail, S. Flannigan, A. M. Marques, A. J. Daley, *et al.*, “Enhanced localization and protection of topological edge states due to geometric frustration,” [Physical Review B](#) **100**, 125123 (2019).
- [449] F. K. Kunst, E. Edvardsson, J. C. Budich, and E. J. Bergholtz, “Biorthogonal Bulk-Boundary Correspondence in Non-Hermitian Systems,” [Physical Review Letters](#) **121**, 026808 (2018).
- [450] E. Edvardsson, F. K. Kunst, T. Yoshida, and E. J. Bergholtz, “Phase transitions and generalized biorthogonal polarization in non-Hermitian systems,” [Physical Review Research](#) **2**, 043046 (2020).
- [451] W. Deng, T. Chen, and X. Zhang, “Nth power root topological phases in Hermitian and non-Hermitian systems,” [Physical Review Research](#) **4**, 033109 (2022).
- [452] D.-S. Ma, Y. Xu, C. S. Chiu, N. Regnault, *et al.*, “Spin-Orbit-Induced Topological Flat Bands in Line and Split Graphs of Bipartite Lattices,” [Physical Review Letters](#) **125**, 266403 (2020).
- [453] T. Mizoguchi, T. Yoshida, and Y. Hatsugai, “Square-root topological semimetals,” [Physical Review B](#) **103**, 045136 (2021).
- [454] Z.-G. Geng, Y.-G. Peng, H. Lv, Z. Xiong, *et al.*, “Square-root-like higher-order topological states in three-dimensional sonic crystals,” [Journal of Physics: Condensed Matter](#) **34**, 104001 (2022).
- [455] S. Palmer, Y. Ignatov, R. V. Craster, and M. Makwana, “Asymptotically exact photonic approximations of chiral symmetric topological tight-binding models,” [New Journal of Physics](#) **24**, 053020 (2022).
- [456] Z. Gao, X. Qiao, M. Pan, S. Wu, *et al.*, “Two-Dimensional Reconfigurable Non-Hermitian Gauged Laser Array,” [Physical Review Letters](#) **130**, 263801 (2023).
- [457] N. Goldman, G. Juzeliūnas, P. Öhberg, and I. B. Spielman, “Light-induced gauge fields for ultracold atoms,” [Reports on Progress in Physics](#) **77**, 126401 (2014).
- [458] R. Hayward and F. Biancalana, “Constructing new nonlinear evolution equations with supersymmetry,” [Journal of Physics A: Mathematical and Theoretical](#) **51**, 275202 (2018).